HYDRODYNAMICS OF WAKE INTERACTIONS FOR OSCILLATING FOILS IN SIMPLE SCHOOLS

BY

AHMET GUNGOR

A THESIS SUBMITTED IN PARTIAL FULFILMENT OF THE REQUIREMENTS FOR THE DEGREE OF DOCTOR OF PHILOSOPHY

DEPARTMENT OF MECHANICAL ENGINEERING

UNIVERSITY OF ALBERTA

ABSTRACT

Hydrodynamics of the flow around multi-foil systems, representing the tailfin dynamics of collectively swimming fish or fish schooling, were investigated by directly solving the Navier-Stokes equations across a range of flow conditions. The wake and performance of the pitching foils in schooling configurations are examined across a broad parameter space, including Reynolds number, Strouhal number, pitching amplitude, phase difference, and foil spacing. The aim of this study is to enhance our understanding of the fluid dynamics associated with fish-like swimmers in schooling configurations. The insights gained are intended to inform the design of advanced man-made propulsors, operating in schooling configurations.

The dynamics of unsteady interactions behind schooling foils were explored at a Reynolds number of 1000-12000, unveiling their correlation with performance metrics. At lower Strouhal numbers, quasi-steady performance characteristics were observed, aligning with the persistence of wake symmetry. Conversely, higher Strouhal numbers exhibited unsteady interactions between vortex streets in the wake behind the foils, leading to intricate transitional behaviors. Specifically, asymmetric vortex streets produced by in-phase pitching foils merged into a symmetric wake, while out-of-phase pitching foils experienced a transition from symmetric to asymmetric wakes. Further analysis of vortex circulation indicated that secondary structures that separate from the lower wake influenced the primary structures of the upper wake, initiating the wake merging process. Wake patterns were categorized by their merged-separated and steady-transient features, prompting the development of a novel mathematical model to differentiate between merged and separated patterns. Additionally, novel scaling laws were formulated to estimate the steady performance metrics of the foils under varying flow conditions, resulting in two sets of scaling equations grounded in empirical and physics-based methodologies. The study also delved into the three-dimensional instability characteristics of parallel pitching foils in the turbulent regime. A unique spanwise instability within the separating shear layer, resulting from the proximity of one foil to another, was identified, and a mechanism responsible for the suppression of spanwise instabilities on leading edge vortices under extreme foil proximity effect was elucidated.

PREFACE

This dissertation is the original work of the author under the supervision of Dr. Arman Hemmati. Dr. Muhammad Saif Ullah Khalid collaborated on the research presented in chapters 6, 7, 9, 10, 11, and 12. Dr. Suyash Verma further collaborated and provided valuable inputs with regards to chapters 11 and 12. The contents of chapters 4, 5, 6, 7, 8, 9, and 10 have been published, and their respective citations are:

- Gungor, A., & Hemmati, A., (2020) Wake symmetry impacts the performance of tandem hydrofoils during in-phase and out-of-phase oscillations differently. *Phys. Rev. E*, 102, 043104.

- Gungor, A., & Hemmati, A., (2021) Implications of changing synchronization in propulsive performance of side-by-side pitching foils. *Bioinspir. Biomim.*, 16(3), 036006.

- Gungor, A., Khalid, M.S.U., & Hemmati, A., (2021) How does switching synchronization of pitching parallel foils from out-of-phase to in-phase change their wake dynamics?. *Phys. Fluids*, 33(8), 081901.

- Gungor, A., Khalid, M.S.U., & Hemmati, A., (2022, August) Effect of Phase Difference on Wake Characteristics and Propulsive Performance of Pitching Foils in Side-by-Side Configurations. *In Fluids Engineering Division Summer Meeting*, Vol. 85840, p. V002T05A031 American Society of Mechanical Engineers.

- Gungor, A., & Hemmati, A., (2021) The scaling and performance of side-by-side pitching hydrofoils. *J. Fluids Struct.*, 104, 103320.

- Gungor, A., Khalid, M.S.U., & Hemmati, A., (2024) Physics-Informed Scaling Laws for the Performance of Pitching Foils in Schooling Configurations. *J. R. Soc. Interface*.

- Gungor, A., Khalid, M.S.U., & Hemmati, A., (2022) Classification of vortex patterns of oscillating foils in side-by-side configurations *J. Fluid Mech.*, 951, A37.

The content of chapter 11 is currently under revision for publication and its citation reads:

- Gungor, A., Verma, S., Khalid, M.S.U., & Hemmati, A., (2024) Foil Proximity Effect Induced Shear Layer Instability Around Oscillating Foils *J. Fluid Mech.*.

The content of chapter 12 is currently under preparation and will be submitted with the following citation:

- Gungor, A., Verma, S., Khalid, M.S.U., & Hemmati, A., (2024) Suppression of LEV Instabilities Under Extreme Foil Proximity Effect. *Phys. Rev. Fluids*.

The papers have been tailored to conform the narrative of the thesis. In particular, their abstracts have been omitted, and the introduction and methodology/problem definition sections have been restructured accordingly.

"Nevertheless, we can never deem our accomplishments sufficient, as we are obliged and determined to undertake more and greater tasks."

ACKNOWLEDGEMENTS

I must begin by expressing my deepest gratitude to my supervisor, Dr. Arman Hemmati, whose leadership made this dissertation possible. Without his unwavering patience, encouragement, and guidance, this work would not have been completed. His encouragement has always inspired me to strive for excellence, knowing that I had his steadfast support. I would also like to acknowledge the invaluable assistance I received from my supervisory committee members and examiners: Dr. Sina Ghaemi, Dr. Alexandra Komrakova, Dr. Carlos F. Lange, Dr. Jovan Nedić, and Dr. Jaime Wong. Their insightful inputs greatly contributed to shaping this work.

I have had the privilege of being part of an outstanding research group in University of Alberta. I have cherished every moment spent with all its members, and their camaraderie has been a source of immense joy and motivation. I am specifically grateful for the collaboration with valuable colleagues, including Dr. Muhammad Saif Ullah Khalid, Dr. Suyash Verma, and Arash Zargar, with whom I had the opportunity to work closey and conduct research.

Finally, I extend my heartfelt thanks to my family for their unwavering support. To my parents, my siblings, Çağrı and Aybıke, and my wife, Mahsa, for always being there for me. This dissertation is dedicated to them as a small token of my immense gratitude for everything they have done.

Contents

List of Tables

List of Figures

LIST OF ABBREVIATIONS, SYMBOLS, AND NOMENCLATURE

Latin Symbols

A	peak-to-peak trailing edge amplitude
A_f	frontal area
A^*	non-dimensional amplitude
b	separation distance between vortex cores
b^*	distance between leading edge vortex and foil surface
c	chord length
D	maximum foil thickness
h	heave motion
h_0	maximum heave amplitude
St	Strouhal number
St_D	thickness-based Strouhal number
f	frequency
f^*	reduced frequency
Re	Reynolds number
U_∞	free-stream velocity
U_{eff}	effective velocity
U_{ind}	induced velocity in horizontal direction
V_{ind}	induced velocity in vertical direction
t	time
p	pressure
u	Cartesian $x-$wise velocity component

v	Cartesian $y-$wise velocity component
x^*	vertical separation distance between the foils
y^*	horizontal separation distance between the foils
r	radial distance
Q	Q-criterion
C_D	coefficient of drag
C_L	coefficient of lift
C_L	coefficient of power
C_S	coefficient of side-force
C_T	coefficient of thrust
C_{press}	coefficient of surface pressure
F_D	drag force
F_x	side force
F_y	side force
F_t	tangential force
F_n	normal force
S	strain tensor
R	rotation tensor
P	period of pitching cycle

Greek Symbols

η	Froude efficiency
η_k	Kolmogorov length scale
α	angle of attack
ϕ	phase difference

θ	pitching motion
θ_0	maximum pitching amplitude
ω_z	spanwise vorticity
ω_z^*	normalized spanwise vorticity
λ_z	spanwise instability wavelength
Γ	circulation
Γ^*	normalized circulation
ρ	density
μ	dynamic viscosity
ν	kinematic viscosity
ξ	phase lag
χ	vortex street function
ψ	geometric angle between circulation center and foil

Other Symbols

$\widetilde{\square}$	mean (cycle-averaged)
$\overline{\square}$	mean (time-averaged)
$\dot{\square}$	first time derivative
$\ddot{\square}$	second time derivative

Abbreviations

$2D$	Two Dimensional
$3D$	Three Dimensional
AUV	Autonomous Underwater Vehicle

BvK	Bénard von Kármán
rBvK	reverse Bénard von Kármán
dBvK	deflected Bénard von Kármán
DNS	Direct Numerical Simulation
PISO	Pressure Implicit with Splitting of Operators
SIMPLE	Semi-Implicit Method for Pressure Linked Equations
LEV	Leading Edge Vortex
TEV	Trailing Edge Vortex
OGA	Overset Grid Assembly
OpenFOAM	Open-source field operation and manipulation

Chapter 1

INTRODUCTION

Swimming fish and flying birds feature some of the most fascinating natural engineering mechanics and designs on earth. Over millions of years, evolution has succeeded in developing a marvel technique for locomotion of natural species. Understanding these natural processes is critical in developing bio-inspired engineering systems for higher performance. To this end, this dissertation investigates the unsteady flow around pitching foils in schooling configurations, representing swimming fish tailfins, with a particular emphasis on wake interactions and their effects on propulsive performance. Specifically, it delves into vortex dynamics behind the foils in bio-inspired schooling configurations, develops scaling laws to estimate and comprehend their performance, and characterizes the three-dimensional instabilities emerging in their wakes.

1.1 Motivations

Fish are known to swim efficiently in groups, but why? This statement outlines the motivation behind this dissertation. That is to delve into the hydrodynamics of collective swimming behavior of fish towards designing fast, efficient, stealth, and agile underwater propulsion systems

The swimming capabilities of fish have been honed over millions of years through the evolutionary process. While not every feature they have adopted can be directly attributed to hydrodynamics, it is undeniable that they rank among the most proficient swimmers in nature. Their

near-perfect anatomies have served as a significant wellspring of inspiration for engineers in the development of next-generation bio-inspired systems. In fact, engineers have achieved remarkable success in developing a variety of robotic platforms that mimic different aspects of fish swimming (Triantafyllou and Triantafyllou, 1995; Marras and Porfiri, 2012; Ay et al., 2018), thus substantiating the efficacy of this approach.

Observing any aquarium housing multiple fish would reveal that many fish species gather in swarms while navigating, a behavior commonly known as fish schooling. It can be argued that this behaviour is driven by their social structures rather than hydrodynamic advantages. This hypothesis seems plausible, especially considering that the relatively confined environment of an aquarium may not necessarily incentivize fish to exploit hydrodynamic advantages for faster, more agile, or efficient swimming. Nevertheless, we have compelling evidence from biological experiments Herskin and Steffensen (1998); Marras et al. (2015) that fish, at least certain species, indeed improve their swimming performance by forming schools. A comprehensive understanding of the intrinsic flow physics responsible for these enhancements is imperative to unravel the potential hydrodynamic advantages that can inform the design of advanced aquatic propulsion systems. Hence, exploring the flow interactions between multiple swimmers, emblematic of schooling fish, constitutes the primary motivation behind this dissertation.

1.2 The Overview

Hydrodynamic interactions among individuals in schooling arrangements have been an intriguing and unexplored topic within the fluid mechanics community for decades (Shaw, 1962). Biological studies have revealed that trailing fish in schools consume significantly less energy compared to those in the leading positions, indicating that members in rear positions exploit wake structures for their hydrodynamic benefits (Herskin and Steffensen, 1998; Svendsen et al., 2003). Controlled experiments in fish tanks (Ashraf et al., 2016, 2017) have shown that red nose tetra fish (*Hemigrammus bleheri*) arrange themselves vertically and synchronize their tail beat frequencies when

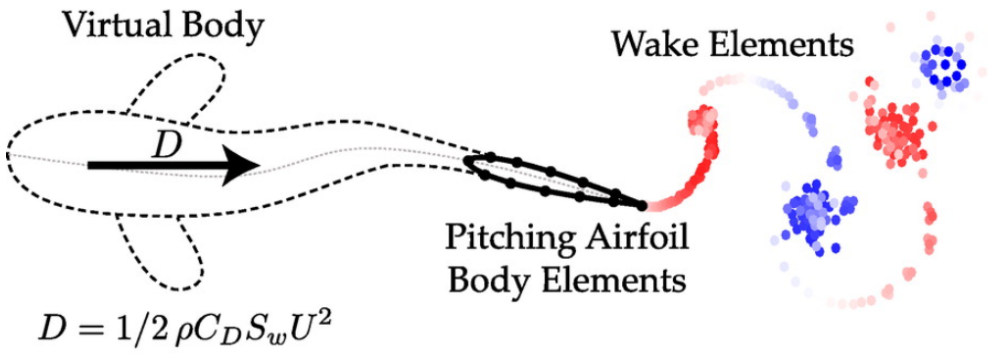

Figure 1.1: Bodies of natural aquatic animals can be decomposed into drag-producing (dashed line) and thrust-generating (full line) components. The process of thrust generation can effectively be represented by an oscillating foil. (Adopted with permission from Moored and Quinn (2019), Copyright 2019, American Institute of Aeronautics and Astronautics (AIAA)).

compelled to swim faster, suggesting a correlation between schooling behavior and improved performance. Three-dimensional ($3D$) numerical studies, simulating realistic fish schools, have similarly indicated enhanced swimming performance for certain positions Daghooghi and Borazjani (2015); Li et al. (2019). However, these investigations are constrained by fixed or limited ranges of kinematic parameters due to the high computational demands arising from the complexity of the problem. Similarly, biological investigations are restricted by the species of fish being studied, posing challenges in deriving conclusions regarding the fundamental flow physics. This underscores the need for a comprehensive study that encompasses a wide range of parameters to fully elucidate the underlying physics behind hydrodynamic interactions in fish schools.

Fish utilize various swimming modes, which are primarily categorized into undulatory and oscillatory movements, each tailored to different environmental and physiological conditions (Webb, 1984). Undulatory swimming involves the propagation of wave-like motions along the body or fins to displace fluid, a mechanism prevalent among species such as eels and knifefish. Conversely, oscillatory swimming, typical of species like tuna, entails periodic side-to-side motion of the relatively rigid caudal fin (Webb, 1984). However, these modes are not strictly distinct but rather exist along a spectrum, particularly evident when considering that the characteristics of oscillatory motion can be regarded as undulations with large wavelengths. A key criterion for distinguishing between these modes is the comparison of the wavelength of motion to body length. Oscillatory

motions exhibit wavelengths greater than their body length, while undulatory motions have wavelengths smaller than the body length (Smits, 2019). The morphology of fish species is exceptionally diverse and intricate, often linked to the type of motion they employ for locomotion (Sfakiotakis et al., 1999). A prevalent method for simplifying the analysis of fish swimming in the literature involves segmenting the fish into a drag-producing stationary body and a thrust-generating oscillatory caudal fin (Floryan et al., 2018; Moored and Quinn, 2019), as depicted in figure 1.1. This simplification may not capture the full complexity of swimming in eels or pike, which use nearly their entire body for propulsion. However, it is a useful approximation for modelling the mechanics of thunniform swimming, renowned for their efficient cruising capabilities, where the caudal fin is almost solely responsible for generating the required thrust force (Shadwick and Syme, 2008). This dissertation adopts the approach of modeling swimmers in schooling configurations as rigid teardrop foils, pitching around the center of their semicircular leading edge. Further elaboration can be found in Section 3.

Can oscillating rigid foils accurately represent the fluid dynamics surrounding swimming fish? Literature suggests that they do so quite effectively, particularly when evaluated based on performance metrics. Triantafyllou et al. (1993) found that optimal efficiency occurs when the non-dimensional oscillation frequency of the foil, commonly referred to as the Strouhal number (St), falls within the narrow range of 0.25 to 0.35. Remarkably, this moderate range closely aligns with the cruising Strouhal number observed in fish, encompassing a diverse size spectrum from daces to sharks (see figure 1.2). It is possible to extend this principle beyond fish to encompass a myriad of other aquatic animals, including amphibians, reptiles, and mammals (Gazzola et al., 2014). What is even more intriguing is that the striking consistency of this narrow Strouhal number range is not confined to the aquatic realm; it also holds true among aerial creatures that employ oscillatory motion during cruising, such as bats, birds, and insects (Taylor et al., 2003).

The applicability of the Strouhal number range across animals of different length scales, from 5-10 centimeter-long goldfish to 20-30 meter-long blue whales Gazzola et al. (2014), underscores the critical significance of non-dimensional analysis. Scaling laws in fluid mechanics have played

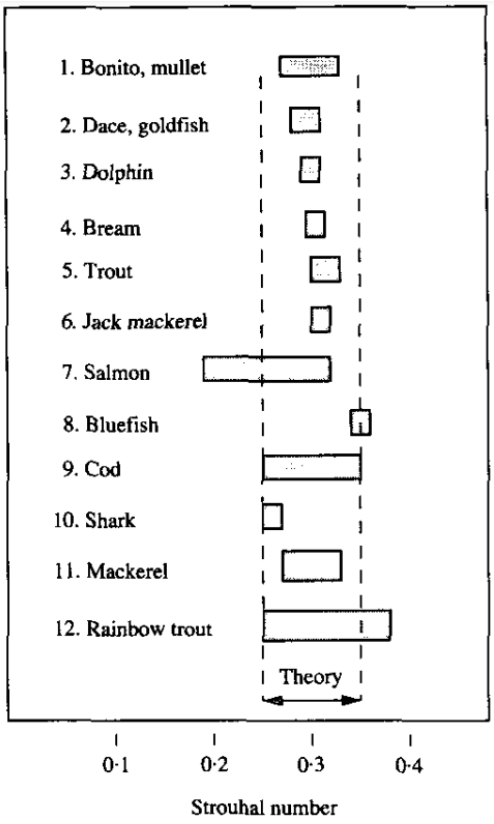

Figure 1.2: Fish navigate through water by flapping their tail fins. The Strouhal number, which characterizes the flapping motion of these tail fins, typically falls within a range of 0.25 to 0.35. (Reprinted with permission from Triantafyllou et al. (1993), Copyright 1993, Elsevier Science & Technology Journals).

a pivotal role in comprehending and predicting the behavior of fluid systems over diverse sizes. These laws operate on the principle that certain key properties of fluid flow remain consistent under proportional scaling of relevant parameters. It is pioneered with the groundbreaking research of Osborne Reynolds in the late 19th century, which introduced one of the most fundamental scaling laws in fluid mechanics: Reynolds number (Reynolds, 1883). This parameter serves as a metric to assess the relative contributions of inertial forces versus viscous forces in a fluid flow, thereby delineating the transition from laminar to turbulent flow regimes. As research has progressed, the application of scaling laws has expanded significantly, now encompassing a diverse array of flow phenomena, such as flow mixing (Wang et al., 2017), multiphase flows (Balachandar, 2009), aeroacoustics (Viswanathan, 2006), and turbulent boundary layers (De Graaff and Eaton, 2000). Scaling laws developed for aquatic locomotion have proven invaluable, shedding light on reasons

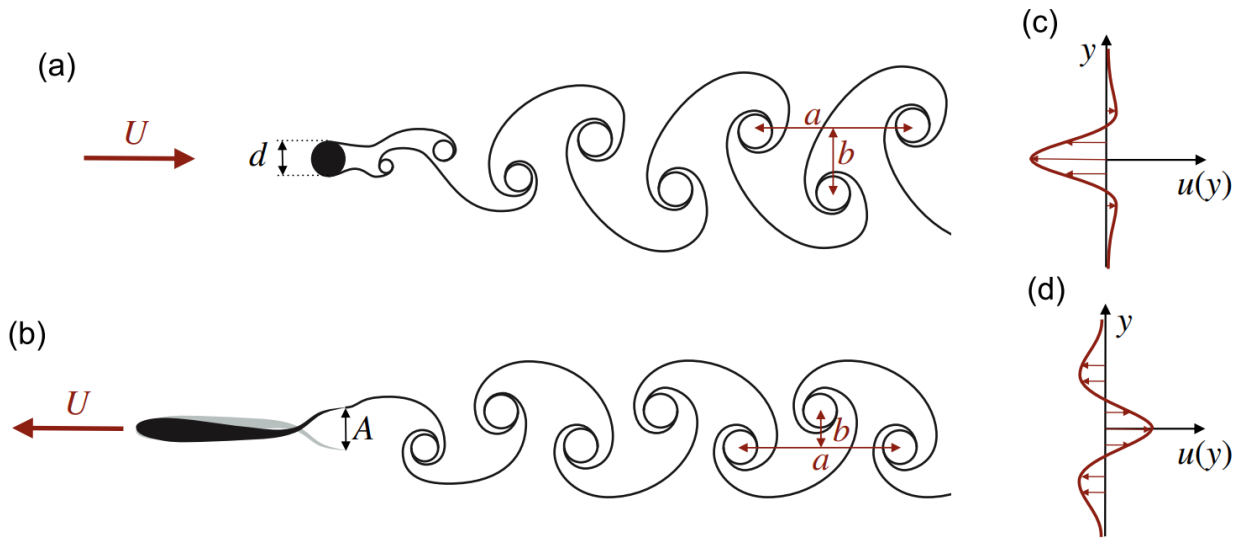

Figure 1.3: Representation of (a) a Bénard–von Kármán (*BvK*) wake behind a stationary cylinder and (b) a reverse Bénard–von Kármán (*rBvK*) wake behind an oscillating foil. The mean flow in *BvK* wakes typically shows (c) a velocity deficit, while *rBvK* wakes exhibit (d) a velocity surplus, respectively. (Reprinted with permission from Eloy (2012), Copyright 2012, Elsevier).

for the previously mentioned observation that the cruising Strouhal number for various animals is confined to a specific and narrow range, mentioned in the previous paragraph. Floryan et al. (2017, 2018) derived scaling equations for thrust generation, power consumption, and propulsive efficiency, demonstrating that the interplay between the frequency of oscillation and drag force is responsible for generating a peak in the efficiency curve. This revelation unveiled that the peak efficiency, and thus the optimal conditions for steady cruising, are dictated by the offset drag exerted on the propulsors. This exemplifies the twofold importance of scaling laws: not only do they play a crucial role in guiding design and optimization efforts, but they also serve as fundamental tools in uncovering the underlying principles that govern natural phenomena.

Another crucial element of fish-like swimming is the vortex topology behind the swimmers, which are frequently linked to their performance (Andersen et al., 2014). A stationary object submerged in a fluid in motion, or conversely an object moving through a fluid at rest, generates a region of disrupted flow trailing behind it, commonly known as a wake. This disruption occurs as the fluid detaches from the surface of the object, often resulting in formation of vortex patterns,

unsteadiness, and turbulence. Beyond their visually captivating nature, examination of wakes provides critical knowledge in the behavior of fluid flow around objects, rendering it a central focus in fluid mechanics research. Flow over a bluff body, as exemplified by a cylinder in figure 1.3(a), gives rise to the formation of a Bénard–von Kármán (*BvK*) vortex street (Eloy, 2012). This phenomenon is characterized by the periodic shedding of vortices with alternating rotations on either side of the body. Clockwise-rotating vortices are positioned above the centerline of the body, while those rotating counterclockwise are located below, jointly inducing a velocity (or momentum) deficit along the centerline, as depicted in figure 1.3(c). In contrast, the wake pattern behind oscillating foils, as illustrated in figure 1.3(b), is known as the reverse Bénard–von Kármán (*rBvK*). This pattern mirrors the *BvK* wake but with vortex rotations reversed, which leads to a velocity (or momentum) jet along the centerline (figure 1.3(d)), hence its name. Additionally, it is worth highlighting that the *BvK* wake also manifests behind foils oscillating at notably low Strouhal numbers Godoy-Diana et al. (2008). The *rBvK* wake often corresponds to net thrust, whereas the *BvK* wake is typically associated with net drag, although exceptions exist (Andersen et al., 2014). It is remarkable that a variety of other configurations are feasible, particularly evident in Schnipper et al. (2009), where numerous distinct wake patterns behind pitching foils were identified and mapped in a phase diagram. Expanding upon existing knowledge of flow physics surrounding individual oscillating foils and their resulting wake patterns, the next logical step is to delve into the dynamics of how multiple oscillating foils interact. The anticipation of diverse and intricate vortex arrangements arising from these interactions underscores the necessity for a thorough and detailed wake analysis.

The study of wake patterns generated by oscillating foils boasts a long and notable history, with Bratt (1950) being among the first to visually depict vortical structures behind foils across various flow conditions. The report demonstrated, without further elaboration, that foils with significantly higher non-dimensional frequencies tend to produce asymmetric vortex shedding patterns, often referred to as deflected Bénard Von Kármán (*dBvK*) wake. Subsequently, Jones et al. (1998), to the best of author's knowledge, were the first to discuss this phenomenon, demonstrating its association

with the generation of non-zero mean lift. Since then, extensive research has been conducted on the deflected wakes behind single oscillating foils, providing a comprehensive understanding of their dynamics Heathcote and Gursul (2007); Godoy-Diana et al. (2009); Cleaver et al. (2012). However, interaction of these vortex patterns in the case of multiple foils remains largely underexplored. A contributing factor to this gap in research is that studies on multi-foil systems typically utilize the moderate Strouhal number. While biologically inspired, this range might not align with the conditions fostering deflected wakes. Hence, Strouhal numbers examined in this dissertation span from 0.15 to 0.5, not only covering the biologically relevant range but also extending beyond it, ensuring a comprehensive assessment that addresses the existing shortfall in literature. Exploring the dynamics of interacting wakes holds the potential to uncover crucial insights into the underlying mechanisms for bio-inspired propulsion, making it essential for devising advanced flow control strategies. This is particularly vital for swarm propulsion systems, where comprehending these dynamics could significantly enhance efficiency and maneuverability.

The discussion thus far has emphasized the pivotal role of the Strouhal number in dictating the vortex shedding pattern behind oscillating foils. With an increase in the Strouhal number, the wake undergoes a sequential transition: it first shifts from the *BvK* to the *rBvK* pattern, and subsequently from the *rBvK* to the *dBvK* (Godoy-Diana et al., 2008). As the Strouhal number further increases, two-dimensional vortices become unstable to spanwise perturbations, leading to formation of three-dimensional flow structures in the wake (Deng et al., 2016; Zurman-Nasution et al., 2020). This $2D$-to-$3D$ transition is characterized by the formation of streamwise vortices, which can significantly alter the flow pattern, increase turbulence, and impact the propulsive performance of the foils.

Three-dimensional instability mechanisms hold critical importance for the aviation industry due to their profound impact on aircraft safety. Encountering the vortex wake from another aircraft, planes can experience a variety of motions including upwash, downwash, and rolling, depending on their position and orientation relative to the wake (Ortega et al., 2002). This poses substantial challenges, particularly during critical phases like landing or takeoff. Vortex pairs,

commonly observed in aircraft wakes, could develop unstable perturbations under specific circumstances, prompting to their rapid disintegration (Scorer and Davenport, 1970). This manifests itself as a rapid decay of their vorticity, a process that unfolds substantially faster than viscous diffusion alone, thus effectively diminishing their threat as a wake hazard. Understanding and predicting these instabilities is crucial for ensuring safe separation distances between airplanes and for the development of operational protocols that mitigate the risks associated with wake vortices (Spalart, 1998). Pairs of vortex rollers are essential components of the wakes of oscillating foils, predisposing them to similar perturbations. These disturbances could result in the emergence of three-dimensional structures, either by amplifying within the vortex core or causing wave-like bending across the entire roller (Leweke et al., 2016). The literature contains extensive and conclusive studies that thoroughly describe the evolution of three-dimensional wake structures behind single foils, linking them to the foil kinematics and spanwise instabilities (Deng and Caulfield, 2015; Zurman-Nasution et al., 2020; Chiereghin et al., 2020; Verma and Hemmati, 2021; Son et al., 2022; Verma et al., 2023). Yet, the influence of kinematic parameters on the emergence of spanwise instabilities in multi-foil systems, including gap distance and phase difference between the foils, remains largely unexplored.

This dissertation explores the flow around two (and in some cases 3 or 5) pitching foils in various schooling configurations and phase differences (ϕ), at a range of Reynolds number (Re) spanning from 1000 to 12000. This range captures the lower spectrum of Reynolds numbers associated with natural aquatic animal locomotion (Gazzola et al., 2014). A detailed examination of two-dimensional characteristics of the wake is carried out at $Re = 4000$, where influence of Reynolds number on the wake topology is anticipated to be negligible (Das et al., 2016). The flow is observed to transition to full turbulence behind oscillating foils at $Re = 8000$, with minimal transitional effects in the shear layer (Verma and Hemmati, 2021; Son et al., 2022). Consequently, three-dimensional numerical simulations are conducted on two infinite span pitching foils in side-by-side configurations, aiming to investigate the development of spanwise instabilities and flow dynamics under foil proximity effect.

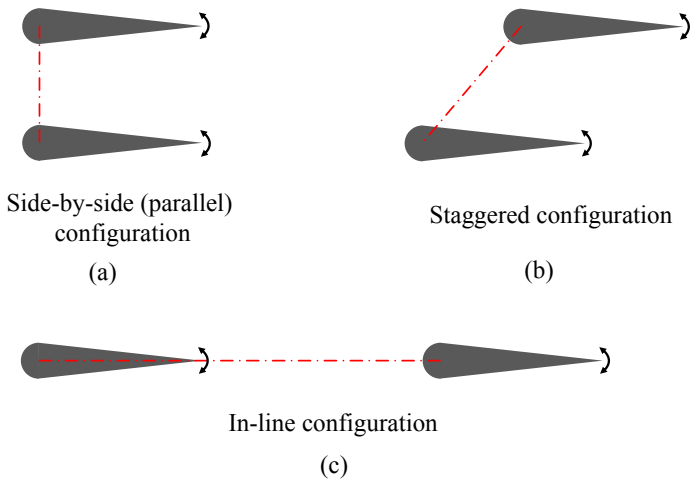

Figure 1.4: Schematics of (a) side-by-side (parallel), (b) staggered, and (c) in-line configurations.

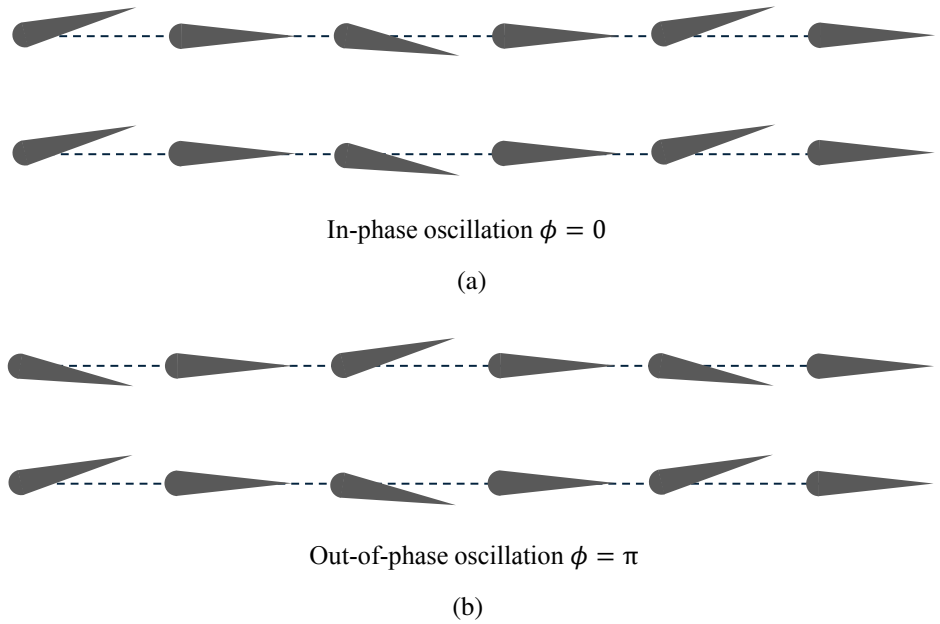

Figure 1.5: Schematics of (a) in-phase (b) out-of-phase pitching parallel foils.

In a two-dimensional plane, two foils can be arranged in different configurations. The “side-by-side” or “parallel” configuration positions the foils adjacent to each other along the vertical axis, as shown in figure 1.4a. Conversely, the "in-line” configuration aligns them horizontally, as shown in figure 1.4c. When the foils are offset both vertically and horizontally, the arrangement is described as “staggered”. While this dissertation focuses mainly on the side-by-side configuration, staggered configurations are also considered. Herein, the term “parallel” synonymously used to describe the side-by-side configuration, and “tandem” is used to describe any two-foil arrangement. For parallel configurations, two predominant phase differences studied at the extreme ends of this spectrum are in-phase and out-of-phase pitching. In-phase pitching involves identical motion of the foils, while out-of-phase pitching involves mirror-image symmetric motion, as depicted in figure 1.5. Typically, vortical structures from in-phase oscillating foils tend to converge near the wake centerline, whereas those from out-of-phase oscillating foils tend to diverge (Dewey et al., 2014).

One crucial term frequently employed in this dissertation is “foil proximity effect.” This term refers to the influence of one pitching foil on the vortex dynamics or propulsive performance of another. When one of the foils is infinite and stationary, this effect reduces to “ground effect”, which in aerodynamics is defined as the impact on forces generated by a lifting surface due to the presence of a solid boundary (Coulliette and Plotkin, 1996). Specifically, the foil proximity effect encompasses flow interactions between foils in staggered or side-by-side configurations. Lastly, the term “quasi-steady,” denotes the absence of significant alterations in flow features (both in wake and performance) from one pitching cycle to the next in this study. In contrast, the term “unsteady” (or “transient”) describes conditions where the flow dynamics exhibit temporal variations across consecutive cycles.

1.3 Objectives

This dissertation examines the complex flow dynamics, unsteady wake interactions, and hydrodynamics of closely positioned pitching foils in bio-inspired schooling configurations. There is

a particular interest in unraveling the cooperative flow mechanisms that influence propulsive performance, vortex topology, and three-dimensional instability characteristics of the flow around multiple (mostly parallel) foils. The research objectives, detailed below, are designed to make unique and novel contributions to fluid mechanics, collective swimming, and bio-inspired underwater locomotion, thereby advancing our understanding and application of these principles.

- **Objective A - Characterizing of Unsteady Vortex Dynamics and Their Implications on Propulsive Performance:** It has been shown that the gap distance and phase difference between multiple oscillating foils play pivotal roles in the development of wake patterns, significantly influencing the propulsive performance (Boschitsch et al., 2014; Dewey et al., 2014; Huera-Huarte, 2018). Yet, a gap in these studies lies in their limited utilization of the parameter space, neglecting the nuanced transient vortex interactions occurring in the wake. Thus, distinct wake patterns that emerge behind the parallel foils shall be identified and characterized, highlighting the effects of foil positioning, phase differences between the foils, pitching amplitude, and Strouhal number on the wake development. Additionally, this research shall examine the dynamics of unsteady wake interactions between the foils, concentrating on their implications on the propulsive performance metrics. The outcomes of this research aim to deepen our comprehension of the governing flow physics and control techniques for innovative underwater propulsors operating in schooling configurations, with the goal of achieving superior swimming performance.

- **Objective B - Developing of Scaling Laws for Schooling Foils:** Scaling laws are pivotal in bio-inspired propulsion, offering a framework to enhance our comprehension of flow physics. Numerous scaling laws have been developed for single oscillating foils, covering a wide array of effects pertinent to different swimming dynamics, including intermittent swimming (Akoz and Moored, 2019), the influence of Reynolds number (Senturk and Smits, 2019), combined motions (Buren et al., 2019b), foil aspect ratio (Ayancik et al., 2019), and ground effect (Mivehchi et al., 2021). Given this groundwork, there is a need to extend these scaling laws to encompass schooling foils. Thus, this research shall formulate scaling laws

for staggered foils, integrating essential parameters of collective swimming, with the goal of uncovering the universal principles that dictate the flow dynamics of fish schools.

- **Objective C - Characterizing of Spanwise Instabilities and Three-dimensional Structures:** Spanwise instabilities evolving within the vortex rollers in the wake of oscillating foils could potentially lead to development of three-dimensional streamwise structures, ultimately influencing force generation and vortex topology. The capability to predict and regulate these three-dimensional instabilities offers opportunities for advanced flow control strategies. For example, Crouch et al. (2001) proposed an active control system designed to introduce a novel instability mechanism for aircraft trailing vortices, which is known as a potential safety hazard. Despite considerable research efforts directed at understanding the evolution of three-dimensional wake structures behind individual oscillating foils, attention to foils in a side-by-side configuration has been minimal, if not entirely absent. Thus, this research shall characterize the spanwise instabilities that emerge around and in the wake of parallel oscillating foils, highlighting their correspondence to the kinematic parameters such as foil spacing, phase difference between the foils, and pitching frequency. Insights gained from this analysis could be instrumental in devising innovative vortex disintegration strategies aimed at improving the stealth features of underwater propulsion systems.

1.4 Novel Contributions

This dissertation makes several novel contributions to fluid mechanics and bio-inspired design:

(1) Identifying unsteady wake interactions behind parallel pitching foils. Particularly, this dissertation focuses on in-phase and out-of-phase motions and their association with wake topology and cycle-averaged propulsive performance. This aligns with Objective A of this thesis.

(2) Investigating the effects of abrupt phase changes from out-of-phase to in-phase on propulsive performance and wake topology. This provides conjectured insights into a peculiar schooling behavior observed in *Hemigrammus bleheri*. This contributions tackles Objective A of this thesis.

(3) Classification of wake patterns behind parallel foils across a wide range of Strouhal numbers, phase differences, and separation distances. This contribution includes the development of a unique mathematical model that quantitatively defines a threshold for distinguishing wake patterns and addresses Objective A of this thesis.

(4) Elucidating the physical mechanism that lead to the merging of vortex streets shed from each foil in a school. This tackles Objective A of this thesis.

(5) Assessing the contribution of the merger to enhanced thrust generation in parallel pitching foils. This contribution coincides with Objective A of this thesis.

(6) Developing semi-empirical scaling laws for parallel foil. The new laws consider the impacts of Reynolds number, Strouhal number, separation distance, and phase difference. This contributions addresses Objective B of this thesis.

(7) Developing physics-based scaling laws for foils in various schooling configurations. These consider the impacts of Strouhal number, positioning of the foils, phase difference, and pitching amplitude. This aligns with Objective B of this thesis.

(8) Identifying of shear layer instability on the leg of developing trailing edge vortcies (TEV) in the wake parallel foils. This contribution coincides with Objective C of this thesis.

(9) Unraveling the mechanism behind the suppression of three-dimensional instabilities in the leading edge vortices (LEVs) of parallel foils. This aligns with Objective C of this thesis.

1.5 Thesis Structures

This dissertation is organized to initially offer, in chapter 2, an extensive literature review focused on the flow dynamics surrounding oscillating bodies, whether individually or in groups. This section compiles a range of experimental, computational, and analytical studies, specifically putting emphasis on vortex dynamics, performance metrics, scaling laws, and three-dimensional instabilities. Chapter 3 delivers a detailed description of the computational methodology designed to accurately simulate the flow around two pitching foils in schooling configurations. This includes

an elaborative discussion of the numerical algorithm, computational domain, boundary conditions, and grid setup. The chapter distinguishes between two-dimensional and three-dimensional simulations, detailing them separately due to their reliance on distinct solution algorithms. Additionally, it features a comprehensive verification and validation assessment, enhancing the reliability of the numerical tools applied to model the complex wake interactions between the foils.

Chapter 4 delves into the exploration of wake interactions behind parallel pitching foils, investigating both in-phase and out-of-phase motions. It elucidates unique unsteady wake transition mechanisms at higher Strouhal numbers and explores their relationship with performance metrics. Building on the insights acquired, chapters 5 and 6 assess how abrupt phase shifts from out-of-phase to in-phase affect wake behavior and propulsive performance. This specific setup draws inspiration from schooling behavior of *Hemigrammus bleheri* observed in fish tank experiments (Ashraf et al., 2016, 2017). Chapter 5 leans towards performance implications, proposing a flow-related explanation for this behaviors, while Chapter 6 focuses on unsteady wake dynamics, considering the effects of Strouhal number and Reynolds number. Chapter 7 broadens the examination to include intermediate phase differences, thus encompassing the full spectrum of phase variation. Chapter 10 categorizes wake patterns behind parallel pitching foils by their steady-unsteady and merged-separated characteristics, introducing a novel quantitative model for wake pattern distinction. It also unveils the physics behind wake merging phenomena and its impact on propulsion. In combination, chapters $4-10$ weave a coherent narrative, culminating in the accomplishment of Objective A.

Chapters 8 and 9 establish scaling laws for predicting the propulsive performance of multiple foils through different approaches, ultimately addressing Objective B. Chapter 8 extends existing scaling relations, initially designed for single oscillating foils, to foils in a side-by-side configuration. It introduces two new empirically derived scaling terms that account for the separation distance and phase difference between the foils. The scaling laws formulated in chapter 9, on the other hand, adopts a physics-based approach to model interactions between foils, enabling ac-

curate estimations of foil performance across any schooling configuration and various kinematic parameters.

Objective C is explored in chapter 11 and 12, which investigate the onset of three-dimensional instabilities in foils arranged in the side-by-side configuration. Chapter 11 investigates a novel shear layer instability on the legs of newly shed trailing edge vortices. The role of foil-foil interactions on the emergence of the instability is characterized through a combination of qualitative and quantitative assessments. Chapter 12 investigates the occurrence of spanwise instabilities in leading edge vortices, introducing a mechanism for their suppression attributed to the pronounced foil proximity effect.

Chapter 13 provides a detailed summary of key findings and conclusions derived from this study, offering an extensive overview of the acquired knowledge and its implications. It then looks forward, identifying opportunities for further exploration and advancement in the field. It emphasizes areas where additional studies could deepen our comprehension, setting the stage for future studies to build upon the foundational work established here.

Chapter 2

BACKGROUND

The integration of bioinspiration into engineering system design necessitates a profound comprehension of animal behaviors, spanning from the advanced aerial maneuverability of birds to the streamlined cruising characteristics of fish. This has catalyzed extensive collaborations between biologists and engineers, particularly in unsteady hydrodynamics for underwater propulsion. Using a combination of experimental analysis, mathematical models, and numerical simulations, researchers aim to gain insight to the natural swimming habits of fish and marine mammals (Triantafyllou et al., 2000), design better underwater propulsors (Buren et al., 2019a), and develop high-efficiency energy harvesting technologies (Peng and Zhu, 2009). Enhancing our comprehension of fluid dynamics in the wake of swimming fish, whether they move individually or in groups, facilitates the identification of mechanisms that promote specific behaviors observed in nature. Numerous studies on oscillatory motion of a foil, serving as a simplified model for fish locomotion, has identified wake features and swimming characteristics associated with high propulsion performance (Triantafyllou and Triantafyllou, 1995; Sfakiotakis et al., 1999).

This chapter presents a comprehensive evolution of the literature in the field of fish swimming and hydrodynamics, related to both individual and collective swimmers. It delves into a detailed examination of past research, highlighting the flow dynamics around oscillating bodies, scaling laws developed for their propulsive performance, the wake patterns behind them, interactions be-

tween these patterns in multi-body swimming scenarios, and the three-dimensional instabilities in their wakes. The aim of this review is to elucidate the intricate flow dynamics governing fish swimming phenomena and investigate their significance for developing efficient propulsion mechanisms.

2.1 Non-dimensional Parameters for Underwater Locomotion

Non-dimensional analysis is vital in studying fish-like swimming research, acting as a key instrument for elucidating and contrasting the fluid dynamics and performance under different scales and operating conditions. This method transforms physical measurements into dimensionless quantities, allowing for a broad generalization of oscillating foil behaviour. It enables the identification of universal patterns and underlying principles that dictate their dynamics. Additionally, non-dimensional analysis bridges the gap between theoretical models and practical applications, thereby advancing the development and refinement of bio-inspired propulsion technologies, and boosting their performance and adaptability to environmental conditions.

Triantafyllou et al. (1993) argued that the Strouhal number is "the governing parameter of the overall problem" in fish-like swimming, defined as:

$$St = \frac{fA}{U_\infty}. \tag{2.1}$$

Here, f denotes the oscillation frequency, A is the peak-to-peak trailing edge amplitude, and U_∞ represents the free-stream flow velocity. The Reynolds number is another important non-dimensional parameter that strongly impacts the wake and performance of oscillating foils (Das et al., 2016), defined as:

$$Re = \frac{U_\infty c}{\nu}, \tag{2.2}$$

where c is the chord length of the foil, and ν is the kinematic viscosity of the fluid. Other non-dimensional parameters frequently used in the literature include reduced frequency (f^*), non-

dimensional amplitude (A), thickness-based Strouhal number (St_D), and Swimming number (Sw). These are defined as,

$$f^* = \frac{fc}{U_\infty}, \quad A^* = \frac{A}{c}, \quad St_D = \frac{fD}{U_\infty} \quad Sw = \frac{fAc}{2\pi\nu}, \tag{2.3}$$

where D is the maximum foil thickness.

The propulsive performance metrics of oscillating foils are also frequently expressed in non-dimensional formats. Coefficients of thrust, side-force, and power are commonly utilized, denoted as:

$$C_T = \frac{F_x}{\frac{1}{2}\rho U_\infty^2 sc}, \quad C_S = \frac{F_y}{\frac{1}{2}\rho U_\infty^2 sc}, \quad C_P = \frac{F_y\dot{h} + M\dot{\theta}}{\frac{1}{2}\rho U_\infty^3 sc}. \tag{2.4}$$

Here, ρ is the fluid density, s is the span of the foil, F_x is the thrust force, F_y is the side force, M is the pitch moment. Additionally, $\dot{h}$ and $\dot{\theta}$ are the time derivatives of the heaving ($h(t)$) and pitching ($\theta(t)$) motions. In this dissertation, on the other hand, the foils undergo pure pitching motions, thereby eliminating any $F_y\dot{h}$ contribution to the power coefficient. For sinusoidal motions, they are defined as:

$$h(t) = h_0 sin(2\pi ft), \quad \theta(t) = \theta_0 sin(2\pi ft) \tag{2.5}$$

where t is time, h_0 is heaving amplitude, and θ_0 is pitching amplitude. Although sinusoidal motion is commonly employed in the literature, nonsinusoidal motion can also be prescribed to the foils (Koochesfahani, 1989; Van Buren et al., 2017). It should be noted that the term C_S is occasionally referred to as the coefficient of lift in the literature. However, this dissertation mainly adopts the term "side-force" rather than "lift" because it more accurately reflects the nuances of fish swimming dynamics. Finally, the propulsive efficiency can be calculated as the ratio of C_T to C_P, given as:

$$\eta = \frac{C_T}{C_P}. \tag{2.6}$$

This definition of efficiency is based on the useful power input and output (Moored and Quinn, 2019). However, it relies on some basic assumptions that can be difficult to justify in fish schools with close proximity.

To determine the mean values for performance metrics, this dissertation utilizes two distinct approaches. The first approach involves calculating cycle-averaged values for the coefficients of thrust, side-force, and power by averaging over the period of one pitching cycle. Here, the cycle period (P) is the duration required for a pitching foil to complete one full cycle, determined by $P = 1/f$. This method is especially beneficial for examining the transient performance characteristics of the foils. The second approach calculates the time-averaged values of these coefficients across 10 pitching cycles, contingent upon reaching statistical convergence within the simulations. Statistical convergence is verified by ensuring the percent change between consecutive pitching cycles remains below 1% for the last 10 cycles, thus reliably indicating steady performance metrics of the foils. Cycle-averaged coefficients are represented with the $\widetilde{\square}$ symbol, e.g., $\widetilde{C_T}$, $\widetilde{C_S}$, and $\widetilde{C_P}$, while time-averaged coefficients use the $\overline{\square}$ symbol, e.g., $\overline{C_T}$, $\overline{C_S}$, and $\overline{C_P}$.

2.2 Wake and Performance of an Oscillating Foil

Wake patterns of oscillating bodies have long been a focal point of research in fluid mechanics research. In this regard, wake manipulation has been extensively employed for control flow purposes. For instance, Clark and Smits (2006) conducted experimental research on a batoid-inspired oscillating fin, revealing that both viscous and pressure forces play crucial roles in thrust generation, which impact the vorticity field. Thus, they suggested that thrust generation is directly related to the vortical structures in the wake. Koochesfahani (1989) showed that foils oscillating at low frequencies produce drag force, while forming a *BvK* vortex street in their wake. The transition from drag producing to thrust generating foils occurs in virtue of wake evolution from *BvK* to reverse *BvK* vortex street, facilitated by an increase in oscillation frequency. While this correlation is

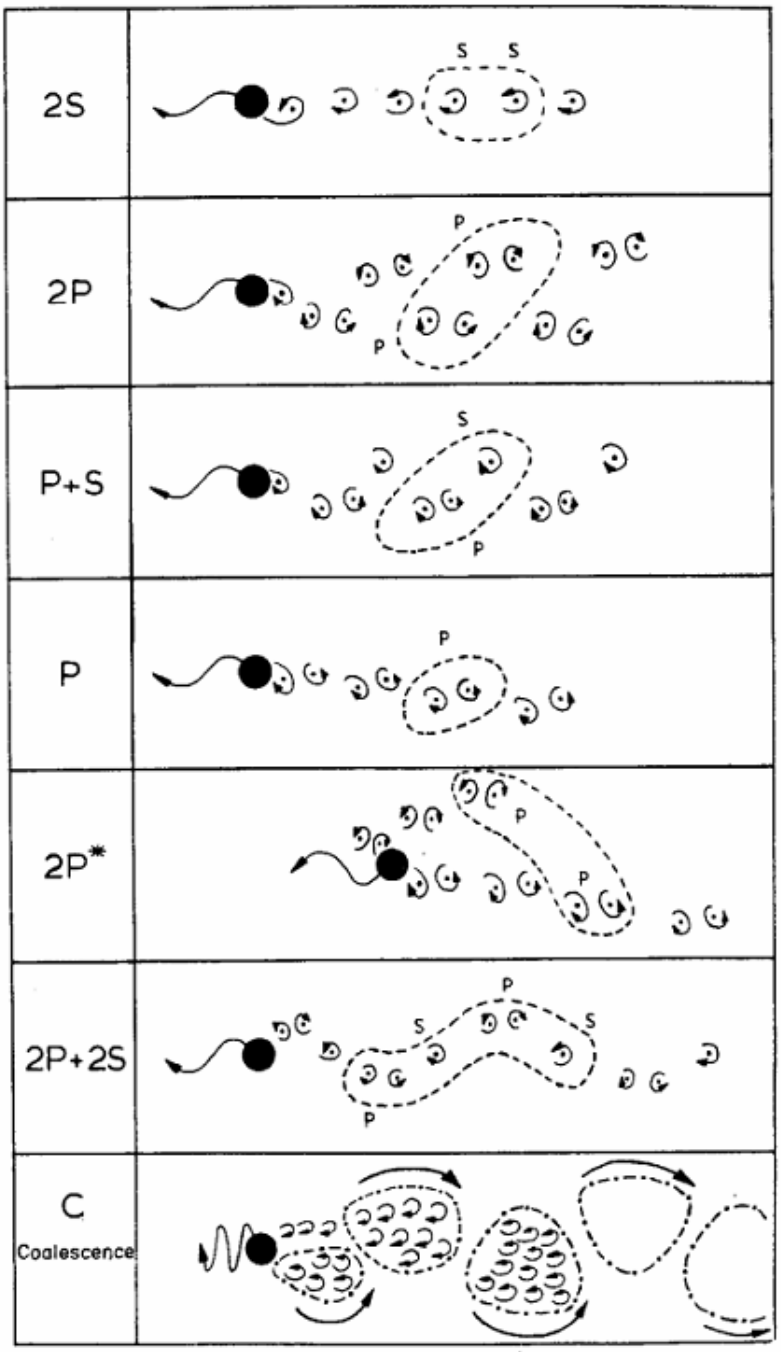

Figure 2.1: Vortex shedding patterns identified behind an oscillating cylinder. Here, "P" and "S" mean a vortex pair and a single vortex, respectively. (Reprinted with permission from Williamson and Roshko (1988), Copyright 1988, Elsevier).

commonly observed, Deng et al. (2016) illustrated that, in certain cases, there can be a noticeable delay between these two transitions, especially in the context of pitching foils.

Controlling the oscillation frequency enables the generation of diverse vortex patterns in the wake of oscillating bodies, extending beyond the standard *BvK* and *rBvK* formations. Williamson and Roshko (1988) determined the regions of major vortex patterns in the non-dimensional amplitude-wavelength (non-dimensional period of the oscillation) plane for the wake of an oscillating cylinder. These patterns, shown in figure 2.1, include P, $2P$, $2S$, $P+S$, and $2P+2S$ wakes. Here, S corresponds to a single vortex and P corresponds to a pair of vortices of opposite sign shed in each cycle, e.g. $2P+2S$ wake consists of two vortex pairs and two single vortices per cycle. Schnipper et al. (2009) performed a similar classification study on the wake of a flapping foil. They identified a wide variety of vortex patterns from well known $2P$ or $2S$ wakes to $8P$ wake that consist of 16 vortices per oscillation cycle. Furthermore, they demonstrated the time evolution of $2P$ wakes in detail as well as the transition from $2P$ to $2S$ with increasing Strouhal number.

2.2.1 Deflected Wake Phenomenon

Oscillating foils can produce asymmetric wakes in particular parameter settings, including oscillation amplitude, Strouhal number, and Reynolds number. Jones et al. (1998) performed experiments on plunging foils, revealing that deflected wakes form when the Strouhal number exceeds a certain value. This finding is consistent with the wake formation being highly reproducible. Crucially, they observed that the emergence of deflected wakes corresponds with the production of non-zero total side-force (lift), establishing a clear link between wake behavior and force generation. Furthermore, these experimental observations were corroborated by simulations using an unsteady, inviscid panel code to numerically capture wake deflection, depicted in figure 2.2. This phenomenon was previously noted but not explored by Bratt (1950). In a detailed parametric study of pitching foils at $Re = 1173$, Godoy-Diana et al. (2008) categorized wake regimes over various Strouhal numbers and dimensionless flapping amplitudes. Their findings led to the creation of a performance-wake diagram, which identified three distinct wake regimes: *BvK*, reverse *BvK*, and

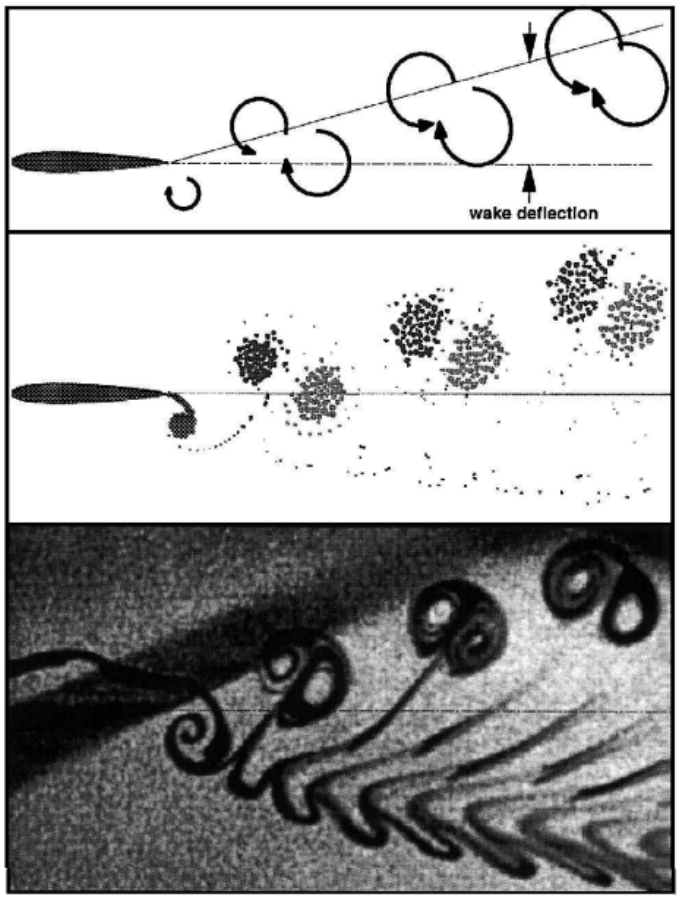

Figure 2.2: An illustrative example of a deflected wake, which is indicative of thrust and lift. (Reprinted with permission from Jones et al. (1998), Copyright 1998, American Institute of Aeronautics and Astronautics (AIAA)).

deflected *BvK*. This diagram underscores the direct impact of Strouhal number on the transitions between wake regimes. Das et al. (2016) expanded on these insights, showing that wake asymmetry is not solely influenced by oscillation amplitude and Strouhal number. Their analysis indicated that an increase in Reynolds number also disrupts the symmetry in reverse *BvK* wakes (see figure 2.3). This resulted in a performance-wake diagram that varies with Strouhal number and Reynolds number at fixed amplitudes, revealing that the diagram reaches an asymptotic range at $Re = 10^3$. Beyond this point, transitions between wake regimes are no longer evident in the flow, providing a broader understanding of the dynamics at play in the wake of oscillating foils.

Comparing biological data with the performance diagram from Godoy-Diana et al. (2008) reveals that the Strouhal number range for fish-like locomotion and flapping flight partially aligns

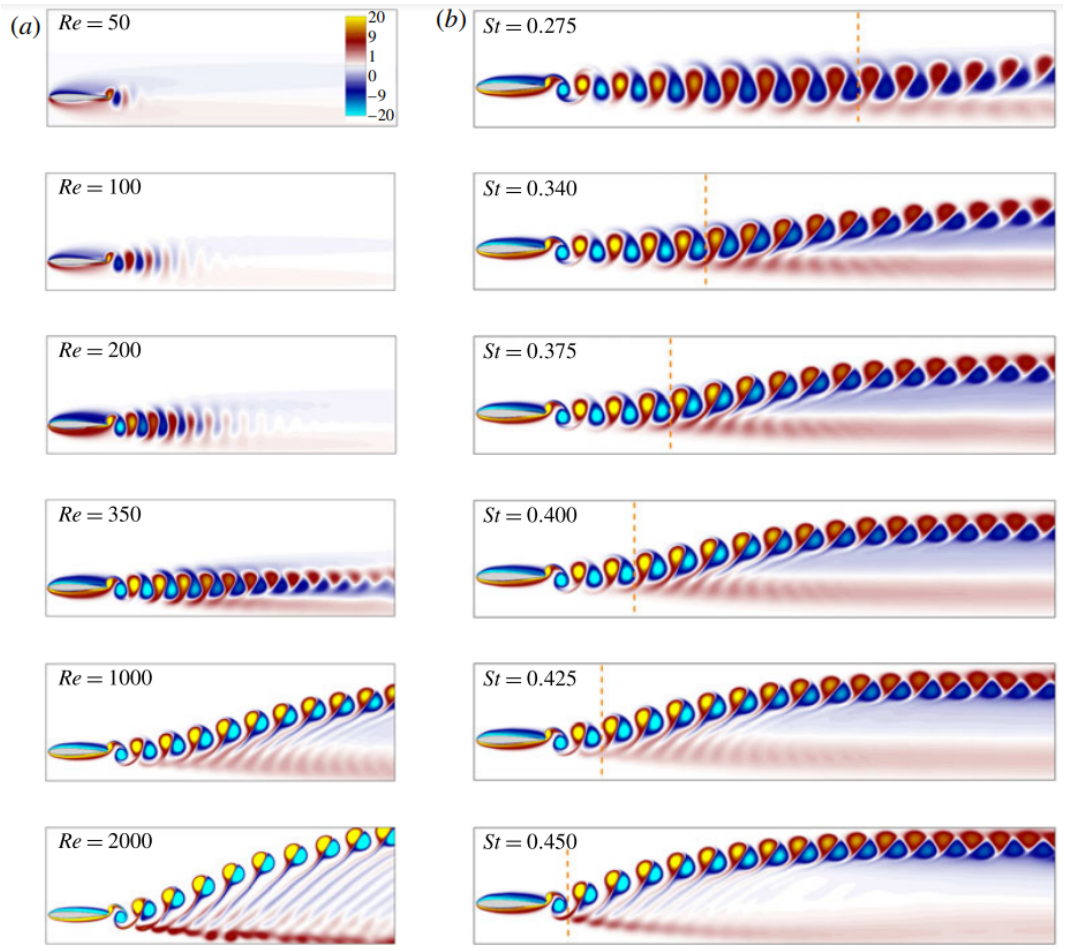

Figure 2.3: Effect of (a) Reynolds number at a fixed Strouhal number of 0.4, and (b) Strouhal number at a fixed Reynolds number of 750 on the wake topology behind a single pitching foil. (Reprinted with permission from Das et al. (2016), Copyright 2016, Cambridge University Press).

with the reverse *BvK* and deflected *BvK* wake regimes. This suggests that animals may either utilize these wake phenomena for maneuvering strategies or to avoid them during steady cruising conditions. Godoy-Diana et al. (2008) contended that while three-dimensional effects do play a role in vortex dynamics of oscillating foils, wake deflection primarily manifests as a quasi-two-dimensional (*Q2D*) phenomenon. However, a further increase in the Strouhal number leads to a transition from two-dimensional to three-dimensional wakes, indicating that transitioning from reverse *BvK* to deflected *BvK* is necessary for the emergence of three-dimensional structures in the wake (Deng et al., 2015). The underlying physical mechanism for deflected wake formation is elucidated by Godoy-Diana et al. (2009), who found that deflection occurs when the self-advection

of the initially shed dipole is strong enough to alter the main flow and subsequent dipoles away from the centerline of the wake. They also introduced a model that quantitatively predicts wake deflection by considering the offset between dipolar velocity and advection velocity of the dipoles.

There is a consensus in the literature that the direction of wake deflection significantly depends on the initial conditions (Liang et al., 2011; Cleaver et al., 2012; Godoy-Diana et al., 2008, 2009; von Ellenrieder and Pothos, 2008; Heathcote and Gursul, 2007; Lewin and Haj-Hariri, 2003; Jones et al., 1998). Liang et al. (2011) showed that direction of the first pitching stroke determines the direction of deflection, such that an upward bent wake is observed when the first stroke is downward and vice versa. This phenomenon is often referred to as dual mode and illustrated in figure 2.4. However, Cleaver et al. (2012) later argued that the deflection phenomenon is a complex process, in which multiple parameters affect the direction of the wake deflection. These parameters include the starting position, the angle of attack, and possibly the initial acceleration. Although Godoy-Diana et al. (2008, 2009), Cleaver et al. (2012), and von Ellenrieder and Pothos (2008) reported that direction of the wake deflection does not change once it is constituted, Jones et al. (1998), Heathcote and Gursul (2007), and Lewin and Haj-Hariri (2003) observed that the direction may switch from upwards to downwards or vice versa over time. For example, the experiments of Jones et al. (1998) showed that the wake deflection switches between modes (downwards and upwards) randomly. Their inviscid model, however, was not able to capture this phenomenon. They argued that this is due to small disturbances in the experimental setup that contribute to the switching of wake deflection. Later on, experimentally observed switching phenomenon was numerically reproduced by Lewin and Haj-Hariri (2003) using a viscous flow solver. However, experiments of Heathcote and Gursul (2007) showed that direction of the wake deflection does not switch randomly. Rather, this process is periodic, where the period is two orders of magnitude larger than that of the plunging cycle.

On the other hand, there are some conditions that inhibit the formation of deflected wakes. For instance,Marais et al. (2012) investigated the influence of flexibility on the wake deflection characteristics of oscillating foils. They demonstrated that the formation of an asymmetric vortex street

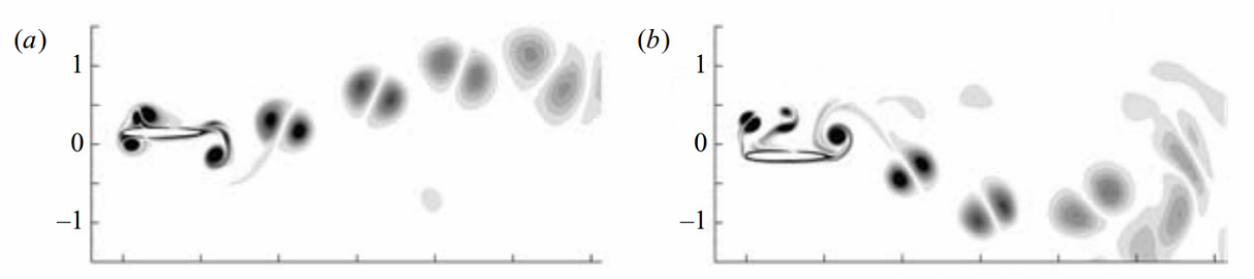

Figure 2.4: Numerical simulations of flow over a heaving foil, illustrating the switching of the wake deflection angle. (Reprinted with permission from Lewin and Haj-Hariri (2003), Copyright 2003, Cambridge University Press).

was hindered for flexible foils, although rigid foils produced deflected wakes under the same flow conditions. This is attributed to interactions between the shed vortices and flexible foils. Likewise, Calderon et al. (2014) showed that 3*D* effects in the wake of finite span foils hindered wake deflection, which was observed for effectively infinite span foils under the same flow conditions. Three-dimensionality introduced by the tip vortex, which prevents the vortex coupling, and the symmetric circulation of interconnected vortex loops, which are due to the vortex topology of a finite span foil, are two underlying reasons that were provided for the absence of wake deflection.

2.2.2 Association of Vortex Dynamics and Propulsive Performance

Efficient propulsion through implementation of effective control of vortex topology has been a great challenge in the engineering community for decades. Leading edge vortices substantially impact and often dominate the wake of oscillating foils, where their development can significantly amplify the propulsive performance of foils depending on their formation and shedding. These dynamics are deeply influenced by the kinematics of the foil. For instance, merging of leading edge and trailing edge vortices occurs when vortical structures are controlled using various parameters of foil kinematics, such as the phase angle between heave and pitch motions, Strouhal number, amplitude of heave motion, or maximum angle of attack (Anderson, 1996; Anderson et al., 1998). This phenomenon coincides with higher propulsive efficiency of foils, and improved thrust generation. In a similar study, it was shown that distinct vortex patterns emerge behind a foil

simultaneously heaving and pitching in the wake of a D-section cylinder (Gopalkrishnan, 1993; Gopalkrishnan et al., 1994; Shao and Pan, 2011). By controlling the foil position and kinematics, the interaction mode—constructive, destructive, or expanding wake modes—can be determined. These modes are respectively associated with troughs, peaks, and mixed responses in efficiency. This correlation underscores the link between vortex interactions, propulsion performance, and kinematics of the foil, showcasing the critical importance of wake topology control in optimizing the propulsion efficiency of oscillatory swimmers.

Saffman and Sheffield (1977) calculated the exact solution for potential flow over a flat plate with a free line vortex positioned on the upper boundary, which estimated highly improved lift generation. An adequately stabilized spanwise vortex can enhance the coefficient of lift by a factor of 10, which can be beneficial for the design of short takeoff and landing aircrafts (Rossow, 1978). Under the inviscid and incompressible flow assumption, trapping a free leading edge vortex on the upper surface of a two-dimensional wing is theoretically capable of increasing lift generation by introducing a low pressure region (Huang and Chow, 1982). Natural swimmers and flyers are known to exploit physical mechanisms for their best interest to achieve the most efficient propulsion in a fluid medium. Reattachment of leading edge vortices that are formed by the flow separation due to dynamic stall on the upper surface of the wing of hawkmoths or fruit flies, during the downstroke of flapping, greatly contributes to lift production (Ellington et al., 1996; Birch and Dickinson, 2001; Bomphrey et al., 2005).

Although balancing the body weight with enhanced lift production plays a crucial role in insect flight, it constitutes insignificant adversity for aquatic animals, owing to their adept exploitation of bouyant forces (Strand et al., 2005). The main concern for aquatic swimmers is overcoming the drag exerted by water, which is three orders of magnitude denser than air. Borazjani and Daghooghi (2013) carried out numerical simulations on self-propelled virtual swimmers with three different tail geometries inspired by the mackerel body. They demonstrated that an attached leading edge vortex is formed on the body during locomotion that resemble natural swimming conditions for most fish. Evolution of the leading edge vortex consequentially influence the pressure distribution

around the fish tail. Thus, different tail shapes result in different lift production. In an experimental study, the propulsive force of actively swimming bottlenose dolphins was calculated digital particle image velocimetry measurements of the vortex generated by the large amplitude fluke stroke of the dolphin (Fish et al., 2014). The effect of body shape (mackerel body or lamprey body) and swimming kinematics (anguilliform or carangiform) on the hydrodynamics of self-propelled virtual body/caudal fin swimmers was numerically examined by Borazjani and Sotiropoulos (2010) for a range of Reynolds numbers. It is noted that the form and kinematics of swimmers differently impact the swimming efficiency in viscous, transitional and inertial regimes. Liu et al. (2017) simulated a more complex model, which includes both fin–fin and body–fin interactions, by reconstructing body shape and kinematics of steady swimming crevalle jack using high-speed cameras. They demonstrated that posterior body vortices captured by the caudal fin strengthens LEVs around the fin, which produces most of the swimming thrust. Building on this, Khalid et al. (2021a) elucidated the physics underpinning the effect of employing large undulatory wavelengths by crevalle jack, demonstrating its significant contribution to enhanced swimming performance.

2.3 Scaling Laws for Energetics of Aquatic Swimmers

Research in the unsteady dynamics of oscillating foils, encompassing analytical formulations and theoretical models, has its roots in early to mid-20th century. Theodorsen (1935) developed the unsteady, linearized equations for lift and moments around oscillating foils or combinations of foils and ailerons to address wing flutter problem. Expanding upon this foundational work, Garrick (1936) formulated expressions for the mean thrust and power generated by an oscillating foil. His derivations were based on the assumptions of infinitesimally small oscillation amplitudes, an infinitely narrow, rectilinear vortex wake, and a perfect fluid. The last assumption overlooks viscous effects, implying the absence of drag force on the foil. Yet, understanding drag is vital for fully grasping the energetics of oscillating foils. Gazzola et al. (2014) established fundamental scaling relations that connect the swimming kinematics of aquatic animals with Reynolds number,

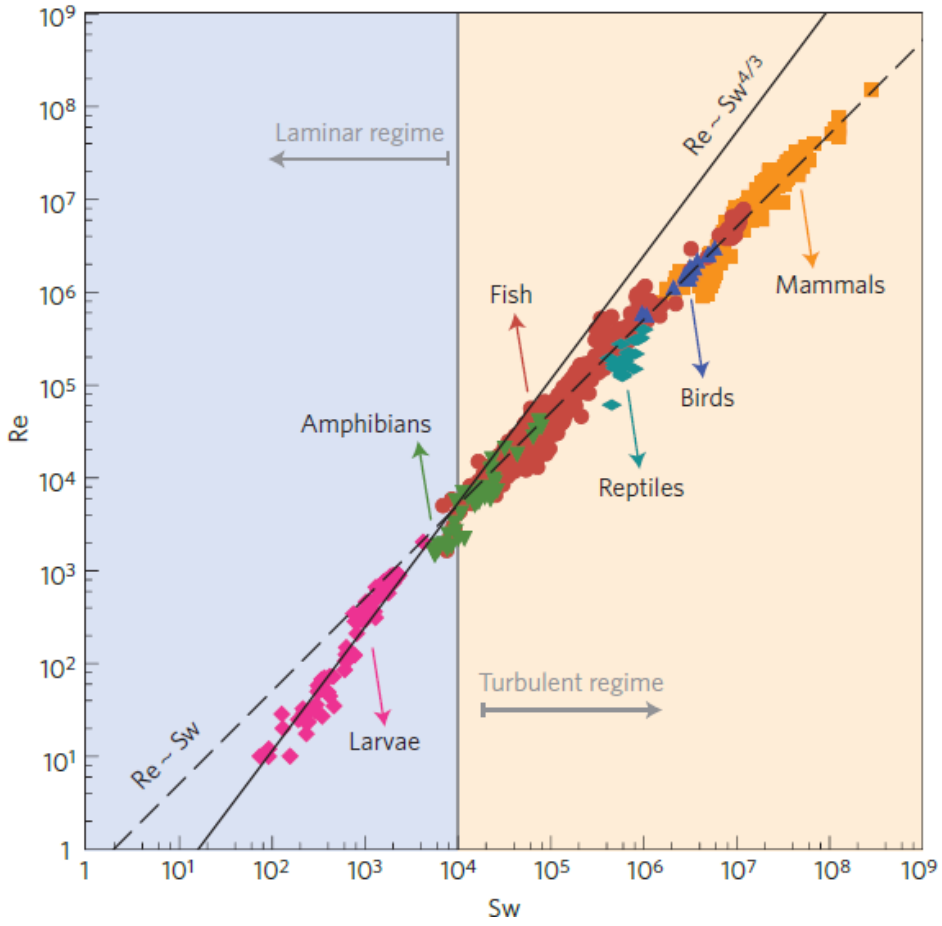

Figure 2.5: (a) Analysis of data from various aquatic animals shows that the Reynolds number of the swimmers scales with the Swimming number. In the laminar regime, the relationship is modeled as $Re = 0.03Sw^{1.33}$ with $R^2 = 0.95$, and in the turbulent regime as $Re = 0.4Sw^{1.02}$ with $R2 = 0.99$. (b) The Strouhal number demonstrates a weak dependency on the Reynolds number, approximated as $St \sim Re^{-1/4}$ for $Sw < 10^4$ (blue), and remains independent of Reynolds number for $Sw > 10^4$ (red)."(Reprinted with permission from Gazzola et al. (2014), Copyright 2014, Springer Nature).

taking into account the equilibrium between thrust and drag forces. They discovered that body kinematics change based on the flow regime, whether it be laminar (skin friction-dominated) or turbulent (pressure drag-dominated). These scaling relations, covering a wide array of aquatic life from larvae to blue whales (see figure 2.5), underscore the significant impact of drag force on aquatic locomotion.

A major limitation of linear theory lies in its assumption that the wake is infinitely narrow, a simplification that even Garrick acknowledged might not align well with experimental findings. In fact, Liu et al. (2015) demonstrated that the linear theory precisely predicts foil performance only under low oscillation amplitude and frequency conditions. When oscillating at large amplitude or high frequency, there is a notable deviation in the magnitudes, phases, and waveforms of forces from those predicted by the linear model. This suggests that certain terms, deemed negligible by linear theory over an oscillation cycle, could have substantial effects in flows with finite wake width. Considering this, Floryan et al. (2017) developed scaling relations for the cycle-averaged thrust, power, and efficiency of heaving and pitching foils, which align perfectly with experimental data (see figure 2.6), thereby offering a more nuanced understanding of flow dynamics beyond the constraints of linear theory. It was further demonstrated that these mathematical models produced results that were consistent with the biological data for aquatic animals. Expanding this work, Senturk and Smits (2019) numerically simulated pitching foils at a range of Reynolds number and Strouhal number to develop scaling relations based on the effects of Reynolds number. They identified that contributions due to the drag force on pitching foils scales with $Re^{-0.5}$, which strongly suggests laminar flow scaling. Buren et al. (2019b) focused on more complex foil kinematics, presenting scaling laws for simultaneously heaving and pitching foils. In another study, Van Buren et al. (2018) performed scaling-based analysis on the same kinematics, which revealed that streamwise speed of the flow had little or no impact on the performance of oscillating foils. This was related to the lateral velocity of the foils, which dominated the forces. Thus, they argued that performance-related conclusions drawn from tethered foils should be applicable to free-swimming conditions.

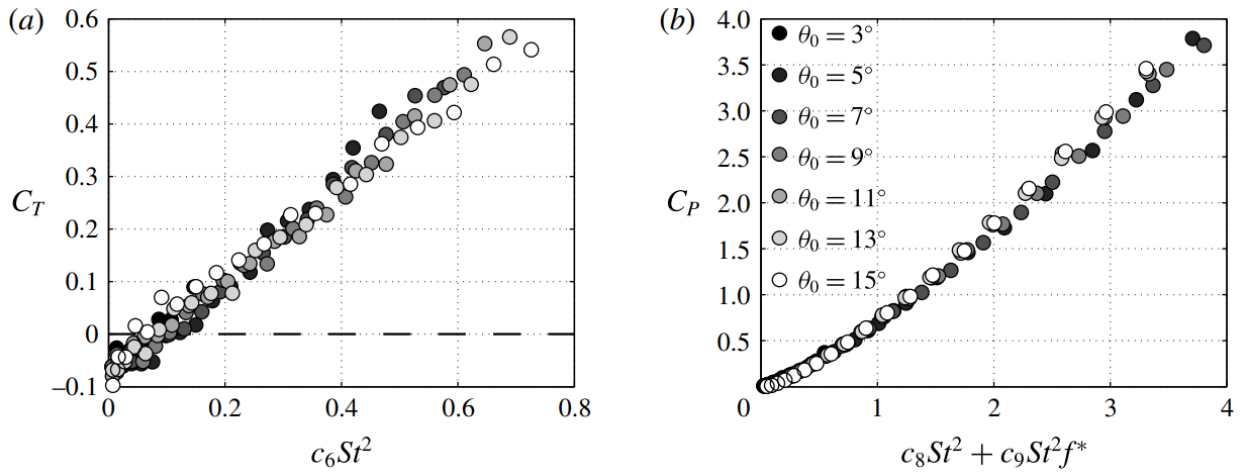

Figure 2.6: Scaling results for time-averaged (a) thrust and (b) power coefficients.(Reprinted with permission from Floryan et al. (2017), Copyright 2017, Cambridge University Press).

Moored and Quinn (2019) argued that Garrick's theory was able to capture mean thrust forces of the foils, whereas it poorly estimated the mean power. They provided a corrected power scaling for self-propelling pitching foils, which incorporated the effects of added-mass forces and large amplitude shear layer that is separated from the trailing edge. They suggested that separating shear layer contributed to the scaling of power through its circulation and vortex proximity. Ayancik et al. (2019, 2020) focused on pitching propulsors of finite spans and modified the formulations provided earlier by Moored and Quinn (2019). The new scaling formulation included modified terms that capture the effects of three-dimensional flows on performance parameters based on the foil aspect ratio. Ayancik et al. (2019, 2020) provided insights on the physical mechanisms responsible for producing forces by catacean flukes. This allowed determining an optimal non-dimensional heaving amplitude that maximizes the propulsive efficiency of oscillating foils. Similarly, Akoz and Moored (2019) altered the scaling relations for intermittently pitching foils and explained the reasons for hydrodynamic benefits of intermittent swimming using these updated relations. These studies suggest that scaling laws, when tailored to accommodate complex flow conditions, can yield profound insights into fluid dynamics and propulsion strategies.

Scaling laws have been refined to evaluate the performance of oscillating foils in interaction with their environment. Quinn et al. (2014) investigated the propulsion of a pitching foil in ground effect and suggested an empirical power-law scaling for both thrust and power. Mivehchi et al. (2021) addressed the same problem using physics-based modifications to the added mass and circulatory forces, which included the ground effect by incorporating the trailing edge vortex and its image. More recently, Han et al. (2024) focused on lift generation by pitching foils operating near a solid boundary and developed scaling laws that estimates the equilibrium altitudes. Simsek et al. (2020) modified the scaling laws of Floryan et al. (2017) and Senturk and Smits (2019) to extend their applicability for pitching foils arranged in an in-line configuration and showed that they performed better by introducing modified empirical coefficients.

2.4 Collective Locomotion of Swimmers

Fish schooling is defined as a collective behaviour in many fish species to navigate and move in the flow. Various reasons were propounded by evolutionary biologists and zoologists to explain this habit. These include, but are not limited to, improved attempts for finding mates, effective defence strategy against predators, and better chances of finding prospection. A fundamental question from engineers interested in bio-inspiration is 'Could coordinated swimming enhance the propulsive performance of an individual swimmer?' One of the pioneer studies, which addressed this question, was presented by Weihs (1973). They argued, based on a highly idealized, two-dimensional and inviscid model, that individual fish in schooling formation might experience hydrodynamic benefits if the spacing and synchronization between swimmers was adequately tuned. Hemelrijk et al. (2015) numerically simulated viscous flows over undulating fish for a range of separation distances for four different infinite schools: diamond, side-by-side, in-line and rectangular. It was demonstrated that entire schooling formations, except very dense ones with side-by-side formations, resulted in improved swimming efficiency. Daghooghi and Borazjani (2015) conducted large-eddy simulations of self-propelled synchronized mackerels in a variety of infinite rectangular school-

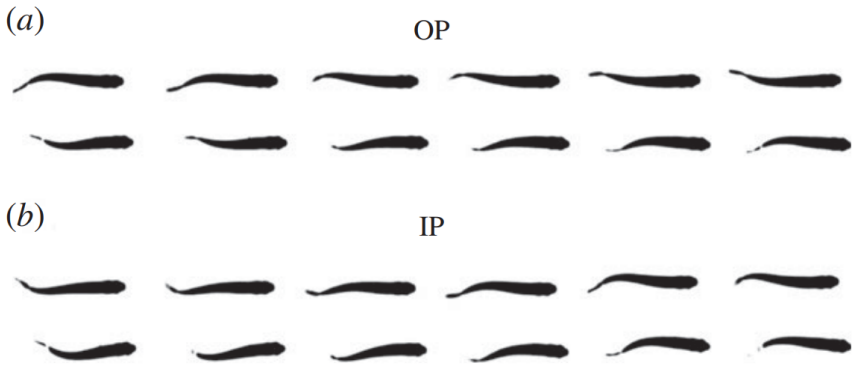

Figure 2.7: (a) Out-of-phase (OP), (b) in-phase (IP) synchronization states observed in two *Hemigrammus bleheri* swimming side-by-side. (Reprinted with permission from Ashraf et al. (2016), Copyright 2017, The Royal Society (U.K.)).

ing patterns. They observed that schooling fish enjoyed significant enhancements in swimming speed without more power requirements. They achieve this through exploitation of the channeling effect. These studies strongly indicate that collective swimmers derive significant hydrodynamic advantages from multi-body configurations.

Empirical evidence from direct observations of living fish also suggests that the energetic benefits motivates the fish schooling behaviour. Marras et al. (2015) revealed that fish within a school experience lower swimming costs than those swimming alone at equivalent speeds. Notably, while fish positioned behind others achieve the most significant energy savings, even those at the forefront of a school benefit energetically compared to solitary swimming. This indicates an overall net energetic advantage for all positions within a school. Ashraf et al. (2016, 2017) further explored this phenomenon by analyzing the swimming behaviors of red nose tetra fish (*Hemigrammus bleheri*) in a controlled-velocity shallow-water tunnel. Through stereoscopic video analysis of fish kinematics, it was explored that fish locomote in a side-by-side configuration while synchronizing their tail beat frequencies either in-phase or out-of-phase as shown in figure 2.7. Remarkably, their synchronized swimming behavior strongly correlated with increased water speed (see figure 2.8), suggesting that proper positioning and coordination among swimmers significantly boost propulsive performance, which is needed for overcoming demanding flow conditions.

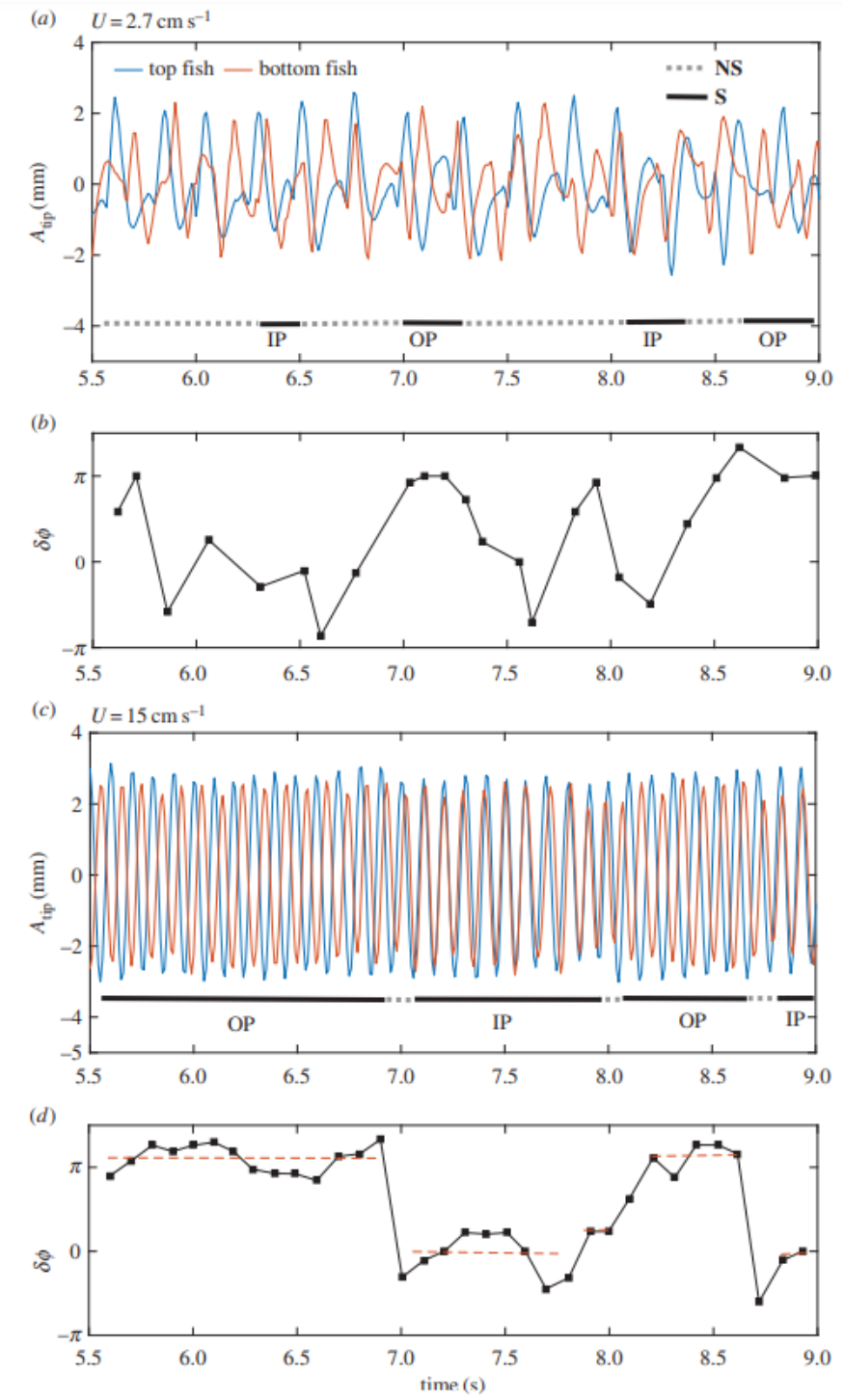

Figure 2.8: Typical caudal fin tip kinematics for (a) slow ($2.7 cms^{-1}$) and (c) fast ($15 cms^{-1}$) swimming velocities. Top and bottom fish from figure 2.7 are represented by blue and red lines, respectively. Phase difference plots for swimming velocities of (b) $2.7 cms^{-1}$ and (d) $15 cms^{-1}$.(Reprinted with permission from Ashraf et al. (2016), Copyright 2017, The Royal Society (U.K.)).

Latest developments in the field of bio-inspired swimming accelerated the efforts to examine the propulsive performance of individual members in fish schools from different perspectives. Measurements of energy consumed by a pair of fish-like robots developed by Li et al. (2020a) displayed that follower fish in a staggered configuration gained energy benefits if the phase difference between tail beat frequencies was linearly conformed with their longitudinal distance. They referred to this phenomenon as vortex phase matching. It was further validated through experiments with real fish that the follower utilized this strategy in order to exploit hydrodynamic interactions to reduce the energy cost during swimming. Later, Li et al. (2021) focused on the swimming of bio-mimetic robots in side-by-side configurations at a range of phase differences and revealed that both swimming speed and efficiency of the pair were enhanced compared to a single swimmer for the entire range. Here in-phase and out-of-phase swimming could be employed to maximize efficiency and speed, respectively. A recent study by Yu et al. (2022) examined self-organization patterns of self-propelled undulatory swimmers using a deep-reinforcement-learning technique. For two in-line swimmers with very small gap distances between them, side-by-side arrangements spontaneously emerged when the solver was set to optimize the swimming efficiency of both individuals. The same solution strategy was applied to fish schools comprised of three to six bodies, which resulted in the formation of optimal subgroups with two to four individuals. For all schooling configurations, swimmers in schools yield considerably enhanced efficiency compared with a single swimmer. Most recent studies confirm that collective locomotion outperforms a solitary one as long as the swimming conditions are appropriately disposed.

2.4.1 Propulsive Performance of Foils in Schooling Configurations

Fish schools are often modelled using multiple oscillating rigid foils arranged in different configurations due to the simplicity that it offers. Notably, dynamics of oscillating foils in side-by-side configurations have been examined through both numerical (Dong and Lu, 2007; Bao et al., 2017) and experimental approaches (Dewey et al., 2014; Kurt and Moored, 2018a; Quinn et al., 2014; Huera-Huarte, 2018). These studies have primarily concentrated on how separation distance and

oscillation phase difference influence the performance of parallel foils. For instance, Dong and Lu (2007) conducted a numerical analysis on the hydrodynamics of oscillating wavy foils positioned side-by-side, demonstrating that power consumption decreases as the separation distance between the foils increases. Moreover, they tend to generate more thrust when they oscillate out-of-phase. Simulations of side-by-side foils oscillating out-of-phase by Bao et al. (2017) explained the effects of separation distance on propulsive performance. They identified that more thrust could be experienced by the foils, when placed close to each other. Also drag-to-thrust transition occurred at lower St with decreasing separation distance. Quinn et al. (2014) investigated propulsion of a pitching foil near a stationary wall, which effectively makes it a system composed of two foils in a side-by-side arrangement with out-of-phase synchronization when the viscous effects are assumed to be negligible. It is shown that the generated lift pushed the foil away from the wall boundary at lower separation distances, while it pulls the foil towards the boundary when it was located at a shorter distance. On the contrary, the ground boundary tend to pull those foils towards itself when the foils were present at a large separation distance. They noticed approximately 40% thrust enhancement when the ground clearance was such that the vertical force acting on the foil was zero. In a more recent study, Liu et al. (2022) demonstrated that the swimming equilibria between the foil and the ground can be manipulated by employing asymmetric kinematics. Dewey et al. (2014) experimentally investigated a wide range of phase difference and separation distances, finding that in-phase oscillations led to a reduction in both thrust and power, thereby increasing efficiency (see figure 2.9). They further demonstrated that one foil could attain improved thrust and efficiency, potentially compromising the hydrodynamic performance of the adjacent foil at intermediate phase differences. Huera-Huarte (2018) compared the hydrodynamic performance of a single foil and a system of two foils arranged in side-by-side and staggered configurations. They found that side-by-side configuration benefited in terms of efficiency for in-phase oscillations, whereas the staggered configurations consistently displayed reduced efficiency.

The investigation of oscillating foils in in-line configurations has garnered interest due to its implications for understanding biological locomotion. In this regard, Akhtar et al. (2007) developed a

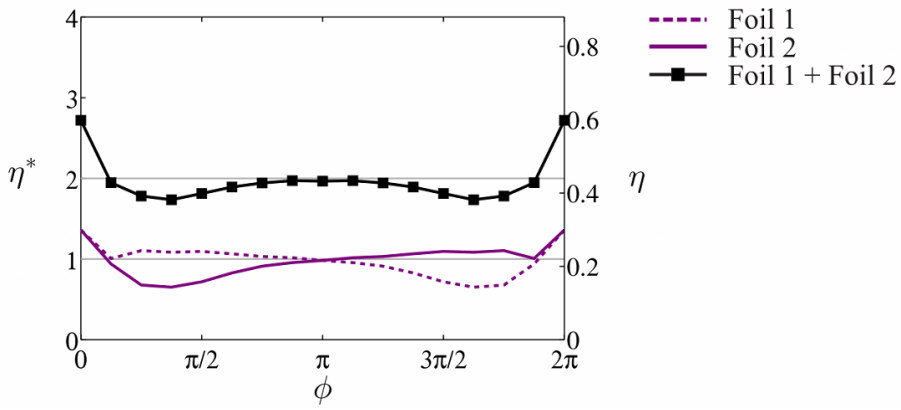

Figure 2.9: Propulsive efficiency of two pitching foils in a side-by-side configuration as a function of phase difference (ϕ). (Reprinted with permission from Dewey et al. (2014), Copyright 2014, AIP Publishing).

hydrodynamic computational model featuring two in-line flapping plates, mimicking both pitching and plunging motions, to study the interactions reminiscent of those between the dorsal and caudal fins of a bluegill sunfish. This approach could similarly apply to two fish swimming in close proximity. Their work elucidated the importance of the phase relationship between the two foils in maximizing thrust production. Furthering this research, Boschitsch et al. (2014) conducted experiments to demonstrate that the gap distance for a pair of pitching foils positioned one behind the other had a significant impact on the propulsive performance of the leading foil. They determined that closely positioned downstream body could cause the augmentation of propulsive performance parameters by around 20%. However, the hydrodynamic features were more sensitive to almost all governing kinematic parameters. Most importantly, this configuration was more beneficial for the following foil with up to 50% greater thrust and efficiency than those of an isolated foil, if the spacing and phase difference from the leading foil were optimal. An inappropriate selection of these factors might result in 50% performance reduction. More recently, Meng et al. (2022) took a further step and simulated flows over multiple flapping foils in in-line configurations. For three wings, they demonstrated that thrust of the system was optimized for a separation distance of two chord lengths with the third wing generating the most thrust. Later, they examined the system with

four, five, six and seven wings, but observed that a further increase in the number of wings did not translate into any alteration in the average thrust produced by the group.

2.4.2 Vortex Topology in Schools

The wake topology of oscillating foils in schooling configurations has been explored to a limited extent. Dong and Lu (2007) depicted the formation of vortex pairs with opposite-signed vorticity in the wake during in-phase oscillations of tandem foils, directing the wake vertically against the freestream flow. Dewey et al. (2014) analyzed vortex patterns for in-phase, mid-phase, and out-of-phase pitching foils in side-by-side configurations at a constant separation distance and Strouhal number. They visualized wake patterns for each scenario, revealing that in-phase, out-of-phase, and mid-phase pitching result in merging symmetric (see figure 2.10a-b), diverging symmetric (see figure 2.10c-d), and asymmetric wakes (see figure 2.10e-f), respectively. Quinn et al. (2014) investigated the wake topology of a pitching foil near a solid boundary and found that the wake structures was significantly affected by distance of the foil from the boundary. At larger separation distances, vortical structures tend to advect away from the surface, forming angled momentum jets, whereas they align parallel to the surface at closer distances. More recently, Ambolkar and Arumuru (2022) numerically studied two parallel foils, which were not equal in size for a range of pitching frequencies and phase differences. They showed that vortex streets shed from the foils were separated from each other as a result of their deflections in opposite directions at higher frequencies, whereas they merged in the near wake at lower frequencies for all phase differences. For intermediate oscillations, on the other hand, merger of the vortex streets occurred only for smaller phase differences.

Huera-Huarte (2018) observed an asymmetric wake in the staggered configuration of two foils but did not investigate the causes of wake deflection and asymmetry. Zhang et al. (2018), through numerical simulations, noticed that the initially symmetric wake of out-of-phase pitching parallel foils transitioned into an asymmetric pattern after 20 cycles. Similarly, Bao et al. (2017) reported emergence of an asymmetric wake behind out-of-phase oscillating parallel foils, without further

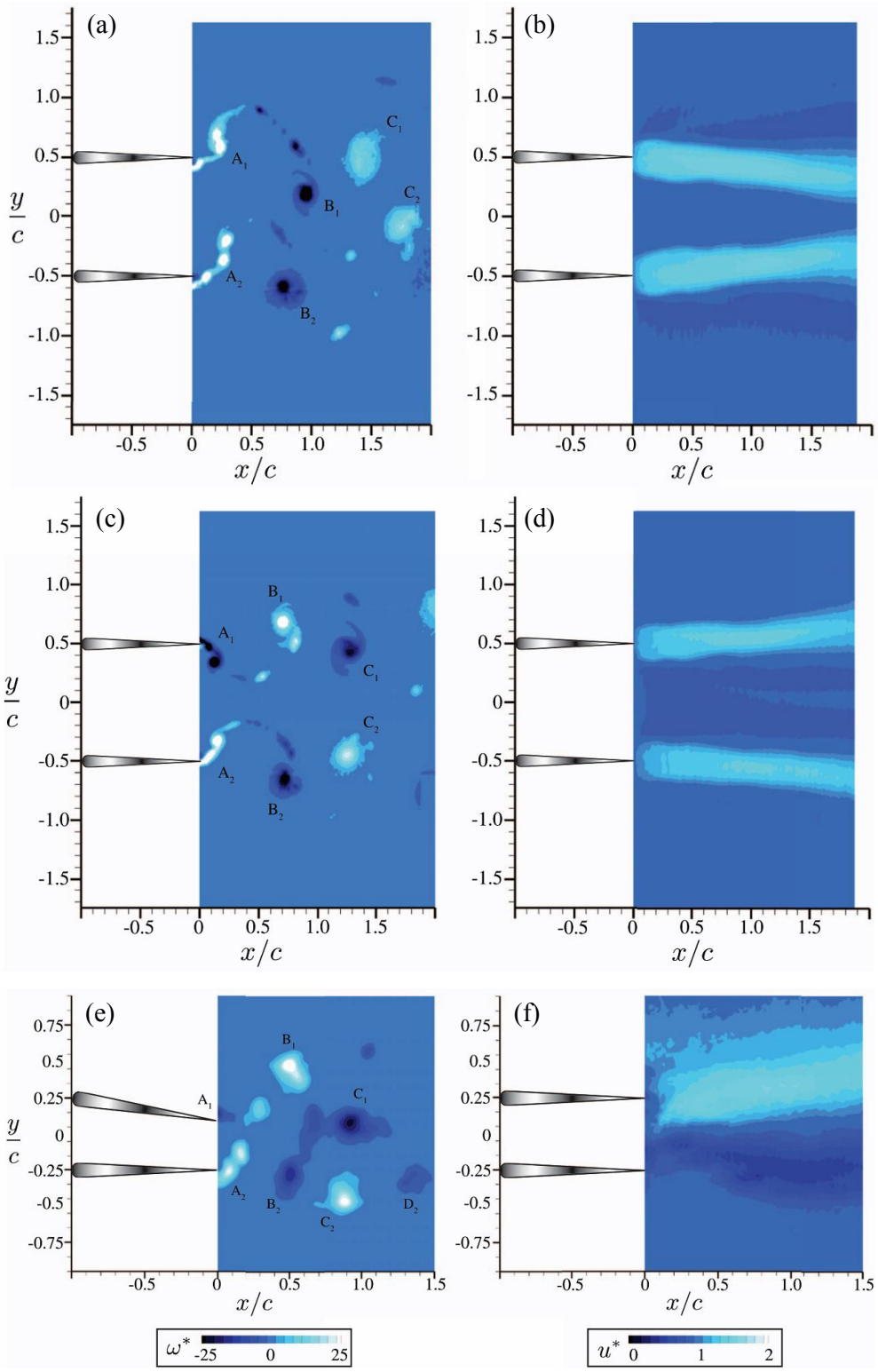

Figure 2.10: Wake structures at $St = 0.25$ for two foils in sde-by-side configurations. Instantaneous vorticity fields for (a) $\phi = 0$, (c) $\phi = \pi$, and (e) $\phi = \pi/2$. Time-averaged velocity fields for (b) $\phi = 0$, (d) $\phi = \pi$, and (f) $\phi = \pi/2$. (Adopted from Dewey et al. (2014), Copyright 2014, AIP Publishing).

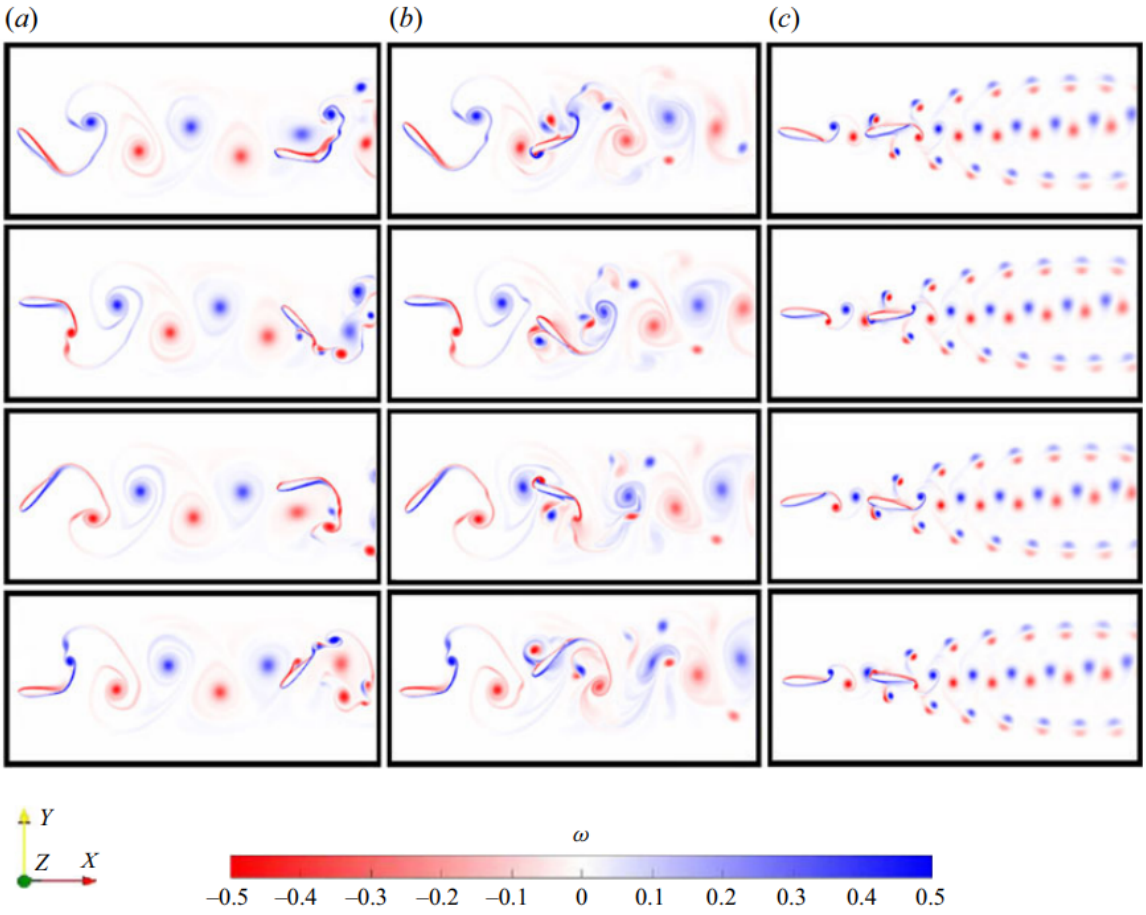

Figure 2.11: Time evolution of normalised vorticity for lift cancelling tandem configurations, depicting three distinct wake patterns. (Reprinted with permission from Lagopoulos et al. (2020), Copyright 2020, Cambridge University Press).

exploration. These studies, however, captured the asymmetric wake at a singular moment, overlooking the transient wake and its interaction process leading to asymmetry. Lagopoulos et al. (2020) demonstrated that in oscillating foils arranged in an in-line configuration, both deflected wakes and total side force production could be mitigated. They identified three distinct interaction scenarios between the leading and trailing foils, as demonstrated in figure 2.11, that enable this mitigation. Additionally, their findings revealed that the trailing foil could significantly affect the performance and wake formation of the leading foil. These studies highlight the importance of a thorough understanding of the relationship between foil kinematics and wake dynamics for effective control of vortices.

2.5 Three-dimensional Wake Instabilities

Exploring fundamental features of the vortex dynamics and wake interactions is important in aviation and marine engineering sectors. Understanding the complex unsteady flow dynamics is crucial for enhancement of safety and productivity of air transportation (Spalart, 1998), development of fish-like autonomous vehicles with high efficiency (Triantafyllou et al., 2000), and designing agile and stealth propulsion systems (Smits, 2019). These vital aspirations have prompted theoretical, experimental, and numerical studies that explore their underlying flow physics. To this end, the dynamics and instabilities of counter-rotating and co-rotating vortex pairs observed in such applications constitute the basis of many fundamental studies.

Counter-rotating vortex pairs are unstable in the presence of three-dimensional displacement perturbations, which amplify due to the combination of mutually and self-induced dynamics of vortices (Leweke et al., 2016). These perturbations appear as sinusoidal deformations with wavelengths significantly longer than the vortex core radius. They are symmetric about the midpoint between the two vortices, and are situated in planes inclined at approximately 45° to the axis connecting the vortex centers (Crow, 1970). Known as Crow instability or long wavelength instability, this phenomenon results in the amplification of deformation amplitude until the vortex cores merge, leading to the formation of a series of vortex rings through a reconnection process (Leweke and Williamson, 2011). Time evolution of the process is presented in figure 2.12. On the other hand, both counter-rotating and co-rotating vortex pairs are susceptible to short-wave instabilities within the vortex cores at sufficiently high Reynolds numbers, triggered by a resonance between the strain induced by one vortex on another and the linear Kelvin modes of the vortex (Leweke et al., 2016). This instability, often referred to as short-wavelength instability or elliptical instability, is characterized by wavelengths comparable to the vortex core diameter. Despite their distinct mechanisms, a vortex pair can manifest both types of instabilities (Leweke and Williamson, 1998), showcasing the complex dynamics at play within vortices (see figure 2.13).

The co-rotating vortices tend to merge into a single vortex unless their separation distance is more than a certain threshold. The underlying mechanism behind the merger was elucidated by

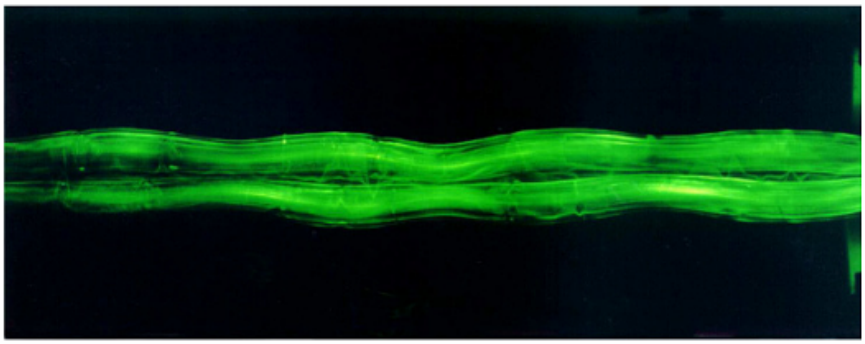

(a)

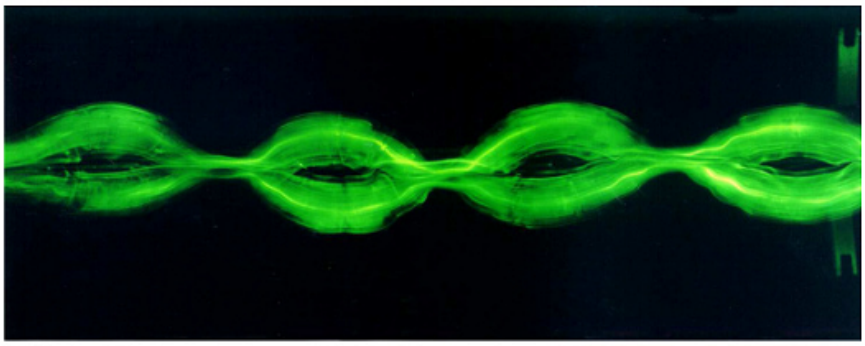

(b)

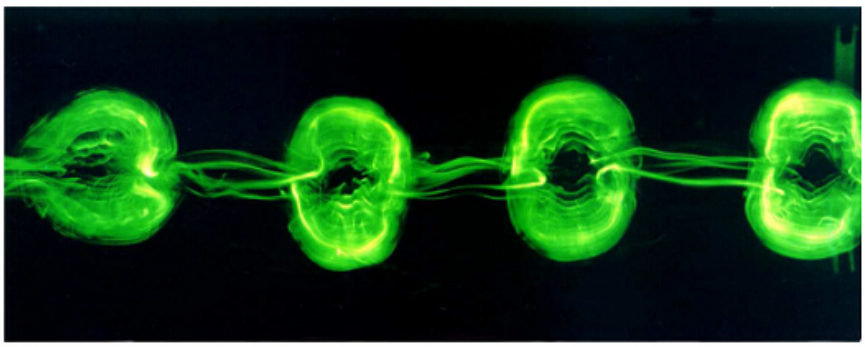

(c)

Figure 2.12: Time evolution of a vortex pair perturbed by a long-wavelength instability at $Re = 1450$. The pair is viewed from the front, with the vortices moving toward the observer. (a) $t^* = 3.2$, (b) $t^* = 5.3$, (c) $t^* = 7.0$. (Reprinted with permission from Leweke and Williamson (2011), Copyright 2011, AIP Publishing).

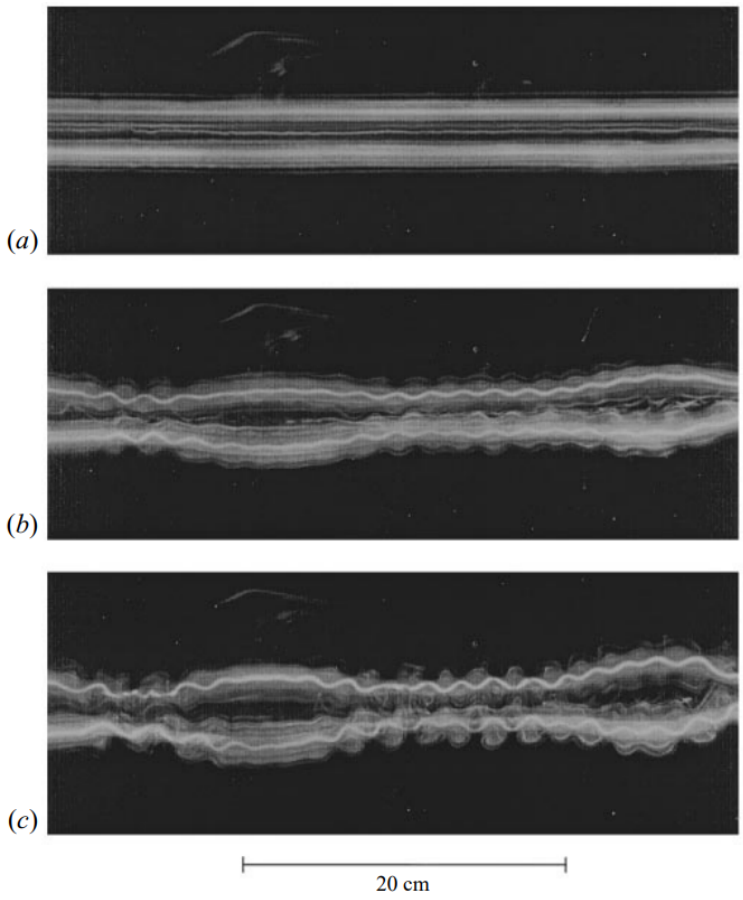

Figure 2.13: Time evolution of a vortex pair perturbed by a combined action of long-wavelength and short-wavelength instabilities at $Re = 2750$. The pair is viewed from the front, with the vortices moving toward the observer.(a) $t^* = 1.7$, (b) $t^* = 5.6$, (c) $t^* = 6.8$.(Reprinted with permission from Leweke and Williamson (1998), Copyright 1998, Cambridge University Press).

Cerretelli and Williamson (2003), which bears resemblance to the "*axisymmetrization*" principle proposed by Melander et al. (1987) for elliptic vortices. While the merger predominantly occurs in a two-dimensional plane, three-dimensionality exerts notable effects on the process, including early merging, quick expansion of the core radius, and a decrease in the maximum swirl velocity of the final vortex (Meunier et al., 2005). Moreover, three-dimensional instabilities can trigger the merging process at a greater separation distance that exceeds the critical limit allowed for merger of two-dimensional vortices (Bristol et al., 2004). This phenomenon arises when the short-wavelength elliptic instability, developing on one of the vortex cores, steers the peripheral vorticity towards the other one and creates a vorticity bridge, connecting the cores. On the other hand, experiments on

the characteristics of the elliptic instability in the pairs of counter-rotating vortices (Leweke and Williamson, 1998) revealed a distinct phase relationship between disturbances on the vortex cores. It indicates that the elliptic instability evolves in a coupled or *"cooperative"* manner. Ortega et al. (2003) delved into the dynamics of initially two-dimensional, counter-rotating vortex pairs with unequal strengths to demonstrate that long-wavelength instabilities occurring on the weaker vortex led to the formation of loops. These encircled the stronger vortex and eventually transitioned into rings. They further noticed that $2D$-to-$3D$ transition unfolded considerably earlier than the onset of visible deformations in an equal-strength counter-rotating vortex pair under similar flow conditions (Ortega et al., 2003).

A vortex in proximity to the ground effectively creates a counter-rotating vortex pair with its mirror image, rendering it susceptible to both short and long-wavelength instabilities (Benton and Bons, 2014). Modeling the ground, whether as a viscous boundary (employing a no-slip condition) or an inviscid boundary (employing slip with no-penetration condition), fundamentally alters the characteristics of the instabilities (Rabinovitch et al., 2012). Although the ground effect due to a stationary wall is well studied (Harvey and Perry, 1971; Peace and Riley, 1983), the influence of a moving boundary requires more attention.

The laminar wake behind a circular cylinder is known to transition to a three-dimensional state with increasing Reynolds number, featuring two distinct small-scale instability modes, Mode A and Mode B (Williamson, 1996). These modes are differentiated by their spanwise wavelengths, yet they share similar spatial structures. Mode A is characterized by a larger wavelength, between 3 to 4 diameters, scaling with the primary vortical structures in the wake (see figure 2.14a). In contrast, wavelength of Mode B is significantly shorter, approximately 1 diameter, and scales with the braid shear layer (see figure 2.14b). Numerical simulations by Zhang et al. (1994) revealed the existence of a third instability, Mode C, with an intermediate wavelength of about 2 diameters. Their analysis provided a concise comparison of these modes, noting that the wavelengths of secondary structures in Modes A and C are consistent in both the near and far wake. Conversely, the

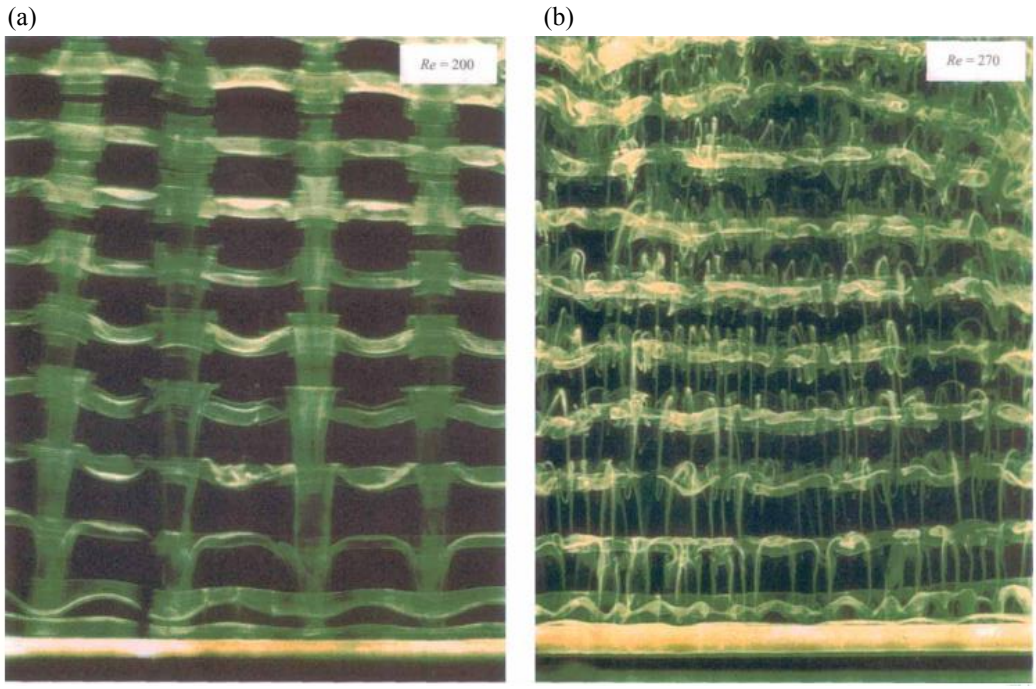

Figure 2.14: Dye visualization of three-dimensional instabilities behind a circular cylinder depicting (a) Mode A at $Re = 200$ and (b) Mode B at $Re = 270$. Flow is from bottom to top. (Reprinted with permission from Williamson (1996), Copyright 1996, Cambridge University Press).

secondary structures in Mode B are observed only in the near wake as they merge into larger-scale structures downstream.

In the context of oscillating foils, the transition from the deflected *BvK* wake to a three-dimensional wake is driven by an increase in the Strouhal number (Deng et al., 2016). Floquet stability analysis by applying three-dimensional spanwise periodic perturbations to a time-periodic two-dimensional base flow by Deng and Caulfield (2015) quantified the inherently three-dimensional linear instabilities in the wake of a pitching foil. They discovered two distinct types of unstable spanwise periodic modes: a long-wavelength mode, analogous to the Mode A instability observed in circular cylinders, and a short-wavelength mode. Subsequently, Deng et al. (2015) expanded on this study by employing Direct Numerical Simulations (DNS) to validate the presence of the instability modes identified by the Floquet analysis. The agreement between the Floquet analysis and DNS results, particularly for the short-wavelength mode, reinforces the validity of

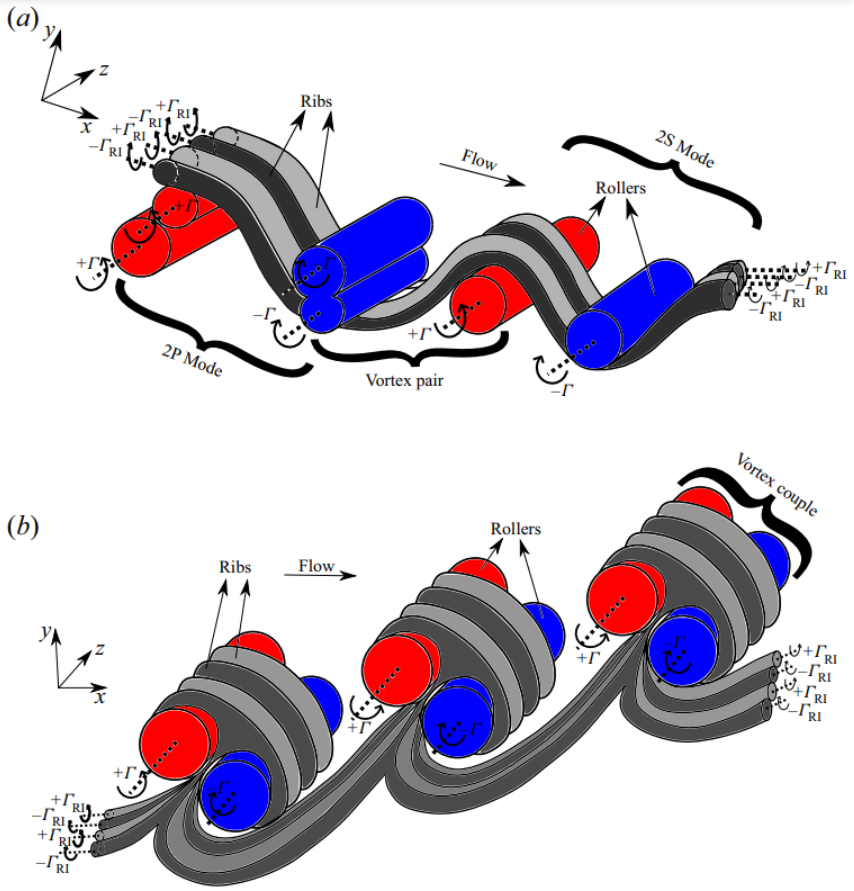

Figure 2.15: Vortex skeleton models illustrating (a) high efficiency and (b) large thrust cases. (Reprinted with permission from Verma and Hemmati (2021), Copyright 2021, Cambridge University Press).

their initial analysis. A recent study by Verma and Hemmati (2021) examined the vortex evolution of simultaneously heaving and pitching foils for two extreme performance conditions: high efficiency and large thrust production. They identified primary (roller) and secondary (ribs) vertex structures and introduced a novel vortex-skeleton model (see figure 2.15) for both kinematic settings. They performed statistical correlation analysis together with qualitative assessment to determine the mode of the secondary instabilities. Wavelength of the secondary structures show similarity with long-wavelength mode identified in the wake of pitching foils.

Three-dimensionality in the wake of oscillating foils, undergoing pure pitching, pure heaving, and combined motions was explored by Zurman-Nasution et al. (2020), unraveling that the transition at larger flapping amplitudes occurred when the circulation of Leading edge vortices exceeded

a universal threshold. Thus, they overcome the damping effect of the viscous dissipation, which consequently resulted in the disintegration of vortices. Verma et al. (2023) investigated the link between the kinematics of foils and three-dimensional characteristics of the wake by covering a wide range of governing parameters. They identified two distinct mechanisms governing the growth of secondary structures across their parametric space, as well as two principal pathways, characterizing the transition between these mechanisms. These studies suggest a distinct relationship between kinematics and three-dimensional instabilities of vortex structures of oscillating foils.

Chiereghin et al. (2020) experimentally examined three-dimensional features of leading edge vortices on high-aspect ratio heaving swept wings, identifying a spanwise instability in the leading edge vortex filament. Investigating the phenomenon quantitatively and qualitatively, Verma and Hemmati (2021) established a connection between spanwise undulation of the leading edge vortex and the elliptic instability of vortex pairs in the wake of foils, with simultaneous heaving and pitching motions. Their research yielded valuable insights into the correlation between spanwise instability and the formation of streamwise vortical structures. Utilizing experiments, numerical simulations, and stability analysis, Son et al. (2022) later elucidated that instabilities on leading edge vortex filaments arose from distinct sources in heaving foils and high-aspect ratio wings. In the case of foils, their observations corroborated with the findings of Verma and Hemmati (2021), where leading edge vortices exhibited spanwise undulations while forming a pair with a counter-rotating vortex. It can be either a trailing edge vortex or a secondary leading edge vortex that rolls up from the surface of the foil. Conversely, for the high-aspect ratio wings, leg of the leading edge vortex remains attached to the wing surface, leading to the formation of helical waves on the leg.

Chapter 3

METHODOLOGY[†]

This chapter presents the research methodology in detail. Section 3.1 delineates the problem addressed in this dissertation, specifically the flow dynamics around pitching foils in schooling configurations. To model the pitching motion of the foils, different dynamic grid techniques are utilized for two-dimensional and three-dimensional simulations, with detailed explanations provided in sections 3.2 and 3.3, respectively. An exhaustive validation and verification analysis is then discussed in section 3.4, ensuring the reliability of the simulation results.

3.1 Geometry and Kinematics

In this dissertation, unsteady flows around the pitching foils in schooling configurations is numerically examined by directly solving the Navier-Stokes equations in the open-source solver Open-

[†]The content of this chapter has been published in whole or part, or under review with the citations:
"Gungor, A., & Hemmati, A., (2020) Wake symmetry impacts the performance of tandem hydrofoils during in-phase and out-of-phase oscillations differently. *Phys. Rev. E*, 102, 043104."
"Gungor, A., Khalid, M.S.U., & Hemmati, A., (2022) Classification of vortex patterns of oscillating foils in side-by-side configurations *J. Fluid Mech.*, 951, A37."
"Gungor, A., & Hemmati, A., (2021) The scaling and performance of side-by-side pitching hydrofoils. *J. Fluids Struct.*, 104, 103320."
"Gungor, A., Khalid, M.S.U., & Hemmati, A., (2024) Physics-Informed Scaling Laws for the Performance of Pitching Foils in Schooling Configurations. *J. R. Soc. Interface*."
"Gungor, A., Verma, S., Khalid, M.S.U., & Hemmati, A., (2024) Foil Proximity Effect-Induced Shear Layer Instability Around Oscillating Foils *J. Fluid Mech.*. "

FOAM which utilizes the finite volume method. Continuity (Eq. 3.1) and momentum (Eq. 3.2) equations are solved directly, considering incompressible and Newtonian fluid flows:

$$\frac{\partial u_i}{\partial x_i} = 0, \tag{3.1}$$

$$\frac{\partial u_i}{\partial t} + \frac{\partial \left(u_i u_j\right)}{\partial x_j} = -\frac{1}{\rho}\left(\frac{\partial p}{\partial x_i}\right) + \nu \frac{\partial}{\partial x_j}\left(\frac{\partial u_i}{\partial x_j}\right). \tag{3.2}$$

Here, u_i is the velocity, x_i is the spatial coordinate, t is time, p is pressure, ρ is density.

Two rigid teardrop foils with a chord length of c and semicircular leading edges at a radius of $0.05c$ are placed in a uniform flow. This foil shape is chosen based on insights from recent numerical and experimental research (Dewey et al., 2014; Senturk and Smits, 2019). A sinusoidal pitching motion about the center of the leading edge is imposed on Foil 1 and Foil 2, which is mathematically defined as:

$$\theta_1(t) = \theta_0 \sin(2\pi f t), \tag{3.3}$$

$$\theta_2(t) = \theta_0 \sin(2\pi f t - \phi). \tag{3.4}$$

Here, θ_0 is the pitching amplitude and ϕ is the phase difference between the two foils. The separation distance between the foils is varied in the x$-$direction (denoted as x^*) and in the y$-$direction (denoted as y^*), as depicted in figure 3.1. In-phase ($\phi = 0$), out-of-phase ($\phi = \pi$), and mid-phase ($\phi = \pi/2$) motions are also depicted in figure 3.1. Throughout this dissertation, Foil 1 is named as the lower, bottom, or leader foil, while Foil 2 is the upper, top, or follower foil.

3.2 Two-dimensional Setup

The mesh morphing technique is applied to simulate the pitching motion in two-dimensional simulations. The solver *pimpleDyMFOAM*, which is an incompressible, transient flow solver for dynamics grid applications is selected for this purpose. It utilizes the PIMPLE algorithm, which is a hybrid of PISO (pressure-implicit with splitting of operators) and SIMPLE (semiimplicit method

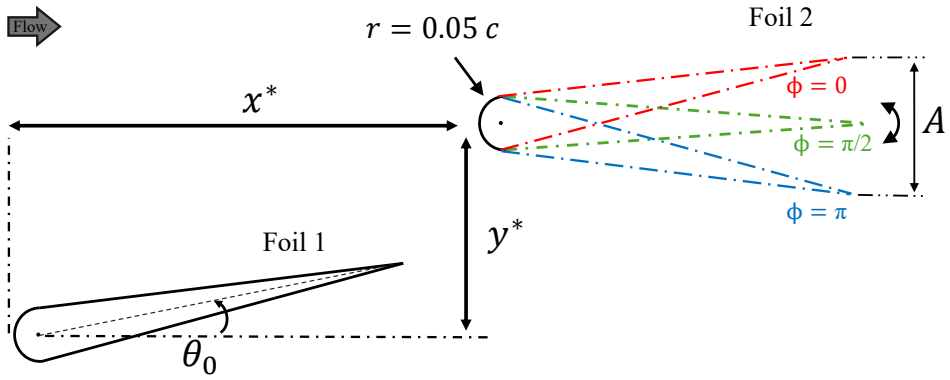

Figure 3.1: Demonstration of the pitching motion of two foils in staggered configuration.

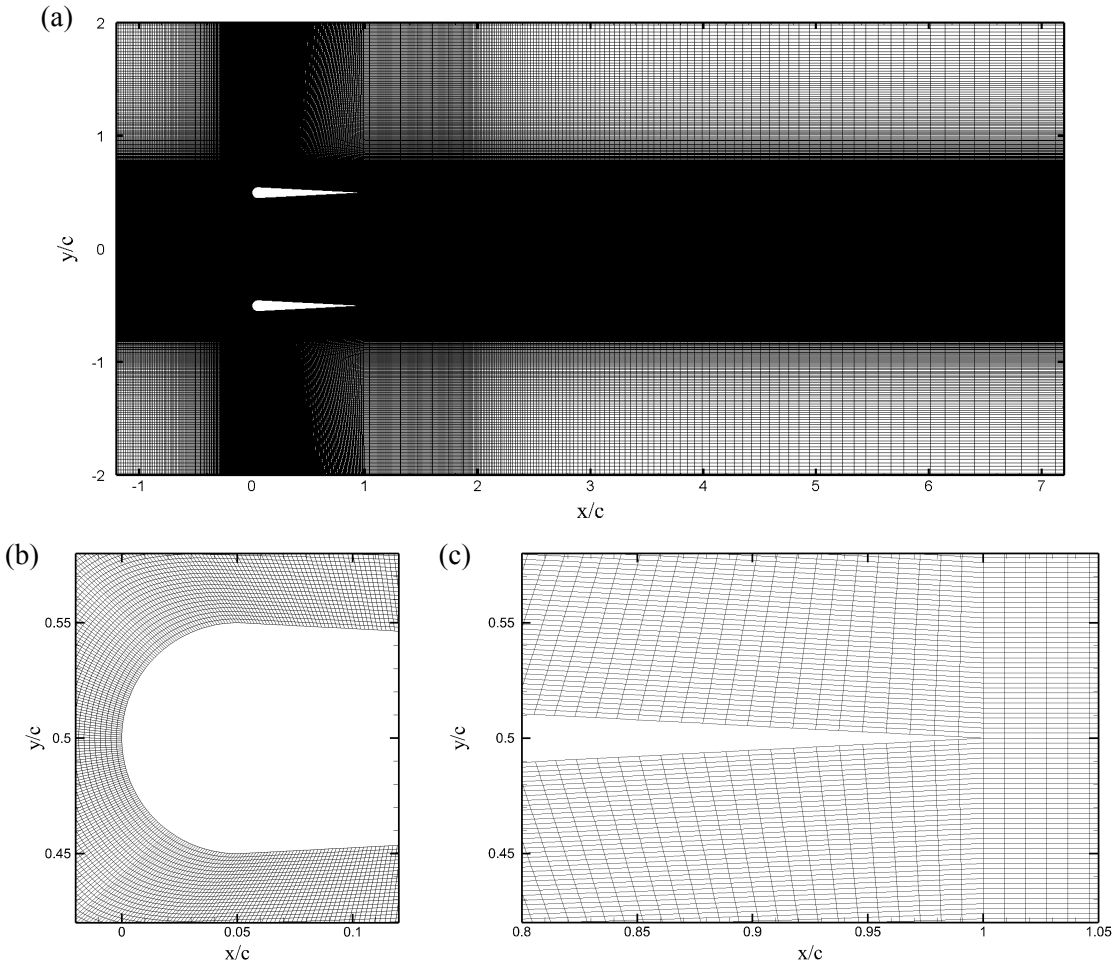

Figure 3.2: Representation of the (a) overall spatial grid utilized for two-dimesional simulations with detailed views around (b) leading edge, and (c) trailing edge.

for pressure-linked equations). The solver deforms the grid in each of time-step following the oscillatory motion assigned to the body. The *inverseDistance* module is utilized as a mesh motion diffusivity model, indicating that deformation diminishes as the distance from the foils increases. Measurements indicate that the maximum mesh skewness remains stable, fluctuating by no more than 5% over a pitching cycle, thus ensuring the grid quality. The time-step size (Δt) is selected such that the maximum Courant number in the domain remains below 0.8, while there are over 3500 time-steps per oscillation cycle. The divergence terms of Navier-Stokes equations are discretized using upwind-biased, second-order accurate "Linear Upwind" technique. Second-order, implicit backward time method is employed for temporal terms. The root-mean-square of the residual of the velocity components and pressure in the momentum equations are used as the convergence criteria, which is set to 10^5.

A non-homogeneous spatial grid, consisting of around 7.5×10^5 hexahedral elements, is generated to simulate the flow. The grid is most refined around the foils with 600 nodes on the surface of each foil, which is consistent with the numerical setup of Senturk and Smits (2019). The grid element size (Δx) expands towards the boundaries without exceeding the expansion ratio of 1.03 in the entire computational domain. More details of the presently utilized grid around the foils are presented in Figure 3.2.

The computational domain is rectangular and extended $30c$ in the streamwise (x$-$) and $5.8c$ in the cross-flow (y$-$) directions (see figure 3.3. The domain is designed so that it could match the experimental setup of Dewey et al. (2014). The leading edge of the foils are placed $8c$ away from the inlet. Neumann condition for both pressure and velocity are applied at the outlet boundary, while a uniform velocity ($u = U_\infty, v = 0, w = 0$) is prescribed to the inlet boundary. Boundary conditions for the upper and lower walls, and foil surfaces are selected to be slip and no-slip, respectively. The assignment of boundary conditions followed that of Hemmati et al. (2019b), which is based on reproducing experiments.

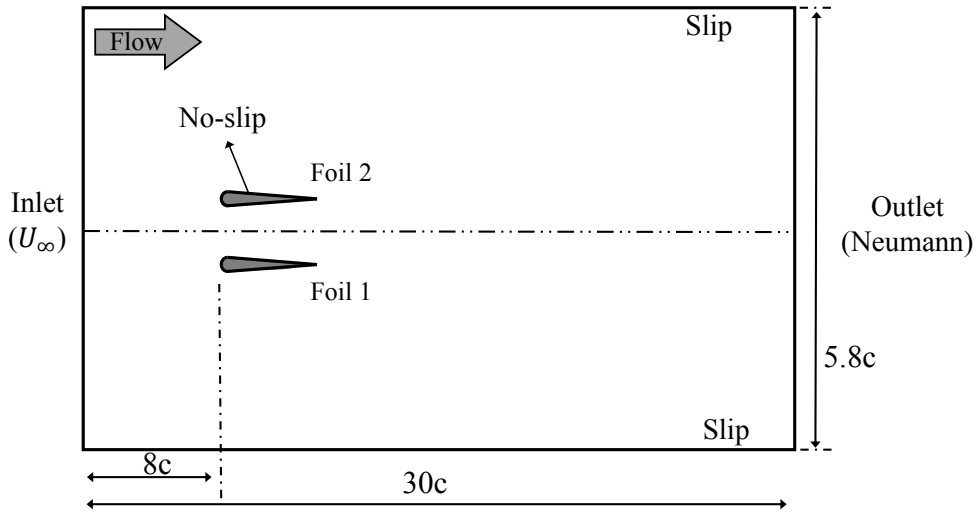

Figure 3.3: Computational domain for two-dimensional simulations with boundary conditions (not to scale).

3.3 Three-dimensional Setup

For three-dimensional simulations, the pitching motion of the foils is modeled using the Overset Grid Assembly (OGA) technique. OGA functions by attaching an overset, where the motion is defined, to a stationary background grid, as illustrated in figure 3.4. Previous research has demonstrated the efficacy of the OGA method in accurately representing the flow dynamics around three-dimensional wakes of both stationary (Verma and Hemmati, 2020) and oscillating bodies (Verma and Hemmati, 2021). The primary rationale for employing the overset technique in three-dimensional simulations is its advantage to keep the background grid stationary, unlike in the mesh morphing technique where the entire grid deforms. In the overset approach, recomputation of node locations is confined only to the overset region, which is significantly smaller compared to the entire background grid. This attribute is anticipated to make it computationally more efficient, especially for grids comprising large number of elements. The *overPimpleDyMFoam* solver, which integrates the functionality of OGA and PIMPLE algorithms, is employed to solve the governing equations. Backward and central difference schemes, both second-order accurate, are employed for temporal and spatial discretizations, respectively. The convergence criteria for the simulation

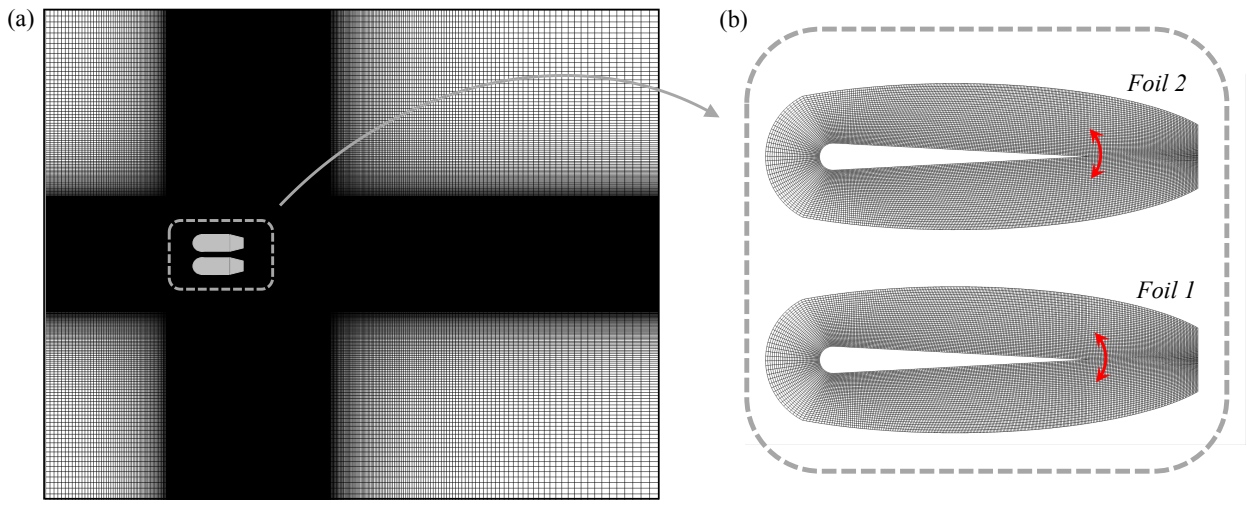

Figure 3.4: Details of the Overset Grid Assembly (OGA) depicting (a) background grid, (b) overset grids.

are established by setting the residual of the velocity and pressure components of the momentum equation to 10^{-6}.

The Overset Grid Assembly (OGA) method classifies cells within the computational domain into three distinct categories: calculated, interpolated, and hole cells (Tisovska, 2019). The assigned cell types is updated by the solver at each time-step, ensuring precise representation of the prescribed dynamic motion. Figure 3.5 illustrates the distribution of these cell types across both the background and overset grids. Calculated cells are where the governing equations are directly solved. Interpolated cells, positioned adjacent to or near an outer boundary, have their values determined through interpolation from the closest elements on the overlapping grid. For example, values for interpolated cells on the background grid are calculated by interpolating from the nearest cells on the overset grid, and vice versa. The overset grids are designed in such a way that they do not overlap at any time during their pitching motion, as depicted in Figure 3.5. This approach is adopted after encountering issues with setups involving overlapping overset regions, which are detailed in appendix A. While various numerical schemes are available for the interpolation process, this dissertation opts for "inverse distance weighting" due to its established effectiveness on finer grids (Chandar, 2019; Verma and Hemmati, 2021). Hole cells define the physical boundaries,

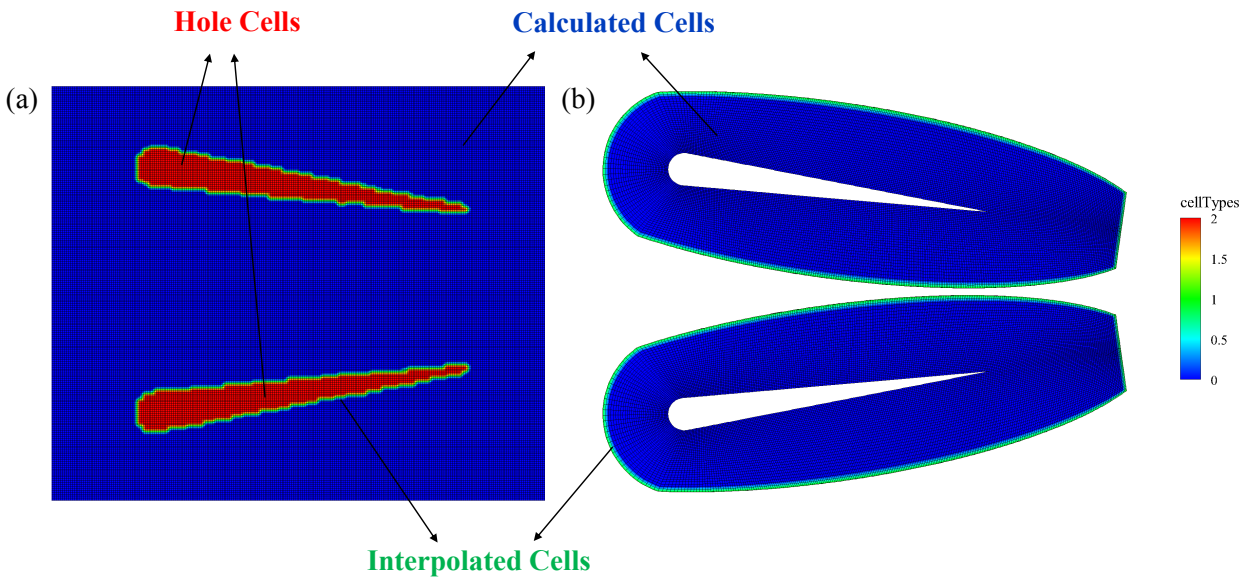

Figure 3.5: Representation of of hole cells (red), calculated cells (blue), and (interpolated cells (green) on (a) background (b) overset grid.

such as the geometry of the foil, where neither calculations nor interpolations are executed. The flow fields generated on the background grid through this method are subsequently used for the analysis.

The rectangular computational domain (see figure 3.6) extends to $20c$, $16c$, and πc in the streamwise (x), cross-flow (y), and spanwise (z) directions, respectively. The size of the domain is determined closely following Verma and Hemmati (2021, 2023). The foils are positioned at a distance of $5c$ from the inlet. Neumann boundary conditions for both pressure and velocity are imposed at the outlet, a uniform velocity boundary condition ($u = U_\infty, v = w = 0$) is applied at the inlet, and slip boundary conditions are prescribed at the upper and lower boundaries of the domain. Surfaces of the foils are set to a no-slip wall boundary condition, while periodic boundary conditions are utilized at the side boundaries. The periodic boundary condition ensures a continuous flow across the side boundaries, effectively mitigating any effects associated with the formation of tip vortices and thereby simulating flow over infinite span parallel pitching foils.

Mesh generation is tailored based on the ratio (δ^*) of the minimum grid element size to the Kolmogorov length scale ($\eta_k \approx (\nu^3/\varepsilon)^{0.25}$), which acts as a benchmark for setting the finest grid

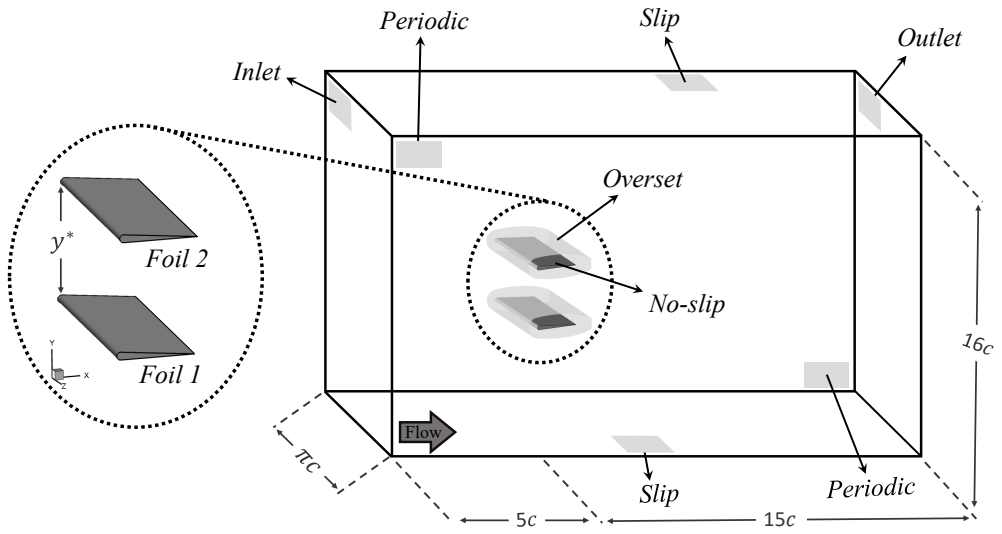

Figure 3.6: Dimensions of the three-dimensional computational domain with boundary conditions (not to scale). Here, y^* is the vertical separation distance between the foils.

size. Here, ε is the rate of dissipation of turbulence kinetic energy. A fine uniform grid is generated close to the foils. Following the recommendations of Moin and Mahesh (1998), we maintain the ratio below 5 around the foils and below 10 in the critical region, where the formation of 3D instabilities is anticipated (Verma and Hemmati, 2023; Verma et al., 2023). Outside of the critical region, the element size gradually increases with an expansion ratio of less than 1.03, toward the boundaries of the domain (see figure 3.4). Thus, at downstream positions of $x/c = 1$, 2, and 4, the values for the ratio are $\delta^* = 4.75$, 4.75, and 9.5, respectively. Consequently, a non-homogeneous spatial grid, comprising of around 40×10^6 hexahedral elements, is employed for the simulations. The dimensionless time-step size, set as $\Delta t^* = \Delta t U_\infty / c = 0.0005$, aligns with the standards established in previous numerical simulations of three-dimensional flow over pitching panels (Senturk and Smits, 2018; Hemmati et al., 2019b).

The spanwise domain size is set to πc following Verma and Hemmati (2023), who compared domain sizes of πc and $2\pi c$. Using spatial autocorrelation, they calculated the wavelength of spanwise instability in leading edge vortex rollers of oscillating foils. Their study confirmed that the wavelengths between the two spanwise domain lengths do not significantly differ, confirming the adequacy of a domain size of πc for capturing the flow physics related to spanwise instabilities.

Table 3.1: Simulation sensitivity analysis for $x^* = 0$, $y^* = 1c$, and $\phi = 0$ at $Re = 4000$ ($St = 0.25$) and $Re = 12000$ ($St = 0.25$). N_{total} is the total number of elements in the grid and Δ denotes the relative percent error with respect to Grid 3.

Study	Re	N_{total}	Domain Size	$\overline{C_{T1}}$	$\Delta\,\overline{C_{T1}}$ (%)	$\overline{C_{T2}}$	$\Delta\,\overline{C_{T2}}$ (%)
Grid 1	4000	2.33×10^5	$30c \times 5.8c$	0.083	1.60	0.083	0.46
Grid 2	4000	3.05×10^5	$30c \times 5.8c$	0.083	0.97	0.084	0.16
Grid 3	4000	7.18×10^5	$30c \times 5.8c$	0.084	–	0.084	–
Grid 4	4000	1.37×10^6	$30c \times 5.8c$	0.081	2.84	0.082	1.40
Domain 1	4000	7.87×10^5	$30c \times 16c$	0.080	4.61	0.080	4.00
Domain 2	4000	7.53×10^5	$35c \times 5.8c$	0.082	2.02	0.084	0.20
Time 1	4000	7.18×10^5	$30c \times 5.8c$	0.084	0.37	0.084	0.40
Grid 1	12000	2.33×10^5	$30c \times 5.8c$	0.206	0.81	0.210	1.01
Grid 2	12000	3.05×10^5	$30c \times 5.8c$	0.208	0.28	0.212	0.46
Grid 3	12000	7.18×10^5	$30c \times 5.8c$	0.208	–	0.213	–
Grid 4	12000	1.37×10^5	$30c \times 5.8c$	0.207	0.41	0.211	0.57

3.4 Validation and Verification

The sensitivity of two-dimensional numerical results to spatial grid, time-step size, and domain size is examined at $x^* = 0$, $y^* = 1$, and $\phi = 0$ for $Re = 4000$ (at $St = 0.25$) and $Re = 12000$ (at $St = 0.3$). Table 3.1 shows the cycle averaged thrust and power coefficients for both foils obtained from seven different simulations for the convergence study. This data also includes corresponding relative errors computed based on the results from Grid 3, that is employed for the actual simulations afterwards. Four different grid sizes (Grid 1, Grid 2, Grid 3 and Grid 4) are used to confirm the grid-independence of our numerical solutions at $Re = 4000$ and 12000. The grid refinement is based on the number of grid points on the foils, which are 300, 400, 600 and 900 grid points for Grid 1, Grid 2, Grid 3 and Grid 4, respectively. A grid refinement ratio of 1.5 was used to systematically coarsen the mesh from 900 grid points, resulting in $900/1.5 = 600$ grid points and then $600/1.5 = 400$ grid points. The coarsest case is an exception, as generating a high-quality

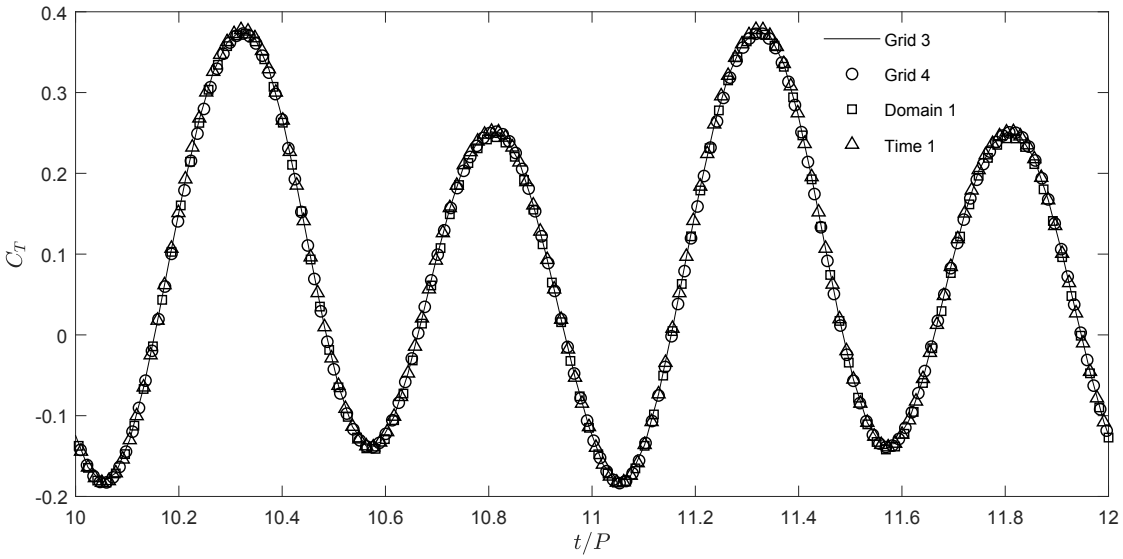

Figure 3.7: Unsteady thrust coefficient variations for Foil 1 for test cases Grid 3, Grid 4, Domain 1 and Time 1.

mesh using $400/1.5 = 267$ grid points was not feasible; therefore, the number is rounded up to 300. Previously, Senturk and Smits (2018) used 500 grid points on the surface of each foil for their study. The relative percentage error is less than 3% for Grid 4 at both Reynolds numbers, which confirms that the mesh in Grid 3 is of high quality to accurately solve the flow features. The grid used in Domain 1 is identical to that of Grid 3 with the width increasing from $5.8c$ to $16c$. Similarly in Domain 2, its length is increased from $30c$ to $35c$ while keeping other dimensions fixed. The results in Table 3.1 shows that the relative error is always less than 5%, implying that the domain of Grid 3 is sufficiently large to accurately capture the flow features. The implications of the time-step size on the computational results are tested by reducing it by half in Time 1, while using the same setup and spatial grid as in Grid 3. The relative error of less than 1% for Time 1 shows that the temporal solution became insensitive to further variations in time-step size.

The unsteady thrust for Foil 1 is compared for Grid 3, Grid 4, Domain 1, and Time 1 at $Re = 4000$ in figure 3.7. For clarity, figure 3.7 focuses on 2 cycles of oscillations between $t/P = 10$ to 12. It is observed that results for Grid 4, Domain 1, and Time 1 matched well with those of Grid 3. It indicates that the settings of the numerical solver reached the convergence for the spatial grid, time-step size, and domain size for Grid 3 in order to resolve unsteady flow features.

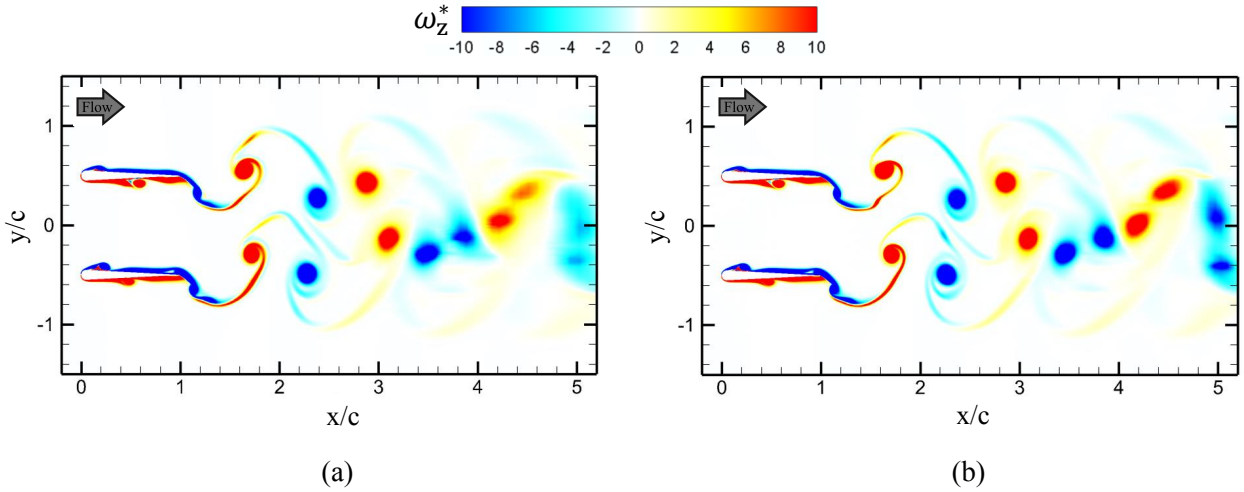

Figure 3.8: Contours of normalized spanwise vorticity ($\omega_z^* = \omega_z\, c/U_\infty$) at the end of $20th$ pitching cycle for pure in-phase oscillations at $St = 0.25$ using (a) Grid 3 and (b) Grid 4.

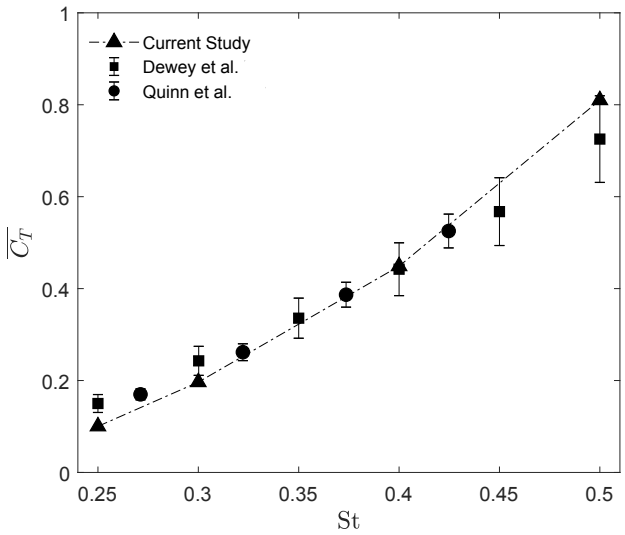

Figure 3.9: Comparing numerically obtained mean thrust coefficients with experimental results of Dewey et al. (2014) and Quinn et al. (2014).

In addition to the verification based on the forces, the grid used in the simulations are sufficiently refined to capture the vortex dynamics in the mid wake region. Figure 3.8 presents the comparison of vorticity contours obtained through the presently employed grid (Grid 3) and finer grid (Grid 4) for pure in-phase oscillations at $St = 0.25$. It is evident that Grid 3 resolves coherent flow structures in the mid wake (around $x/c = 4$) quite well and the dynamics of the coherent structures can be captured with sufficient details.

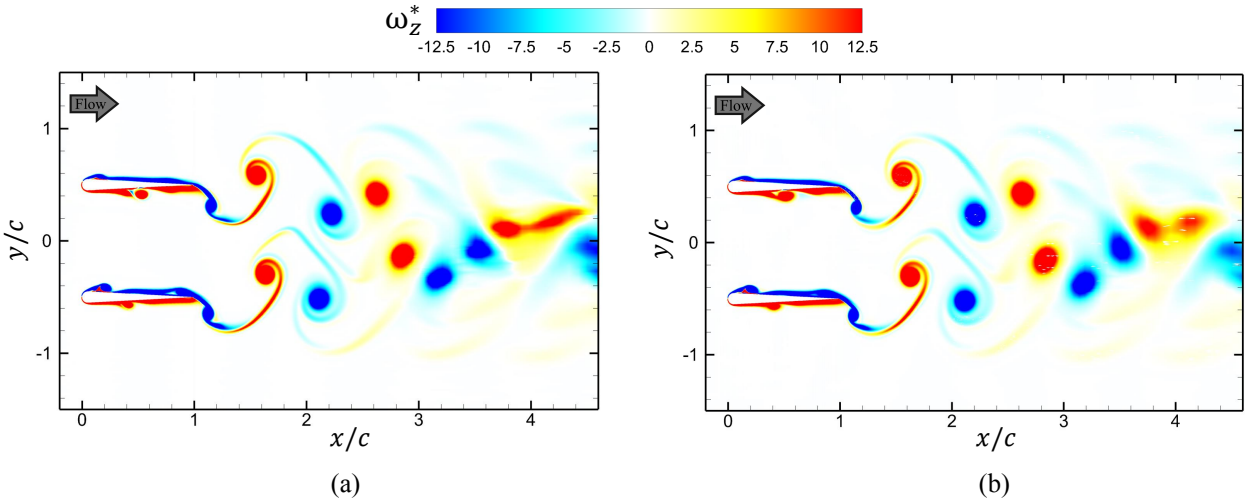

Figure 3.10: Comparing contour plots of spanwise vorticity ($\omega_z^* = \omega_z\, c/U_\infty$) of in-phase pitching foils between (a) two- and (b) three-dimensional simulations for $Re = 4000$ and $St = 0.3$ at $t = 10P$. The 3D case renders results on the mid $xy-$plane.

The validation study is performed through the verified simulation setup, using the selected domain size and spatial-temporal grids, for a single foil compared with the experiments of Dewey et al. (2014) and Quinn et al. (2014) at $Re = 4000$. The results in figure 3.9 showed that the current numerical results agreed well with existing experimental studies for oscillating foils. Thus, the numerical setup is capable of accurately capturing the primary flow features.

Three-dimensional numerical simulations exhibit important complexities that can have implications on wake dynamics at high Re. To this effect, three-dimensional sensitivity studies are carried out to confirm that underlying physics of coherent structures in the flow, including wake deflection, wake merging, and vortex interactions, follow a two-dimensional or Q2D mechanism (Godoy-Diana et al., 2008, 2009; Dewey et al., 2014; Shoele and Zhu, 2015; Lagopoulos et al., 2020). Contour plots in figure 3.10 compare coherent structures, and their interactions, along the center $xy-$plane of the wake of in-phase pitching foils at $Re = 4000$, $St = 0.3$, and $d^* = 1$ with those from two-dimensional simulations. These results confirm that two- and three-dimensional simulations render very similar results in terms of coherent structures, wake dynamics and vortex

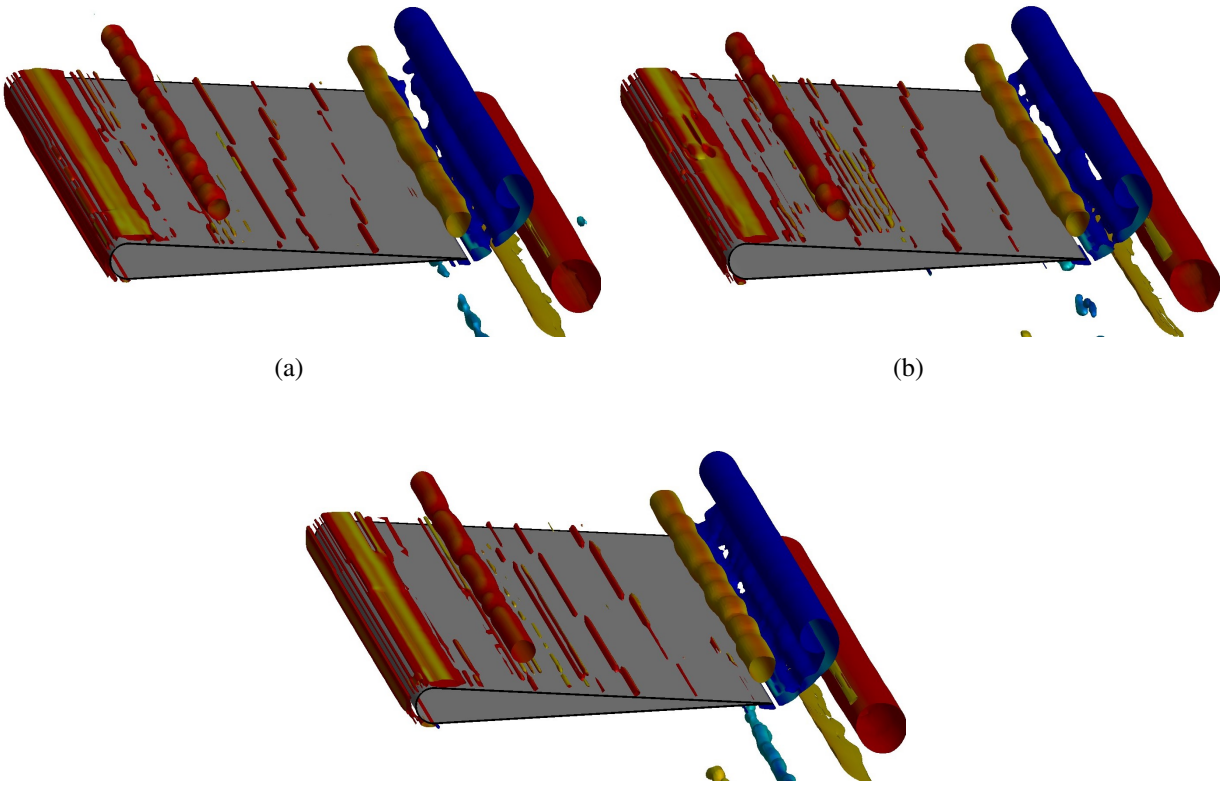

(a) (b) (c)

Figure 3.11: Iso-surfaces of Q-criterion ($Q\,c^2/U_\infty^2 = 10$) depicting spanwise instabilities in the wake of out-of-phase pitching parallel foils at $St = 0.5$ and $y^* = 1c$ for (a) Span1, (b) Span2, and (c) Span3. Iso-surfaces are colored using normalized spanwise vorticity ($\omega_z^* = \omega\, c/U_\infty = -40$ for blue and $\omega_z^* = 40$ for red).

interactions. It has been already shown in literature (Zurman-Nasution et al., 2020) that two-dimensional simulations are sufficient for capturing accurate hydrodynamic performance results.

For three-dimensional simulations, the selection of spanwise domain size and grid refinement is informed by established practices in the literature. Spanwise length of the domain is partitioned into 64 equally spaced elements, consistent with literature on flow over infinite span bodies (Najjar and Balachandar, 1998; Hemmati et al., 2016, 2018; Verma and Hemmati, 2021; Verma et al., 2023). Najjar and Balachandar (1998) effectively simulated flow over an infinite span flat plate with a domain comprising 48 spanwise elements, successfully capturing the formation of streamwise vortices. Hemmati et al. (2018) conducted a comprehensive grid sensitivity analysis for a DNS study, comparing grids with 64 and 96 spanwise elements. Their findings indicated a neg-

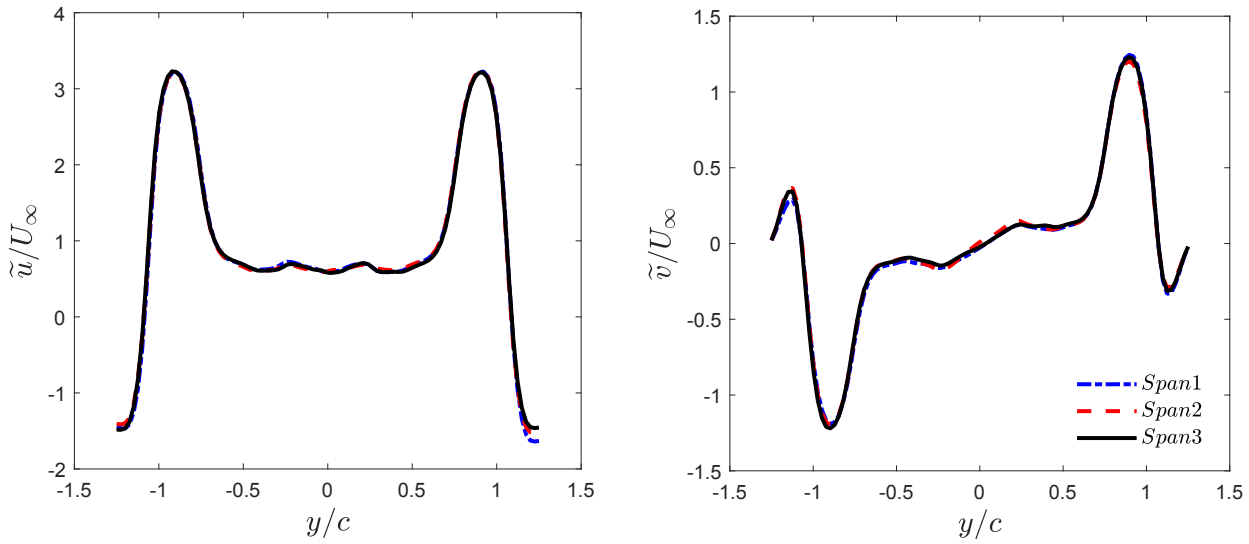

(a) (b)

Figure 3.12: Profiles of normalized (a) streamwise ($\widetilde{u}/U_\infty$) (b) crosswise velocity ($\widetilde{v}/U_\infty$) along cross wise direction (y/c) at $x/c = 2$ and $z/c = 0$ for different spanwise grid refinement cases at $Re = 8000$.

ligible difference between the two, concluding that a grid with 64 spanwise elements is sufficient to resolve the three-dimensional flow field. Likewise, Verma and Hemmati (2021); Verma et al. (2023) employed grids with 64 spanwise elements in their investigation of three-dimensional instabilities in wake oscillating foils, thus corroborating the spanwise refinement utilized in this study. Nonetheless, a grid sensitivity analysis is conducted to further validate the three-dimensional grid utilized in this dissertation. Figure 3.11 showcases a comparison of spanwise instabilities in the leading-edge vortices at $Re = 8000$ captured by three distinct grids (Span1, Span2, Span3), comprising 48, 56, and 64 spanwise elements, respectively. Qualitatively, the results are consistent across the grids, with each configuration revealing 5-7 bulges on the vortices. A quantitative analysis of the grids is illustrated in figure 3.12, which compares the mean spanwise velocities across the span of the domain. The minimal deviation between Span3 and Span2 suggests that Span3 is sufficiently refined to accurately represent the flow physics.

Chapter 4

IMPACT OF WAKE SYMMETRY ON PERFORMANCE[†]

Bio-mimicking represents a cutting-edge approach in the creation of highly efficient robotic platforms, with wide-ranging applications in engineering. This methodology draws inspiration from the physical mechanisms utilized by natural species. Such an approach is pivotal for the design of advanced underwater swimming platform, as it allows engineers to harness the evolved efficiencies of aquatic animals (Smits, 2019). Particularly, a deeper understanding of the fluid flow in the wake of swimming fish, moving in isolation or as a group, enables determining mechanisms that encourages certain behaviors observed in nature. As previously mentioned in section 2.4, two red nose tetra fish tend to swim side-by-side while synchronizing their tailbeat kinematics as the freestream flow is adjusted Ashraf et al. (2016, 2017). However, there is no justification proposed for their behavior in terms of wake dynamics and its implications on propulsive performance. This poses a fundamental question on the implications of external effects and flow physics on the natural behavior of biological species, which can be addressed using experimental and numerical analysis of the wake.

[†]The content of this chapter has been published in whole or part, in *Phys. Rev. E* with the citation: "Gungor, A., & Hemmati, A., (2020) Wake symmetry impacts the performance of tandem hydrofoils during in-phase and out-of-phase oscillations differently. *Phys. Rev. E*, 102, 043104."

As detailed in section 2.2.1, the wake deflection phenomena for single oscillating foils is extensively investigated, there are not any comprehensive studies of this type for tandem foils. Particularly, there are no detailed analysis of the dynamics associated with deflected wakes of two foils in side-by-side configuration, their unsteady interactions, and its implications on the propulsive performance of the foils. This knowledge is critical in providing insight to the swimming habit of fish, which in turn contributes greatly to developing more efficient, stable and effective underwater propulsors and energy harvesting technologies. In this chapter, we aim to address this knowledge gap by numerically examining the wakes of two foils in side-by-side configuration that oscillate in-phase and out-of-phase. Here, we explore the asymmetric wake phenomenon by comparing the performance and wake dynamics of tandem foils oscillating in-phase with those oscillating out-of-phase. This chapter includes a description of the problem in section 4.1, followed by the main results and discussions in section 4.2. A summary is presented in section 4.3.

4.1 Problem Definition

Two-dimensional flow simulations around two pitching foils in side-by-side configuration is conducted for a fixed Reynolds number of $Re = 4000$. The in-phase ($\phi = 0$) and out-of-phase ($\phi = \pi$) pitching motion of parallel foils are considered, while the separation distance between the foils and the amplitude of pitching is fixed at $y^* = 1c$ and $\theta_0 = 8^\circ$, respectively. The Strouhal number of the pitching motion is varied between $St = 0.15$ and $St = 0.5$. However, particular focus is given to $St = 0.25$ and $St = 0.5$. The higher limit of St typically applies to fish swimming in abnormal conditions, such as fast maneuvering and speeding due to faster freestream flow (Ashraf et al., 2016, 2017). The lower St, on the other hand, represents the efficient swimming range for wide variety of aquatic animals (see figure 1.2). Although simulations are carried out at $St = 0.15$ and 0.175 as well, the wake dynamics for these cases are not relevant here due to their drag producing or nearly zero thrust generating nature.

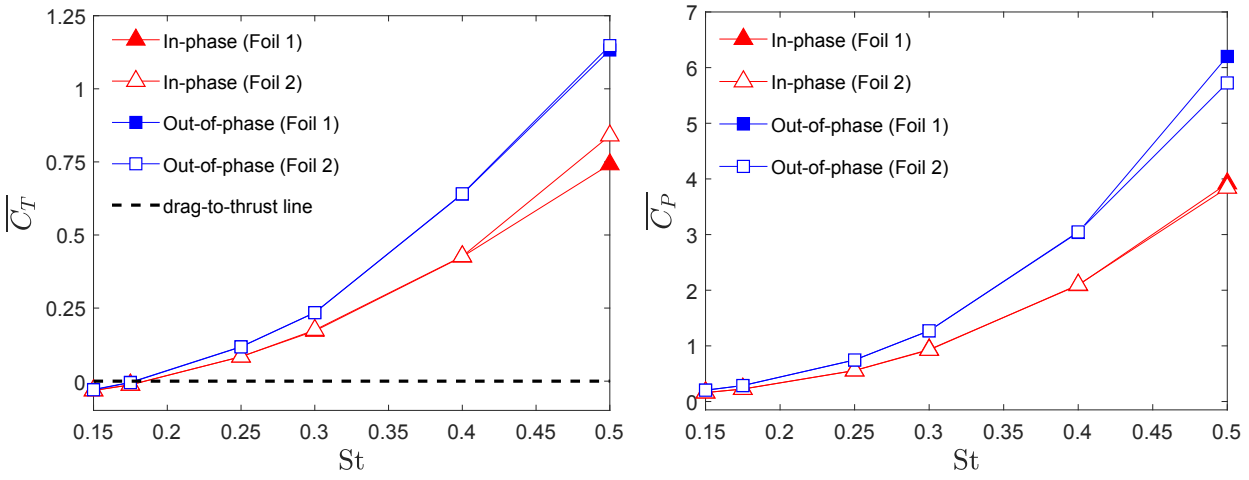

Figure 4.1: The time-averaged coefficients of (a) thrust and (b) power for tandem foils at a range of St.

4.2 Results and Discussion

We begin by examining the performance of the two foils in the range of $St = 0.15 - 0.5$. First, we look at the mean coefficient of thrust and power in figure 4.1. Tandem foils oscillating both in-phase and out-of-phase exhibit drag-producing characteristics at $St \leq 0.175$, as shown in figure 4.1a. However at $St \geq 0.25$, both foils have already transitioned to thrust generating systems. The range of St at which drag-producing tandem foils transition to thrust-generating oscillations, for both in-phase and out-of-phase motion, is $0.175 < St < 0.25$. Based on the current results, the transition is likely occurring at $St = 0.178$ and 0.185 for in-phase and out-of-phase foils, respectively. This coincides with a sharp rise in thrust as well as power for both in-phase and out-of-phase cases. Throughout the entire range of St considered here, out-of-phase oscillating tandem foils generate larger thrust and power than in-phase oscillations with the gap between the two cases widening as St increases. The performance parameters are observed to be uneven between Foil 1 and Foil 2 at $St = 0.5$ where the foils generate unequal thrust and power for in-phase and out of-phase oscillations, respectively. To better appreciate the impact of wake dynamics and distinguish between the characteristics of the in-phase and out-of-phase oscillations, we focus our attention on the wake behavior at $St = 0.25$ and 0.5, showcasing lower and higher St. Here, we focus on how the out-of-phase oscillating tandem foils behave differently from those oscillating in-phase.

We now focus on examining the wake of tandem foils in side-by-side configuration at $St = 0.25$. The unsteady wake development is examined for the in-phase and out-of phase oscillations in order to track the evolution of the wake asymmetry. A similar procedure is also followed for the case of $St = 0.5$. Simulations are repeated for a single oscillatory foil to investigate the effect of tandem configuration on the wake symmetry. Although the wake results for a single foil are used for comparison, they are not shown explicitly here for brevity. We then proceed with examining the cycle-averaged performance of the foils in conjunction with the wake analysis to identify the correspondence between the wake behavior and propulsive characteristics of the foils.

4.2.1 Symmetric Wake Regimes ($St = 0.25$)

The wakes of two foils oscillating in-phase and out-of-phase are shown in figure 4.2 at $St = 0.25$ and $Re = 4000$. The unsteady wake evolution is studied at two timesteps: $t_1 = 10P$ and $t_2 = 20P$, where "P" is the period of pitching. The wake is observed to remain unchanged between each of the oscillation cycles from $t = 10P$ to $20P$, which suggest that a quasi-steady solution is achieved. Thus, we can accurately portray the wake and obtain a clear perspective of the performance of these foils within only 20 oscillation cycles. In the in-phase pitching case, two opposite-sign vortices that are shed by each foil in one pitching cycle form a dipole structure. The dipole shed by one of the foils (Dipole 1 in figure 4.2a) moves in the cross-flow direction downstream towards the centerline until it encounters its counterpart dipole (Dipole 2 in figure 4.2a) shed by the other foil. The interactions between these dipoles begin after they reach $x/c = 3.5$, which aligns the vortical structures along the centerline in a symmetric manner. Conversely, a similar interaction of dipole structures does not appear in the wake of out-of-phase pitching foils. In this case, each of the dipoles (Dipoles 3 and 4 in figure 4.2b) move away from the centerline at an angle that constitutes a perfect mirror symmetry about the centerline. Qualitative results are in perfect agreement with both numerical (Huera-Huarte, 2018) and experimental (Dewey et al., 2014) studies.

Dipole structures in the wake of single pitching foils are said to lead to wake deflections and a change of wake symmetry at specific ranges of Re, St, and reduced frequencies (Godoy-Diana

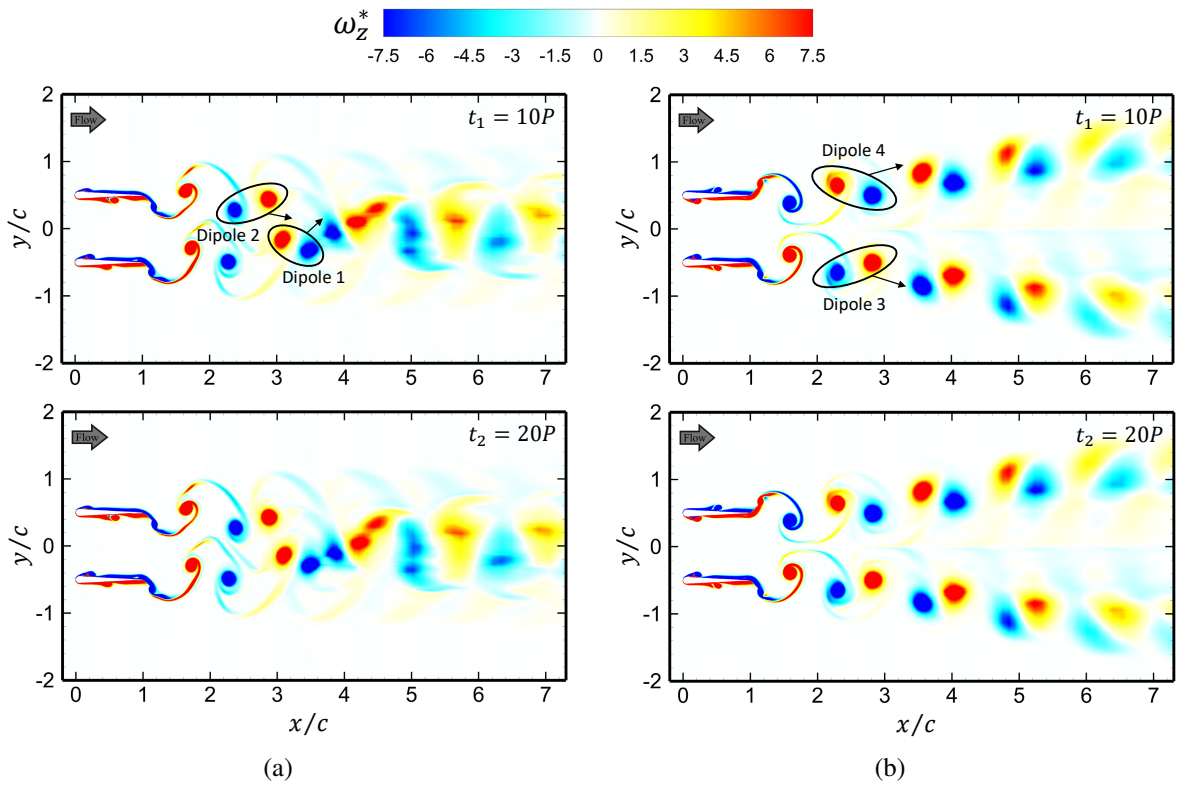

Figure 4.2: Time evolution of contours of normalized spanwise vorticity ($\omega_z^* = \omega_z\, c/U_\infty$) for tandem foils pitching (a) in-phase (left column) and (b) out-of-phase (right column) at $St = 0.25$.

et al., 2008, 2009; Calderon et al., 2014). For example, the wake of a single foil remains symmetric at $St = 0.25$, but there are no dipoles formed in the wake (Godoy-Diana et al., 2008). At a higher St, for example $St = 0.4$, dipole structures are formed in the wake, which Godoy-Diana et al. (2008) relate to the wake deflection. Here, despite observing dipole structures in the wake of tandem foils at $St = 0.25$ (see figure 4.2), the wake remains symmetric about its centerline ($y/c = 0$). Thus, this presents an example, in which dipole structures have not led to the formation of deflected wakes. We refer to this flow regime as the "Symmetric Wake Regime", in which an initially symmetric wake remains symmetric as long as the oscillation is preserved. The symmetric wake of the tandem foils obtained here is consistent with previous studies (Dewey et al., 2014; Huera-Huarte, 2018) of similar setup in terms of St, Re and θ_0.

The cycle-averaged streamwise velocity profiles ($\widetilde{u}$) obtained from both in-phase and out-of-phase pitching cases are shown for three streamwise locations in figures 4.3 and 4.4. These results

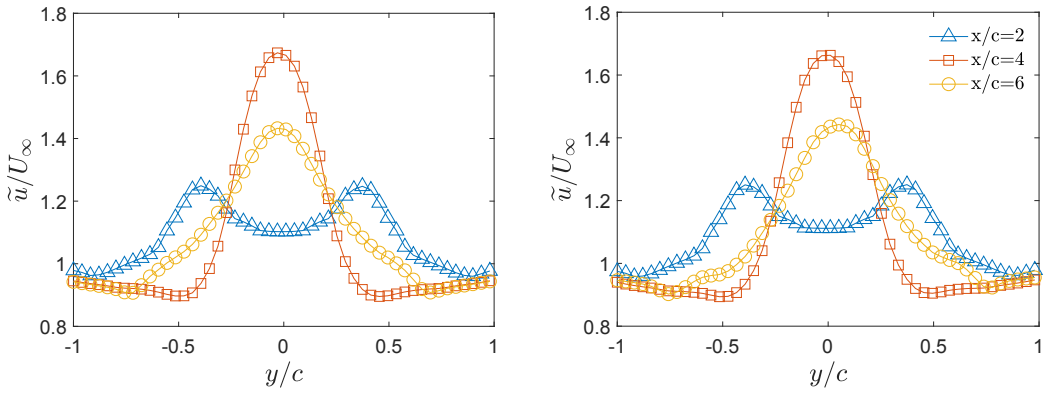

(a) (b)

Figure 4.3: Mean velocity profiles at different locations in the wake. Normalized cycle-averaged streamwise velocity profiles ($\widetilde{u}/U_\infty$) of in-phase pitching foils at $St = 0.25$ for (a) $t_1 = 10P$, (b) $t_2 = 20P$.

provide further insight into the symmetric wake regime. Two local peaks in figure 4.3a at $x/c = 2$, which corresponds to two local high velocity regions shed by each of the foils, merge and create a single, higher velocity jet at $x/= 4$. Farther downstream at $x/c = 6$, the jet diminishes in magnitude but expands in width. For the out-of-phase case in figure 4.4a, the two local peaks are observed, however they do not hint at any interactions since they individually coexist at all downstream locations. Velocity profiles for both of the oscillation phase differences exhibit symmetric behavior in cross-flow direction (about $y/c = 0$) in the wake. Since these behaviors do not change over times (figures 4.3b and 4.4b), the flow can be described as quasi-steadily symmetric.

4.2.2 Transitioning Wake Regimes ($St = 0.5$)

Contrary to the quasi-steadily symmetric wakes observed at $St = 0.25$ for both in-phase and out-of-phase pitching foils, the wake at $St = 0.5$ exhibits highly interactive and asymmetric wake characteristics. This occurs initially for the in-phase pitching, and subsequently for the out-of-phase pitching foils. Furthermore, a transitioning process is observed in the wake of tandem foils from symmetric to asymmetric wakes, or vice versa, when the pitching St increases beyond 0.5, as shown in figure 4.5. This transition occurs at 27th and 13th cycle for in-phase and out-of-phase cases, respectively. Based on long-term analysis of the foils upto the 60th cycle, not shown here

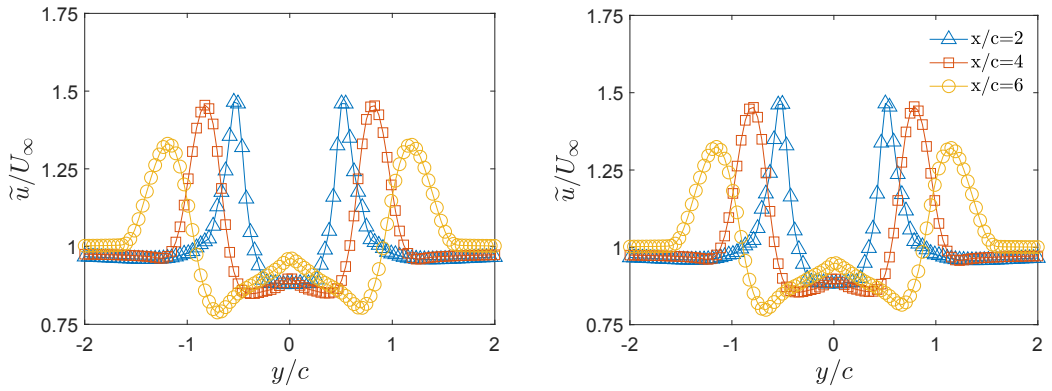

Figure 4.4: Mean velocity profiles at different locations in the wake. Normalized cycle-averaged streamwise velocity profiles ($\widetilde{u}/U_\infty$) of out-of-phase pitching foils at $St = 0.25$ for (a) $t_1 = 10P$, (b) $t_2 = 20P$.

for brevity, a total of 50 pitching cycles are needed to reach a quasi-steady solution. We refer to this wake behavior as "Transitioning Wake Regime", where the wake is initially symmetric and it transitions to asymmetric wake, or vice-versa. The unsteady evolution of vortical structures in the wake of both in-phase and out-of-phase pitching foils is demonstrated over the course of 50 cycles in figure 4.5 at $10P$ increments.

First, we look at the in-phase pitching case of tandem foils in figure 4.5a. At $t_1 = 10P$ in figure 4.5a, two distinct downwards deflected reverse BvK vortex streets are formed behind each of the foils. Unlike the "Symmetric Wake Regime", in which dipoles interact with each other to form complex structures, the dipoles in the "Transitioning Wake Regime" (Dipole 1 and Dipole 2) coexist in the absence of interaction until their diffusion farther downstream. The latter wake is similar to the deflected wake seen behind a single pitching foil (not shown here for brevity), and it agrees with existing numerical and experimental studies (Jones et al., 1998; Heathcote and Gursul, 2007; Godoy-Diana et al., 2008; Das et al., 2016) with a similar configuration. It is notable to mention that the first pitching stroke is upwards, which coincides with a downward wake deflection. This behavior is consistent with the observations of Liang et al. (2011). When the direction of the initial pitching stroke is switched from upwards to downwards (not shown here for brevity), the wake deflection also switches from downwards to upwards. Thus, there exits a reverse correspondence

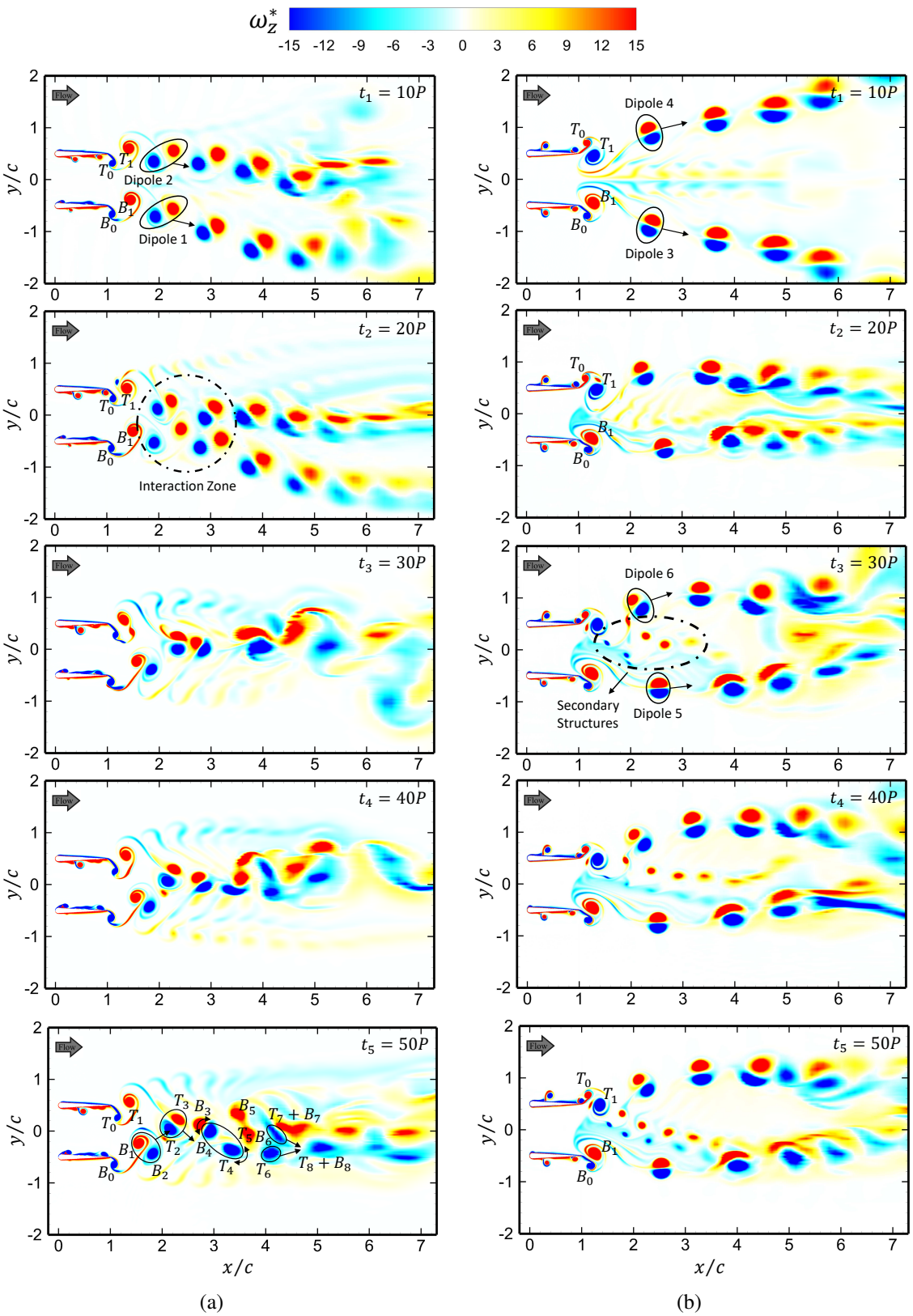

Figure 4.5: Time evolution of contours of spanwise vorticity ($\omega_z^* = \omega_z\, c/U_\infty$) for tandem foils pitching (a) in-phase (left column) and (b) out-of-phase (right column) at $St = 0.5$.

between the pitching initiation direction and the wake deflection. There also appears to be a difference between the deflection angles of the upper (Foil 1) and lower (Foil 2) wakes. The wake deflection angle for Foil 1 is 16.98°, calculated following the same procedure as Godoy-Diana et al. (2009) and von Ellenrieder and Pothos (2008), whereas the angle of deflection for Foil 2 is 5.18°. This suggests that the two wakes are not dynamically independent from one another since they are expected to have the same angle of deflection in the absence of any dynamic interactions. Although the physics remains unclear, this hints that there exists an embedded interaction between the foils leading to such wake behavior. At $t_2 = 20P$ in figure 4.5a, vortical structures from upper and lower wakes begin interacting at the range of $2.5 < x/c < 3.5$. At $x/c > 3.5$, the upper and lower dipoles move downstream and they are distinctly deflected downwards. There appears to be severe distortions associated with structures at $t_3 = 30P$, after which point the wake becomes mostly quasi-symmetric with some minor irregularities. By $t_5 = 50P$, the wake is quasi-symmetric along the centerline, and it appears to be qualitatively similar to the case of $St = 0.25$ (see figure 4.2a), where the flow follows the "Symmetric Wake Regime". The dipole shed by Foil 1 (B_0 and B_1 at $t_5 = 50P$) moves laterally towards the centerline and interact with its counterpart (T_2 and T_3) shed by Foil 2 at $x/c \approx 2.5$. The structures rotating in the same direction (e.g., B_4 and T_4) form a new vortex pair with an internally induced motion that for example moves B_4 upwards and T_4 downwards. Farther downstream, these structures merge at $x/c \approx 5$. This wake transition has not been previously reported in other studies, possibly because the transition occurs at a late cycle.

On the contrary, the transition from symmetry to asymmetry in the wake is observed for tandem foils pitching out-of-phase in figure 4.5b. The wake appears to be initially symmetric and well-ordered at $t_1 = 10P$ with the dipoles (Dipole 3 and Dipole 4) moving away from the centerline. This is qualitatively similar to the wake of out-of-phase pitching foils at $St = 0.25$ (see figure 4.2b). Note that the wake of in-phase pitching foils are asymmetric at the same St and number of cycles (see figure 4.5a). It can be argued that the perfect mirror image symmetry of the motion of out-of-phase oscillation inhibits the formation of the deflected wake. At $t_2 = 20P$, the first indicators of symmetry breaking is observed as the perfect mirror image symmetry about the centerline ($y/c = 0$)

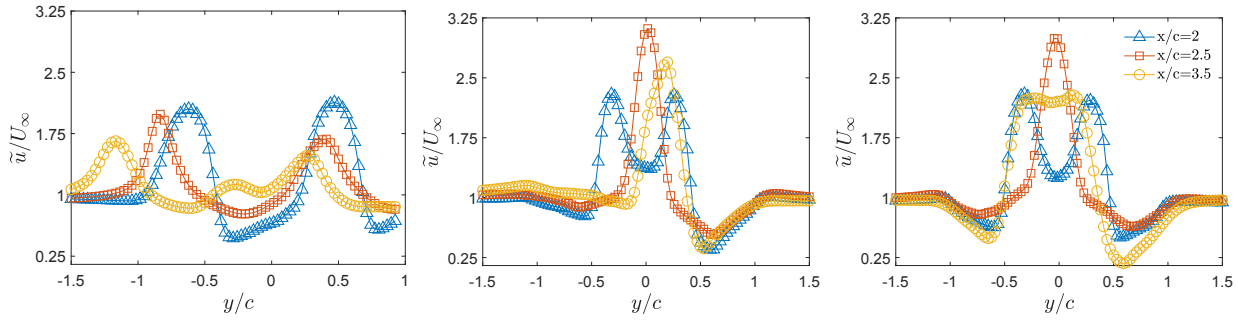

(a) (b) (c)

Figure 4.6: Mean velocity profiles at different locations in the wake. Normalized cycle-averaged streamwise velocity profiles ($\widetilde{u}/U_\infty$) of in-phase pitching foils at $St = 0.5$ for (a) $t_1 = 10P$, (b) $t_2 = 30P$, (c) $t_3 = 50P$.

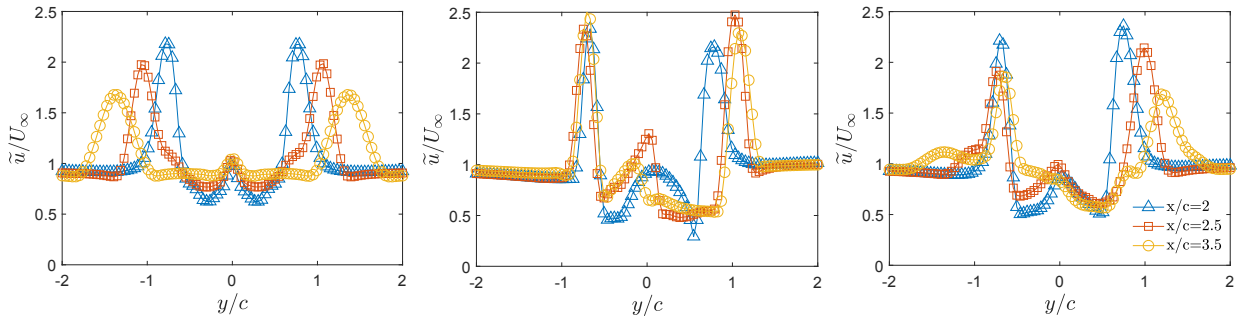

(a) (b) (c)

Figure 4.7: Mean velocity profiles at different locations in the wake. Normalized cycle-averaged streamwise velocity profiles ($\widetilde{u}/U_\infty$) of out-of-phase pitching foils at $St = 0.5$ for (a) $t_1 = 10P$, (b) $t_2 = 30P$, (c) $t_3 = 50P$.

is slightly disturbed, although the wake remains mostly symmetric. This is similar to the findings of Zhang et al. (2018), who reported but did not further investigate that symmetry breaking is triggered after 20 oscillation cycles for side-by-side tandem foils oscillating out-of-phase. At $t_3 = 30P$, we observe the initial formation of secondary structures, which coincides with disappearance of the symmetric features of the dipoles (see Dipole 5 and Dipole 6 for comparison). There are quantitatively insignificant differences between the wake at $t_4 = 40P$ and $t_5 = 50P$, which suggests that the wake will not further change considerably. Although not shown here for brevity, our simulations up to 60 cycles indicated no change in the wake topology.

The transitioning trend of in-phase and out-of-phase oscillating tandem foils at $St = 0.5$ are quantified using cycle-averaged streamwise velocity profiles ($\widetilde{u}/U_\infty$) in figures 4.6 and 4.7, respec-

tively. In-phase oscillating foils initially (at $t_1 = 10P$) have two legs at each streamwise location (that is $x/c = 2$, 2.5, and 3.5), which are not symmetric about $y/c = 0$. Velocity peaks that correspond to the structures formed by Foil 1 are centered around $y/c = -1$, whereas the velocity peaks for Foil 2 are centered around $y/c = 0.5$. This implies that the wake is deflected towards the negative y$-$direction (downwards). It is evident that symmetry is partially restored at $t_2 = 30P$, especially in the near wake ($x/c = 2$ and 2.5) and around the centerline ($-0.5 < y/c < 0.5$). Symmetry is further improved in the wake at $t_3 = 50P$, where most of the wake irregularities are severely distorted or diffused. Figure 4.7 demonstrates an opposite trend in the wake transition for out-of-phase oscillating foils. The symmetric velocity profiles at $t_1 = 10P$ are distorted and lose their symmetric features at $t_2 = 30P$ in figure 4.7b. They eventually transform to a fully asymmetric (non-symmetric) profile at $t_3 = 50P$ in figure 4.7c.

Figures 4.8 and 4.9 show the lateral tracking of the vortex cores in the wake of in-phase and out-of-phase oscillating foils at $St = 0.5$, respectively. These results enable further analysis of the motion of vortical structures in time. Four vortex cores (T_0, T_1, B_0 and B_1 in figure 4.5) are monitored following their formation at $t_{in} = 10P$, $20P$ and $50P$ over three oscillating cycles. Moreover, we also include the collective (spatial-averaged) location of the structures, approximating the true collective wake centerline, in these plots to display the trends of the wake symmetry. For in-phase oscillations in figure 4.8, two vortex dipoles are shed at $t_{in,1} = 10P$ (B_0 and B_1 by Foil 1 and T_0 and T_1 for Foil 2), which move downwards without directly interacting with one another. This is apparent from the non-intersecting track lines in figure 4.8a with a negative slope that implies the negative lateral convective velocity of vortices. However, the vortex dipoles formed at $t_{in,2} = 20P$ start interacting during the 21st cycle, which is apparent by the intersection of the track-lines in figure 4.8b. This induces a laterally positive convective velocity on the wake of Foil 1 (B_0 and B_1), which moves it upwards (in the positive $y-$direction). The convective velocity of the wake of Foil 2 remains negative. The restoration of symmetry is apparent when tracking the structures formed at $t_{in,3} = 50P$ in figure 4.8c. Here, the collective location of vortex cores in the $y-$direction remains stable at $y/c = 0$ over the three cycles shown. Contrary to the case of in-phase oscillations,

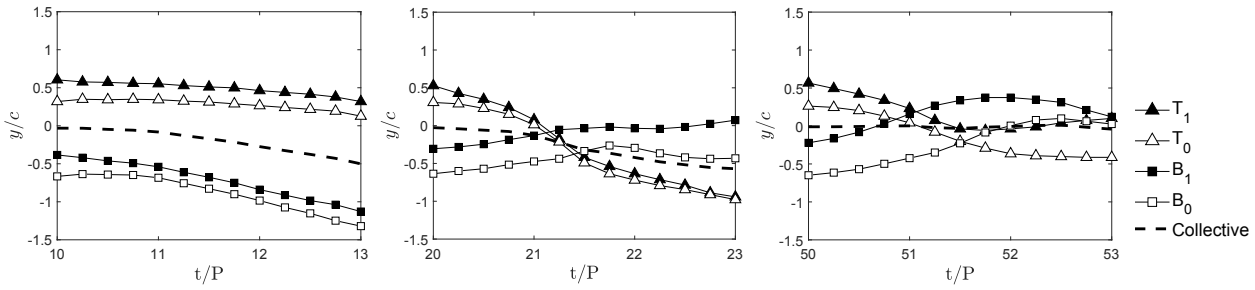

(a) (b) (c)

Figure 4.8: Trace of lateral ($y-$) location of the vortex cores for T_0, T_1, B_0 and B_1 in the wake that is initiated at three different times (a) $t_{in,1} = 10P$, (b) $t_{in,2} = 20P$, (c) $t_{in,3} = 50P$ for the in-phase oscillating foils at $St = 0.5$. The vortex core labels refer to those shown in figure 4.5a.

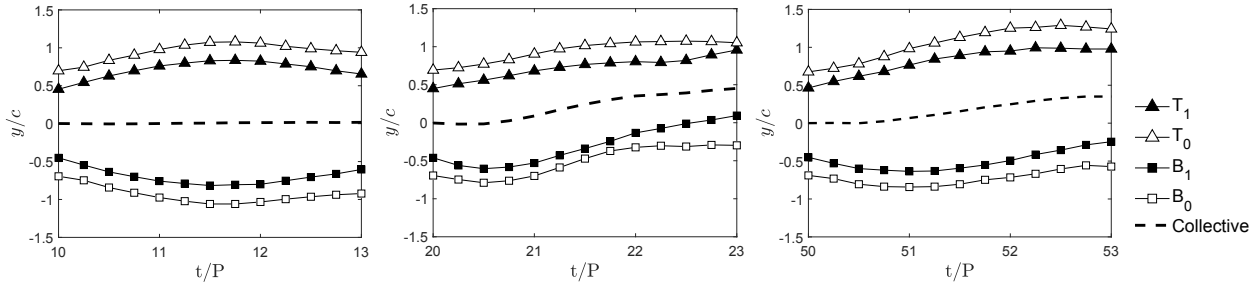

(a) (b) (c)

Figure 4.9: Trace of lateral ($y-$) location of the vortex cores for T_0, T_1, B_0 and B_1 in the wake that is initiated at three different times (a) $t_{in,1} = 10P$, (b) $t_{in,2} = 20P$, (c) $t_{in,3} = 50P$ for the out-of-phase oscillating foils at $St = 0.5$. The vortex core labels refer to those shown in figure 4.5b.

there exists a symmetry breaking point in the wake of out-phase pitching foils that is identifiable in figure 4.9. The wake symmetry is initially apparent from the vortex core track-lines in figure 4.9a, in which the collective location lays exactly at $y/c = 0$. This symmetry is disturbed over time and the collective location of structures deviate from $y/c = 0$. For example, the wake is distorted with structures moving upwards in figure 4.9b. This behavior continues further in figure 4.9c, in which case structures formed at $t_{in,3} = 50P$ collectively deviate by $\approx +0.4c$ from $y/c = 0$.

The examination of the wake structures suggests that there exists a dynamic interaction in the wake of the two foils that is greatly affected by their St and phase differences. Although changes in St and ϕ severely alters the unsteady wake evolution, it is apparent that the separation distance between the two foils also influences the nature of vortex interactions. This topic deserves

a detailed study of its own, which falls outside the scope of this chapter. Chapter 7 investigates the influence of intermediate phase differences ($0 < \phi < \pi$), and chapter 10 expands the discussion with a thorough analysis encompassing a wide range of separation distances.

4.2.3 Evolutionary Propulsive Performance

The transitioning wake regime observed for both in-phase and out-of-phase pitching foils suggests that there may also be a change in propulsive performance of the foils that have remained unexplored. This transition in performance may have been overlooked by most studies since they either focused only on the collective (time-averaged) performance of the foils, or that their range of *St* only exhibited the "Symmetric Wake Regime". To investigate the unsteady behavior of performance, we looked at cycle-averaged coefficients of thrust, power and side-force over 50 pitching cycles.

Figure 4.10 shows the cycle-averaged coefficient of thrust ($\widetilde{C_T}$) plotted against the number of pitching cycles at $St = 0.25$ and $St = 0.5$, which correspond to cases with symmetric and transitioning wake regimes, respectively. Similarly, the cycle-averaged coefficient of power ($\widetilde{C_P}$) and side-force ($\widetilde{C_S}$) are shown for different *St* in figures 4.11 and 4.12, respectively. The latter also includes the total (collective for both foils) side-force for in-phase and out-of-phase pitching foils at $St = 0.25$ and $St = 0.5$. The first main observation hints that the performance of both foils reaches a quasi-steady behavior (asymptotic range) within only 20 cycles at lower *St* of 0.25, at which case the wake follows the symmetric wake regime. At the higher Strouhal number of $St = 0.5$, however, the foils approach their quasi-steady performance after the 40th cycle. This is the case, at which the flow exhibits features associated with the transitioning wake regime. This observation hints that the change in wake dynamics coincides with a change in propulsive performance of the foils.

The evolution of $\widetilde{C_T}$, $\widetilde{C_P}$ and $\widetilde{C_S}$ in figures 4.10a, 4.11a and 4.12a appear to involve no major variations after the 10th cycle, which agrees with the quasi-steadily symmetric wake behavior observed in figure 4.2. Moreover, the wake symmetry is corroborated by the identical thrust gen-

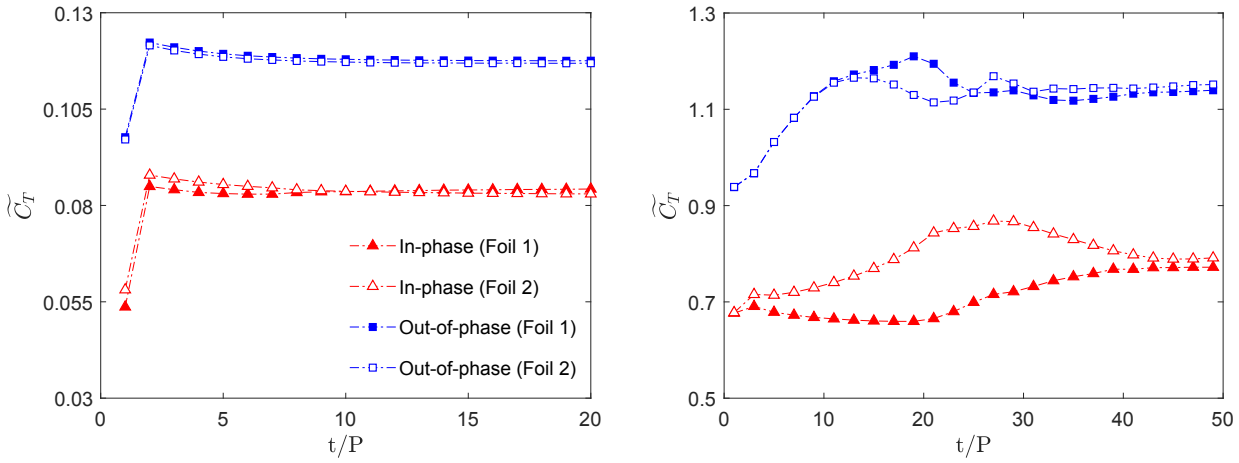

(a) (b)

Figure 4.10: The variation of cycle-averaged thrust coefficient for Foil 1 and Foil 2 in time for in-phase and out-of-phase oscillations at (a) $St = 0.25$, (b) $St = 0.5$.

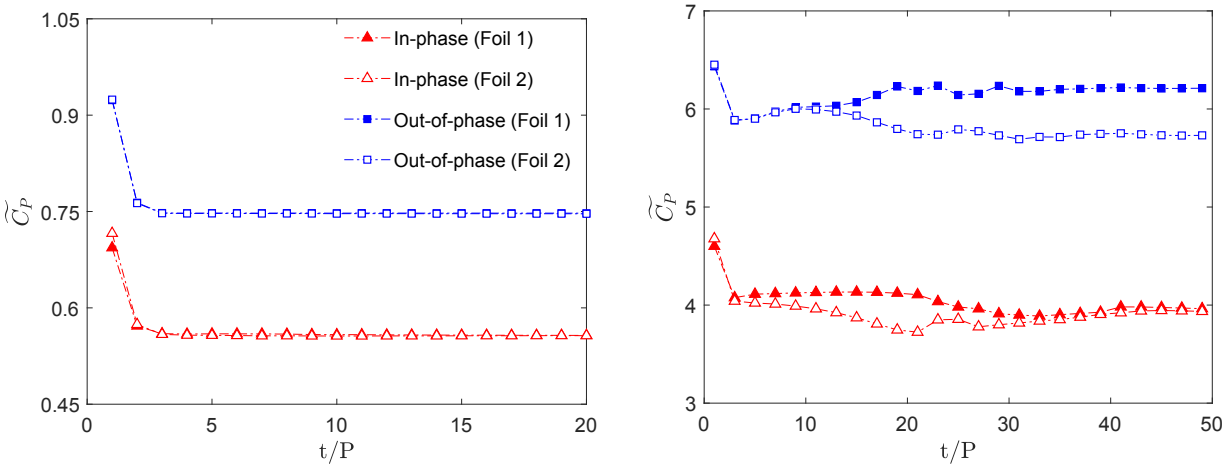

(a) (b)

Figure 4.11: The variation of cycle-averaged coefficient of power of Foil 1 and Foil 2 in time for in-phase and out-of-phase oscillations at (a) $St = 0.25$, (b) $St = 0.5$.

eration and power consumption of Foil 1 and Foil 2. This is further confirmed by the zero total (collective) side-force produced by the foils in figure 4.12a.

At higher St, the performance of the foils appear to change over time for both in-phase and out-of-phase pitching cases. We start with the former, where the foils are pitching in-phase. Initially, the thrust generation between Foil 1 and Foil 2 inhibits a difference that favors Foil 2, which is also observed in lower power consumption of Foil 2. This gap in performance enlarges until the

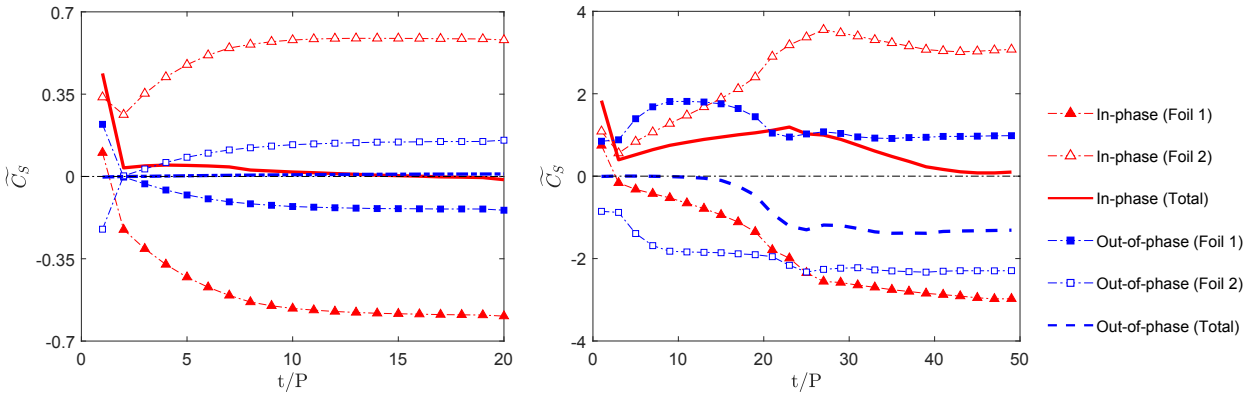

(a) (b)

Figure 4.12: The variation of cycle-averaged coefficient of side-force of Foil 1, Foil 2 and total (Foil 1 + Foil 2) in time for in-phase and out-of-phase oscillations at (a) $St = 0.25$, (b) $St = 0.5$.

20th cycle, at which point the wake is predominantly asymmetric (see figure 4.5a). However, this behavior starts to reverse itself after the 20th cycle, when the wake starts becoming more regular and aligned with the streamwise direction (see figure 4.5a). This behavior diffuses over time with similar thrust generated and power consumed by both foils after the 40th cycle. Although the average $\widetilde{C_P}$ of Foil 1 and Foil 2 does not change significantly during the transitioning wake regime, there appears to be a dramatic increase in the average $\widetilde{C_T}$. This improves the overall performance of the system. It is also observed that the initially non-zero total (collective) side-force ($\widetilde{C_S}$) produced by the system coincides with the wake asymmetry. This implies that the symmetric wake leads to a zero total side-force, whereas a non-symmetric wake results in a total non-zero side-force. This is important in understanding the change in swimming synchronization of fish. Due to the downward deflected wake (negative $y-$direction in figure 4.5a), foils produce positive $\widetilde{C_S}$, which diminishes and converges to zero as quasi-symmetric wake is restored in time.

During the out-of-phase pitching, the performance of both foils appear identical in the initial cycles in figure 4.10b, which agrees with the symmetric wake characteristics previously discussed in section 4.2.2. At the 13th cycle, the first evidence of a departure from identical performance of the two foils is observed, where the thrust generated by Foil 1 is starting to surpass that of Foil 2. This departure from symmetry occurs earlier that the first indicators of wake symmetry

breaking prior to the 20th cycle in the wake (e.g., figure 4.5b). By the 25th cycle, the performance appears to start stabilizing to what eventually become a quasi-steady behavior in the 40th cycle. This coincides with the timeline at which the wake also appears to have transitioned to a fully non-symmetric regime. More substantial effect on performance of the out-of-phase pitching foils is seen in figure 4.11b for the power consumption. The break in wake symmetry coincides with an increase in $\widetilde{C_P}$ for Foil 1 and a decreased in $\widetilde{C_P}$ for Foil 2. However, average $\widetilde{C_P}$ of the foils stays nearly the same with the power consumption prior to the start of any changes on wake topology. Similar to the case of in-phase pitching, there is a correspondence between asymmetry and non-zero total side-force production for out-of-phase pitching in figure 4.12b. Here, the negative total $\widetilde{C_S}$ starts when symmetry is broken after the 13th cycle, which persists for the remainder of pitching cycles.

The difference in side-force production complemented by the changes in thrust generation and power consumption of tandem foils during the in-phase and out-of-phase pitching configurations hints at the reasoning for certain swimming habit of fish in nature. For example, Ashraf et al. (2016, 2017) showed in an aquarium experiment that the red nose tetra fish (*Hemigrammus bleheri*) prefer to swim in side-by-side configuration with their body kinematics synchronizing such that their caudal fins oscillate either in-phase or out-of-phase. However, the selected oscillation phase difference (in-phase or out-of-phase) is not permanent since they switch the phase synchrony after a number of cycles during swimming. This habit of fish in switching their synchronization in side-by-side configuration could be related to the total non-zero side-force production observed in the current chapter. This hints at the fact that switching from out-of-phase pitching, which coincides with start of producing negative total side-force after the 13th cycle, to the in-phase pitching configuration, which produces a positive total side-force, allows fish to maintain their lateral position. Although the fundamental physics discussed here appear to address this natural fish behavior, the specific case study on the experiments of (Ashraf et al., 2016, 2017) requires a special attention that is outside the scope of the current chapter.

4.3 Summary

The wake topology of two foils in tandem side-by-side configuration that are pitching either in-phase or out-of-phase are studied at low and high St at $Re = 4000$. Fundamental dissimilarities in the wakes are observed at the extreme cases of $St = 0.25$ and 0.5. At low St, flow is found to be quasi-steady since the propulsive performance parameters, such as coefficients of thrust, power and side-force, appear to exhibit no major changes over time. This appears to be consistent with the wake topology that remains symmetric over time. However, the wake topology and variations of the propulsive performance of tandem pitching foils change over time at higher St. The wake appears to exhibit what is referred to as the transitioning wake regime, in which initial wake topology changes due to interactions in the wake. For the in-phase case, wakes of the foils does not exhibit interaction at the beginning so that two distinct, deflected BvK vortex streets are shed similar to the deflected wake of a single pitching foil. Interactions between the wakes initiates the merging of the two vortex streets. This leads to restoration of a wake alignment with the freestream, or what is referred to as a quasi-symmetric wake. On the contrary, the wake created due to the out-of-phase pitching of tandem foils is initially symmetric due to the perfect mirror-image symmetry of the out-of-phase motion. However, symmetry breaking is triggered after a number of pitching cycles, which results in a non-symmetric wake with disordered vortical structures. This provides insight to the swimming habit of fish, which switch between in-phase and out-of-phase configurations in nature. This is best illustrated by the change in propulsive performance of the foils during each of these configurations.

It is observed that propulsive performance parameters, such as coefficients of thrust, power and side-force, follow closely the change in symmetric characteristics of the wake. At low St, where the wake appears regular and symmetric, identical thrust generation and power consumption is observed for both foils. Moreover, the same magnitude of side-force is also generated but in opposite directions for each foil, leading to a zero total side-force in the system. A similar behavior is also observed for high St pitching foils as long as the wake remains symmetric, i.e. quasi-steady conditions for the in-phase pitching, and the initial cycles of the out-of-phase pitching. Foils

oscillating in-phase at high *St* exhibit considerable improvement in thrust generation as the wake regularity (quasi-symmetric characteristics) is restored in time. The power consumption of the foils does not change significantly during this time, which implies an overall improvement in the propulsive performance. However, the symmetry breaking in the out-of-phase pitching wake seems not to affect the overall performance of the system since the collective (averaged) coefficient of thrust and power for the two foils does not change significantly after the wake symmetry breaking is triggered. Furthermore, the total non zero side-force production (collective between Foil 1 and Foil 2) is found to closely follow the wake asymmetry. Initially positive total side-force production of the foils drops to zero as their wake transitions from asymmetric to symmetric. However, foils begin to produce negative total side-force after symmetry breaking is triggered. This hints at a reasoning for fish alternating between in-phase and out-of-phase swimming synchronization in their natural environment. Next chapter presents a case study inspired by this phenomenon, aiming to delve deeper into its nuance.

Chapter 5

IMPLICATIONS OF CHANGING SYNCHRONIZATION ON PROPULSIVE PERFORMANCE[†]

Several fish species exhibit a tendency to form schools, a behavior driven by various factors such as reproduction, hunting, predator defense, and hydrodynamic advantages (Shaw, 1962). Numerous studies have delved into this phenomenon, shedding light on the advantages and ramifications of different school formations in fish locomotion. For instance, Weihs (1973) proposed that the diamond-shaped school offers the greatest hydrodynamic benefits to fish. However, Ashraf et al. (2016, 2017) demonstrated that red nose tetra fish prefer a side-by-side arrangement, with either in-phase or out-of-phase synchronization. Notably, their research revealed that these fish do not maintain consistent phase synchronization during locomotion; instead, they alternate between out-of-phase and in-phase synchronizations (see figure 2.8). Although Ashraf et al. (2016, 2017) provided insightful explanations on the effect of swimming configuration and synchronization on the fish propulsive performance, physical reasoning behind such swimming habit in changing the

[†]The content of this chapter has been published in whole or part, in *Bioinspir. Biomim.* with the citation: "Gungor, A., & Hemmati, A., (2021) Implications of changing synchronization in propulsive performance of side-by-side pitching foils. *Bioinspir. Biomim.*, 16(3), 036006."

synchronization of their tailfin oscillations remains unclear. Yet, this physical phenomenon inspired the current study that could lead to new design and operational strategies for Autonomous Underwater Vehicles (AUVs) and underwater energy harvesting technologies.

The wake deflection phenomenon behind single oscillating foils is discussed in detail in section 2.2.1. The emergence of asymmetry in the wake of parallel oscillating foils is reported by Bao et al. (2017) and Zhang et al. (2018) for out-of-phase motion without thorough discussion. In the previous chapter, the development of deflected wakes for side-by-side pitching foils is identified, and their implications for propulsive performance are documented. It is demonstrated that the symmetric characteristics of the wake are strongly correlated with the total side-force production of the foils. Lagopoulos et al. (2020) showed that deflected wake and total side force production can be eliminated for oscillating foils in an in-line configuration. They reported three different cases of interaction between the wake of the front foil and the back foil in which elimination is observed. Moreover, they showed that back foils can have a significant effect on the performance and wake of the front foil.

Nature of the asymmetric wakes could be coinciding with the fish swimming habits, such as change of synchronization, as hinted in chapter 4. However, more in-depth studies are needed to clearly identify the physical implications of such natural behaviors when incorporated in man-made systems. Here, we study pure in-phase and out-of-phase oscillations combined with hybrid swimming modes that incorporate a change in oscillation synchronization from in-phase to out-of-phase in various stages of pitching. This chapter is structured, such that the details of the numerical setup is discussed in section 5.1. This is followed by the main results and discussions in section 5.2. A brief summary is provided in section 5.3.

5.1 Problem Definition

Four hybrid synchronization modes, inspired by the experiments of Ashraf et al. (2016, 2017) on red nose tetra fish, are simulated at $St = 0.5$ to identify their implications on both performance and

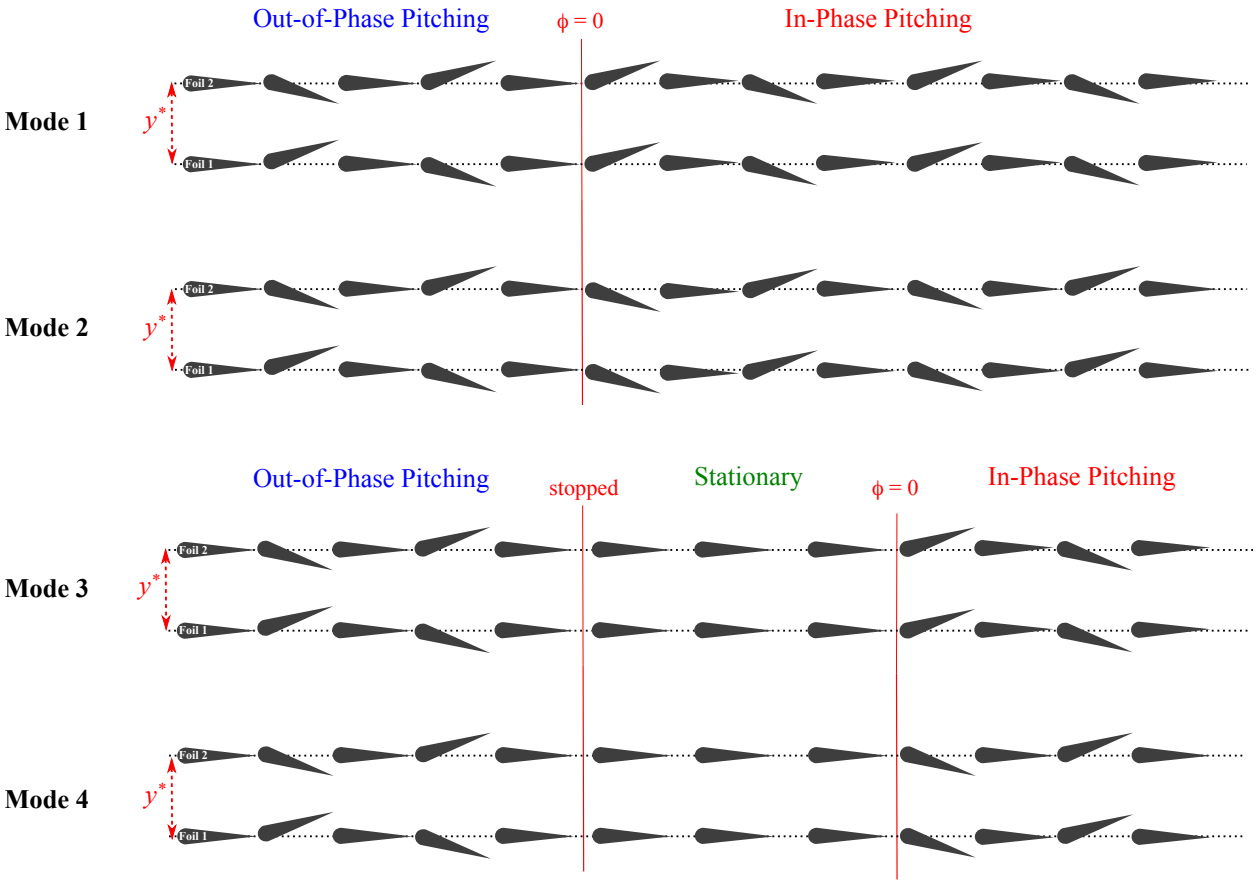

Figure 5.1: Graphical demonstration of the hybrid oscillation modes.

wake dynamics for man-made systems. Cases with pure in-phase and out-of-phase oscillations, examined in chapter 4, serve as reference studies. Other parameters used in the hybrid modes, such as Reynolds number, separation distance, and pitching amplitude, are kept the same as in chapter 4. A summary of the motion of the foils are illustrated in Figure 5.1. In in-phase pitching, the foils follow the identical angular path, while they have perfect mirror-image symmetric motion in out-of-phase oscillations. Modes $1-4$ represent hybrid synchronization modes, characterized by a transition from initially out-of-phase synchronization, spanning 20 oscillating cycles, to in-phase synchronization. The wake and propulsive performance of each of these cases are investigated for total 40 oscillation cycles. In Mode 1 and Mode 2, the change of synchronization (from out-of-phase to in-phase) occur instantly. The initial direction of the foil motion after the change of synchronization is counter-clockwise for Mode 1, while the first stroke is in the clockwise direction

for Mode 2. The primary aim of this part of the study is to evaluate the effect of initialization on the foil performance, since Liang et al. (2011) identified major impacts on both wake dynamics and performance due to the initial behavior of oscillating foils. The complexity of these hybrid modes is further extended, such that Mode 3 and Mode 4 present cases of delayed swimming with a change in synchronization. Thus, there is a no-oscillation period during which the foils stop pitching for the duration of two oscillation cycles just after the end of the 20th out-of-phase pitching cycle. Thereafter, the foils continue their motion by pitching in-phase with a counterclockwise first stroke for Mode 3, and vice versa for Mode 4. It is important to note that Mode 3 and Mode 4 were inspired by the burst-and-coast swimming in fish schools (Fish et al., 1991), in which the fish swimming is not steady. In such cases, the fish follow an intermittent swimming with periods of active oscillation (burst) and gliding (coast). Although the current two-dimensional simulations may not directly correspond to the three-dimensional self-propelled burst-and-coast swimming in fish (Kern and Koumoutsakos, 2006), they provide great insight into the hydrodynamics of man-made systems, the performance characteristics of which should remain similar. Moreover, the recent results of Zurman-Nasution et al. (2020) revealed that two-dimensional simulations of flapping foils yield adequate results compared to three-dimensional simulations in a certain parameter space that align with those in this dissertation.

5.2 Results and Discussion

We begin by revisiting the findings of Ashraf et al. (2017, 2016) as an inspiration for the current study on man-made systems, which showed that proper swimming pattern and synchronization improve the swimming performance in fish schools. Particularly, two red nose tetra fish were observed to arrange their position in side-by-side swimming, while synchronizing their tailfin beating frequency either in-phase or out-of-phase, to move faster in a shallow water channel. Moreover, it was reported that they switched their tailfin synchronization from out-of-phase to in-phase, or vice versa, in the course of their swimming exercise. This poses an interesting question on what are

the implications of changing phase angle between side-by-side foils, e.g., switching of synchronization, in the course of their locomotion. It is futile to address this problem from the perspective of swimming efficiency since fish have certain position and synchronization that allows them to exploit the wake for the best propulsive performance in a given setting (Weihs, 1973; Liao et al., 2003).

Initially, we look at the cycle-averaged thrust and power coefficients ($\widetilde{C_T}$ and $\widetilde{C_P}$) for pure in-phase and out-of-phase oscillations of side-by-side pitching foils in figures 4.10b and 4.11b. Out-of-phase oscillating foils produce significantly larger thrust than that of in-phase oscillating foils at a cost of more power consumption. These serve as reference cases for understanding the implications of switching synchronization in side-by-side foils, and the preference for out-of-phase compared to in-phase oscillations. Given the smaller thrust generation for in-phase pitching foils, it is hypothesized that such thrust generation is not sufficient and the configuration is not adequately stable for side-by-side foils to maintain their position steadily with increasing flow speed. It is also significant to identify that non-equivalent thrust generation and power consumption for these cases are highly correlated with asymmetry in the wake due to in-phase and out-of-phase oscillations. Similarly, the wake asymmetry coincides with a non-zero total side-force generated by side-by-side foils, which are shown in figure 4.12b. Out-of-phase oscillating foils produce negative total side-force after the symmetry in the wake is disturbed at approximately the 13th cycle. On the other hand, positive total side-force produced by in-phase oscillating foils approaches zero as the symmetry in the wake was restored in time. Detailed discussion on the correlation of wake asymmetry and propulsive performance for side-by-side foils is provided in chapter 4.

Based on the existing evidence on the performance and wake of oscillating side-by-side foils, inspired by red nose tetra fish tailfin locomotion, we hypothesize that symmetry breaking in the wake of out-of-phase oscillating side-by-side foils motivates abrupt switching of synchronization for enhanced performance. Although $2D$ simulations on oscillating side-by-side foils overlook fundamental flow features in $3D$ fish swimming, balancing the production of side force correlated with the wake symmetry could be a contributing factor for abrupt change of synchronization in-

spired from natural fish swimming habits. This physical processes motivates better hydrodynamic performance, i.e., maintaining lateral positioning and minimizing side- (lift-) force, in AUVs and man-made underwater energy harvesting systems. It is naturally preferred that side-by-side foils oscillate out-of-phase since it leads to larger thrust generation. However, this only remains true until the negative total side-force production begins, at which point foils would be displaced from their current or desired position if not properly constrained. Switching to in-phase oscillations, which exhibits positive side-force production, allowing them to maintain or stabilize their lateral position. Once the zero total side-force production is achieved, they can return to their out-of-phase oscillation to generate more thrust. Similar observations were also reported by Lagopoulos et al. (2020) for the effect of synchronization on side-force (or lift in their terminology) for in-line tandem foils. They remarked that under specific synchronization conditions between the front foil wake and back foil, the tandem configuration produced negligible side force with a considerable enhancement in thrust. This only provides a very brief explanation on why such variations may be observed in nature, and more detailed studies of a $3D$ self-propelled fish swimming may be needed for deeper insights into their swimming habits. Here, however, we focus on the implications of change in performance and wake development in man-made systems due to sudden or gradual change of oscillation synchronization in side-by-side foils inspired by tailfin locomotion of swimming fish.

5.2.1 Propulsive Performance of the Hybrid Modes

We consider four hybrid synchronization modes, all of which are based on an initially out-of-phase oscillations for 20 cycles. Each mode, thereafter, is designed based on different times for the on-set of switch of synchronization to in-phase oscillations, details of which are previously explained in section 5.1. Figure 5.2 presents the propulsive performance of both foils during all four hybrid modes, which are compared with the reference case of pure out-of-phase oscillations. Thrust and power coefficients in all cases converge to similar performance characteristics observed for pure in-

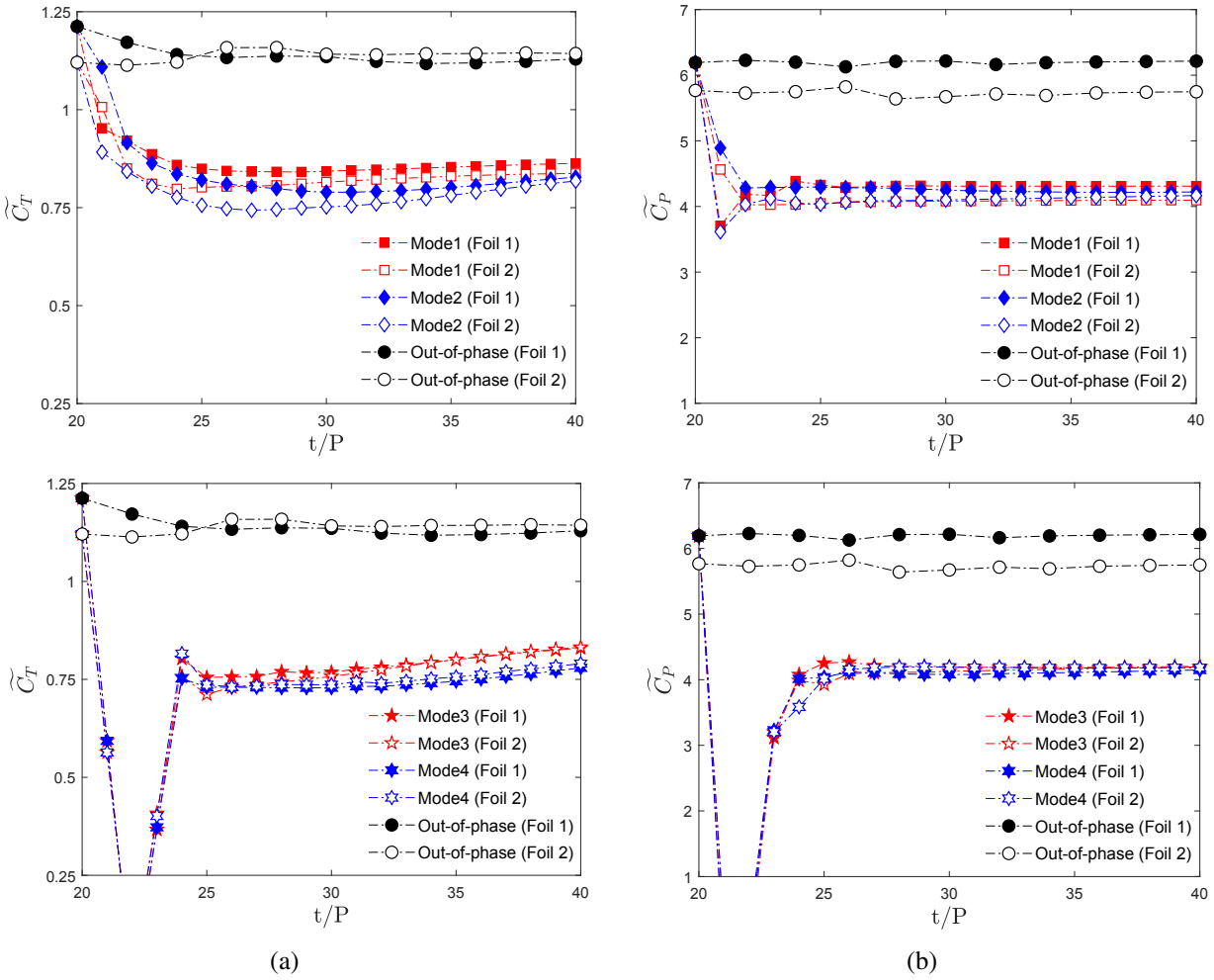

Figure 5.2: The variation of cycle-averaged (a) thrust and (b) power coefficients for Foil 1 and Foil 2 in time for modes $1-4$ and out-of-phase oscillation.

phase oscillations shortly after the switch in synchronization. However, there are major differences between each case that require further discussion.

First, there is a difference in the rate at which foils approaches quasi-steady performance in thrust compared to power following the flow disturbances introduced by the change in oscillations. To this effect, coefficient of power adjusts quickly within 3 cycles to in-phase characteristics (see figure 5.2), while $\widetilde{C_T}$ required significantly more cycles to approach quasi-steady behavior. Particularly, Mode 1 is the fastest in reaching stable thrust production within 3 cycles after the switch occurred, while thrust generation for Foil 2 slowly approaches that of Foil 1 until 30th$-$35th cycle. Mode 2, Mode 3 and Mode 4 are slow in their recovery, in which a prolong effect on the

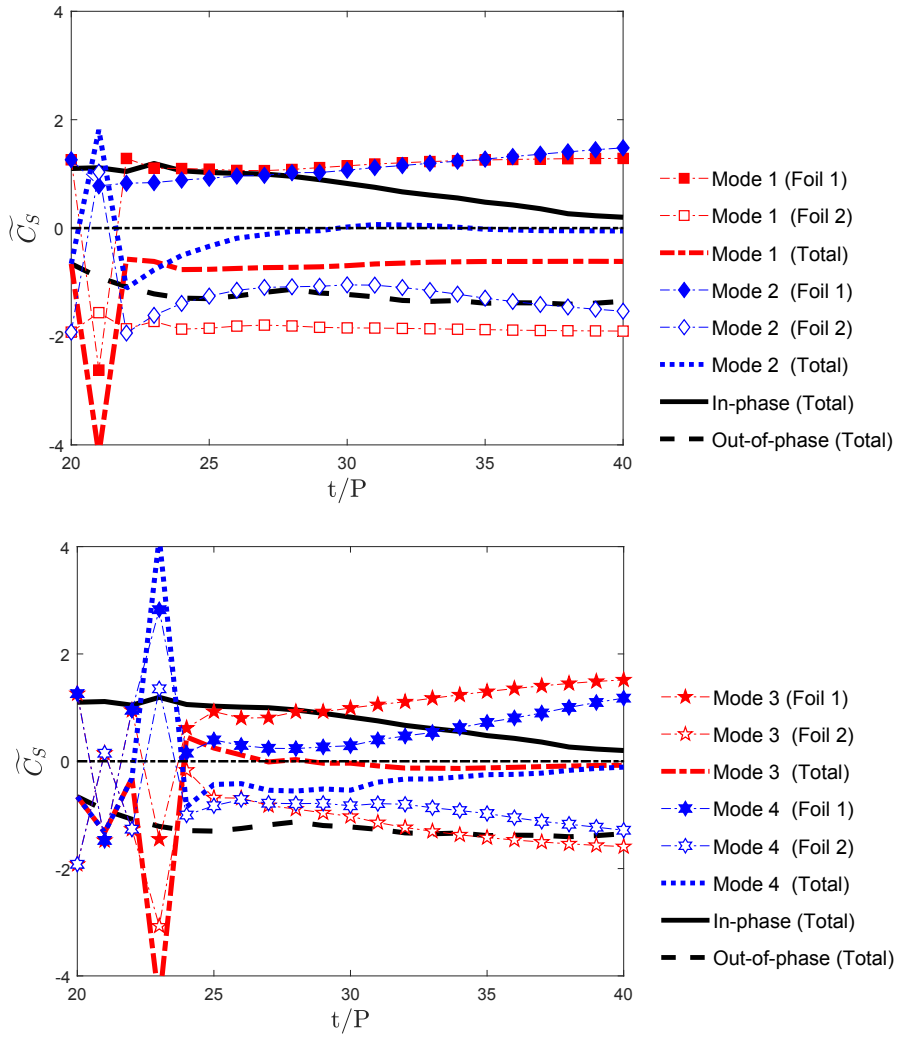

Figure 5.3: The variation of cycle-averaged side-force coefficient for Foil 1, Foil 2 and the system (Foil 1 and Foil 2) for modes $1-4$ and in-phase and out-of-phase oscillations.

performance of both foils is apparent until end of the 40th cycle. It is also important to note that differences in thrust generation between Foil 1 and Foil 2 at the onset of stability for Mode 4 (say 30th cycle) is 1.9% lower than those for Mode 1, 79.3% lower than Mode 2, and 28.1% lower than Mode 3. Since power variations are very similar for all cases, it is apparent that the larger thrust generation of Mode 1 and Mode 3 translates to improved efficiency, which are not shown here for brevity.

There are significant differences in terms of side-force production for both foils amongst the hybrid modes of oscillation, which are shown in Figure 5.3. All hybrid modes, except for Mode

1, experiences a major reduction in the total side-force production after a small number of cycles. This hints that the change in oscillation in mid-swimming has more implications on retaining position or separation distance than it does on improved propulsion. Although the long-term production of the side-force for Mode 2, Mode 3 and Mode 4 collapse to zero by the 40th cycle, Mode 2 appears to achieve zero total side-force production faster than other modes. Particularly, Mode 2 reaches zero total side-force production by the 30th cycle, while Mode 3 and Mode 4 does not get to zero production until the 38th cycle. It is also intriguing that zero total side-force production is achieved faster with changing the oscillation synchronization mid-swimming compared to the case of pure in-phase pitching by more than 20 cycles. The near zero total side-force production implies that the two foils, inspired by fish tailfins, will be able to retained their collective position inside the fluid medium. The non-zero total $\widetilde{C_S}$ indicates that the two constrained foils will drift apart at a large rate over long periods of time if they do not change their oscillation correlation.

The apparent large difference in total side-force production between Mode 1 and Mode 2, which only differ on the initiation of oscillations (direction of first stroke), implies a very complex wake dynamics in play, which deserve a detailed wake analysis. One possibility is the effect of pitching initiation (direction of first pitch), and another can be related to vortex interactions and wake history. The observation of the difference between Mode 1 and Mode 2 is consistent with those on the propulsive performance of single foils (Liang et al., 2011; Cleaver et al., 2012), as well as tandem foils (see chapter 4). However, it expands on these observation by indicating that the effect of initiation remains significant even if there exists a wake history. Thus, the differences in performance are mostly related to the formation and detachment of structures from the body, rather than their interactions in the wake. The combination of differences between hybrid modes themselves, and that of pure in-phase pitching case in general, brings out the need to study the wake topology that may be related to variations in $\widetilde{C_S}$ for each foil. While a general discussion of the wake dynamics is provided in the next section to support our hypothesis, a more comprehensive study of the wake structures as well as their developments, interactions and models for four hybrid modes with abrupt changes in synchronization are provided in the next chapter (chapter 6).

5.2.2 Wake Analysis

The study of Godoy-Diana et al. (2008) on wake dynamics and performance of pitching foils at a range of Strouhal numbers revealed that there is a general coincidence in appearance of wake asymmetry and hydrodynamics benefits. They identified that the wake asymmetry occurs at a certain range of Strouhal number and non-dimensional amplitude for pure-pitching foils, which coincides with the Strouhal number range of natural swimming of fish. This was further discussed by Khalid et al. (2020), who observed that swimmers achieve their maximum efficiency just before the onset of the wake deflection, after which their performance deteriorates with asymmetric wakes. Based on this, they suggested that fish must be exploiting the asymmetric wake regime for maneuvering purposes or avoiding it for stability. Thus, the wake asymmetry and its implications in the case of intermediate change in oscillations is critical in understanding the swimming habit of fish for inspiration to achieve better performing man-made systems, e.g., underwater propulsors and energy harvesters.

The Strouhal number of $St = 0.5$ in the current study is the median St in the experiments of Ashraf et al. (2017, 2016), in which the switching of swimming synchronization is observed in fish. It is also larger than $St = 0.3$, which Godoy-Diana et al.Godoy-Diana et al. (2008) reported as the threshold after which the wake appears asymmetric. This indicates that there may be a major change in wake asymmetric characteristics due to the switch in synchronization that requires a more detailed investigation. To this end, contours of spanwise vorticity (ω_z^*) are shown in figure 5.4 for both reference cases and the hybrid modes of oscillations at the 40th cycle ($t/P = 40$). Although the in-phase pitching motion is assigned to the hybrid oscillation cases between the 20th (or 22th for Mode 3 and Mode 4) and 40th cycles ($t/P = 20 - 40$), the wake of pure in-phase pitching foils significantly differed from that of all hybrid modes. As shown in figure 5.4a, an in-phase pitching system of side-by-side foils produces a single horizontal wake at $St = 0.5$. Moreover, it initially forms a split-wake that does not fully merge to create a single vortex street until the 30th cycle (see figure 4.5a). The hybrid modes of oscillations, on the other hand, all retain a split-wake (figures 5.4c$-$5.4f), similar to the pure out-of-phase pitching case in figure 5.4b. We measured

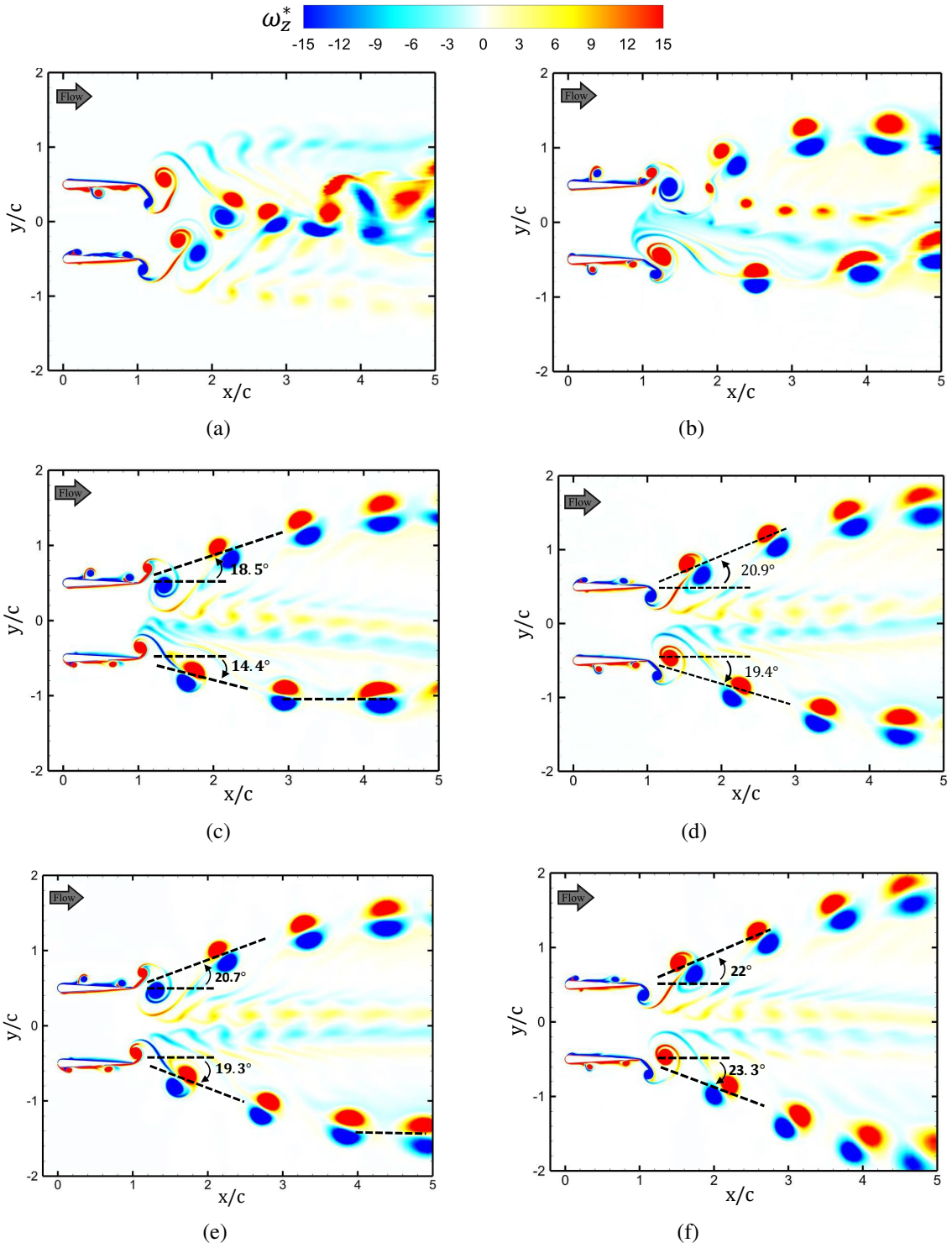

Figure 5.4: Contours of spanwise vorticity ($\omega_z^* = \omega_z\, c/U_\infty$) for side-by-side foils pitching (a) in-phase, (b) out-of-phase, (c) Mode 1, (d) Mode 2, (e) Mode 3, (f) Mode 4 at $t/P = 40$.

the wake width at $x/c = 3$ and $t/P = 40$ for all cases, based on the method of Sarkar and Sarkar (2010). In discussion of the the wake, we only focus on how the wake development and width changes with the change in prescribed motion. Here, the width is defined as the distance between two points, where the velocity deficit drops below half of the maximum value of the streamwise velocity deficit in the wake. Since the wake in all hybrid modes have two distinct branches, the wake width is calculated between the maximum of the upper branch and the minimum of the lower branch. The width of the wake of Mode 3 and Mode 4 were $2.66c$ and $2.67c$, respectively, which are both higher than $2.45c$ for Mode 1 and $2.55c$ for Mode 2. Note that Mode 3 and Mode 4 experience interruption in swimming for 2 cycles, compared to Mode 1 and Mode 2, after which they switch their synchronization from out-of-phase to in-phase pitching. This observation implies that the changes in thrust generation, power, and side-force amongst different hybrid oscillatory modes coincide with differences in terms of wake dynamics.

We next quantify the angle of wake deflection for both vortex streets for all cases. Although none of the wakes considered are mirror image symmetric, the angle of deflection for the upper and lower streets were similar between Mode 2, Mode 3 and Mode 4 (see figure5.4). In case of Mode 1, however, the deflection angle for one street is significantly different than that of the other. This coincides with the total non-zero side-force generation diverging from zero for Mode 1 compared to the other hybrid modes of oscillation. There also appears to be a split in the path of vortical structures at $x/c \approx 4.5$ in the lower street for Mode 3, which is only observed in the lower branch of Mode 1 at $x/c \approx 3$. Mode 2 and Mode 4 does not exhibit a similar split in the near and mid-wake, that is $x/c \leq 5$.

Figure 5.5 shows the trace of vortical structures in the wakes of modes $1-4$. Two pairs of counter-rotating vortices shed by Foil 1 and Foil 2 are tracked for a time equal to 3 oscillation cycles starting from $t_{in} = 37P$. Trails of Mode 2 and Mode 4 follows a v$-$shape, while vortices shed in Mode 1 and Mode 3 follows an arched path that straightened after $x/c \approx 3.5$. Collective location of the vortices, however, remains close to the centerline ($y/c = 0$) for all hybrid modes, except for Mode 1, which experiences a divergence at $x/c > 4$. This deviation from the centerline,

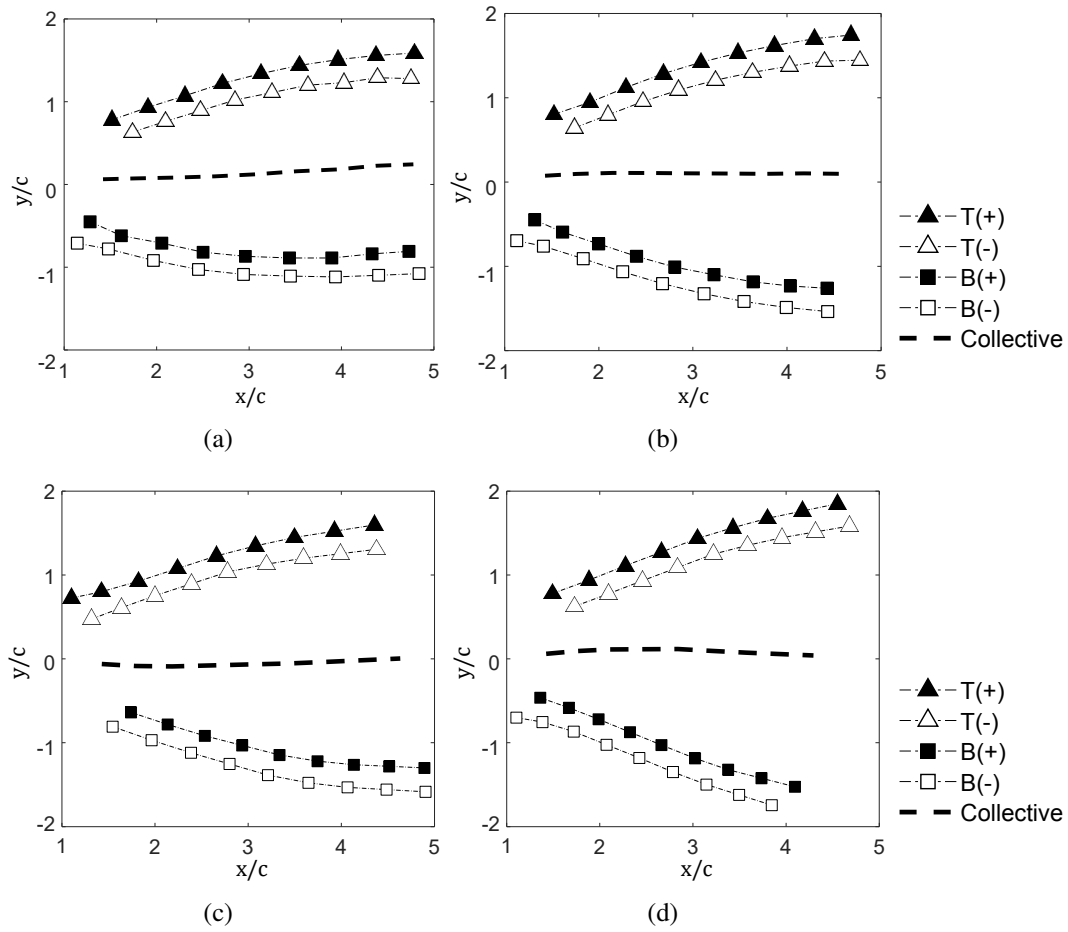

Figure 5.5: Trace of location of vortex cores shed by Foil 1 (B) and Foil 2 (T) for 3 oscillation cycles starting from $t_{in}/P = 37$ for (a) Mode 1, (b) Mode 2, (c) Mode 3, (d) Mode 4. (+) and (-) correspond to positive and negative vortex cores, respectively.

similar to the comparison of deflection angles, coincides with the fact that Mode 1 is the only mode in which non-zero total side force production is observed.

The difference in wake structures are proportionally more significant than small changes in performance characteristics (mostly on thrust generation and efficiency) of the foils. This is based on the observation that time-averaged thrust coefficient for hybrid modes appear to only vary by $1.3\% - 12.5\%$ compared to pure in-phase pitching foils. However, their wakes are fundamentally different. The combination of these observations indicates that wake structures only relate to performance on certain control settings, which does not include the presence of a wake history, similar to the simulations here. This agrees with the findings of Floryan et al. (2020), which suggested

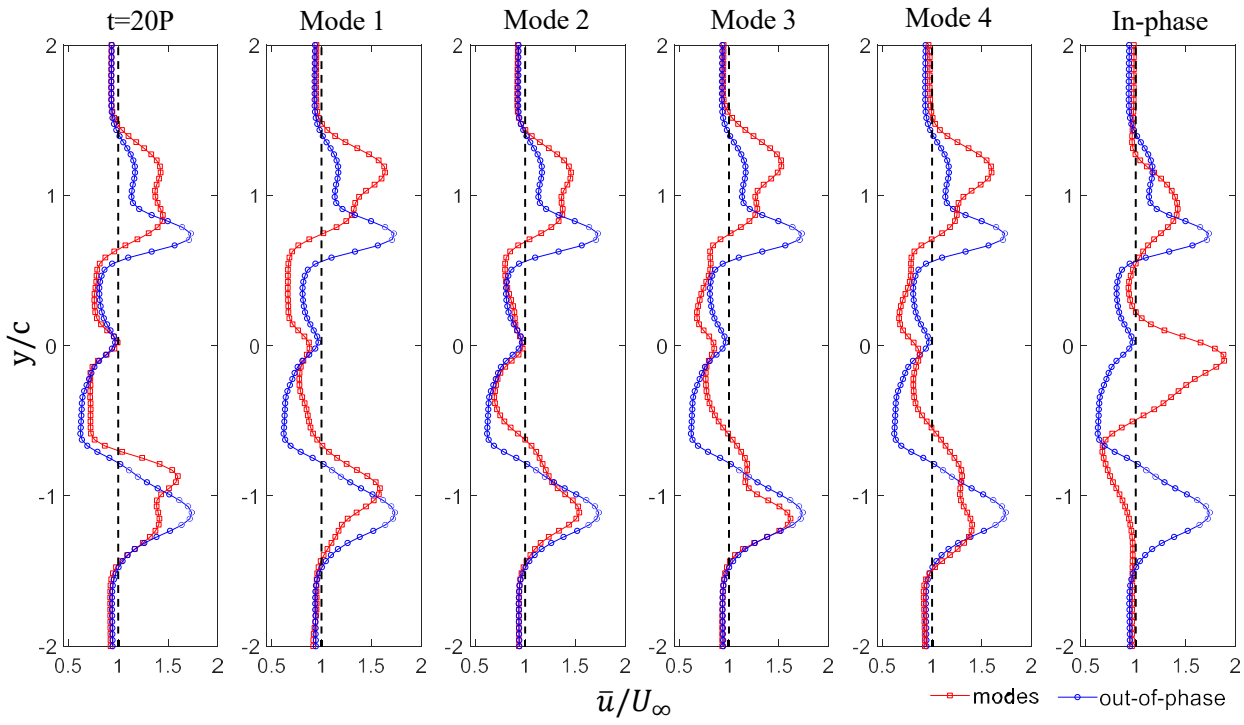

Figure 5.6: The profiles of mean streamwise velocity for all hybrid modes at $x/c = 3$ and the 40th cycle.

that swimming performance is not directly indicated by the wake structures. They further reported that vortex spacing, pattern and interactions could be misleading to interpret the swimming performance in some cases. Although we provide information here that verifies their reporting, we have also observed that there are certain correspondence in simple contentious oscillatory motions between performance and wake structures, which may not necessary be reciprocal between the two.

The time-averaged streamwise velocity profiles in figure 5.6 identify the variations in the structure of mean wake amongst hybrid modes of oscillations. The velocity profile at the 20th cycle consists of double peaks for both vortex streets, which suggests a thrust generating wake. This, however, is changed for hybrid modes, in which the mean velocity profiles consist of a single peak for both upper and lower vortex streets. The mean wake for Modes $2-4$ appear distorted, such that there is for example a resemblance of two small, and closely assembled, peaks at $y/c \approx 1$ for Mode 2 and at $y/c \approx -1$ for Mode 4. Thus, it is plausible that the wake in Mode 2, Mode 3 and

Mode 4 require more time for recovery compared to Mode 1. This suggests that the fast recovery of Mode 1, compared to Modes $2-4$ that have a different initial direction of pitching, translates to differences in the mean wake. Given the direction of initial pitching for Mode 2 and Mode 3 are opposite of one another, it is apparent that the wake development does not necessarily correlate closely with the initial direction of pitching.

5.3 Summary

The propulsive performance and wake of side-by-side pitching foils are studied numerically at $St = 0.5$ and $Re = 4000$. Cycle-averaged coefficients of thrust, power and side-force are investigated for in-phase, out-of-phase and hybrid oscillations to investigate the implications of abrupt change in phase difference inspired from swimming fish observed in nature. Non-zero total side-force generation by pitching foils could be a major contributing factor that motivates adopting such habit in design and operation of underwater propellers and energy harvesters. The results show that abruptly changing the phase difference between side-by-side foils, from out-of-phase to in-phase, compensates for zero total side-force generation to maintain lateral positioning or other maneuvering desires. This hypothesis is further supported by the findings based on hybrid modes of oscillations, Modes $1-4$, which consist of both out-of-phase and in-phase pitching, similar to experimental observations of Ashraf et al. (2017, 2016) for red nose tetra fish. In the case of Modes $2-4$, negative total side-force generation drops to zero relatively quickly ($5-7$ cycles) after the switch from out-of-phase to in-phase pitching.

The coefficient of thrust and power differed amongst different hybrid modes of oscillation, which show the importance of correct timing in change of synchronization for optimum benefit. They also differed from the case of pure in-phase pitching foils. While the variations in thrust were more apparent, there appeared to be minimal changes in power requirements, which hints at improvements in efficiency depending on onset of the hybrid modes. Despite small changes in performance amongst the hybrid modes and in-phase pitching, the former oscillations exhibited

fundamentally distinct wakes than that of the pure in-phase pitching foils. The upper and lower vortex streets merged to form a single vortex street at the wake centerline for pure in-phase pitching ($y/c = 0$), while two distinct vortex streets were observed for all hybrid modes that diverged from one another. These two streets in the wake of Modes $1-4$ were qualitatively similar to the wake of pure out-of-phase pitching foils even though the foil performance was very different and more similar to the in-phase pitching. This indicated that using only wake structures may be misleading in determining the performance characteristics of fish in the presence of a wake history, similar to abrupt change of synchronization or interruption in swimming.

The differences in wake structures amongst hybrid modes of oscillation hint at a change in how newly formed structures, following the change in oscillation pattern, interact with exiting structures in the wake. Consequently, the subsequent chapter is dedicated to examining this dynamic behavior of unsteady wakes and exploring vortex models.

Chapter 6

IMPLICATIONS OF CHANGING SYNCHRONIZATION ON WAKE DYNAMICS[†]

There exists a known correlation between the side (lateral) force production and asymmetric wakes (Khalid et al., 2015; Lagopoulos et al., 2020) for pitching and heaving foils. As hinted in the previous chapter, this may also be relevant to the case of tandem foils undergoing abrupt changes in their pitching synchronization. Chapter 5 revealed that varying synchronization patterns enabled the foils to maintain their lateral positions inside the multi-foil arrangement. Furthermore, it is observed that the foils require a period of $10-20$ cycles to reach quasi-steady performance depending on the onset of change in synchronization. The current chapter expands on these findings by exploring the implications of such effects on the unsteady wake dynamics for tandem foils. Here, the central theme is to identify and illustrate underlying flow control mechanisms fish may employ during swimming in order to modify their wakes and consequent hydrodynamic forces over their bodies for propulsion. The paper is organized in the following manner. The problem

[†]The content of this chapter has been published in whole or part, in *Phys. Fluids* with the citation: "Gungor, A., Khalid, M.S.U., & Hemmati, A., (2021) How does switching synchronization of pitching parallel foils from out-of-phase to in-phase change their wake dynamics?. *Phys. Fluids*, 33(8), 081901."

description is provided in section 6.1 followed by the discussion on the results in section 6.2. A brief summary and conclusion is included in section 6.3.

6.1 Problem Definition

The same four hybrid synchronization modes discussed in chapter 5 (see figure 5.1) are employed in this analysis. However, the parameter space for both the Reynolds number and the Strouhal number is expanded here, aiming to comprehensively characterize the effects of sudden phase changes on the propulsive performance and the unsteady wake dynamics of parallel pitching foils. The detailed wake dynamic analysis initially focuses on the case of $St = 0.5$ and $Re = 4000$, while the effect of St is examined by comparing the wake and performance of the two foils at $St = 0.25 - 0.40$ in conjunction with the results discussed for $St = 0.5$. Finally, the special case of a lower Reynolds number is studied for $St = 0.5$ at $Re = 1000$ to examine the applicability of wake and performance observations in flow conditions mostly observed in low-speed underwater maneuvers. At low St ($St = 0.25$ and 0.3), foils maintained $\phi = \pi$ for the initial 10 pitching cycles, at which they had established a quasi-steady behavior as depicted in figure 4.2 while phase change took place at the 20th cycle for high St cases ($St = 0.4$ and 0.5) following chapter 5. Therefore, the wake and propulsive performance of each of these modes were investigated for a total of 30 and 60 oscillation cycles for low and high St cases, respectively.

6.2 Results and Discussion

The hydrodynamic performance of the system of side-by-side pitching foils for $St = 0.5$ and $Re = 4000$ is detailed in chapter 5. When comparing the performance of the foils between Mode 1 and Mode 2 (see figures 5.2 and 5.3), an inherent difference is observed between the two hybrid modes. This difference can be attributed to the existing wake and performance asymmetry at such high St and Re. This phenomenon leads to lack of symmetry in both performance and the wake between the two foils at the 20th cycle, which is retained following the phase change between

them. Interestingly, thrust generation for the foils start approaching one another at the 40th cycle, but their side-force variations remain substantially different even in quasi-steady conditions, i.e., 40th cycle. It hints at potential variations in wake dynamics that remain intact despite quasi-steady state of the flow. Similar observations are apparent for Mode 3 and Mode 4 in terms of thrust generation. However, side-force differences between the two modes appear to shrink approaching the quasi-steady conditions. This further depicts a potential alteration of the wake dynamics, which appear to be suppressed by the suspension of oscillations after the 20th cycle for Modes 3 and 4 compared to Modes 1 and 2.

6.2.1 Unsteady wake evolution

In this section, we focus on the vortex dynamics in the wake of two parallel foils in side-by-side configurations at $St = 0.5$ and $Re = 4000$. This is meant to illustrate how the wake dynamics and coherent structures influence the production of lateral (side-) force. For this purpose, not only the vortex shedding process from the individual foils are described, but also the interference of these vortices, their shape and orientation in the overall wake are explained in detail. It establishes how they affect the lateral force acting on the foils for all four hybrid modes despite their similar kinematics, particularly Mode 1 versus Mode 2, and Mode 3 versus Mode 4.

Secondary vortex street (Mode 1)

In mode 1, foils begin their in-phase oscillations with an upstroke motion during the 20th cycle. Throughout the motion, including the out-of-phase pitching before the abrupt phase change, positive and negative leading edge vortices (LEVs) are formed on the leading edge of the foils (see figure 6.1a). LEVs travel on the lower side of Foil 1 and the upper side of Foil 2 towards the trailing edges of the two foils. One LEV per pitching cycle separate from the foils only to be merged with structures formed at the trailing edges, which are referred to as trailing edge vortices (TEVs). These are then shed into the wake. Figure 6.1a show the alignment of vortices at the onset of switch in phase difference, i.e., $t = 20.5P$. Two vortex dipoles are observed (D_{u_1} and D_{l_1}) moving down-

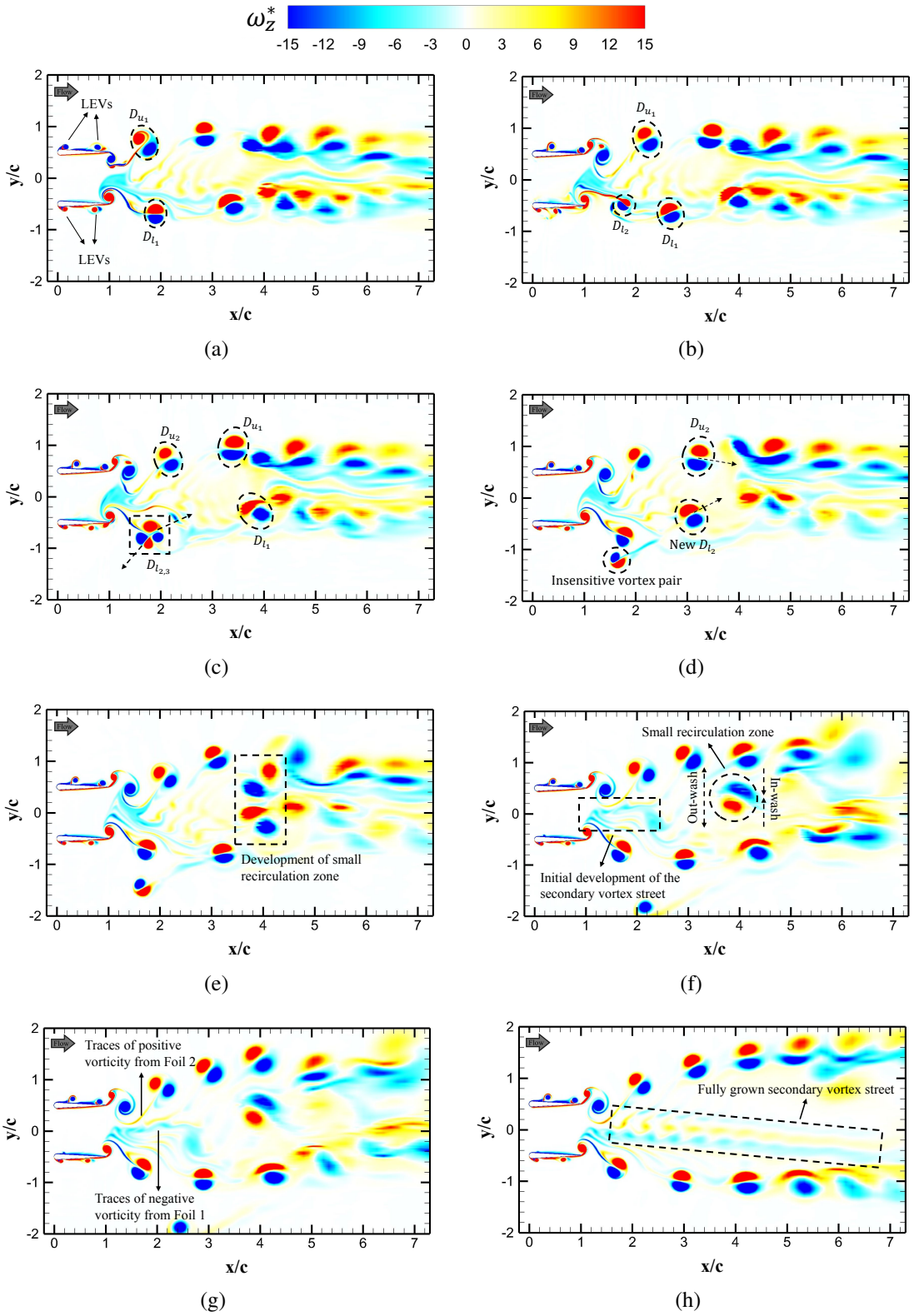

Figure 6.1: Contours of spanwise vorticity ($\omega_z^* = \omega_z c/U_\infty$) at (a) 20th, (b) 21th, (c) 22nd, (d) 23rd, (e) 24th, (f) 27th, (g) 28th, and (h) 40th pitching cycle for flows over side-by-side foil following Mode 1 for $St = 0.5$ and $Re = 4000$.

stream. These dipole structures are the last vortex pairs formed by the initial out-of-phase motion, and they do not appear symmetric about the horizontal axis ($y/c = 0$). D_{l_1} traveled upwards due to its higher cross-stream velocity, whereas D_{u_1} exhibits a very small cross-stream displacement with a large stream-wise convective speed (see figure 6.1b). During the 22nd pitching cycle, D_{l_2} begins to traverse upstream to interact with the consecutive pair shed from Foil 1. One of the poles of D_{l_2} that has a negative vorticity (blue color in figure 6.1c) paired with a pole of D_{l_3} with opposite sign vorticity (positive - red color). This forms two new dipoles that are separated and move in opposite directions in the wake (see arrows in figure 6.1c). The newly formed dipole structure moving upstream remains under the lower primary vortex street and diffuses after a few more cycles without making further significant contributions to the wake dynamics.

Newly formed D_{l_2} and D_{u_2} approach each other until their initial interactions in the 24th cycle form a small recirculatory zone, which is identified by the dashed rectangle in figure 6.1e. Two vortices in the middle of this region retain their position, hence forming a small region of consistent recirculatory fluid. The other two structures are convected downstream. The newly formed recirculary flow region between the two vortex streets remains intact for 4 cycles, until the end of the 28th cycle in figure 6.1g. Although this local recirculatry region moves downstream, its convective speed is slow. Moreover, the circulatory motion of the fluid inside this region induces secondary upwash and downwash flows after and prior to this zone, which are identified in figure 6.1f at $x/c = 4$. This intermediate dynamics provides some additional space for a secondary vortex street to be formed by the traces of positive vorticity from the wake of Foil 2 and negative vorticity from that of Foil 1. These are highlighted in the rectangular region in figure 6.1h. On the contrary, Raj and Arumuru (2020) found the jet deflecting on one side due to the interaction of vortices shed from their foils in a similar configuration but oscillating in a quiescent fluid. For the remaining oscillation cycles, this secondary vortex street grows from which the induced flow keeps the two primary streets from merging with each other. It is important to note that the vortex pair in the recirculation zone, shown in figure 6.1f, stays in the middle of the two primary vortex streets only to diffuse at a later stage by the induced momentum from the newly forming secondary

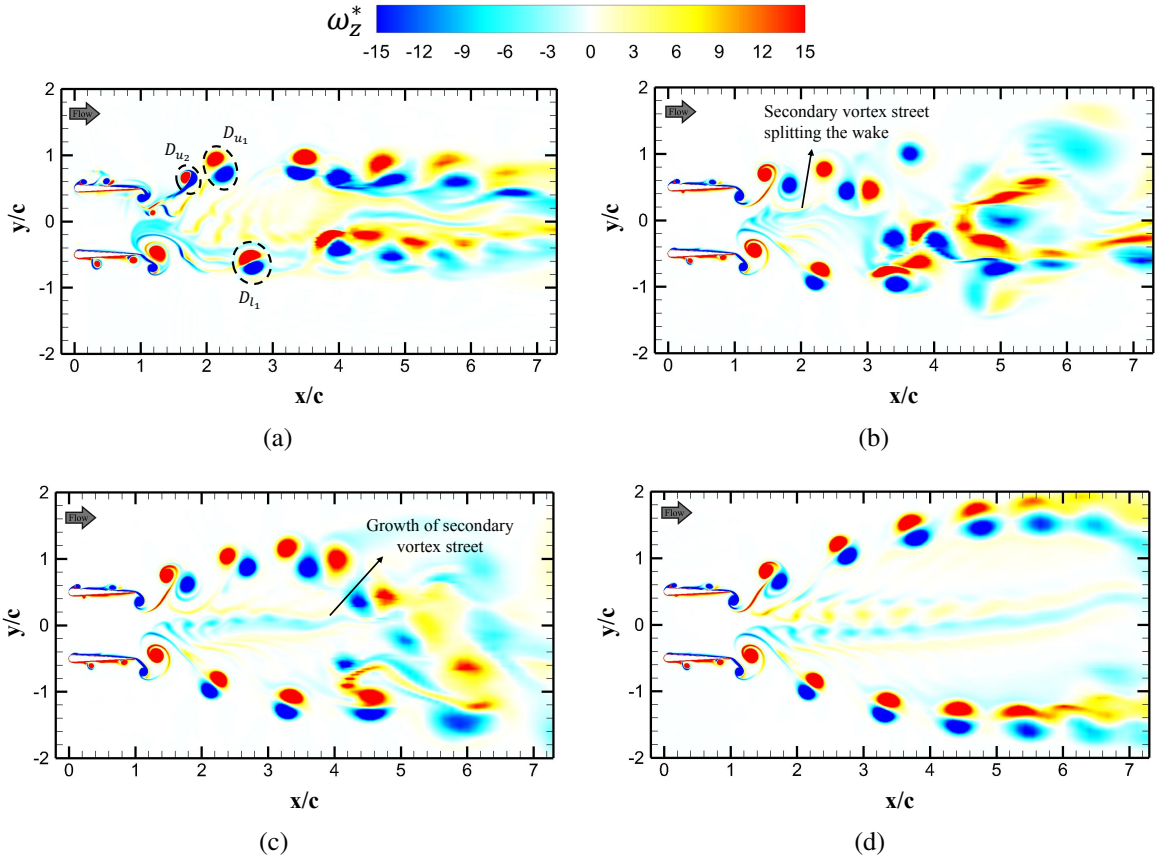

Figure 6.2: Contours of spanwise vorticity ($\omega_z^* = \omega_z\, c/U_\infty$) at (a) 21th, (b) 27th, (c) 32th, and (d) 40th pitching cycle for flows over side-by-side foils following Mode 2 for $St = 0.5$ and $Re = 4000$.

vortex street. Hence, the wake does not merge to form a single vortex street similar to that for a pure in-phase pitching case (Dewey et al., 2014). On the contrary, foils develop a two vortex street tilted away from each other similar to pure out-of-phase pitching foils in side-by-side configurations (Bao et al., 2017; Quinn et al., 2014). The same wake mechanism is also observed for Mode 2 in quasi-steady conditions.

Effect of initiation (Mode 1 versus Mode 2)

The time-lapse of wake contours for Mode 2 are shown here for only limited time instants for brevity. It is suffice to state that the wake experiences the formation of a secondary vortex street portrayed in figure 6.2. At this stage, this formation is dominated by small structures with negative vorticity from both foils. From the 27th pitching cycle shown in figure 6.2b, the secondary vortex

street grows downstream and becomes more prominent. Interestingly, this expanding vortex street splits the overall wake by pushing the intermittently interacting coherent structures further downstream. The presence of this circulatory flow region deflects the primary vortex streets. Thus, there are no apparent interactions between the two vortex streets, hinting that their dynamics appears not to depend on one-another. As the secondary vortex grows past the 32nd cycle in figure 6.2d, the wake deflections persist throughout the remaining oscillation cycles, approaching a quasi-steady behavior. This aligns with the variations in thrust, power, and side-force.

The wake immediately following the change in phase angle for Mode 2 experiences subtle differences with Mode 1, which attributes to the variations previously described in their performances. Particularly, the wake asymmetry leads to a close interaction of D_{u_1} and D_{u_2} in Mode 2 (figure 6.2a) compared to their counterpart in Mode 1 (D_{l_1} and D_{l_2} in figure 6.1b). The separation distance between the pairs is almost zero for Mode 2, whereas they are separated by $\approx 1c$ in Mode 1. This separation between the pairs in Mode 1 allows D_{l_1} (figure 6.1b$-$f) to separate and interact in the wake, initiates the formation of what is then referred to as a "small recirculation zone" for Mode 1 in figure 6.1f. Contrarily, the interactions of D_{u_1} and D_{u_2} in Mode 2 (figure 6.2a$-$b) do not allow for D_{u_1} to act as a rogue structure in the wake. Thus, there is no local recirculation zone formed between the 25th to the 32nd cycle, as observed for Mode 1. This coincides with the total side-force approaching zero for Mode 2, whereas it remains non-zero for Mode 1. Finally at the quasi-steady state, both modes experience a secondary vortex street formed in between the two primary streets. However, the one for Mode 2 is not tilted as seen for Mode 1 on the account of a "small recirculation zone" that does not form for Mode 2. This has a long lasting effect on the wake, as well as thrust generation and side-force production of the foils, in Mode 1 compared to Mode 2.

Effect of suppressed oscillations (Mode 3 & Mode 4)

The oscillatory motion of foils in Mode 3 and Mode 4 are suspended for 2 cycles after the 20th cycle. Then, they begin their in-phase oscillations. Two vortex pairs, shed just before the foils

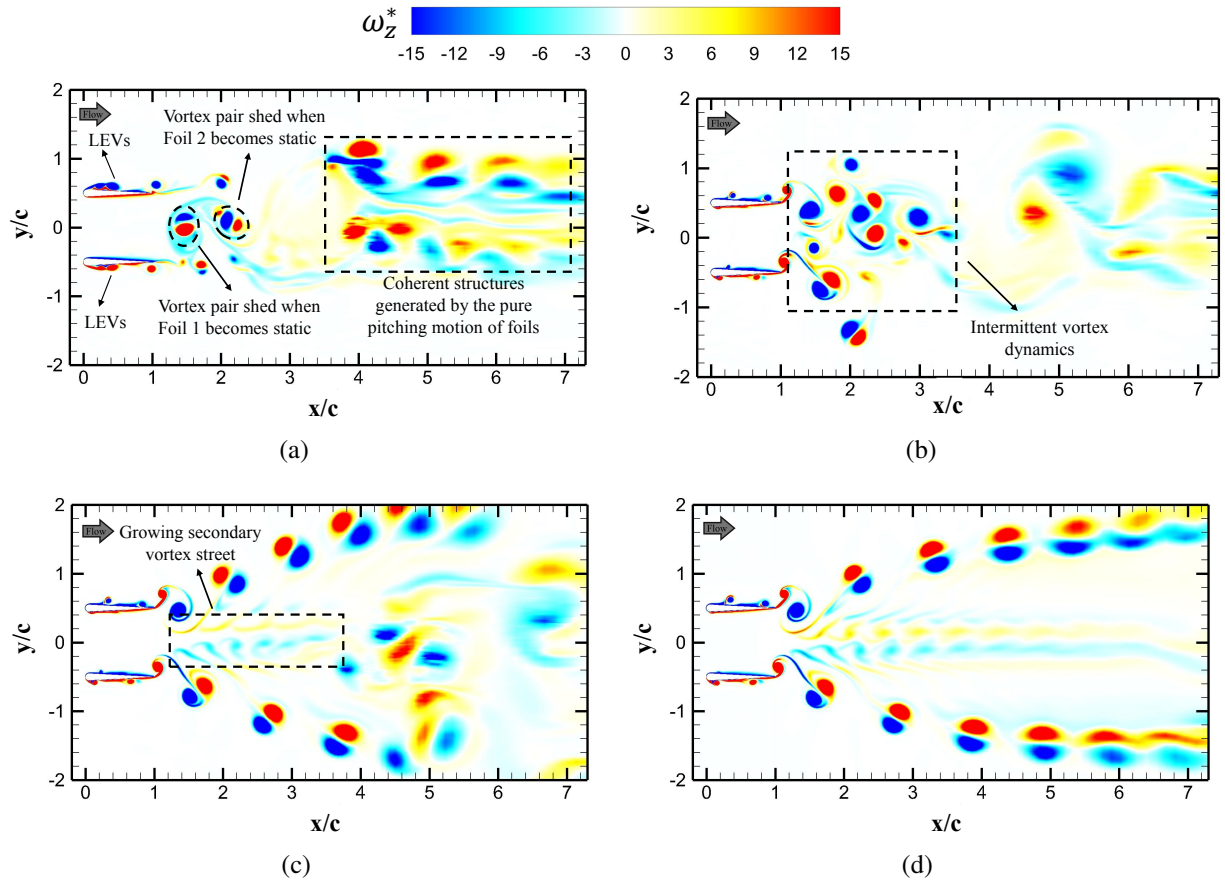

Figure 6.3: Contours of spanwise vorticity ($\omega_z^* = \omega_z c/U_\infty$) at (a) 22.5th, (b) 25th, (c) 32nd, and (d) 40th pitching cycle for flows over side-by-side foils following Mode 3 for $St = 0.5$ and $Re = 4000$.

became static, are trapped in a recirculation region in the near wake as seen in figure 6.3a. Upon the start of oscillations in Mode 3, the formation and shedding of more vortex pairs for the next three oscillation cycles form a region with intermittent flow dynamics that is identified by a dashed rectangular enclosure in figure 6.3b. This region is referred to as an intermittent regime because these vortices undergo intense interactions within this region, and no distinct pairing mechanisms may be identified. During three more oscillation periods, two interesting phenomena are observed: (1) a secondary vortex street, identified by a box in figure 6.3c, is formed by the trailing parts of larger structures with negative vorticity (blue color in figure 6.3) that are shed from Foil 1 in the middle of the two primary vortex streets, and (2) a circulatory fluid zone is formed by the vortices shed during the 23rd to 28th cycles, which convects downstream. The circulatory zone appears to

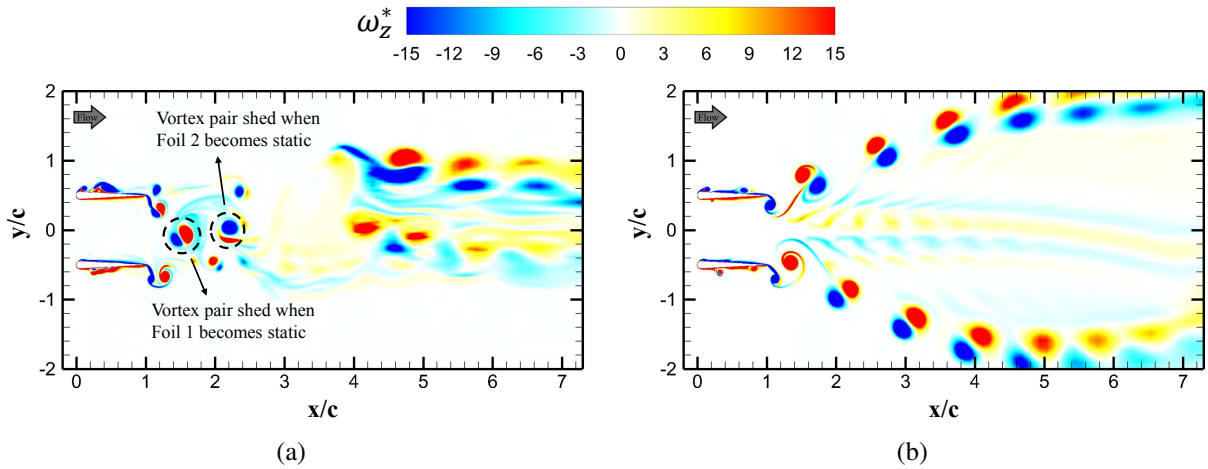

Figure 6.4: Contours of spanwise vorticity ($\omega_z^* = \omega_z\, c/U_\infty$) at (a) 23rd and (b) 40th pitching cycle for flows over side-by-side foils following Mode 4. for $St = 0.5$ and $Re = 4000$.

experience a large convective speed, such that it moves downstream quickly compared to previous observations of similar processes in Mode 1.

The growth of the secondary vortex street (shown in figure 6.3d) appears to be the key factor in the primary vortex streets attaining their quasi-steady behavior by bifurcating the region of the main flow activity. Evidently, the angles of the primary vortex street do not change after the 30th cycle, that is after the secondary vortex street grows to dominate the centre of the wake. To this effect, the dynamics of these vortex streets approaches a quasi-steady nature after the 36th cycle.

The wake configurations resulted from Mode 4 are also presented in figure 6.4 to account for the effect of suspended oscillations and wake alternations arose by changing the initiation of foil oscillations. The foils in Mode 4 has a similar general behavior to Mode 3 with the opposite direction of initial pitch. There are, however, very subtle differences in the wake compared to Mode 3, which are substantially less significant than differences observed between Mode 1 and Mode 2. First, the suspended oscillation periods allow for the wake to settle, such that there are no rogue structures formed in the wake for one mode versus the other, compared to what is observed for Mode 1. Second, the wake developments appear to be very similar, but yet slightly get altered by the convective speed and direction of structures immediately behind the two foils (compare figure 6.4a with 6.3a). These small variations in the intermittent stage of the wake development

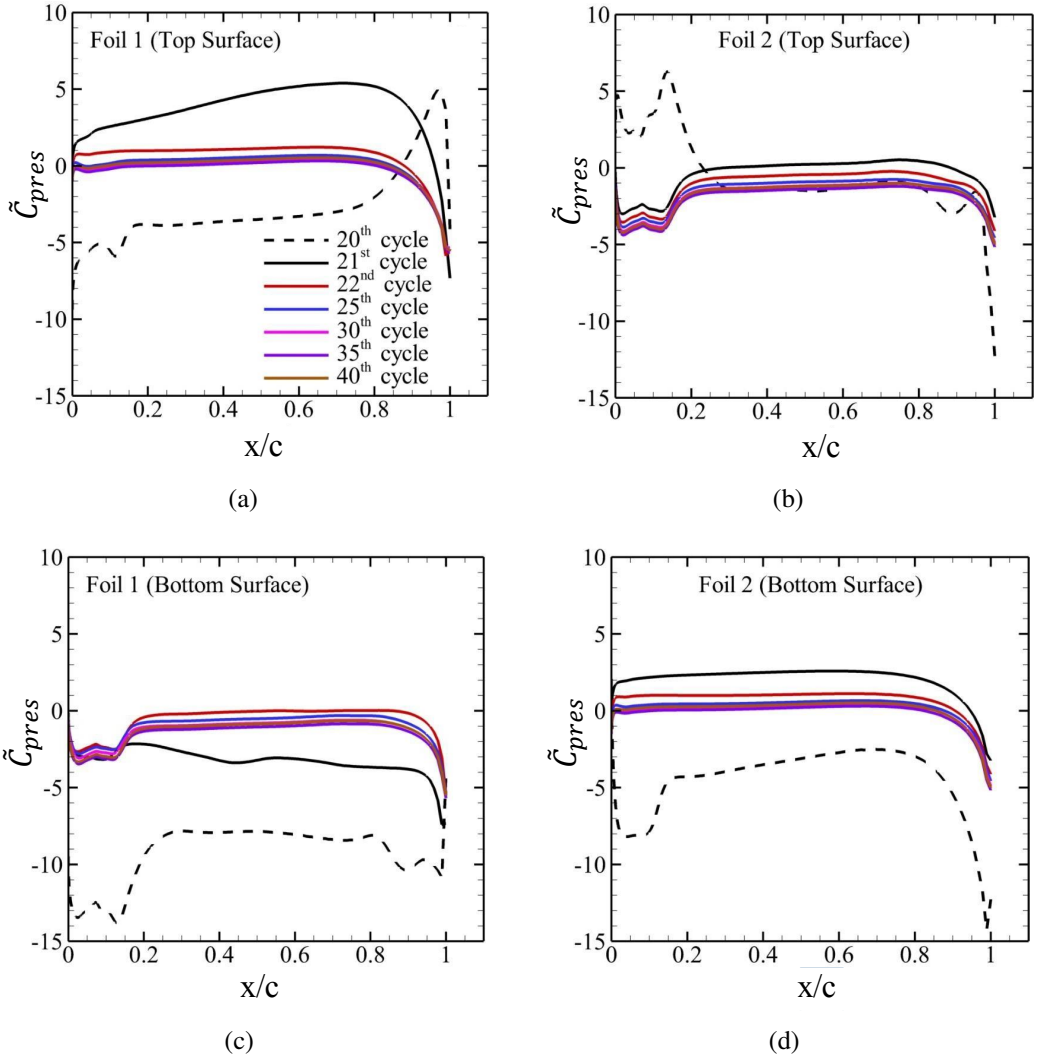

Figure 6.5: Cycle-averaged pressure variation on (a) top surface of Foil 1, (b) top surface of Foil 2, (c) bottom surface of Foil 1, and (d) bottom surface of Foil 2 in the case of Mode 1 at $St = 0.5$ and $Re = 4000$.

lead to Mode 4 reaching quasi-steady settings earlier (32nd cycle) compared to Mode 3. These results are not shown here for brevity. However, the wake appears fairly similar between the two modes once reaching quasi-steady conditions (compare figure 6.4b and figure 6.3d). Thus, it is evident that the suspension of oscillations significantly limits the effect of initiation of oscillations in both performance and wake dynamics for this problem.

6.2.2 Surface Pressure Distributions and Secondary Vortex Street

Surface pressure variations are expected to dominate in alleviating side-forces. To examine this hypothesis, the phase-averaged distribution of the surface pressure coefficient ($\widetilde{C}_{pres} = p/0.5\rho U_{\infty}^2$) are shown in figure 6.5 for Mode 1 at $St = 0.5$ and $Re = 4000$. The profiles of pressure on upper surfaces of both foils are presented in the first row, whereas those on lower surfaces are shown in the second row. It is interesting that pressure variations on the foils approach their respective quasi-steady states in all cases faster than the wake. Figure 6.5a shows the phase-averaged pressure data on the upper surface of Foil 1. At the end of their out-of-phase oscillations in the 20th cycle, negative pressure is observed on 80% of this surface, with a large negative variation towards the foil's trailing edge, which is mostly attributed to the detachment of TEVs. After the phase is switched, surface pressure transforms to positive values on the leading 90% of the foil's surface, while remaining negative on the remaining part. There is a sharp decrement in pressure in the 22nd cycle and no significant changes are observed afterwards. A similar pattern is exhibited by pressure on the lower surface of Foil 1. Considering the side-force mathematically defined by the area between respective curves for each cycle in figures 6.5a and 6.5b, it depicts mitigation of the side-force right after the 22nd pitching cycle.

For Foil 2, pressure is positive on the leading 20% part of the upper surface, whereas it becomes negative for $x/c > 0.20$. For its whole lower surface, pressure remains negative. Similar to Foil 1, the pressure distribution remains the same for all pitching cycles following the 22nd period. The only side-force likely to be experienced by Foil 2 is due to small pressure differences on the leading 18% of upper and lower surfaces. Hence, quantitative and qualitative analyses demonstrate here that abrupt change of the phase angle attributes to the mitigation of side-force experienced by the system of foils, similar to solitary swimmers, due to wake deflection. Similar pressure related phenomena are also observed around the two foils for the remaining hybrid modes, which are not shown here for brevity.

To examine the dynamics of the secondary vortex street formed in all hybrid modes, the time-averaged stream-wise velocity profiles are presented at $x/c = 2.50$ and $x/c = 3.50$ in Figures 6.6a

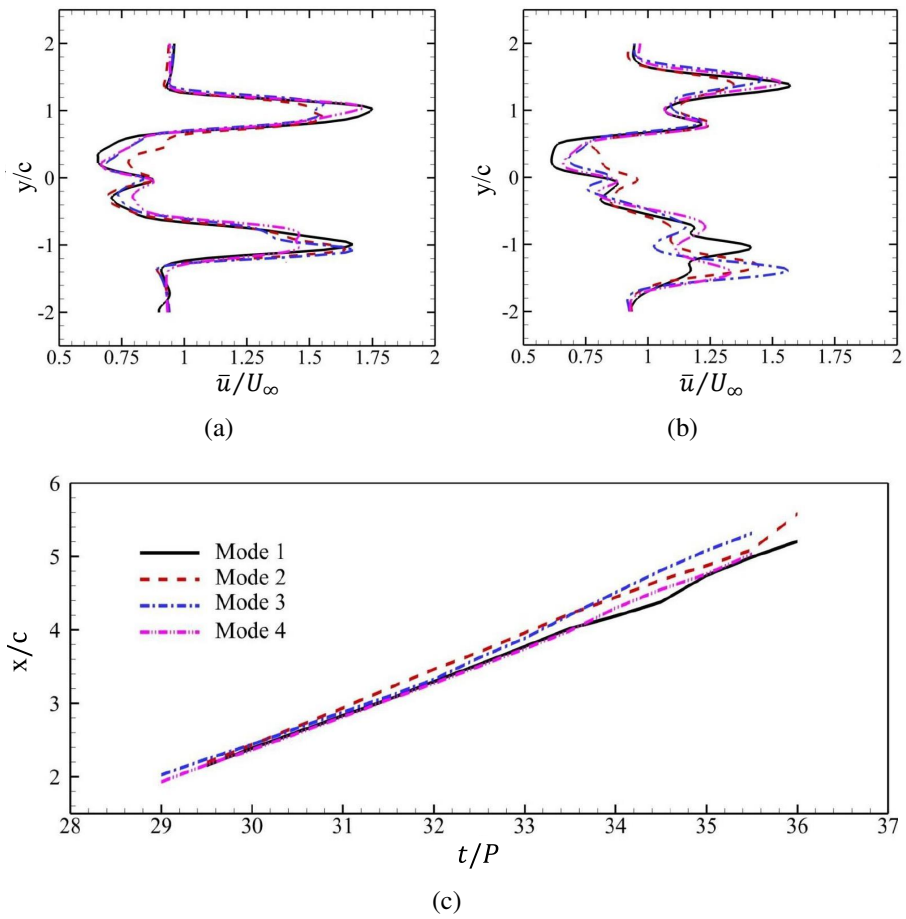

Figure 6.6: Normalized stream-wise velocity profiles in the wake at (a) $x/c = 2.50$ and (b) $x/c = 3.50$, (c) x/c coordinates of the leading coherent structures of the secondary vortex streets for all four hybrid modes at $St = 0.5$ and $Re = 4000$.

and 6.6b, respectively. It is evident that the presence of the secondary vortex streets attributes to velocity deficits for all four modes. The upper and lower momentum-surfeit regions exist here due to the two primary vortex streets formed by both foils. The overall (total) thrust generation is also adversely affected after the switching of phase angle as manifested by the reduction in the strength of these velocity-surfeit regions compared to those depicted in figure 5.6 for purely out-of-phase pitching kinematics. Figure 6.6b presents the stream-wise velocity profiles for all hybrid modes considered in this study at $x/c = 3.50$. It is observed that the primary vortex streets has slightly shifted their positions downstream, which is also noticed in the vorticity contours of figure 6.1. Velocity profiles in figures 6.6a and 6.6b for all four modes demonstrate a similarity in the overall

wake dynamics as well as specifically for secondary vortex streets. It is important to mention that the secondary vortex street does not maintain its coherence for pure out-of-phase pitching oscillations, as shown in figure 4.5b. Its formation is observed after around 25 oscillation cycles. However, it does not bifurcate the wake and diffuses quickly providing an opportunity for the two primary vortex streets to interact with each other.

In order to understand the growth rate of the secondary vortex streets for all four hybrid modes, the coherent structures in the secondary vortex streets are visualized to track the motion of the leading vortices (positive vortex for Mode 4 and negative vortices for the remaining modes) in the wake. The abscissa coordinates of the core of these vortices are shown in figure 6.6c. It is apparent that the growth rate of secondary vortex streets is almost the same for all hybrid modes and their leading vortices traverse the same distance, although the phase is switched from $\phi = \pi$ to 0 in different ways. The results thus far reveal an underlying flow physics in the wake of a simplified side-by-side foil system due to abrupt changes in their phase angle, which involves the formation and interaction of a secondary vortex street. This wake mechanism can be a contributing factor in fish switching their synchronization to adjust to external environmental changes or to maintain their orientation at higher speeds (Re) and faster oscillatory conditions (St).

6.2.3 The effect of Strouhal number

In order to extend this study and identify the effect of Strouhal number on hydrodynamic performance parameters and wake dynamics, the cases of $St = 0.25 - 0.4$ are examined at $Re = 4000$. However, the results presented for these studies are limited to hybrid Mode 2 and Mode 4 for brevity. These results indicate that there exists a change in performance of the two foils for the lower St cases compared to $St = 0.5$ that is extensively discussed earlier. Figure 6.7 shows the unsteady variations of $\widetilde{C_S}$, $\widetilde{C_T}$, and $\widetilde{C_P}$ for $St = 0.3$. Note that for the case of $St = 0.3$, the quasi-steady conditions are achieved within 10 oscillation cycles, which is why the onset of the abrupt change in the phase angle occurs at $t = 10P$. It is also evident that the overall side-force gets reduced to zero within 9 oscillation cycles following the change in the phase-angle. For the other cases not shown

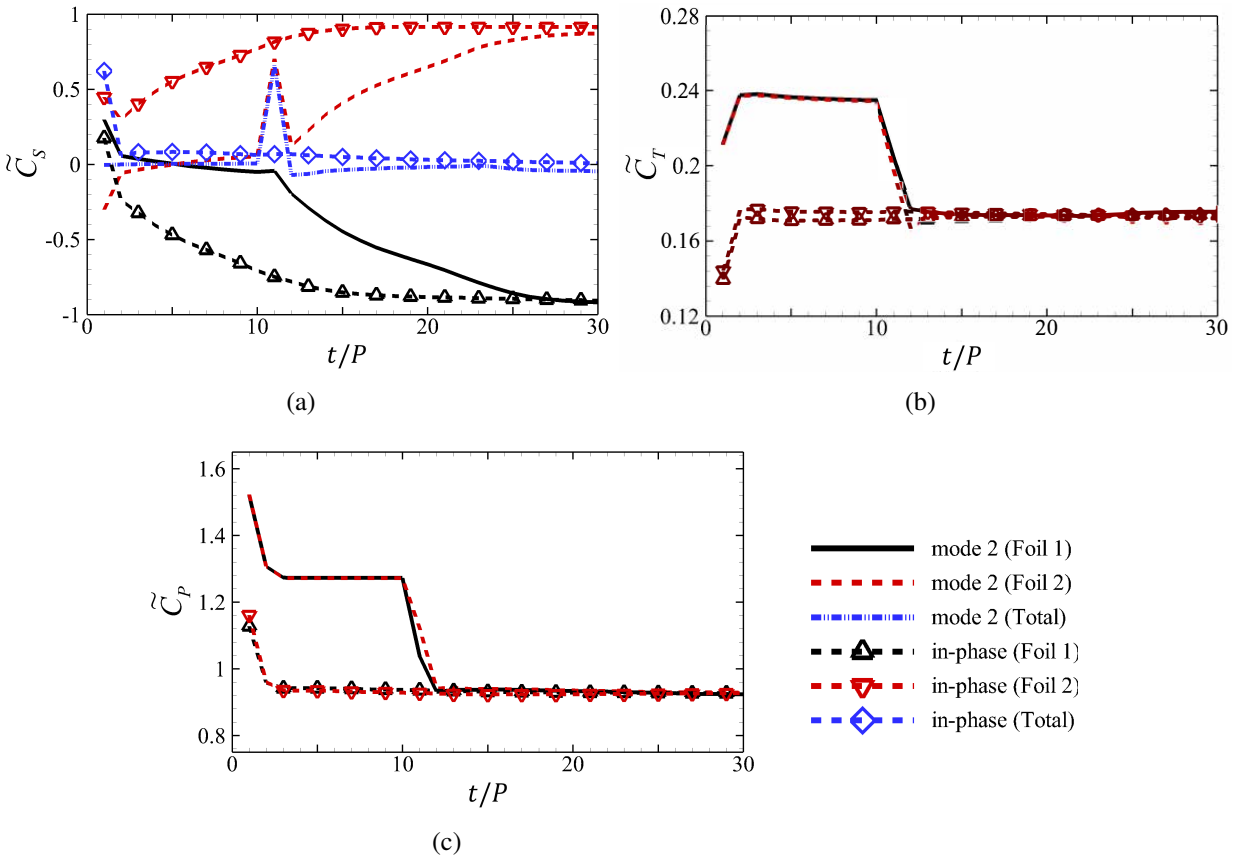

Figure 6.7: Hydrodynamic performance parameters, (a) $\widetilde{C_S}$, (b) $\widetilde{C_T}$, and (c) $\widetilde{C_P}$ for the two pitching foils at $St = 0.3$ and $Re = 4000$.

here, the zero total side-force is achieved after 10 cycles for $St = 0.25$ in Mode 2 and Mode 4, 15 cycles for $St = 0.3$ in Mode 4, 25 cycles for $St = 0.4$ in Mode 2, and 27 cycles for $St = 0.4$ in Mode 4. The side-forces of both Foil 1 and Foil 2 approach their respective values for the case with pure in-phase pitching motion within 12 oscillation cycles after the phase switching for $St = 0.3$ (Mode 2) as shown in figure 6.7(a). These observations imply that mid swimming phase-alteration is an important flow control technique for a wide range of Strouhal numbers. Under these conditions, the two foils generate thrust equal to what they produce in the case with pure in-phase motion, while consuming equal power.

Naturally, the focus moves to the vortex dynamics in the wake of the two pitching foils at the lower St cases, which are presented in figure 6.8 for $Re = 4000$ and $St = 0.25$, when the foils oscillate following the kinematics of Mode 2. The results elucidate that the secondary vortex street

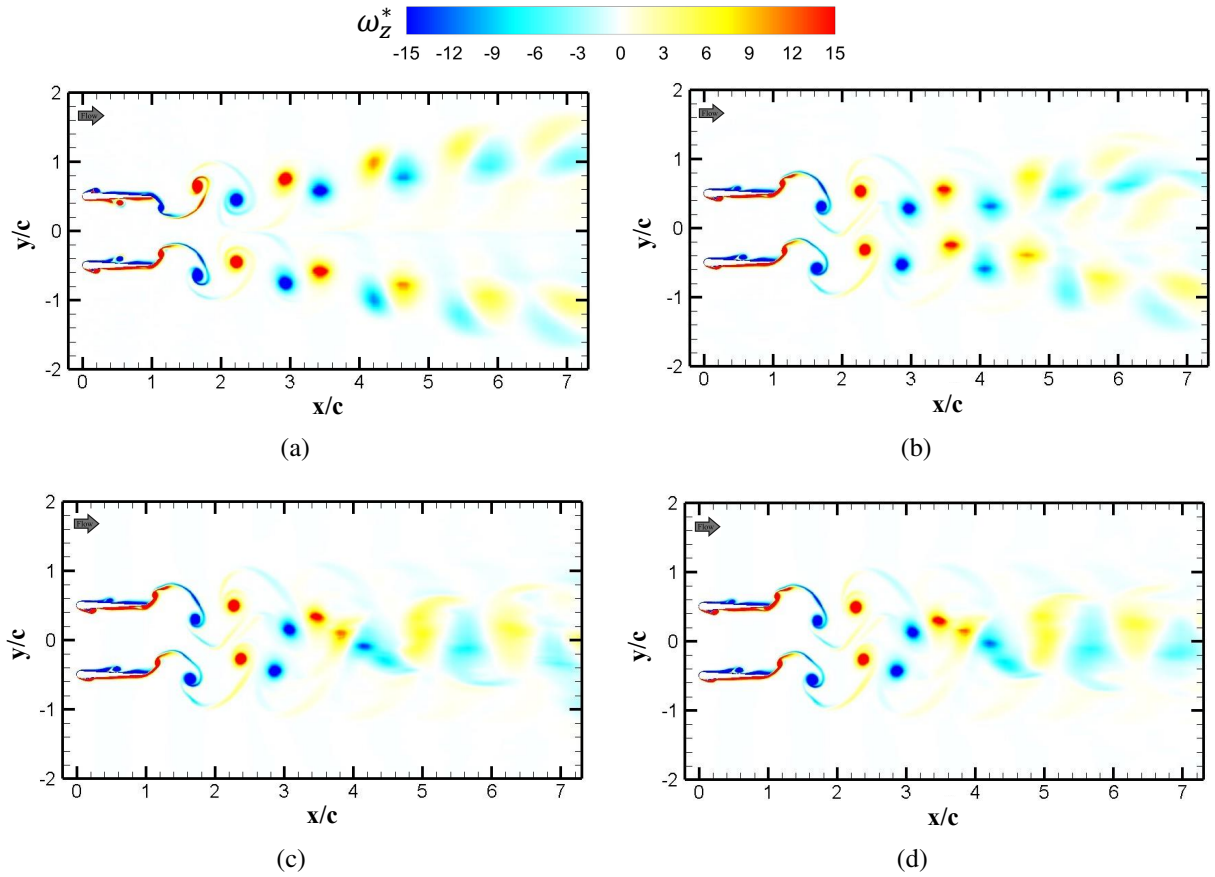

Figure 6.8: Contours of spanwise vorticity ($\omega_z^* = \omega_z\, c/U_\infty$) at (a) 10th, (b) 15th, (c) 19th, and (d) 25th pitching cycle for flows over side-by-side foils following Mode 2 for $St = 0.25$ and $Re = 4000$.

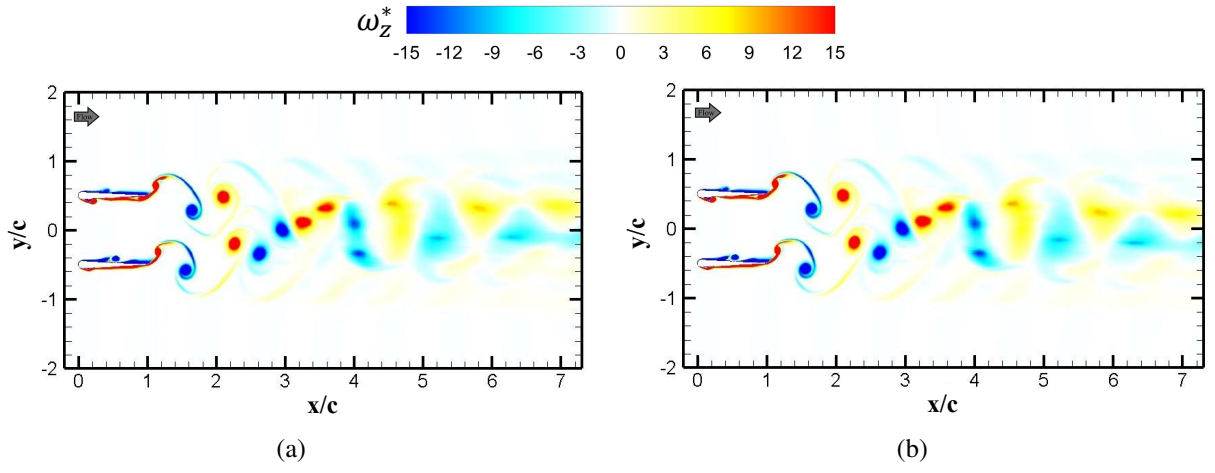

Figure 6.9: Contours of spanwise vorticity ($\omega_z^* = \omega_z\, c/U_\infty$) at 30th pitching cycle for flows over side-by-side foils following (a) Mode 2 and (b) Mode 4 for $St = 0.3$ and $Re = 4000$

.

only appears at higher St cases. Thus, the two wakes merged to form a single vortex street in the absence of the secondary vortex street at lower St. This wake topology resembles that of observed in chapter 4 for pure in-phase pitching parallel foils (see figure 4.2a). In brief, a double-street wake is observed at the end of the 10th pitching cycle, which coincides with the time right before the switch in phase angle occurs. Thus, the wake is symmetric around the horizontal axis ($y/c = 0$) based on its generic shape (not for the exact alignments of positive and negative vortices in those two streets). In this configuration, vortices shed from the two foils traverse in the wake at an angle from the respective foils. After the phase is altered, the vortices produced by the two foils follow straight horizontal paths for three oscillation cycles. During the 4th pitching cycle after the phase switching, the two streets start approaching each other at a distance of $x/c = 1$ from the trailing edges of the foils. It is important to observe the constructive interference between vortices, i.e., the merging of similar signed vortices from the two streets, which would form bigger coherent structures arranged into a single street, looking like a traditional reverse von Karman vortex street. For the phase switching in Mode 4, stationary states of foils for the time equal to two periods of oscillations allow the previously shed vortices to traverse farther downstream, which would not let the newly formed vortices interact with them in any way. In this scenario, the vortices produced by the two foils follow straight horizontal paths symmetrically around $y/c = 0$ axis for three oscillation cycles after the phase is changed. In this case, similarly, a wake with single vortex street is formed. The only change at a slightly higher St, i.e., still lower than 0.5, is that the merging of two vortex streets into a single street is delayed. Thus, the wake requires a few additional oscillation cycles (i.e., 10 cycles for $St = 0.3$) to reach the same quasi-steady behavior observed for $St = 0.3$, as shown in figure 6.9. It is important to notice that the wake and performance at $St = 0.30$ exhibit very stable characteristics for both Modes 2 and 4. Earlier, Khalid and Akhtar (2017) examined the effect of different initial conditions on the force production by flapping airfoils at $St = 0.10$ and $St = 0.30$ to reveal the existence of limit cycles. It means that the dynamical response of airfoils remains independent of the initial conditions for low Strouhal numbers. When the foils change their out-of-phase oscillations to in-phase motion in the present

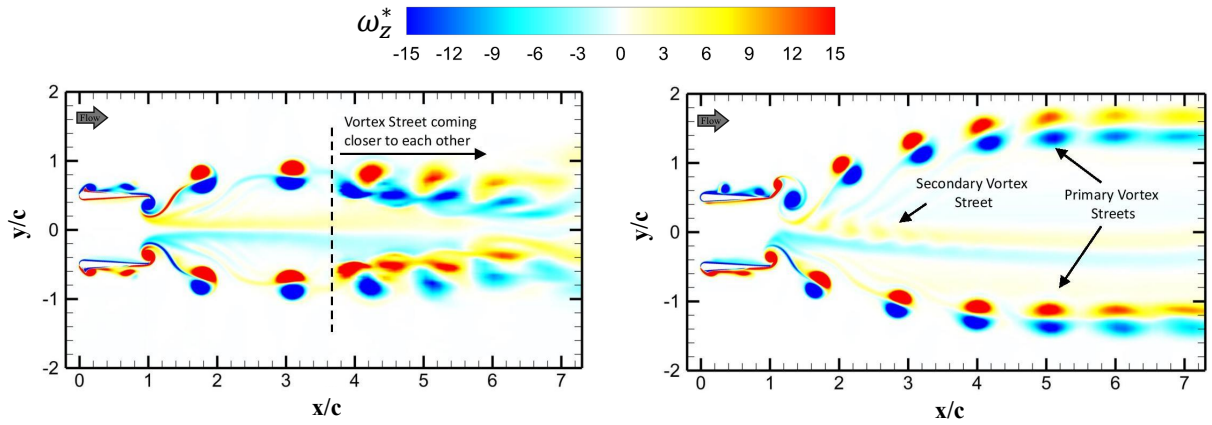

Figure 6.10: Contours of spanwise vorticity ($\omega_z^* = \omega_z\, c/U_\infty$) at (a) 20^{th} and (b) 43^{th} pitching cycle for flows over side-by-side foils following Mode 2 for $Re = 1000$ and $St = 0.5$.

simulations, it may be considered equivalent to another condition to initiate the flow dynamics. Because this dynamical system exhibits the limit cycle phenomenon, the motion with the switched phase brings this dynamical system to a response after some number of oscillation cycles which it would experience for foils beginning their motion from rest. Hence, the wake topology of Modes 2 and 4 shows conditions similar to those with foils pitching in-phase.

6.2.4 The special case of a lower Reynolds number

The applicability of the observed mechanisms to lower Reynolds number cases are further evaluated by repeating the same simulations at $St = 0.5$ for the case of $Re = 1000$. From the results, it is clear that the role of phase alteration is not substantially different from that of higher Re flows at the same St. The out-of-phase pitching motion of the two parallel foils at $St = 0.5$ produces two distinct vortex streets, which would start coming close to each other by the end of the 20th oscillation cycle, shown in figure 6.10a. This interaction is anticipated to lead to more incoherent vortex dynamics in subsequent cycles, similar to the phenomena observed in figure 4.5b for $Re = 4000$. At this time instant, switching the phase helps stabilize the flow and forms two vortex streets for a bow-shaped wake configuration, which coincides with the formation of the secondary vortex street as presented in figure 6.10b. It is evident from figure 6.11a that the overall side-force ($\widetilde{C_S}$) does

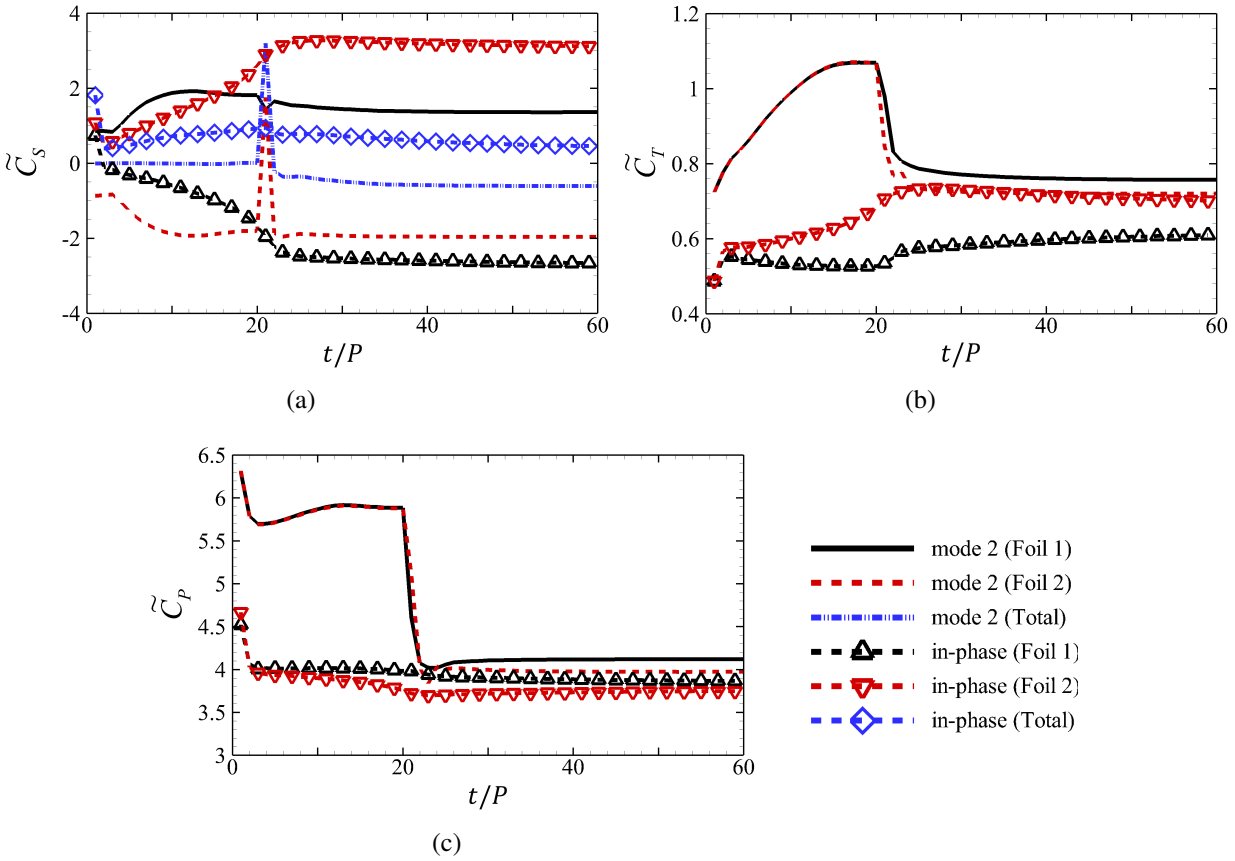

Figure 6.11: Hydrodynamic performance parameters, (a) $\widetilde{C_S}$, (b) $\widetilde{C_T}$ and (c) $\widetilde{C_P}$ for the two pitching foils at $St = 0.5$ and $Re = 1000$

.

not reduce to zero for Mode 2 contrary to $Re = 4000$ as in figure 5.3a. On the other hand, zero total side force production is observed for Mode 4 both at $Re = 1000$ and $Re = 4000$. Thrust generation by Foil 1 is substantially enhanced compared to the pure in-phase oscillations (see figure 6.11b). However, Foil 2 generates almost the same thrust with the altered phase compared to the pure in-phase pitching oscillations. Moreover, these foils expend slightly higher power compared to those undergoing pure in-phase motion, which is observed in figure 6.11c. This translates to an improvement in total efficiency of the system since the enhancement in thrust is greater than the increased power consumption.

6.3 Summary

Numerical simulations of the flow over two foils pitching in side-by-side arrangement reveals unique unsteady wake modifications induced by abrupt changes in the phase angle between them. Four different hybrid modes are considered for $St = 0.25 - 0.5$ at $Re = 1000$ and 4000, where the phase angle of oscillations is changed from π to 0. The modes considered in this study are distinguished by either the direction of the first pitching stroke, or suspension of oscillations prior to the switch in the phase angle. Although we observe no major deviations in the performance and wake behavior due to suspended oscillations (Mode 3 and Mode 4) compared to Mode 1 and Mode 2, examining the implications of the suspension period forms the basis of a future study. Three main and novel observations related to flow physics in this study were: (1) identifying a secondary vortex street in the wake, which dictates the interaction of primary vortex streets behind parallel foils; (2) characterizing the implications of suspended oscillations mid-swimming on performance and wake topology of oscillating parallel foils with abrupt change in their synchronization; (3) the dominance of Strouhal number relative to Reynolds number on performance and wake topology due to abrupt switch in synchronization of parallel foils.

In all modes at $St = 0.5$ and $Re = 4000$, the quasi-steady wake consists of two distinct vortex streets, angled away from the centerline ($y/c = 0$). This is contrary to the wake topology commonly observed for in-phase pitching parallel foils, which consists of a single vortex street and no secondary streets. The unsteady evolution of the wake exhibits the formation of a secondary vortex street between the two primary streets behind individual foils. These contribute to the wake retaining its split pattern by suppressing any interactions between the two primary vortex streets formed behind each foil. This is attributed to the induced upward-downward flow by the resultant vortex interactions. Further examinations of variation in surface pressure shows that changes in the phase angle reduce the pressure difference, which is attributed to alleviating side-forces for the overall dynamical system. Moreover, velocity profiles identify major changes to the wake due to the formation of, and dynamics related to the secondary vortex streets. It is also revealed that this new vortex street grows at the same rate for all four hybrid modes. Thus, its dynamics appears

independent from the initial dynamics associated with the foils motions. There are subtle but apparent differences in both performance and wake dynamics due to opposite initial oscillations for foils in Mode 1 versus Mode 2, which is substantially suppressed by the suspension of oscillations in Mode 3 and Mode 4.

Changing the oscillating *St* reveals that the wake dynamics and performance of the foils strongly depends on *St* following an abrupt change in the phase angle. Contrary to the case for $St = 0.5$, the two foils approach the conditions of pure in-phase pitching within $9-27$ oscillation cycles at $St = 0.25-0.4$. While the total side-force production is reduced to zero, the time required to attain this condition increases at higher *St*. The wake topology also exhibits the conditions of pure in-phase pitching foils with a single vortex street. The effect of lower Reynolds number ($Re = 1000$) at $St = 0.5$ is insignificant. Main characteristics of performance parameters and wake features at $St = 0.5$ are similar between $Re = 1000$ and 4000. The main difference is that the total side force generated by Mode 2 drops to zero at $Re = 4000$ but it only decreases significantly at $Re = 1000$. Thus, it is apparent that for this particular kinematic setting, the implications of Strouhal number dominate those of Reynolds number. Given the profound impact of the Strouhal number and phase synchronization on the flow dynamics around parallel pitching foils, the natural next step is to explore the impact of intermediate phase differences ($0 < \phi < \pi$) for a range of Strouhal numbers. This investigation constitutes the primary emphasis of the subsequent chapter.

Chapter 7

EFFECT OF PHASE DIFFERENCE ON WAKE CHARACTERISTICS AND PROPULSIVE PERFORMANCE[†]

The influence of phase difference on the wake dynamics and performance of parallel oscillating foils has received some attention, albeit limited. Dewey et al. (2014) conducted experiments in a water channel on parallel pitching foils over a wide range of phase difference and separation distances. Their observations revealed that different phase angles resulted in unique wake patterns, leading to the development of wake interpretation models for in-phase, out-of-phase, and intermediate phase motions. Experiments with similar range of parameters at higher Reynolds numbers were reported by Kurt and Moored (2018a). Their study showed that foils in side-by-side configurations could enhance their efficiency by 17%, and thrust by nearly 20%, with phase differences of $\phi = \pi/2$ and $\phi = 3\pi/2$ when the separation distance was equal to one chord-length. A shared limitation of these experiments, however, was the fixation of the Strouhal number at $St = 0.25$.

[†]The content of this chapter has been published in whole or part, in *In Fluids Engineering Division Summer Meeting* with the citation: "Gungor, A., Khalid, M.S.U., & Hemmati, A., (2022, August) Effect of Phase Difference on Wake Characteristics and Propulsive Performance of Pitching Foils in Side-by-Side Configurations. *In Fluids Engineering Division Summer Meeting*, Vol. 85840, p. V002T05A031 American Society of Mechanical Engineers."

In Chapter 4, the effects of in-phase and out-of-phase kinematics on the unsteady wake evolution and the propulsive performance of foils operating across a range of Strouhal numbers is explored. Following this, chapters 5 and 6 delves into the dynamics of sudden shifts from out-of-phase to in-phase pitching motions. These studies underscored the significant role of Strouhal number in influencing both the wake dynamics and the performance of foils in parallel configurations. Building upon these findings, the current chapter aims to further investigate the influence of phase differences on flow characteristics at a range of St. Employing a comprehensive range of phase differences, from in-phase ($\phi = 0$) to out-of-phase ($\phi = \pi$), at increments of $\pi/6$, and Strouhal numbers spanning from $St = 0.15$ to $St = 0.5$, this chapter addresses a notable gap in the literature regarding the combined effects of phase difference and Strouhal number on biomimetic robotics. This aspect is crucial for advancing our understanding of bio-inspired marine locomotion. The structure of this chapter is organized to first present the main findings in Section 7.1, followed by a concise summary in Section 7.2.

7.1 Results and Discussion

Chapter 4 provides an in-depth analysis comparing the wake dynamics and performance metrics of oscillating foils in both in-phase ($\phi = 0$) and out-of-phase ($\phi = \pi$) motions, highlighting the significant influence of the Strouhal number. For both phase angles, wakes at low St reach quasi-steady characteristics after a few oscillation cycles (see figure 4.2), whereas the foils at higher St exhibit unsteady transitions in their wake patterns and require more than 30 cycles to attain quasi-steady features (see figure 4.5). This observation aligns well with the temporal evolution of cycle-averaged performance metrics (see figures 4.10, 4.11, and 4.12). Consequently, this chapter narrows its focus to examining intermediate phase differences ($\pi/6 < \phi < 5\pi/6$) at $St = 0.25$ and $St = 0.4$, representing lower and higher Strouhal numbers, respectively. The ensuing analysis, therefore, considers 20 and 45 oscillation cycles for $St = 0.25$ and $St = 0.4$, respectively, to account for the distinct unsteady behaviors exhibited by these systems at different Strouhal numbers.

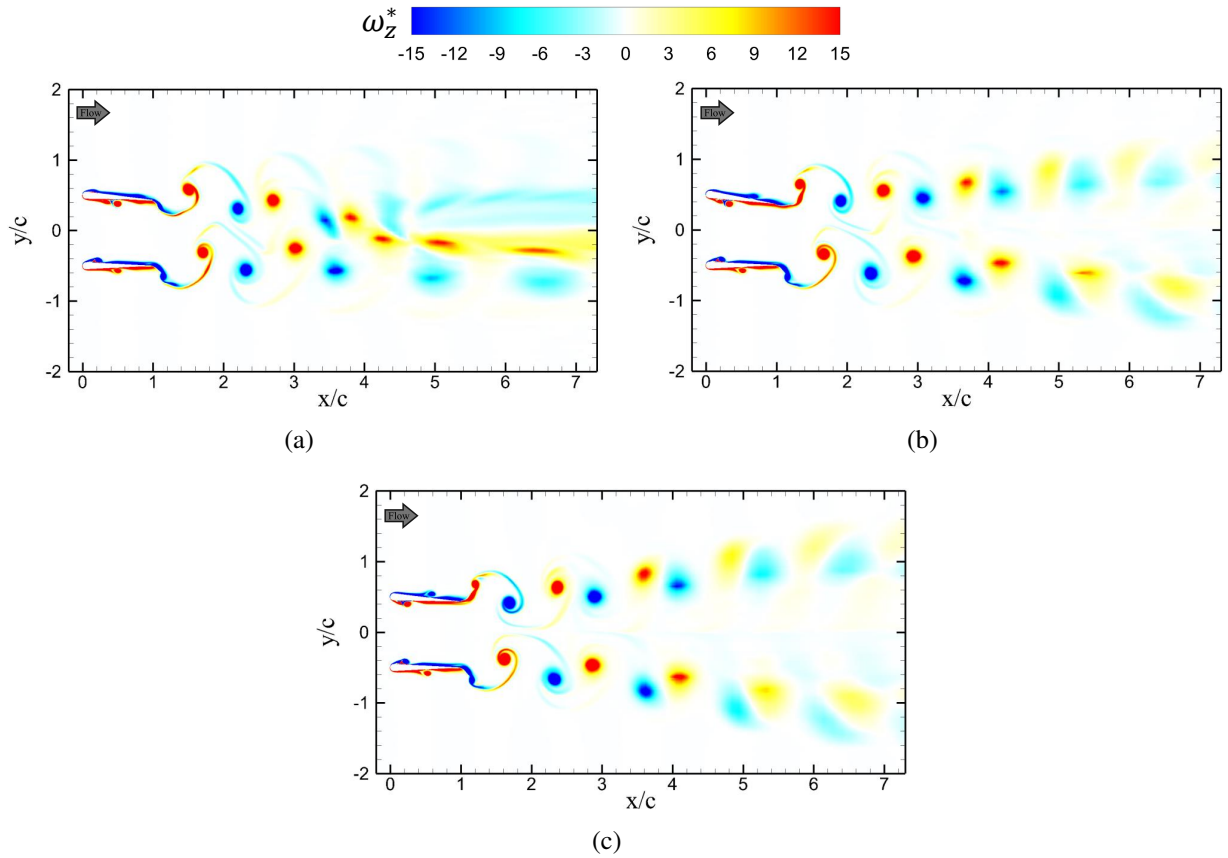

Figure 7.1: Contours of spanwise vorticity ($\omega_z^* = \omega_z\, c/U_\infty$) of parallel foils pitching at $St = 0.25$ and $t = 10P$ for (a) $\phi = \pi/6$, (b) $\phi = \pi/2$, (c) $\phi = 5\pi/6$.

7.1.1 Wake Evolution

Evolution of the wake at intermediate phase angles display similar steady characteristics with in-phase and out-of-phase kinematics at low St. When coherent vortical structures are formed behind the foils, the wake preserve its features without any significant alteration between pitching cycles. Therefore, contours of spanwise vorticity are plotted in figure 7.1 only at $t = 10P$, where P is the period of a pitching cycle for varied phase angles at $St = 0.25$. For $\phi = \pi/6$, the foils produce a merging wake that is qualitatively similar to the wake of in-phase pitching foils (see figure 4.2a), where new coherent structures are formed in the mid-wake around the centerline. It occurs as a result of amalgamation of the upper and lower wakes. Here, the mean motion of the vortical structures exhibit a slightly downward slope contrary to the wake at $\phi = 0$, where the structures are symmetric around the centerline. This can be attributed to the asymmetry introduced by the phase

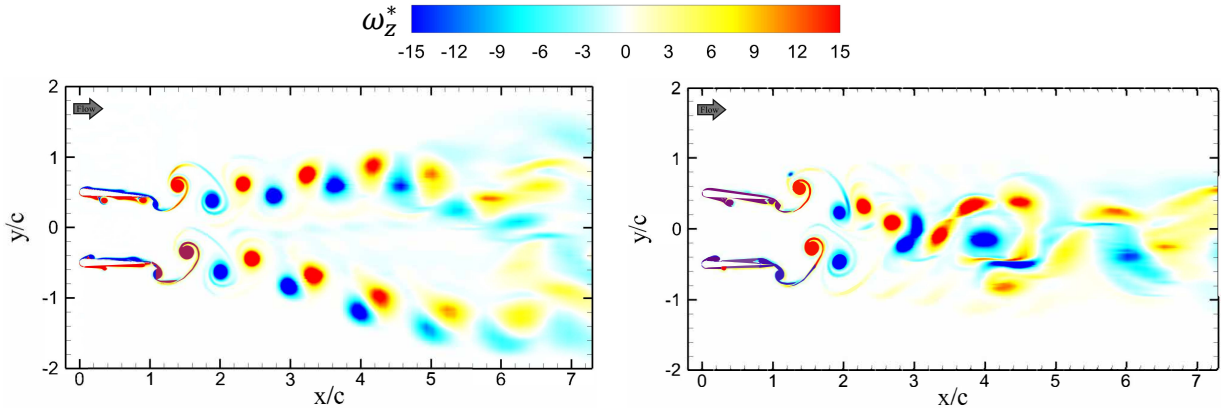

Figure 7.2: Contours of spanwise vorticity ($\omega_z^* = \omega_z\, c/U_\infty$) of parallel foils pitching for $St = 0.4$ and $\phi = \pi/6$ at (a) $t_1 = 10P$, (b) $t_2 = 40P$.

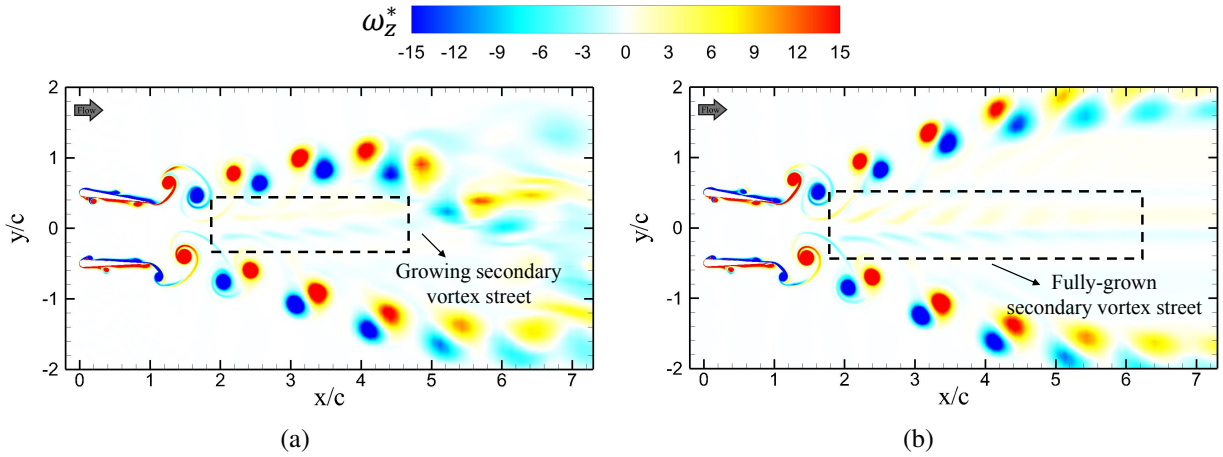

Figure 7.3: Contours of spanwise vorticity ($\omega_z^* = \omega_z\, c/U_\infty$) of parallel foils pitching for $St = 0.4$ and $\phi = \pi/2$ at (a) $t_1 = 10P$, (b) $t_2 = 40P$.

difference of the pitching motion. Similar to the correspondence between $\phi = 0$ and $\phi = \pi/6$, wake structures at $\phi = 5\pi/6$ resemble those of foils pitching at $\phi = \pi$ (see figure 4.2b), which is expected considering the small alteration between phase angles. Here, vortex streets of the upper and lower foils drift apart from each other at an inclination angle without any merging. Vortex streets at $\phi = \pi/2$ constitute a "v-shaped" formation that is symmetric about the centerline. It appears similar to the case of $\phi = 5\pi/6$ but with a smaller inclination angle. However, it contradicts with the experiments of Dewey et al. (2014). They observed that negative vortices approached each other and concentrated on the centerline, resulting in the formation of asymmetric wakes.

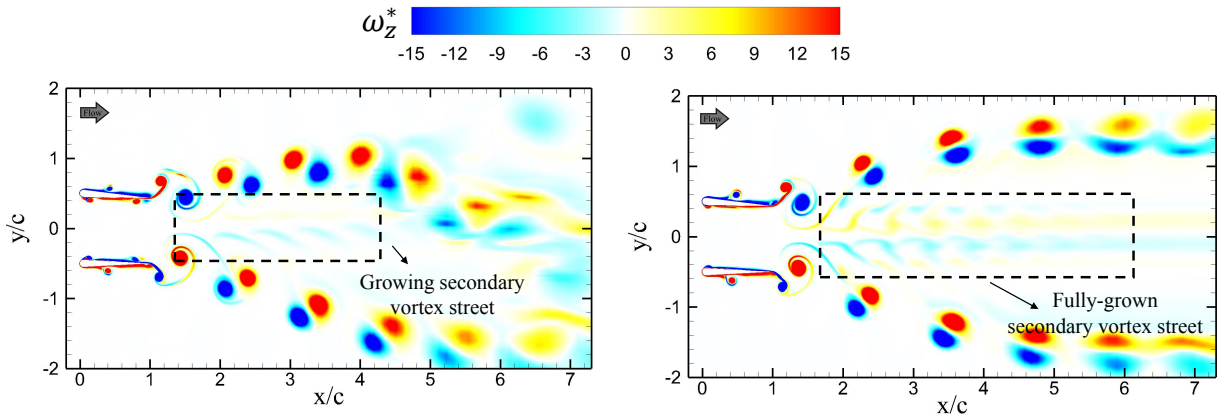

Figure 7.4: Contours of spanwise vorticity ($\omega_z^* = \omega_z\, c/U_\infty$) of parallel foils pitching for St = 0.4 and $\phi = 5\pi/6$ at (a) $t_1 = 10P$, (b) $t_2 = 40P$.

Steady characteristics of the wake, which are highly prominent at lower St, disappears with increasing St. Temporal variations in the wake structures at $St = 0.4$ are demonstrated in figures 7.2, 7.3, and 7.4 at $\phi = \pi/6$, $\phi = \pi/2$, and $\phi = 5\pi/6$, respectively. The wakes exhibit consequential transition between $t_1 = 10P$ and $t_2 = 40P$ in all three cases. Unsteadiness in the wake diminishes once the vortex patterns achieve their terminal forms after more than 20 pitching cycles (not shown here for brevity). A major difference between the cases with lower and higher St is the evolution process of the wake rather than the vortex patterns when steady-state conditions are achieved. This is apparent from the resemblance between figures 7.1a and 7.2b, where the foils pitching at $\phi = \pi/6$ experience merged wakes at both lower and higher St, respectively. Similarly at $\phi = \pi/2$ and $\phi = 5\pi/6$, qualitatively analogous "v-shaped" separated vortex patterns are observed at low St (figures 7.1b and figure 7.1c) as well as at high St for quasi-steady conditions (figures 7.3b, 7.4b).

The presence of secondary vortex structures on the centerline is only observed in the cases with high St. It can be best explained considering the phenomenon of deflected wakes. Oscillating foils produce deflected von Karman streets at a considerably high St, as shown by many studies (Cleaver et al., 2012; Godoy-Diana et al., 2009; von Ellenrieder and Pothos, 2008). When a deflected wake is formed, secondary structures are also shed, which originates from the main street but moves with opposite inclinations. They are observed in the wake of solitary oscillating foils (Jones et al., 1998;

Godoy-Diana et al., 2008; Liang et al., 2011) as well as tandem foils (chapter 4). It is important to note that a deflected wake with a secondary street is also observed in our cases of an isolated foil at high St, $St \geq 0.4$, but those are not shown here for brevity. The formation and growth of these structures is expected to play an important role in splitting the wake and establishing the "v-shaped" vortex pattern. It is plausible to state that split wakes at high St (see figures 7.3b and 7.4b) have greater deflection angles, which can be explained by the separating effect of the secondary street. In chapter 6, it is shown that similar structures played a crucial role to separate the wakes of parallel foils, when the phase angle was abruptly switched from out-of-phase to in-phase. However, they also appear, even though barely visible, in the early cycles of $\phi = \pi/6$ at $St = 0.4$ (see figure 7.2a) before the merger of the upper and lower wakes.

7.1.2 Propulsive Performance

Here, the propulsive performance of this dynamical system is assessed using cycle averaged values of coefficients of thrust and power for each foil as well as efficiency of the overall system (Foil 1 + Foil 2) in figures 7.5 and 7.6 for $St = 0.25$ and 0.4, respectively. Quasi-steady wake characteristics in the cases with low St are observed in their performance metrics. These parameters reach their stable solutions within the first 10 cycles and remain unchanged thereafter as long as kinematics of the foils does not change (see figure 7.5). On the other hand, more than 30 cycles are necessary to reach a quasi-steady solution for $St = 0.4$ (see figure 7.6). Although unsteadiness of the solution is clearly highlighted in the thrust generation, there exist some variations in the power coefficient.

Generation of thrust by the system (Foil 1 + Foil 2) displays an enhancement with increasing phase angle from 0 to π at both high and low St in the current study. The same trend persists in the power consumption, which is aligned with findings of Dewey et al. (2014). On the other hand, efficiency of the system exhibit dissimilar characteristics for high and low St. There is an amplification in efficiency with increasing phase difference for $St = 0.25$ whereas efficiency of the system at $\phi = \pi/2$ is significantly smaller than other phase differences at $St = 0.4$. This could be the reason for the behaviour of red nose tetra fish in experiments of Ashraf et al. (2016,

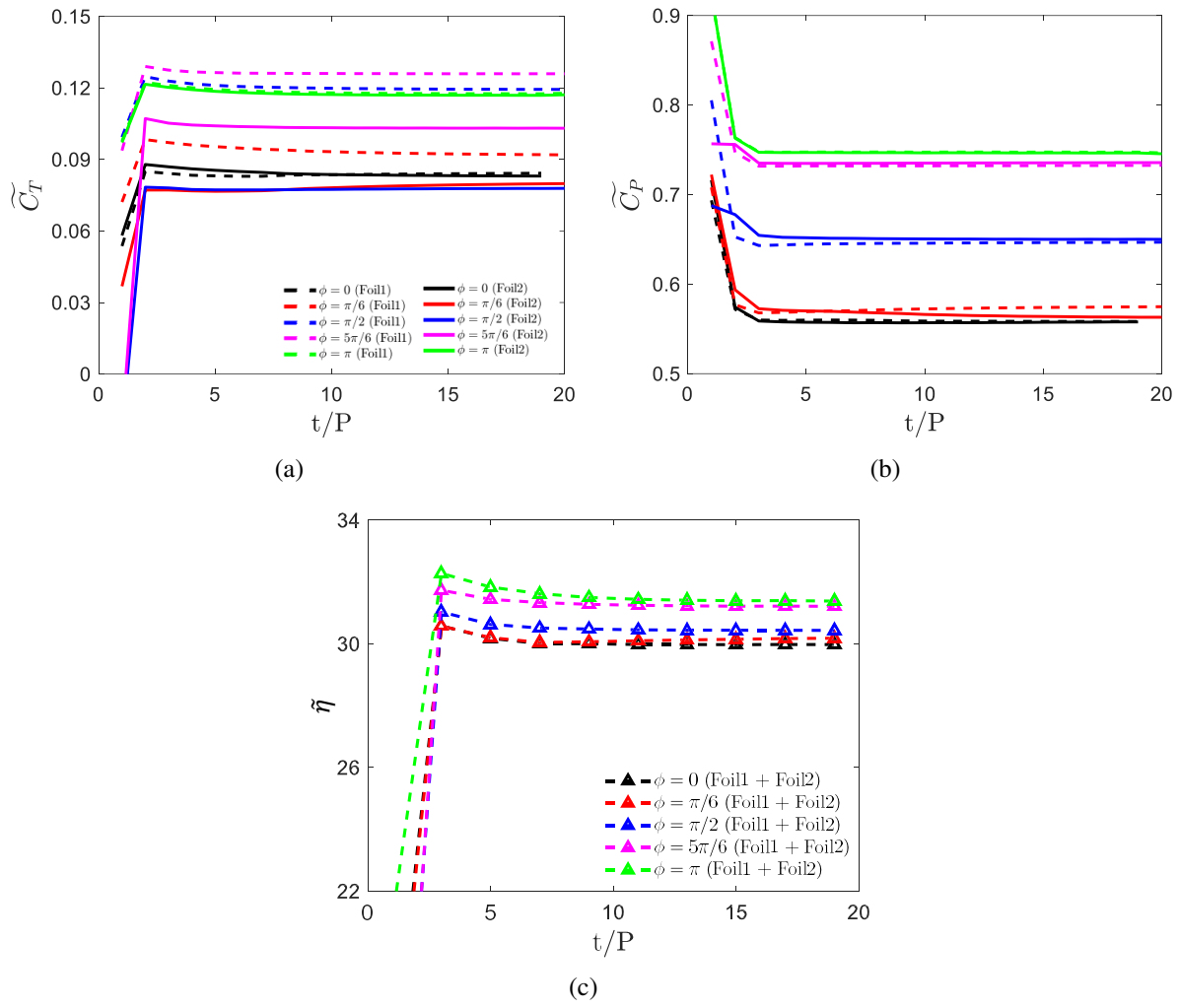

Figure 7.5: The unsteady variation of cycle-averaged (a) coefficient of thrust, (b) coefficient of power, and (c) efficiency at different phase angles for $St = 0.25$

2017) preferred to swim in either in-phase or out-of-phase rather than using intermediate phase differences.

It is important to note here that the propulsive performance parameters for the case with $\phi = \pi/2$ are significantly different from those at $\phi = 5\pi/6$ or π, although they all yield similar characteristics for the wake development. This finding suggests that wake features of an oscillating foil alone cannot be a reasonable reference for assessing the foil's performance. This also supports the argument of Floryan et al. (2020), illustrating that similar wake configurations yield disparate characteristics of propulsive performance.

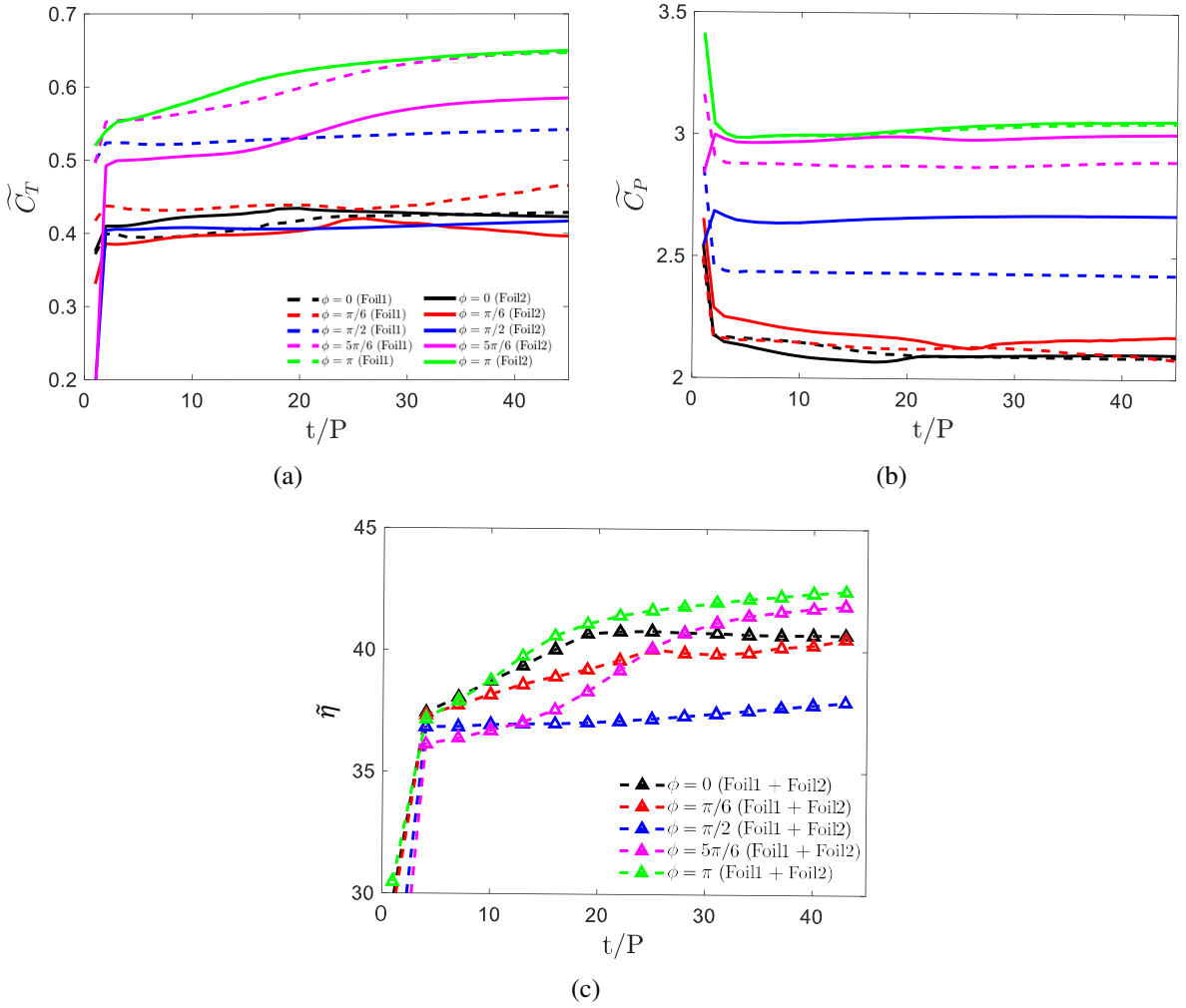

Figure 7.6: The unsteady variation of cycle-averaged (a) coefficient of thrust, (b) coefficient of power, and (c) efficiency at different phase angles for $St = 0.4$

Table 7.1: Percent deviation in the cycle-averaged coefficient of thrust ($\Delta\widetilde{C_T}$) and power ($\Delta\widetilde{C_P}$) between Foil 1 and Foil 2 at a range of phase differences for $St = 0.25$ and $St = 0.4$.

	$St = 0.25$		$St = 0.4$	
	$\Delta\widetilde{C_T}$	$\Delta\widetilde{C_p}$	$\Delta\widetilde{C_T}$	$\Delta\widetilde{C_p}$
$\phi = 0$	%1.4	%0.1	%1.4	%0.3
$\phi = \pi/6$	%13.1	%2.1	%14.9	%4.7
$\phi = \pi/2$	%34.7	%0.5	%23.1	%10.1
$\phi = 5\pi/6$	%18.1	%0.4	%19.8	%3.6
$\phi = \pi$	%0.0	%0.0	%0.4	%0.3

Another major outcome of this study is uneven thrust generation by Foil 1 and Foil 2 for intermediate phase difference ($\pi/6 \leq \phi \leq 5\pi/6$), which achieves its peak at $\phi = \pi/2$. This disparity gradually disappears as the phase difference approaches in-phase ($\phi = 0$) or out-of-phase ($\phi = \pi$) conditions. For example, Foil 1 yields 33% and 21% more thrust than Foil 2 at $\phi = \pi/2$ for $St = 0.25$ and $St = 0.4$, respectively. However, there is no substantial difference between the thrust coefficients of the foils. It is also important to note that there exists a similar trend in the coefficient of power only at high St. Table 7.1 summarizes these results in terms percentage of differences in $\widetilde{C_T}$ and $\widetilde{C_P}$ between the foils, that are calculated at the end of the 20th and 45th cycle at $St = 0.25$ and 0.4, respectively.

7.2 Summary

The effect of phase difference and St on evolution of the wake and propulsive performance characteristics of pitching foils in side-by-side configurations is numerically examined. It is revealed that low Strouhal number ($St \leq 0.3$) and high St ($St \geq 0.3$) regimes have distinct impacts on the wake and performance. Vortex streets shed by the upper and lower foils merge around the centerline at small phase differences ($\phi \leq \pi/6$), whereas a split wake with vortex streets moving away from each other in opposite directions is formed at higher phase differences ($\phi \geq \pi/3$). Formation and growth of the secondary vortex street around the centerline of the wake is conjectured to be an underlying reason for splitting of wakes. Development of similar wake structures is also observed in parallel pitching foils when the phase difference is abruptly switched from in-phase to out-of-phase.

Phase difference between the foils and St are observed to directly influence the propulsive performance characteristics of the system. Generation of thrust by this coupled dynamic system is augmented as the phase difference increases for both high and low values of St, which is accompanied by more consumption of power. Both foils produce nearly identical thrust when they undergo in-phase ($\phi = 0$) or out-of-phase ($\phi = \pi$) pitching. However, there exists a discrepancy

between the thrust coefficients of the foils for intermediate phase differences. This contrast attains its peak at $\phi = \pi/2$ such that one of the foils outperforms the other. Outcomes of this study provide adequate flow control strategies for bio-inspired underwater propulsors. In particular, an intermediate phase difference can be utilized as a maneuvering technique due to the production of unequal thrust by the foils, whereas steady swimming can be achieved by employing in-phase or out-of-phase pitching motion.

Expanding on chapters 4-6, this chapter has delved into various facets of the flow dynamics around pitching foils in a side-by-side configuration, characterizing the wake dynamics and propulsive performance. A thorough understanding of performance characteristics obtained from these chapters lays the groundwork for developing scaling laws for pitching foils operating in schooling configurations. This topic will be explored in depth in the subsequent two chapters, collectively fulfilling Objective B.

Chapter 8

SCALING LAWS FOR PROPULSIVE PERFORMANCE OF FOILS IN SIDE-BY-SIDE CONFIGURATION[†]

Driven by the growing interest of the scientific community in fish-like swimming, analytical models were developed to accurately estimate the propulsive performance metrics of oscillating foils and plates. Floryan et al. (2017) used the formulations of lift-based forces by Garrick (1936) and added mass force formulation by Sedov (1965) to develop new scaling laws for thrust coefficient, power coefficient and efficiency of a single (isolated) heaving and pitching foil. Buren et al. (2019b) adapted these scaling laws to the combined motion of heaving and pitching for a single foil. Floryan et al. (2018) later identified the importance of the offset drag term, which depends on Reynolds number to determine the peak efficiency. Based on their model, Senturk and Smits (2019) developed scaling based on Reynolds number for propulsive performance of an isolated foil performing purely pitching oscillations. Expanding this work to tandem foils, Quinn et al. (2014) scaled the thrust and power of a single foil oscillating near a solid boundary, which repre-

[†]The content of this chapter has been published in whole or part, in *J. Fluids Struct.* with the citation: "Gungor, A., & Hemmati, A., (2021) The scaling and performance of side-by-side pitching hydrofoils. *J. Fluids Struct.*, 104, 103320."

Table 8.1: The parameter space.

Parameters	**Value**
Number of Foils	2
Configuration	Side-by-Side (Parallel)
Strouhal Number (St)	$0.15 - 0.5$
Reynolds Number (Re)	$1000 - 12000$
Phase Difference (ϕ)	$0 - \pi$
Separation Distance (y^*)	$0.5c - 2c$
Amplitude of Oscillations (θ_0)	8°
Incoming Flow	Uniform (U_∞)
Oscillations	Prescribed sinusoidal

sents out-of-phase oscillating foils in side-by-side configuration, as a function of St and separation distance.

Despite these studies, there is limited understanding on how the performance of pitching foils in side-by-side configurations, in terms of thrust and power, scale over a wide parametric space. This motivated the current chapter to examined the performance and scaling of such systems over a wide parametric space, which includes variations in Reynolds number, Strouhal number, separation distance, and phase difference. The complete list of parameters used in the current study is given in table 8.1. In contrast to the previous chapters, this chapter adopts a Reynolds number range of $Re = 1000 - 12000$. Because Senturk and Smits (2019) identified that the flow around isolated pitching foils did not change significantly after $Re = 8000$, the current range of Re would be sufficient in capturing potential Re effects. Furthermore, this range coincides with the lower spectrum of the cruising Reynolds number observed in fish swimming (Gazzola et al., 2014). In this analysis, steady-state performance metrics are examined, leading to the coefficients of thrust and power, as well as efficiency, being expressed as time-averaged values, denoted by $\overline{C_T}$, $\overline{C_P}$, and $\overline{\eta}$, respectively. The approach for calculating these time-averaged quantities, and a discussion on their distinction from cycle-averaged ones, are provided in detail in section 2.1. The structure

of this chapter is designed such that the developed scaling laws and the results showcasing their predictive capabilities are detailed in section 8.1, followed by a summary of the study provided in section 8.2.

8.1 Results and Discussion

We begin by looking at the propulsive performance of an isolated foil and two parallel foils by evaluating their coefficients of thrust and power as well as their hydrodynamics efficiency. We, then, develop scaling laws for coefficients of thrust and power for the two foils oscillating in side-by-side configurations.

8.1.1 Propulsive Performance

The variation of time-averaged coefficients of power ($\overline{C_P}$) and thrust ($\overline{C_T}$) with St are shown for Foil 1 and Foil 2 in figure 8.1 along with the performance of an isolated foil at different Reynolds numbers for fixed separation distance ($y^* = 1c$) and phase difference ($\phi = 0^\circ$). The results indicates that power increased slightly with Re for the solitary foil and two parallel foils. Moreover, the foils in a side-by-side configuration consumes significantly less power in comparison to the single foil. Senturk and Smits (2019) also reported similar upsizing effects of Re on $\overline{C_P}$ for an isolated foil, while Huera-Huarte (2018) made similar observations for the case of side-by-side configurations. Moreover, this variation in power coefficient is amplified with increasing St, such that the differences in $\overline{C_P}$ were insignificant at $St = 0.15$ and grow to a maximum of 20% at $St = 0.5$.

The more substantial effect of Re is observed on the time-averaged coefficient of thrust due to considerable thrust enhancement associated with increasing Reynolds number for the entire range of St in figure 8.1b. This trend is consistent with the findings of Senturk and Smits (2019) at $Re = 500 - 32000$ for an isolated foil, and those of Borazjani and Sotiropoulos (2008) at $Re = 300$ to infinity (inviscid flow). At a given Re, parallel foils generates slightly smaller thrust compared to isolated foils. However, the difference in thrust generation between combined parallel foils (av-

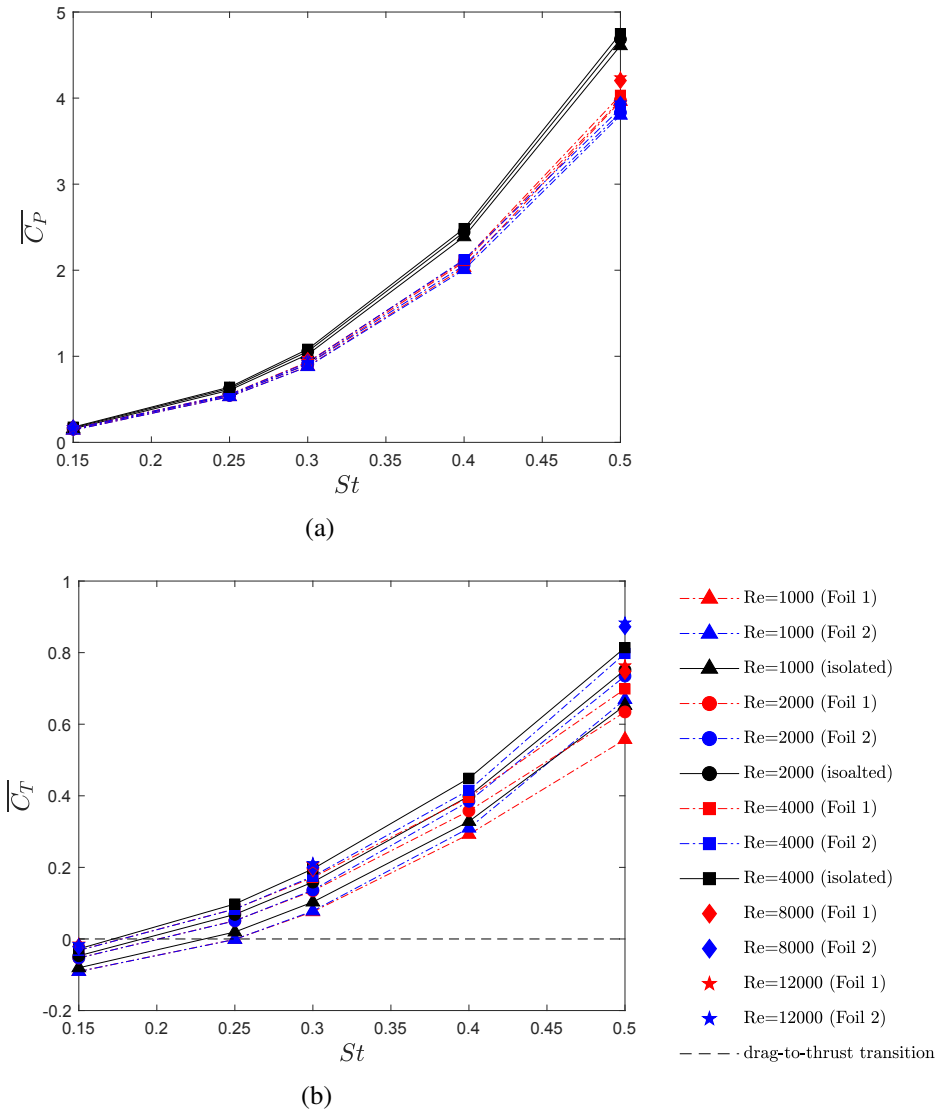

Figure 8.1: The variation of time-averaged (a) coefficients of power and (b) coefficients of thrust in a range of St and Re for both tandem and isolated foils at $y^* = 1c$ and $\phi = 0$.

erage of two foils) and an isolated foil is observed to remain constant for the range of St considered here. Another important observation is that Foil 2 generates larger thrust than Foil 1. This disparity becomes more pronounced at higher St, which might be due to the initial movement of the foils. Although the foils are configured, such that they are mirror image symmetric about the centerline, it is shown in chapter 4 that the in-phase pitching motion of the foils could not be described as symmetric about the centerline. Similar patterns are also shown in the non-identical performance of the two foils despite their symmetric configuration and oscillations.

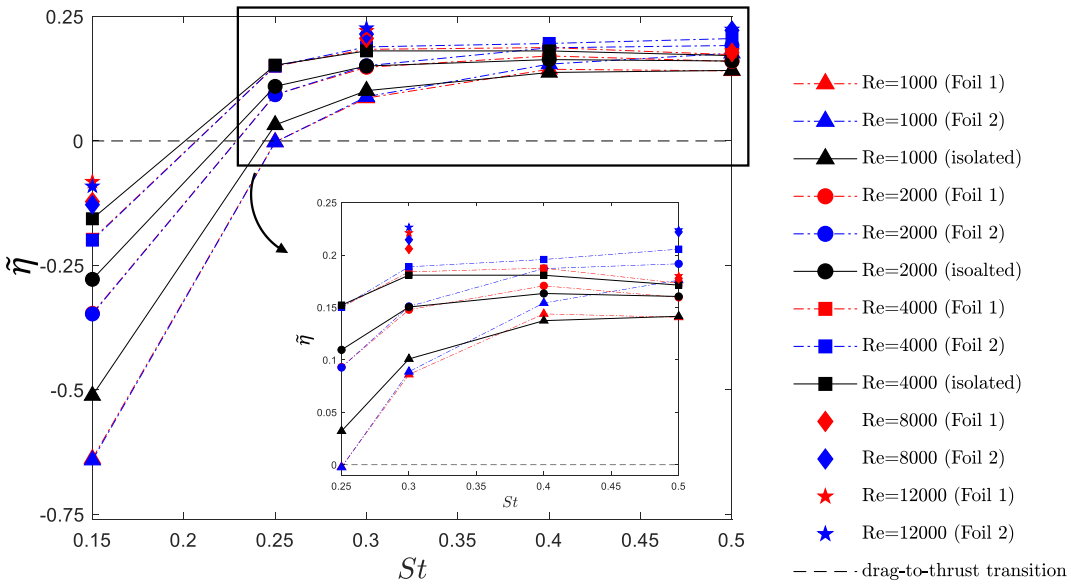

Figure 8.2: The variation of propulsive efficiency of tandem and isolated foils in a range of St and Re at $y^* = 1c$ and $\phi = 0$.

As mentioned, oscillating foils produces drag rather than thrust at considerably low St (Triantafyllou et al., 1991; Koochesfahani, 1989; Triantafyllou et al., 1993). Effects of Reynolds number and side-by-side configuration on the characteristics of drag-to-thrust transition of parallel foils is also shown in figure 8.1b. As expected, increase in Re helps the foils start producing thrust at lower St. The side-by-side configuration, however, has the opposite effect on the transition. It increases the St at which transition occurs compared to an isolated foil. Moreover, the delay due to the side-by-side configuration of the foils is less apparent at higher Res.

The impact of Reynolds number on the propulsive efficiency of parallel pitching foils are shown in figure 8.2. At lower St and Re, a single oscillating foil have higher efficient compared to those two arranged in parallel, whereas the latter configuration become more beneficial at higher Re and St. For example, in the case of $St = 0.3$, parallel foils exhibit lower efficiency than the isolated foil at $Re = 1000$. The performance of parallel foils surpass that of an isolated foil when Re increases to 4000. It have already been shown that St for the maximum efficiency got shifted to lower values for higher Re (Senturk and Smits, 2019; Das et al., 2016). Similarly, decreasing the separation distance shifts the St at which transition occurs for side-by-side foils oscillating out-of-phase (Bao

et al., 2017). However, Reynolds number and separation distance are not the only parameters that affect the performance. Here, it is apparent that the parallel foils attain their maximum $\overline{\eta}$ at higher St values compared to an isolated foil and this trend is persisted for all Reynolds numbers. At $Re = 4000$, the efficiency of an isolated foil is maximum at $St = 0.3$, while the average efficiency of two parallel foils continues to rise for the whole range of St. Cases for the remaining Re values also exhibit similar trends.

8.1.2 Scaling laws

There have been several studies aimed at scaling the propulsive parameters for oscillating foils (Floryan et al., 2017; Garrick, 1936; Sedov, 1965; Buren et al., 2019b; Floryan et al., 2018; Senturk and Smits, 2019). These studies focused to developing scaling relations for thrust coefficient and hydrodynamic efficiency of solitary pitching foils based on St and f^*. Senturk and Smits (2019) presented the following simple and reduced forms of scaling relationships for a single pitching foil.

$$C_T = \gamma St^2 - C_D, \tag{8.1}$$

$$C_P = \zeta St^2 f^*, \tag{8.2}$$

where γ, C_D and ζ denoted empirically computed coefficients. Senturk and Smits (2019) further determined that these empirical coefficients depended on $Re^{-1/2}$, which resembled a laminar flow scaling. Moreover, Simsek et al. (2020) showed that a similar Reynolds number scaling existed for in-line tandem foils oscillating at a fixed separation distance and phase difference. They reported that Reynolds number-based scaling perfectly modeled the performance of tandem foils by incorporating the term f^{*-1} to find γ and ζ.

To begin, the collapse of data on existing scaling relations developed for tandem foils (Simsek et al., 2020) is evaluated for parallel foils for a fixed separation distance and phase difference. These relations are then expanded to incorporate the effects of phase difference and separation distance within the range considered in this study. Therefore, two new terms are introduced in the

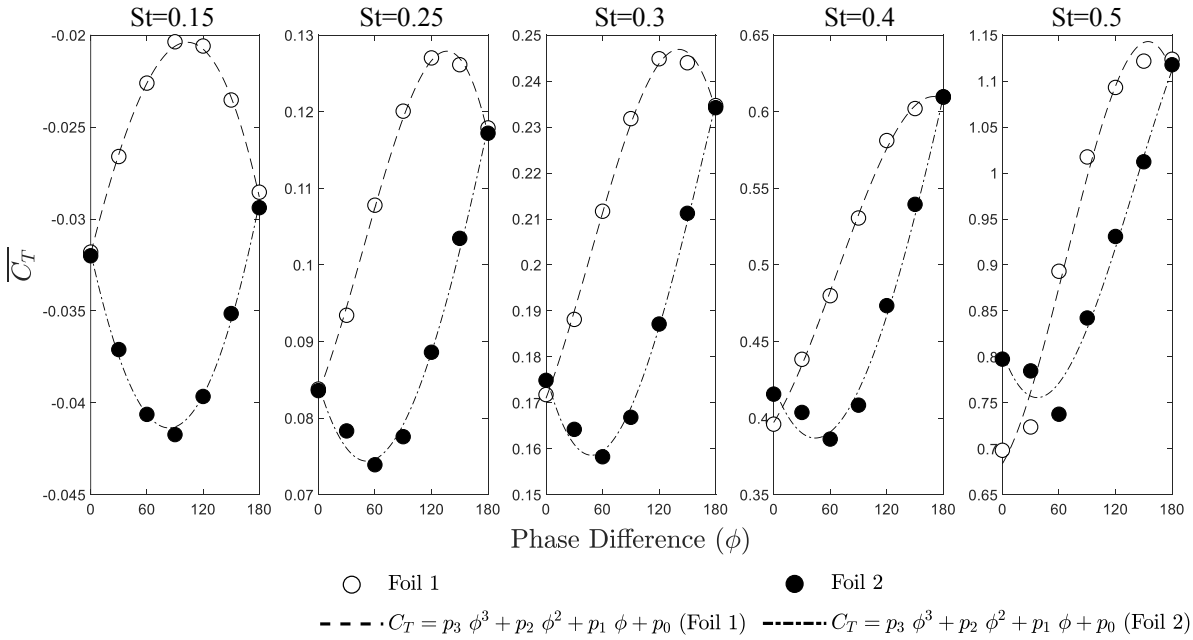

Figure 8.3: The variation of coefficient of thrust of tandem foils in a range of phase difference and St.

scaling relations for $\overline{C_T}$ and $\overline{C_P}$, which modified the scaling equations to the following forms:

$$C_T = \tau\ \beta\ \gamma\ St^2 - C_D, \tag{8.3}$$

$$C_P = \varepsilon\ \kappa\ \zeta\ St^2 f^*, \tag{8.4}$$

where τ and ε denotes coefficients of phase difference, and β and κ represents coefficients of separation distance for $\overline{C_T}$ and $\overline{C_P}$, respectively. These coefficients are computed empirically similar to γ and ζ, that consider only the effect of Reynolds number on thrust and power.

In order to determine the formulations for τ and ε, we vary the separation distance and examined their effects on thrust and power. Figures 8.3 and 8.4 present the plots for variations of $\overline{C_T}$ and $\overline{C_P}$ for Foil 1 and Foil 2 as a function of phase difference for a range of St, respectively. It is evident that $\overline{C_T}$ and $\overline{C_P}$ follow different patterns for Foil 1 and Foil 2 for each St. It is observed that these trends can be best represented by third-order polynomials. Thus, the terms τ and ε are

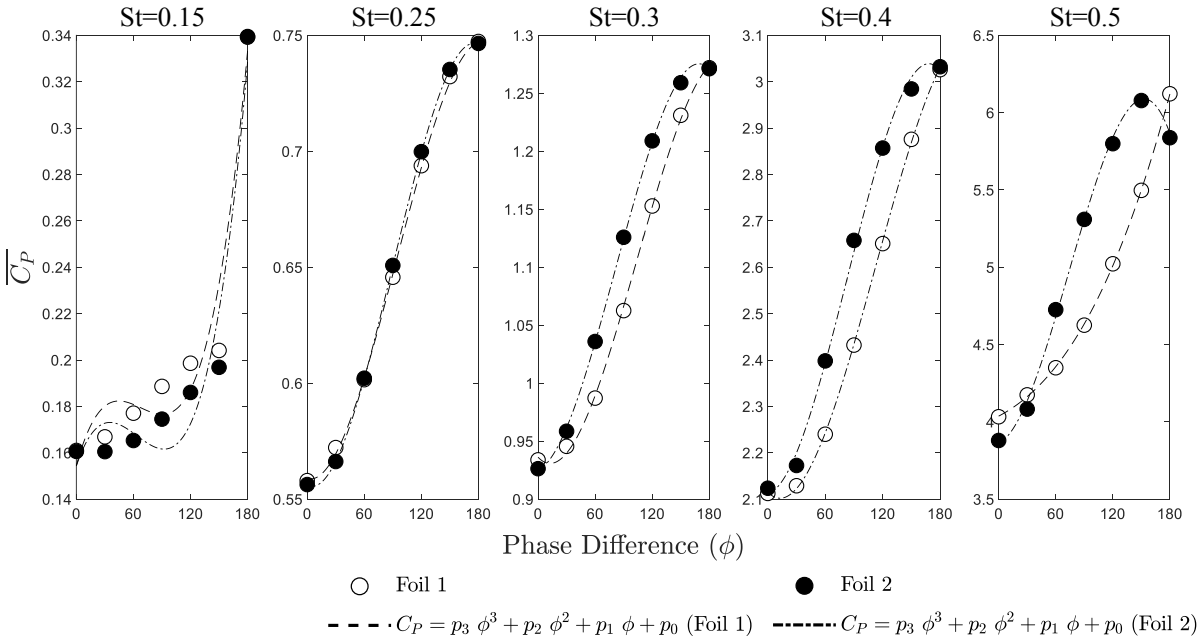

Figure 8.4: The variation of coefficient of power of tandem foils in a range of phase difference and *St*.

determined as functions of phase difference with third order polynomial coefficients, such that

$$\tau = c_{t6}\ \phi^3 + c_{t7}\ \phi^2 + c_{t8}\ \phi + c_{t9},$$

$$\varepsilon = c_{p4}\ \phi^3 + c_{p5}\ \phi^2 + c_{p6}\ \phi + c_{p7}.$$

Similar analyses are used to determine β and κ. Figures 8.5 and 8.6 show the variations of $\overline{C_T}$ and $\overline{C_P}$ for Foil 1 and Foil 2 for a range of separation distances at different Strouhal numbers, respectively. Moreover, it is considered that the effects due to separation distance should disappear if the foils are sufficiently far apart. Thus, a power function in the form of $a + b\,y^{*-2}$, similar to that proposed by Mivehchi et al. (2021), is employed to modify the scaling model. This function works well to mathematically model both $\overline{C_T}$ and $\overline{C_P}$. Therefore, β and κ took the following forms:

$$\beta = c_{t10} + c_{t11}\,y^{*-2},$$

$$\kappa = c_{p8} + c_{p9}\,y^{*-2}.$$

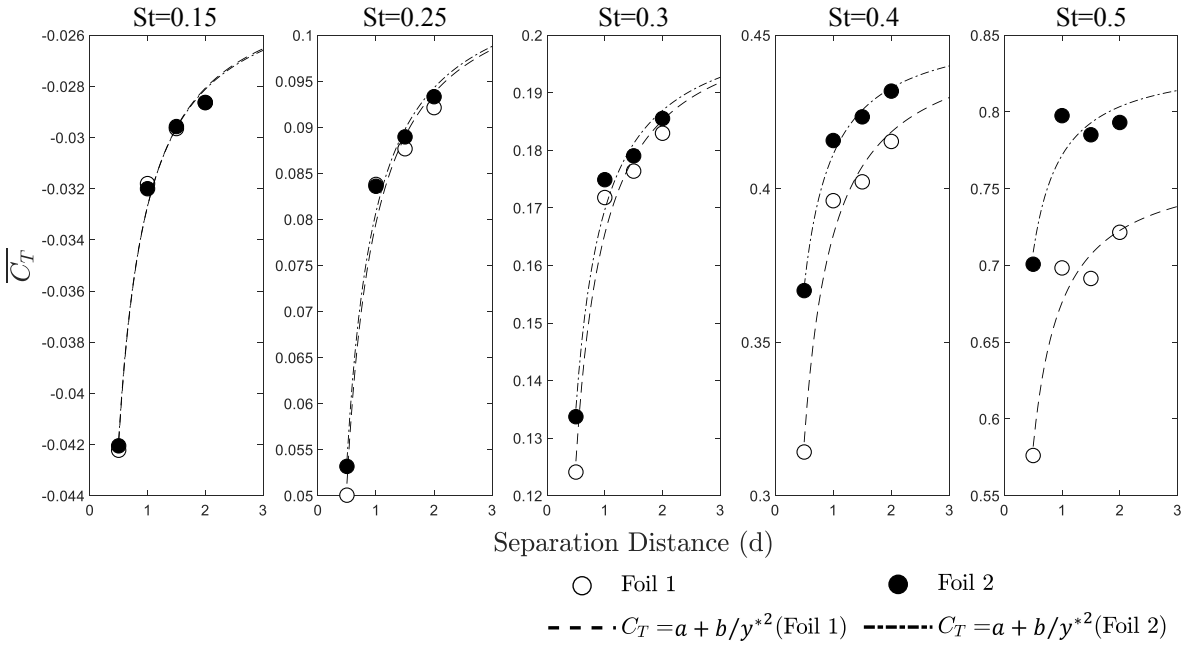

Figure 8.5: The variation of coefficient of thrust of tandem foils in a range of separation distance and St.

Consequently, the final form of the scaling relations are:

$$\begin{aligned} C_T &= \tau\ \beta\ \gamma\ St^2 - C_D \\ &= (c_{t6}\phi^3 + c_{t7}\phi^2 + c_{t8}\phi + c_{t9})(c_{t10} + c_{t11}/y^{*-2})(c_{t1} + c_{t2}Re^{-0.5} + c_{t3}f^{*-1})St^2 - (c_{t4} + c_{t5}), \end{aligned} \tag{8.5}$$

$$\begin{aligned} C_P &= \varepsilon\ \kappa\ \zeta\ St^2\ f^* \\ &= (c_{p4}\phi^3 + c_{p5}\phi^2 + c_{p6}\phi + c_{p7})(c_{p8} + c_{p9}/y^{*-2})(c_{p1} + c_{p2}Re^{-0.5} + c_{p3}f^{*-1})St^2\ f^*. \end{aligned} \tag{8.6}$$

Coefficients $c_{t1} - c_{t11}$ and $c_{p1} - c_{p9}$ are empirically calculated for Foil 1 and Foil 2 separately, since the deviation of $\overline{C_T}$ and $\overline{C_P}$ between the foils obstructs defining a single scaling relation for both foils. Using linear regression to minimize the square of deviation from the results obtained through numerical simulations for each case determines the optimum coefficients. Consequently,

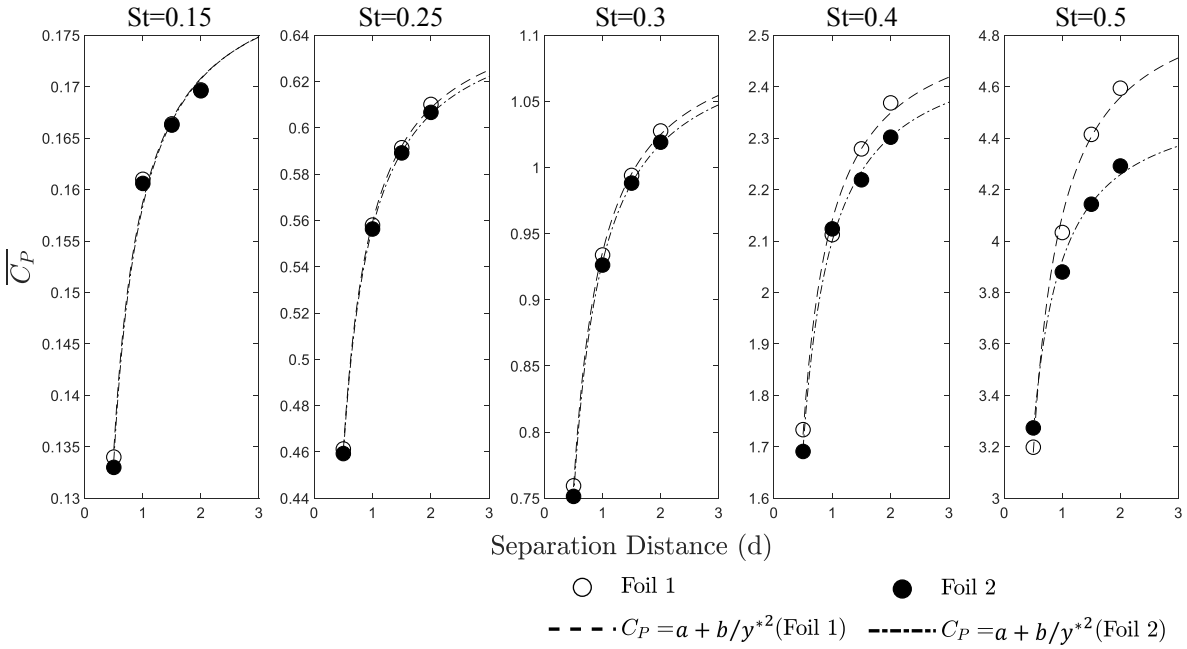

Figure 8.6: The variation of coefficient of power of tandem foils in a range of separation distance and *St*.

the coefficients for the scaling model of $\overline{C_T}$ for Foil 1 are determined as:

$$\begin{aligned} \tau &= 0.035\ \phi^3 - 0.319\ \phi^2 + 3.20\ \phi + 11.91 \\ \beta &= 0.218 - 0.0122\, y^{*-2} \\ \gamma &= 1.86 - 7.71\ Re^{-0.5} - 1.04\ f^{*-1} \\ C_D &= -0.041 + 3.43\ Re^{-0.5} \end{aligned} \tag{8.7}$$

Similarly for Foil 2, the coefficient were:

$$\begin{aligned} \tau &= -0.357\ \phi^3 + 2.54\ \phi^2 - 2.75\ \phi + 14.07 \\ \beta &= 0.763 - 0.0256\, y^{*-2} \\ \gamma &= 0.51 - 1.54\ Re^{-0.5} - 0.32\ f^{*-1} \\ C_D &= -0.055 + 4.04\ Re^{-0.5}. \end{aligned} \tag{8.8}$$

Data from the modified scaling of $\overline{C_T}$ collapse perfectly in the parametric space considered in the current study for Foil 1 and Foil 2, as shown in figure 8.7. The scaling coefficients for $\overline{C_P}$ for Foil 1 are:

$$\begin{aligned}
\varepsilon &= -0.037\ \phi^3 + 0.277\ \phi^2 - 0.1737\ \phi + 2.52 \\
\kappa &= 5.47 - 0.417\, y^{*-2} \\
\zeta &= 0.73 - 2.79\ Re^{-0.5} + 0.092\ f^{*-1}
\end{aligned} \tag{8.9}$$

Similarly, the coefficients for Foil 2 were:

$$\begin{aligned}
\varepsilon &= -0.105\ \phi^3 + 0.432\ \phi^2 - 0332\ \phi + 2.01 \\
\kappa &= 5.91 - 0.372\, y^{*-2} \\
\zeta &= 0.80 - 2.55\ Re^{-0.5} + 0.087\ f^{*-1}.
\end{aligned} \tag{8.10}$$

As shown in figure 8.8, the modified scaling model for $\overline{C_P}$ also yields a good collapse for both foils. We also present a combined scaling relation for $\overline{C_T}$ and $\overline{C_P}$ that applies to both foils. The scaling coefficients for $\overline{C_T}$ are calculated as:

$$\begin{aligned}
\tau &= -1.25\ \phi^3 + 5.77\ \phi^2 - 2.05\ \phi + 28.65 \\
\beta &= 0.19 - 0.008\, y^{*-2} \\
\gamma &= 0.94 - 2.72\ Re^{-0.5} - 0.54\ f^{*-1} \\
C_D &= -0.048 + 4.08\ Re^{-0.5}.
\end{aligned} \tag{8.11}$$

Similarly for $\overline{C_P}$, the scaling coefficients were:

$$\begin{aligned}
\varepsilon &= -0.309\ \phi^3 + 1.50\ \phi^2 + 0.416\ \phi + 1.65 \\
\kappa &= 5.08 - 0.6911\, y^{*-2} \\
\zeta &= 2.85 - 33.08\ Re^{-0.5} - 1.38\ f^{*-1}.
\end{aligned} \tag{8.12}$$

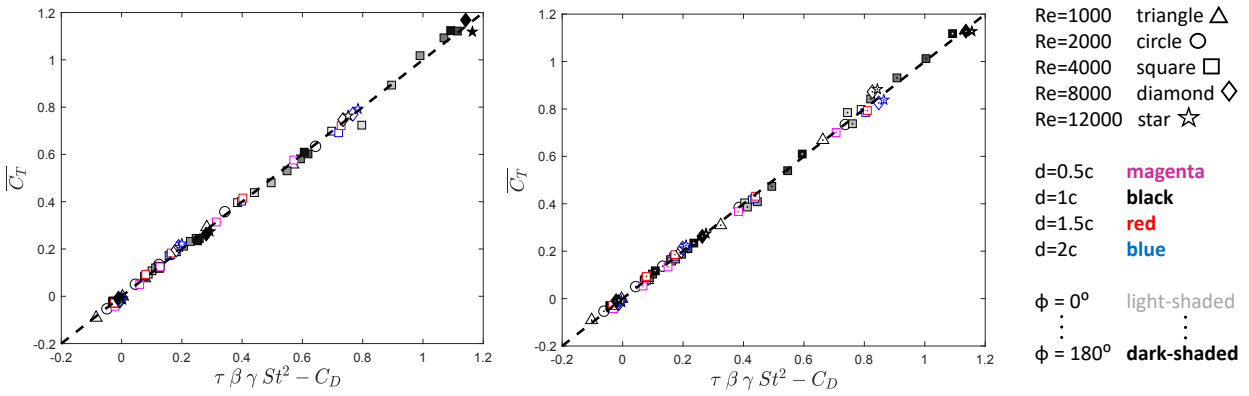

(a) (b)

Figure 8.7: The scaling relations for coefficient of thrust for (a) Foil 1 (b) Foil 2.

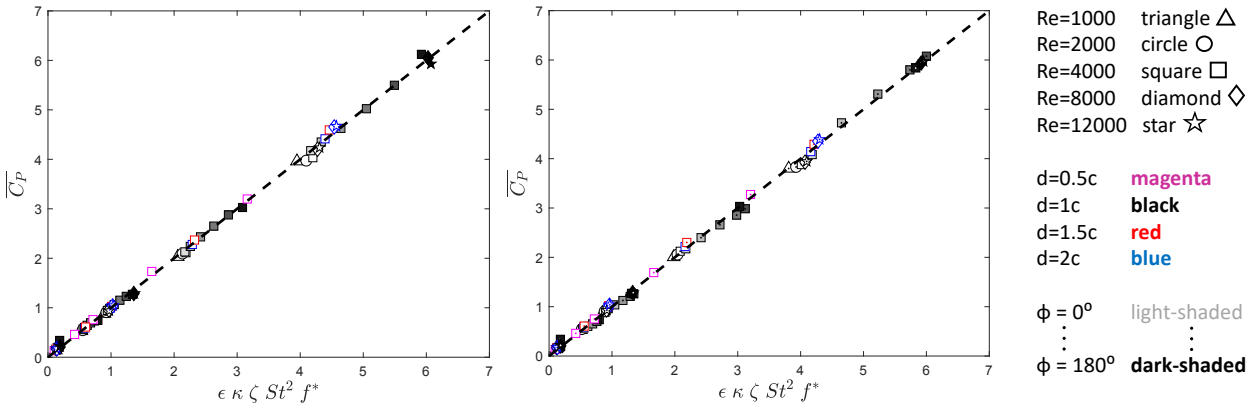

(a) (b)

Figure 8.8: The scaling relations for coefficient of power for (a) Foil 1 (b) Foil 2.

As shown in figure 8.9, data from both scaling models collapse well at lower *St*. However, there exists a deviation with increasing *St* that closely coincides with variations in phase difference. It is apparent from figures 8.3−8.6 that the disparity of $\overline{C_T}$ and $\overline{C_P}$ between the two foils is more pronounced with varying phase differences. Asymmetry of the motion introduced by phase difference could be the reason for this disparity because the wake and performance of the two foils differs despite their symmetric configuration and oscillations as shown in chapter 4. This suggests that one scaling relation would not work well for both foils if the positioning of the foils are not incorporated in the model.

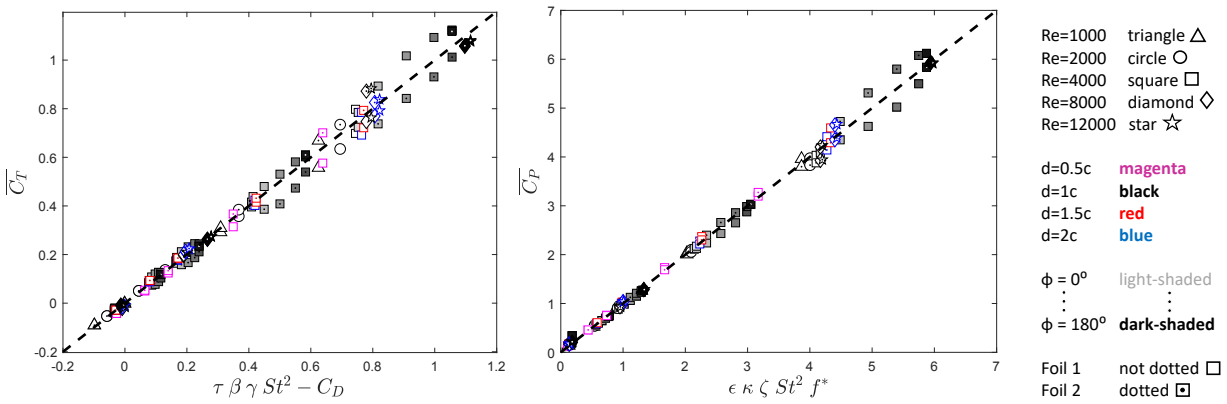

(a) (b)

Figure 8.9: The scaling relations for coefficient of (a) thrust and (b) power for tandem foils.

Table 8.2: Comparison of $\overline{C_T}$ and $\overline{C_P}$ of isolated foil between numerical simulation and scaling relation at a range of St for $Re = 4000$. Δ indicates the relative error.

St	$\overline{C}_{T-sim}$	$\overline{C}_{T-scale}$	$\Delta\overline{C}_T$ (%)	$\overline{C}_{P-sim}$	$\overline{C}_{P-scale}$	$\Delta\overline{C_P}$ (%)
0.25	0.10	0.08	22.23	0.64	0.59	7.92
0.3	0.20	0.17	12.98	1.08	1.00	7.95
0.4	0.45	0.43	4.83	2.48	2.30	7.91
0.5	0.81	0.78	4.41	4.75	4.41	7.68

The capability of the scaling models to estimate the performance of an isolated foil is further examined for the entire parameter space. Table 8.2 shows the numerically obtained $\overline{C_T}$ and $\overline{C_P}$ in comparison to those estimated by the scaling relations for two parallel foils. At a sufficiently large separation distance, it is expected that the two side-by-side foils behaves independently from one another, resembling the case of two isolated foils. For convenience, we considered the case of $y^* = 100$ and $\phi = 0^\circ$ to model the case of isolated foils. Even though isolated foil data are not used in determining the scaling coefficients for $\overline{C_T}$ and $\overline{C_P}$, the estimated power and thrust coefficients by the scaling relations at sufficiently large separation distance approach that of the data obtained through numerical simulations for an isolated foil. For $\overline{C_T}$, the largest relative error is observed to be 22.23% at $St = 0.25$, which decreases at higher St to only 4.41% at $St = 0.5$. The relative error in the prediction of $\overline{C_P}$, however, have a substantially reduced maximum value of 7.95% at $St = 0.3$.

8.2 Summary

The propulsive performance and scaling of pitching rigid foils in side-by-side configuration are studied over a broad parameter space, including a range of Reynolds numbers, Strouhal numbers, separation distances, and phase differences. The performance of pitching foils arranged in side-by-side are compared with isolated foils. The results suggests that the side-by-side configuration only enhances hydrodynamic performance, in terms of power requirement and efficiency, at higher Re and St. However, the side-by-side configuration increases St at which the maximum efficiency is attained by the foils for any given Re. This optimum St decreases with increasing Re, which is in agreement with previous observations for isolated foils. Moreover, it is observed that foils in side-by-side configuration scaled with $Re^{-0.5}$, which indicates a laminar flow scaling.

Modified scaling models are developed for pitching foils in side-by-side configurations. Two additional parameters are introduced based on the separation distance and phase difference between pitching foils. The data obtained from our scaling models collapses well on the parameters for individual foils. A combined scaling model for both foils, however, shows deviations between the two foils, especially at higher St, which is attributed to the non-uniform production of thrust and power consumption by the foils under such conditions. It is also observed that the scaling models adequately estimates the performance parameters of isolated foils as well assuming sufficiently large separation distance between parallel foils. Recognizing the limitations inherent in the derived scaling model, the following chapter presents physics-based scaling laws that estimate the propulsive performance of pitching foils in various schooling configurations.

Chapter 9

PHYSICS-INFORMED SCALING LAWS FOR SCHOOLING CONFIGURATIONS[†]

Scaling equations for propulsive performance of pitching foils in side-by-side configurations we explored in chapter 8, utilizing empirical expressions for spacing between the foils and their phase difference. However, limitations of these very recent research efforts in terms of their slender parametric space or more reliance on empirical formulations are clear. In order to design bio-inspired swimming robots, it is critical to construct physics-informed scaling laws applicable to a broad range of design and schooling parameters, including relative positions of oscillating foils and their phase differences. This primarily lays the foundation and motivation for the present study to develop scaling relations for a wide parametric space, including oscillation amplitude, oscillation frequency, separation distance, and phase difference. It is important to mention that developing universal scaling laws applicable to a variety of fish schooling configurations needs incorporation of flow conditions (Reynolds numbers), geometric characteristics (separation distance between the members of a school), kinematic parameters (oscillation frequencies and amplitudes, and phase difference), and physiological features of different aquatic species. In this context, this newly

[†]The content of this chapter has been published in whole or part, in *J. R. Soc. Interface* with the citation: "Gungor, A., Khalid, M.S.U., & Hemmati, A., (2024) Physics-Informed Scaling Laws for the Performance of Pitching Foils in Schooling Configurations. *J. R. Soc. Interface*."

Table 9.1: Parametric space of the study.

Parameter	x^*	y^*	St	Re	f^*	ϕ	θ_0
Range	$0c-3c$	$0.5c-2c$	$0.15-0.4$	$1000-10000$	$0.3-1.7$	$0-\pi$	$5^\circ-14^\circ$

proposed scaling relations for the propulsive metrics of individual members cover a wide, though not full, spectrum of the governing conditions in fish schools. This chapter is structured as follows: section 9.1 provides an overview of the problem definition and introduces the parametric space. The derivation of the novel scaling laws for staggered foils, highlighting their formulation and underlying principles, is presented in Section 9.2. The results obtained from the analysis are presented in Section 9.3. Finally, conclusions are drawn from the study, and the findings are summarized in Section 9.4.

9.1 Problem Definition

A wide range of spatial configurations are simulated in this study, including two-foil, three-foil, and five-foil configurations. This range of schooling systems demonstrates the extensiveness of the scaling approach. The horizontal and vertical separation distances between the foils, denoted by x^* and y^*, respectively, are varied between $0.5c-2c$ and $0c-3c$, respectively, with increments of $0.5c$. The amplitude-based Strouhal number of the flow was set to $St = 0.15-0.4$, which encompasses the range in which fish naturally swim (Godoy-Diana et al., 2008; Triantafyllou et al., 1993). Additionally, the phase difference between the foils was varied from $\phi = 0$ (in-phase motion) to $\phi = \pi$ (out-of-phase motion), with increments of $\pi/6$. The pitching amplitude was also varied between $5^\circ \leq \theta_0 \leq 14^\circ$ with increments of 3°. The simulations are conducted at $Re = 1000$, $Re = 2000$, $Re = 4000$, $Re = 6000$, and $Re = 10000$. A summary of the parameter space used in this study is provided in table 9.1.

9.2 Scaling laws

In this section, we elucidate the construction of a new physics-based scaling formulation for propulsion metrics, thrust and power, for synchronously pitching foils. We consider a wide range of schooling arrangements and design parameters. The term 'synchronous' implies that the foils in the system utilize the same pitching frequency. Pitching frequencies of the foils are kept the same, following the natural swimming habits of various fish species swimming in schooling configurations. Different biological studies (Herskin and Steffensen, 1998; Svendsen et al., 2003) revealed that the following members of fish schools could reduce their energy consumption by beating their tails with lower frequencies than those of their leaders. However, the difference in frequencies was found to be less than 15% (Herskin and Steffensen, 1998; Svendsen et al., 2003). From Khalid et al. (2016) and Newbolt et al. (2019), it is evident that there exists a very small range of governing kinematic parameters that allow for hydrodynamic advantages for follower fish, which led to the formation of stable configurations in fish schools. Additionally, oscillation frequencies of schooling red nose tetra fish are measured to be in close proximity in both two-fish and three-fish schools (Ashraf et al., 2016). These observations serve as a justification for considering synchronized kinematics for the members of fish schools in this study.

9.2.1 Scaling Approach

We employ an approach similar to Floryan et al. (2017) and Buren et al. (2019b), who established scaling relations for isolated foils based on lift-based forces (Theodorsen, 1935), added mass forces (Sedov, 1965), and contributions from the drag due to fluid flow over the oscillating bodies. A novel element of our present work originates from our analysis considering the impact on a foil through the vortex-induced velocity imposed by the other foils in the schooling configuration and their wakes. We excluded systems consisting of in-line foils because such configurations inherently involve direct vortex-body interactions. These interactions are heavily reliant on the advection velocities of the vortices and viscous effects (Boschitsch et al., 2014; Kurt and Moored, 2018b),

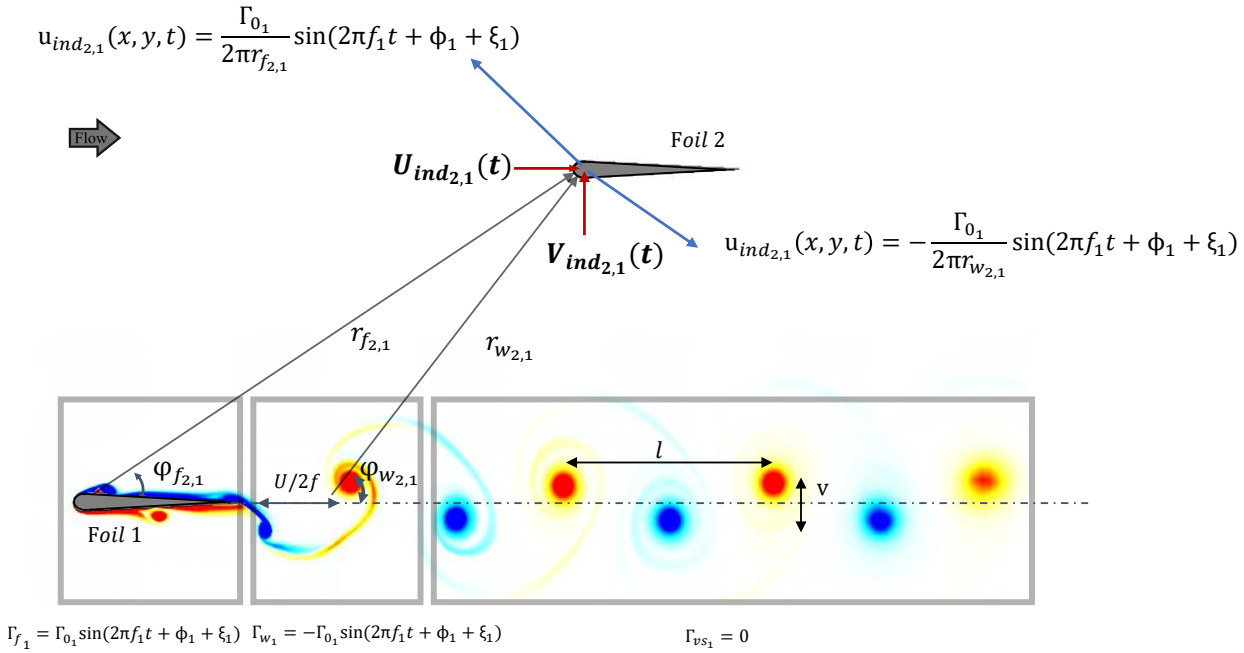

Figure 9.1: Induced velocities on the follower foil due to the circulation around and in the wake of the leader foil, together with the geometric quantities used in the analysis. Here, Γ_f, Γ_0, Γ_w, and Γ_{vs} represent the circulation around the foil, the amplitude of circulation, the circulation in the wake, and the circulation in the vortex street, respectively.

significantly altering the propulsive performance metrics for the follower foil by directly impacting the development of leading-edge vortices (Pourfarzan and Wong, 2022). Therefore, they cannot be accurately modeled using induced velocities. We derive the scaling equations not for each foil individually but in a generalized manner. To this end, we utilize the subscript i to represent the foil number, while double subscripts i and j are employed to describe the interaction between the foils and its direction. For instance, $\overline{C_{T_i}}$ corresponds to the cycle-averaged thrust of Foil i, whereas $V_{ind_{i,j}}$ defines the velocity on Foil i induced by Foil j. It is important to mention that we employ small-angle approximation throughout the derivation process for our scaling formulations.

Now, we begin with the description of lift-based forces and their contribution to the scaling relations. Pitching foils produce unsteady lift that follows their sinusoidal motion, $\theta_i(t) = \theta_0 \sin(2\pi f_i t - \phi_i)$, but with a phase lag ξ_i that depends on the reduced frequency f^*. This phase lag indicates the lag of lift data compared to the pitching motion of the foil. This is a conse-

quence of the time taken during the development of the vortex shedding process. The relationship between the phase lag and the reduced frequency can be estimated by Theodorsen's reduced order model (Theodorsen, 1935), which provides an accurate approximation except for very small reduced frequencies (Chiereghin et al., 2019). Hence, unsteady lift force on a foil is expressed as $L_{uns_i} = L_{0_i} \sin(2\pi f_i t - \xi_i)$, where L_0 is the amplitude of lift. Since the lift force is proportional to the circulation around the foil through the Kutta-Joukowski theorem (*i.e.,* $\Gamma_i = L_{uns_i}/\rho s U_\infty$), it induces a momentum (velocity) on the other foil in its vicinity. Employing Kelvin's circulation theorem, it can be assumed that circulation with the same strength but opposite sign is developed in the wake (see figure 9.1). This circulation is centered in the immediate vicinity of the trailing edge since the circulations of oppositely sign vortices in the rest of the wake cancel each other. The underlying reason for this cancellation is their equal strength that is opposite in sign at moderate St (Godoy-Diana et al., 2009). We estimate the center of wake circulation to be located $U/2f$ from the trailing edge, as this is the lateral distance between two consecutively shed vortices, also quantifying the wavelength of the near-wake. While it is true that the vertical location of the circulation may not align with the wake centerline for cases where the wake is deflected (see chapter 4), we expect its impact on the induced velocity to be minimal. It is because the shift in the vertical location of vortices is considerably smaller compared to the distance between the foils for any possible wake topology (see figure 10.1). Circulation around a foil and in its wake is counter-productive since they possess opposite-signs. Their combined effect induces a velocity in both vertical and horizontal directions. Thus, these induced velocities allow us to consider swimmer's performance as a single foil, which undergoes combined heaving and pitching motion. This argument is based on the induced velocity in vertical direction that may be analogous to heave velocity of the simultaneously heaving and pitching foil. Hence, we can compute the induced

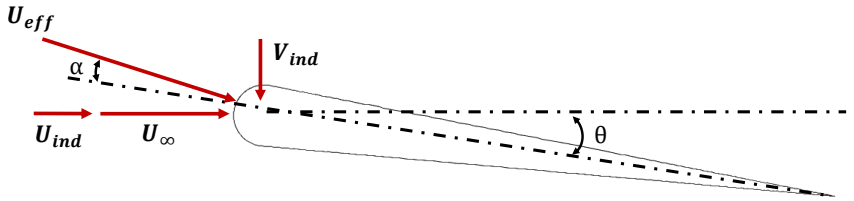

Figure 9.2: Velocity components arise on the pitching foils in staggered configurations.

velocities in the $x-$ and $y-$ directions for a foil using the Biot-Savart rule as follows:

$$\begin{aligned} V_{ind_i} &= \sum_{\substack{j=1 \\ j\neq i}}^{n} \frac{\Gamma_j}{2\pi}\left[\frac{\cos\psi_{f_{i,j}}}{|r_{f_{i,j}}|} - \frac{\cos\psi_{w_{i,j}}}{|r_{w_{i,j}}|}\right] \\ &= \sum_{\substack{j=1 \\ j\neq i}}^{n} \frac{L_0\sin(2\pi ft - \xi_j - \phi_j)}{2\pi\rho s U_\infty}\left[\frac{\cos\psi_{f_{i,j}}}{|r_{f_{i,j}}|} - \frac{\cos\psi_{w_{i,j}}}{|r_{w_{i,j}}|}\right] \end{aligned} \tag{9.1}$$

$$\begin{aligned} U_{ind_i} &= \sum_{\substack{j=1 \\ j\neq i}}^{n} \frac{\Gamma_j}{2\pi}\left[\frac{\sin\psi_{f_{i,j}}}{|r_{f_{i,j}}|} - \frac{\sin\psi_{w_{i,j}}}{|r_{w_{i,j}}|}\right] + U^*_{i,j} \\ &= \sum_{\substack{j=1 \\ j\neq i}}^{n} \frac{L_0 sin(2\pi ft - \xi_j - \phi_j)}{2\pi\rho s U_\infty}\left[\frac{sin\psi_{f_{i,j}}}{|r_{f_{i,j}}|} - \frac{sin\psi_{w_{i,j}}}{|r_{w_{i,j}}|}\right] + U^*_{i,j} \end{aligned} \tag{9.2}$$

where n denotes the total number of foils in the school, Γ_j is the quasi-steady sinusoidal circulation generated by the foils, $r_{f_{i,j}}$ is the radial distance vector (from the center of the circulation around Foil j to the leading edge of Foil i), $r_{w_{i,j}}$ is the radial distance vector (from the center of the wake circulation of Foil j to the leading edge of Foil i), $\psi_{f_{i,j}}$ denotes the angle from the center-line of Foil j to $r_{f_{i,j}}$, $\psi_{w_{i,j}}$ denotes the angle from the center-line of Foil j to $r_{w_{i,j}}$, and $U^*_{i,j}$ shows the time-independent velocity contribution on Foil i due to the vortex street of Foil j that is further explained in the following paragraph. Note that the lift force discussed in this chapter is identical to the side force considered in previous chapters. As mentioned earlier, the term "side force" was adopted in this dissertation due to its relevance to fish swimming. However, "lift" is used here to align with the terminology more commonly employed in the scaling literature.

In addition to the velocities induced by circulation around the foil and its counterpart in the immediate wake, the rest of the wake also contributes to the induced velocities. It forms a vortex street with apparently net zero circulation as previously explained. However, the vortices in the vortex street have varying vertical distances from the foil; therefore, their total contribution to the induces velocities can be non-zero. Schaefer and Eskinazi (1959) and Griffin and Ramberg (1959) provided potential flow solutions for velocities at a point induced by an infinite vortex street generated by tripping and vibrating cylinders, respectively. Following Griffin and Ramberg (1959), the induced velocity in the horizontal direction can be estimated as:

$$U^*_{i,j} = -\frac{\Gamma_{TEV_j}}{l_j} \frac{\cosh 2\pi\gamma_j(\sinh 2\pi\gamma_j - \sin 2\pi\varsigma_j \sinh 2\pi\delta_j)}{sinh^2 2\pi\gamma_j sinh^2 2\pi\delta_j + \cos^2 2\pi\varsigma_j - 2sinh 2\pi\gamma_j \sin 2\pi\varsigma_j \sinh 2\pi\delta_j}, \tag{9.3}$$

where Γ_{TEV_j} is the circulation of trailing edge vortex (TEV), $\gamma_j = v_j/2l_j$, $\varsigma = (x^*_{i,j} - c)/l_j$, and $\delta_j = y^*_{i,j}/l_j$. The terms l_j and v_j are the longitudinal and vertical spacings between the vortices in the vortex street of Foil j, respectively (see figure 9.1). They can be approximated as $l_j \approx U_\infty/f_j$ and $v_j \approx A_j$. Hence, $U^*_{i,j}$ can be represented in a simpler form:

$$U^*_{i,j} \approx \sum_{\substack{j=1 \\ j\neq i}}^{n} \frac{\Gamma_{TEV_j} f_k}{U_\infty} \chi_{i,j}(f, A, U_\infty, x^*, y^*), \tag{9.4}$$

where $\chi_{i,j}$ is a vortex street function which depends on the oscillation frequency and amplitude, free-stream velocity, and longitudinal and vertical spacing between the foils. Note that Griffin and Ramberg (1959) also derived more complex formulation for the induced velocities by incorporating viscous decay of the vorticity term. However, we use inviscid solution in our formulation because of its simplicity.

9.2.2 Lift-based (circulatory) forces

Now, we explain the derivation from Theodorsen's lift-based forces (circulatory) (Theodorsen, 1935). Oscillating foils produce unsteady lift as a result of its continuously varying angle-of-attack.

Figure 9.2 illustrates velocity components generated and corresponding angles on a pitching foil in the two-foil system. The instantaneous angle-of-attack and the corresponding effective velocity of the foil is given by $\alpha_i = \theta_i - \arctan(V_{ind_i}/(U_\infty + U_{ind_i}))$ and $U_{eff_i} = \sqrt{V_{ind_i}^2 + (U_\infty + U_{ind_i})^2}$, respectively. Lift-based forces in $x-$ direction, in $y-$ direction and moment about the leading edge are given as follows:

$$F_{x,L_i} = -L_i \sin(\theta_i - \alpha_i) = -L_i V_{ind_i}/U_{eff_i}, \tag{9.5}$$

$$F_{y,L_i} = L_i \cos(\theta_i - \alpha_i) = -L_i (U_\infty + U_{ind_i})/U_{eff_i}, \tag{9.6}$$

$$M_{z,L_i} = -cL_i/4, \tag{9.7}$$

where $L_i = (1/2)\rho U_{eff_i}^2 scC_{L_i}$ and $C_{L_i} = 2\pi \sin\alpha_i + (3/2)\pi\dot{\alpha}_i c/U_\infty$.

Considering the induced velocities are very small compared to the free-stream velocity and the trailing edge velocity, we can approximate α_i as $\alpha_i \approx \theta_i - V_{ind_i}/(U_\infty + U_{ind_i}) \approx \theta_i - V_{ind_i}/U_\infty$. Consequently, $\dot{\alpha}_i = \dot{\theta}_i - \dot{V}_{ind_i}/U_\infty$. Now the lift-based forces and moment adopt the following forms:

$$F_{x,L_i} \sim \rho sc \left(\theta_i V_{ind_i} U_{eff_i} - \frac{V_{ind_i}^2}{U_\infty} U_{eff_i} + c\dot{\theta}_i V_{ind_i} - c\frac{\dot{V}_{ind_i}}{U_\infty} V_{ind_i} \right) \tag{9.8}$$

$$F_{y,L_i} \sim \rho sc \left(\theta_i U_\infty U_{eff_i} - V_{ind_i} U_{eff} + c\dot{\theta}_i U_{eff_i} - c\dot{V}_{ind_i} \right) \tag{9.9}$$

$$M_{z,L_i} \sim \rho sc^2 \left(\theta_i U_{eff_i}^2 - \frac{V_{ind_i}}{U_\infty} U_{eff_i}^2 + c\dot{\theta}_i \frac{U_{eff_i}^2}{U_\infty} - c\dot{V}_{ind_i} \frac{U_{eff_i}^2}{U_\infty^2} \right) \tag{9.10}$$

9.2.3 Added mass forces

Next, we proceed with formulating the added mass forces, acting on the foils, by following Sedov's approach (Sedov, 1965). Tangential force (F_t), normal force (F_n), and moment (M_z) on the foils are:

$$F_{t,AM_i} = \rho\pi sc \left(\frac{c}{4} V_i \dot{\theta}_i - \frac{c^2}{8} {\dot{\theta}_i}^2 \right) \tag{9.11}$$

$$F_{n,AM_i} = \rho\pi sc \left(\frac{c}{4} \dot{V}_i + \frac{c^2}{8} \ddot{\theta}_i \right) \tag{9.12}$$

$$M_{z,AM_i} = \rho \pi s c^2 \left(\frac{c}{8} \dot{V}_i - \frac{9c^2}{128} \ddot{\theta}_i \frac{1}{4} U_i V_i + \frac{c}{8} U_i \dot{\theta}_i \right) \tag{9.13}$$

where U_i and V_i are normal and tangential velocity components impinging on Foil i, given as $U_i = V_{ind_i} \sin\theta_i + (U_\infty + U_{ind_i}) \cos\theta_i$ and $V_i = V_{ind_i} \cos\theta_i - (U_\infty + U_{ind_i}) \sin\theta_i$, respectively. In $x-y$ coordinates, the forces and the moment reduce to

$$F_{x,AM_i} \sim \rho s c \left[c\dot{\theta}_i V_{ind_i}(1+\theta_i^2) + c\theta_i \dot{\theta}_i U_\infty + c\theta_i \dot{\theta}_i U_{ind_i} + c^2 {\dot{\theta}_i}^2 + c\theta_i \dot{V}_{ind_i} + c\theta_i^2 \dot{U}_{ind_i} + c^2 \theta_i \ddot{\theta}_i \right] \tag{9.14}$$

$$F_{y,AM_i} \sim \rho s c \left[c\theta_i \dot{\theta}_i V_{ind_i} + c\dot{\theta}_i U_\infty (1+\theta_i^2) + c\dot{\theta}_i U_{ind_i}(1+\theta_i^2) + c^2 \theta_i {\dot{\theta}_i}^2 + c\dot{V}_{ind_i} + c\theta_i \dot{U}_{ind_i} + c^2 \ddot{\theta}_i \right] \tag{9.15}$$

$$\begin{aligned} M_{z,AM_i} \sim \rho s c^2 \big[& c\dot{V}_{ind_i} + c\theta_i \dot{\theta}_i V_{ind_i} + c\dot{\theta}_i U_\infty + c\dot{\theta}_i U_{ind_i} + c^2 \ddot{\theta}_i + V_{ind_i} U_\infty (1+\theta_i^2) \\ & + V_{ind_i} U_{ind_i} (1+\theta_i^2) + \theta_i V_{ind_i}^2 + \theta_i U_\infty^2 + \theta_i U_\infty U_{ind_i} + \theta U_{ind_i}^2 \big] \end{aligned} \tag{9.16}$$

9.2.4 Derivation of cycle-averaged coefficients

Now, we combine the lift-based and added mass forces and moments to determine the scaling relations for schooling foils. Following Buren et al. (2019b), we approximate that $1+\theta^2 \approx 1$, considering θ is small and its contribution is negligible. The thrust and lift forces on the foils can be expressed in the following form:

$$\begin{aligned} F_{x_i} \sim \rho s c \Bigg(& \theta V_{ind_i} U_{eff_i} - \frac{V_{ind_i}^2}{U_\infty} U_{eff_i} + c\dot{\theta}_i V_{ind_i} - c\frac{\dot{V}_{ind_i}}{U_\infty} V_{ind_i} + c\theta_i \dot{\theta}_i U_\infty + c\theta_i \dot{\theta}_i U_{ind_i} \\ & + c^2 {\dot{\theta}_i}^2 + c\theta_i \dot{V}_{ind_i} + c\theta_i^2 \dot{U_{ind_i}} + c^2 \theta_i \ddot{\theta}_i \Bigg) - F_{D_i}, \end{aligned} \tag{9.17}$$

$$\begin{aligned} F_{y_i} \sim \rho s c \Big(& \theta_i U_\infty U_{eff_i} + V_{ind_i} U_{eff_i} + c\dot{\theta}_i U_{eff_i} + c\dot{V}_{ind_i} + c\theta_i \dot{\theta}_i V_{ind_i} + c\dot{\theta}_i U_\infty + c\dot{\theta}_i U_{ind_i} \\ & + c^2 \theta_i {\dot{\theta}_i}^2 + c\theta_i \dot{U}_{ind_i} + c^2 \ddot{\theta}_i \Big), \end{aligned} \tag{9.18}$$

where F_D is the drag force on the foil. Since the drag force arises from viscous effects, it is not considered in lift-based forces or added mass forces, which both are inviscid in nature. Therefore,

it needs to be superimposed into the formulation. The drag experienced by a bluff body is proportional to the frontal area, A_f, which scales with $\sim U_\infty^2 A_f$. In the absence of large leading edge flow separation, drag on a pitching foil can be considered to be akin to that of a stationary foil. In this regard, frontal area of a stationary foil can be replaced with an averaged frontal area over a pitching cycle, which is proportional to the pitching amplitude, A (Floryan et al., 2019, 2018). This relationship is supported by a quantitative evidence presented by Buren et al. (2019b), who demonstrated that the drag was a linear function of pitching amplitude and independent of heaving amplitude. Hence, drag offset should scale as $F_D \sim U_\infty^2 A$.

Next, we proceed with the derivation of the scaling relation for power consumed by tethered foils to continue producing propulsive forces. Power for simultaneously heaving and pitching foils is $P = F_y \dot{h} + M_z \dot{\theta}$ (Verma and Hemmati, 2021). However, it can be approximated here as $P = F_y V_{ind} + M_z \dot{\theta}$, because heave velocity of the foil, $\dot{h}$, is akin to the induced velocity in the vertical direction, V_{ind}. Therefore, P can be expressed as:

$$\begin{aligned} P_i \sim \rho sc \Big(& \theta_i U_\infty U_{eff_i} V_{ind_i} + V_{ind_i}^2 U_{eff_i} + c\dot{\theta}_i V_{ind_i} U_{eff_i} + c V_{ind_i} \dot{V}_{ind_i} + c\theta_i \dot{\theta}_i V_{ind_i}^2 + c\dot{\theta}_i V_{ind_i} U_\infty \\ & + c\dot{\theta}_i V_{ind_i} U_{ind_i} + c^2 \theta_i \dot{\theta}_i^2 V_{ind_i} + c\theta_i V_{ind_i} \dot{U}_{ind_i} + c^2 \ddot{\theta}_i V_{ind_i} + c^2 \dot{\theta}_i \dot{V}_{ind_i} + c^2 \dot{\theta}_i^2 U_\infty + c^2 \dot{\theta}_i^2 U_{ind_i} \\ & + c^3 \dot{\theta}_i \ddot{\theta}_i + c\dot{\theta}_i V_{ind_i} U_{ind_i} + c\theta_i \dot{\theta}_i U_\infty^2 + c\theta_i \dot{\theta}_i U_\infty U_{ind_i} + c\theta_i \dot{\theta}_i U_{ind_i}^2 \Big). \end{aligned} \tag{9.19}$$

To finalize these laws, we should determine how V_{ind} and U_{ind} scale with the flow quantities. As previously explained, induced velocities arise from the circulation of the foils, which is related to the generated lift (see equation 9.1 and equation 9.2). Therefore, we approximate L_0 from the equation for the lift force (equation 9.18). To simplify the approximation, only a pure-pitching motion is considered, reducing equation 9.18 to $F_{y_i} \sim \theta_i U_\infty^2 + c\dot{\theta}_i U_\infty + c^2 \theta_i \dot{\theta}_i^2 + c^2 \ddot{\theta}_i$. Upon expansion, it is found that the third term can be neglected by employing the small angle approximation since it contains θ_0^3, whereas the other terms contain θ_0. The equation is further simplified by assuming that the fourth term, which scales as $c^2 \ddot{\theta}$, is the dominant term. To confirm this assumption, we analyzed the dominance of $c^2 \ddot{\theta}$ term to represent unsteady lift amplitude data alone. As illustrated in figure 9.3, $c^2 \ddot{\theta}$ provides an adequate approximation for the amplitude of unsteady lift, even though

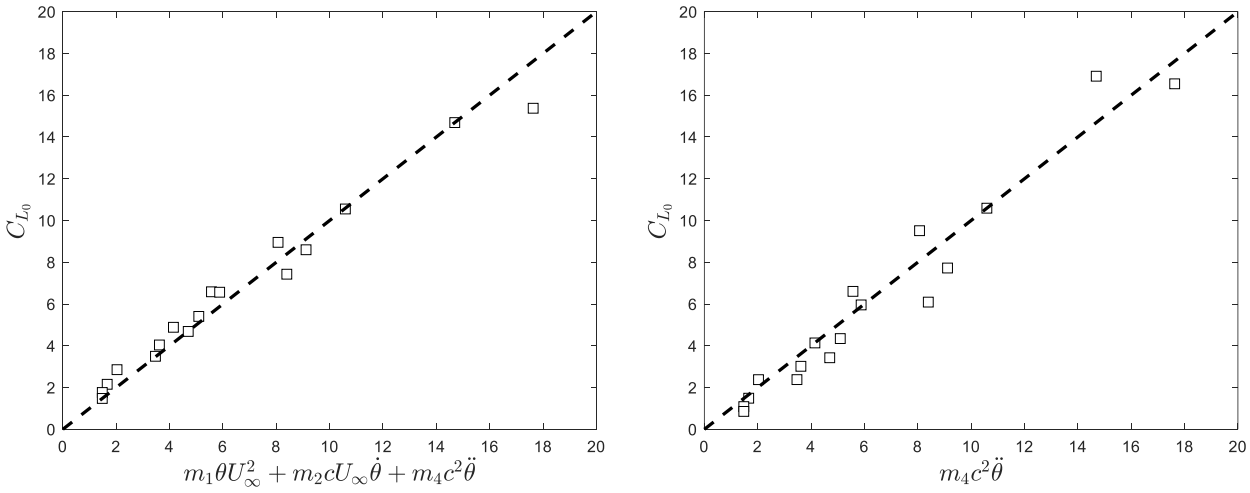

Figure 9.3: Coefficient of unsteady lift amplitude, $C_{L_0} = L_0/\frac{1}{2}\rho U_\infty^2 sc$, scaled with (a) $m_1\theta U_\infty^2 + m_2 c U_\infty \dot{\theta} + m_4 c^2 \ddot{\theta}$ and (b) $m_4 c^2 \ddot{\theta}$ where m_{1-4} are empirical coefficients determined through a least-squares linear regression analysis over randomly selected data points.

inclusion of the terms θU_∞^2 and $c\dot{\theta}U_\infty$ improves the fit. Thus, we assume that the amplitude of lift would scale as $L_0 \sim f^2 c^2 \theta_0$. Similarly, we need an approximation for Γ_{TEV}, which was presented by Schnipper et al. (2009) as:

$$\Gamma_{TEV_i} = \frac{1}{2}\int_0^{1/2f} V_{TE_i}^2 dt \approx \frac{1}{2}\pi^2 f c^2 \theta_0^2, \tag{9.20}$$

where V_{TE} is the trailing edge velocity magnitude, calculated as $V_{TE_i} = c\dot{\theta}_i$. This elucidates that Γ_{TEV} scales as $\Gamma_{TEV} \sim f c^2 \theta_0^2$ (Van Buren et al., 2018). Next, we integrate the thrust and power relations over a pitching cycle and non-dimensionalize them through equation 2.4 to obtain $\overline{C_T}$ and $\overline{C_P}$, respectively. We assume cycle-averaged effective velocity to be similar to the free-stream flow, *i.e.,* $\overline{U_{eff}} \approx U_\infty$ as its contribution would be negligible compared to other flow quantities (Buren et al., 2019a). Hence, $\overline{C_{T,i}}$ and $\overline{C_{P,i}}$ can be expressed as:

$$\begin{aligned}\overline{C_{T,i}} = {} & ct_1\Lambda_{T1_i} + ct_2\Lambda_{T2_i} + ct_3\Lambda_{T3_i} + ct_4\Lambda_{T4_i} + ct_5\Lambda_{T5_i} \\ & + ct_6\Lambda_{T6_i} + ct_7\Lambda_{T7_i} + ct_8\Lambda_{T8_i} + ct_9\Lambda_{T9_i} + ct_{10}\Lambda_{T10_i},\end{aligned} \tag{9.21}$$

$$\begin{aligned}\overline{C_{P,i}} = {} & cp_1\Lambda_{P1_i} + cp_2\Lambda_{P2_i} + cp_3\Lambda_{P3_i} + cp_4\Lambda_{P4_i} + cp_5\Lambda_{P5_i} + cp_6\Lambda_{P6_i} + cp_7\Lambda_{P7_i} \\ & + cp_8\Lambda_{P8_i} + cp_9\Lambda_{P9_i} + cp_{10}\Lambda_{P10_i} + cp_{11}\Lambda_{P11_i} + cp_{12}\Lambda_{P12_i} + cp_{13}\Lambda_{P13_i} \\ & + cp_{14}\Lambda_{P14_i} + cp_{15}\Lambda_{P15_i} + cp_{16}\Lambda_{P16_i} + cp_{17}\Lambda_{P17_i} + cp_{18}\Lambda_{P18_i} + cp_{19}\Lambda_{P19_i},\end{aligned} \tag{9.22}$$

where definitions of expressions Λ_{T1-10} and Λ_{P1-19} are given in table 9.2 and table 9.3, respectively.

Table 9.2: Definitions of the thrust terms in the derived scaling equations.

Thrust Term	Definition
Λ_{T1_i}	$\sum_{\substack{j=1 \\ j\neq i}}^{n} St^2 \cos(\xi_j + \phi_j - \phi_i)\left(\frac{\cos\psi_{f_{i,j}}}{r_{f_{i,j}}} - \frac{\cos\psi_{w_{i,j}}}{r_{w_{i,j}}}\right)$
Λ_{T2_i}	$\sum_{\substack{j=1 \\ j\neq i}}^{n} St^2 f^{*2}\left(\frac{\cos\psi_{f_{i,j}}}{r_{f_{i,j}}} - \frac{\cos\psi_{w_{i,j}}}{r_{w_{i,j}}}\right)^2$
Λ_{T3_i}	$\sum_{\substack{j=1 \\ j\neq i}}^{n} St^2 f^{*} \sin(\xi_j + \phi_j - \phi_i)\left(\frac{\cos\psi_{f_{i,j}}}{r_{f_{i,j}}} - \frac{\cos\psi_{w_{i,j}}}{r_{w_{i,j}}}\right)$
Λ_{T4_i}	$\sum_{\substack{j=1 \\ j\neq i}}^{n} \underline{St^2 f^{*3}\left(\frac{\cos\psi_{f_{i,j}}}{r_{f_{i,j}}} - \frac{\cos\psi_{w_{i,j}}}{r_{w_{i,j}}}\right)^2}$
Λ_{T5_i}	St^2
Λ_{T6_i}	$\sum_{\substack{j=1 \\ j\neq i}}^{n} St^2 f^{*} \sin(\xi_j + \phi_j - \phi_i)\left(\frac{\sin\psi_{f_{i,j}}}{r_{f_{i,j}}} - \frac{\sin\psi_{w_{i,j}}}{r_{w_{i,j}}}\right)$
Λ_{T7_i}	$\underline{StA^*}$
Λ_{T8_i}	$\sum_{\substack{j=1 \\ j\neq i}}^{n} \underline{St^3\left(\frac{\sin\psi_{f_{i,j}}}{r_{f_{i,j}}} - \frac{\sin\psi_{w_{i,j}}}{r_{w_{i,j}}}\right)}$
Λ_{T9_i}	$\sum_{\substack{j=1 \\ j\neq i}}^{n} \underline{St^3 A^* \chi_{i,j}}$
Λ_{T10_i}	A^*

Table 9.3: Definitions of the power terms in the derived scaling equations.

Power Term	Definition
Λ_{P1_i}	$\sum_{\substack{j=1 \\ j\neq i}}^{n} St^2 \cos(\xi_j + \phi_j - \phi_i) \left(\frac{\cos\psi_{f_{i,j}}}{r_{f_{i,j}}} - \frac{\cos\psi_{w_{i,j}}}{r_{w_{i,j}}} \right)$
Λ_{P2_i}	$\sum_{\substack{j=1 \\ j\neq i}}^{n} St^4 \left(\frac{\cos\psi_{f_{i,j}}}{r_{f_{i,j}}} - \frac{\cos\psi_{w_{i,j}}}{r_{w_{i,j}}} \right)^2$
Λ_{P3_i}	$\sum_{\substack{j=1 \\ j\neq i}}^{n} St^2 f^* \sin(\xi_j + \phi_j - \phi_i) \left(\frac{\cos\psi_{f_{i,j}}}{r_{f_{i,j}}} - \frac{\cos\psi_{w_{i,j}}}{r_{w_{i,j}}} \right)$
Λ_{P4_i}	$\sum_{\substack{j=1 \\ j\neq i}}^{n} \underline{St^2 f^{*3} \left(\frac{\cos\psi_{f_{i,j}}}{r_{f_{i,j}}} - \frac{\cos\psi_{w_{i,j}}}{r_{w_{i,j}}} \right)^2}$
Λ_{P5_i}	$\sum_{\substack{j=1 \\ j\neq i}}^{n} St^4 f^* \sin(2\xi_j + 2\phi_j - 2\phi_i) \left(\frac{\cos\psi_{f_{i,j}}}{r_{f_{i,j}}} - \frac{\cos\psi_{w_{i,j}}}{r_{w_{i,j}}} \right)^2$
Λ_{P6_i}	$\sum_{\substack{j=1 \\ j\neq i}}^{n} \underline{St^3 f^{*2} \left(\frac{\cos\psi_{f_{i,j}}}{r_{f_{i,j}}} - \frac{\cos\psi_{w_{i,j}}}{r_{w_{i,j}}} \right) \left(\frac{\sin\psi_{f_{i,j}}}{r_{f_{i,j}}} - \frac{\sin\psi_{w_{i,j}}}{r_{w_{i,j}}} \right)}$
Λ_{P7_i}	$\sum_{\substack{j=1 \\ j\neq i}}^{n} St^4 \cos(\xi_j + \phi_j - \phi_i) \left(\frac{\cos\psi_{f_{i,j}}}{r_{f_{i,j}}} - \frac{\cos\psi_{w_{i,j}}}{r_{w_{i,j}}} \right)$
Λ_{P8_i}	$\sum_{\substack{j=1 \\ j\neq i}}^{n} St^2 f^{*2} \cos(\xi_j + \phi_j - \phi_i) \left(\frac{\cos\psi_{f_{i,j}}}{r_{f_{i,j}}} - \frac{\cos\psi_{w_{i,j}}}{r_{w_{i,j}}} \right)$
Λ_{P9_i}	St^2
Λ_{P10_i}	$\sum_{\substack{j=1 \\ j\neq i}}^{n} \underline{St^3 f^* \left(\frac{\sin\psi_{f_{i,j}}}{r_{f_{i,j}}} - \frac{\sin\psi_{w_{i,j}}}{r_{w_{i,j}}} \right)}$
Λ_{P11_i}	$\underline{St^2 f^*}$
Λ_{P12_i}	$\underline{StA^*}$
Λ_{P13_i}	$\sum_{\substack{j=1 \\ j\neq i}}^{n} \underline{St^3 \left(\frac{\sin\psi_{f_{i,j}}}{r_{f_{i,j}}} - \frac{\sin\psi_{w_{i,j}}}{r_{w_{i,j}}} \right)}$
Λ_{P14_i}	$\sum_{\substack{j=1 \\ j\neq i}}^{n} St^4 f^* \cos(2\xi_j + 2\phi_j - 2\phi_i) \left(\frac{\sin\psi_{f_{i,j}}}{r_{f_{i,j}}} - \frac{\sin\psi_{w_{i,j}}}{r_{w_{i,j}}} \right)^2$
Λ_{P15_i}	$\sum_{\substack{j=1 \\ j\neq i}}^{n} St^4 f^* \sin(\xi_j + \phi_j - \phi_i) \left(\frac{\cos\psi_{f_{i,j}}}{r_{f_{i,j}}} - \frac{\cos\psi_{w_{i,j}}}{r_{w_{i,j}}} \right) \chi_{i,j}$

Table 9.3 – continued from previous page

Power Term	Definition
Λ_{P16_i}	$\sum_{\substack{j=1 \\ j\neq i}}^{n} St^4 \chi_{i,j}$
Λ_{P17_i}	$\sum_{\substack{j=1 \\ j\neq i}}^{n} St^3 A^* \chi_{i,j}$
Λ_{P18_i}	$\sum_{\substack{j=1 \\ j\neq i}}^{n} St^5 \left(\frac{\sin\psi_{f_{i,j}}}{r_{f_{i,j}}} - \frac{\sin\psi_{w_{i,j}}}{r_{w_{i,j}}} \right) \chi_{i,j}$
Λ_{P19_i}	$\sum_{\substack{j=1 \\ j\neq i}}^{n} St^5 A^* \chi_{i,j}^2$

9.3 Results and Discussion

We now continue with computing the terms in equation 9.21 and equation 9.22 to assess the effectiveness of the derived equations in capturing the fundamental flow physics. For the purpose of this analysis, we focus on the case of two-foil systems, since these configurations represent the majority of our dataset. To calculate the equations for the two foils, we simply substitute $i = 1$ and $i = 2$ to represent Foils 1 and 2, respectively, while keeping the value of n fixed at 2. Note that j can get only one value since it represents the contribution due to the other foil in the system, *i.e.,* $j = 2$ for $i = 1$ and $j = 1$ for $i = 2$. Here, ct_{1-10} and cp_{1-19} are scaling coefficients that are determined numerically. In accordance with Floryan et al. (2017) and Buren et al. (2019b), we underline inherently out-of-phase terms, such as displacement-velocity or velocity-acceleration terms, *i.e.,* $\theta - \dot{\theta}$ or $\dot{\theta} - \ddot{\theta}$. These terms have 90° phase lag between them; therefore, a time-averaged quantity of their product should be very small. However, it is possible for strong non-linear effects to exist in such complex flows as suggested by Liu et al. (2015), which may break the inherent out-of-phase synchronization of these terms. Hence, we chose to keep these terms in our analysis.

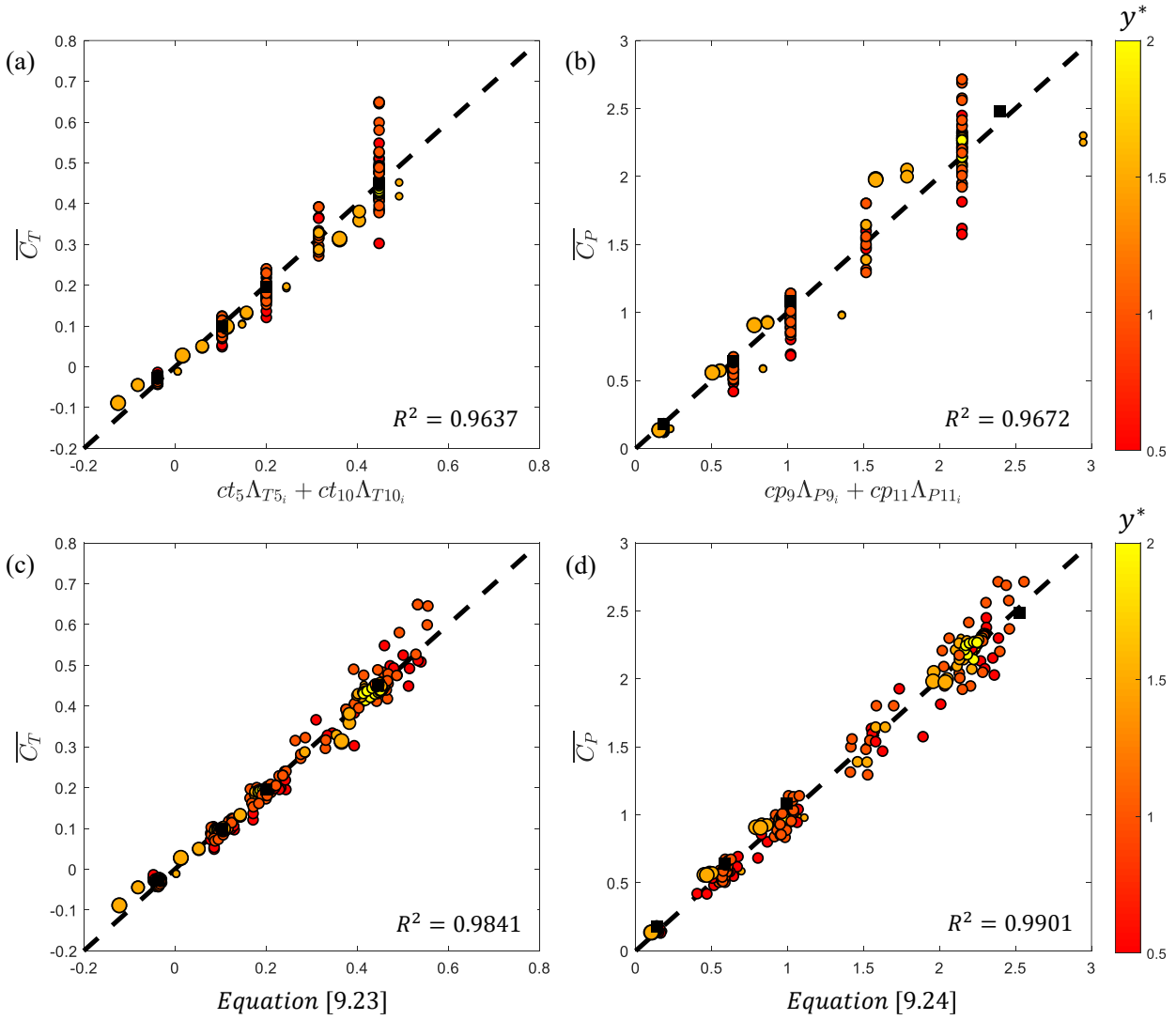

Figure 9.4: (a-c) Thrust and (b-d) power scaling results of pitching foils in two-foil configurations for varying pitching amplitude and phase difference at $Re = 4000$. Numerical data is plotted against (a-b) only pure-pitching terms, (c-d) full scaling equations. Color and size indicates the radial distance between the foils (y^*) and pitching amplitude (A^*), respectively. Isolated foil data is illustrated with black squares.

9.3.1 Two-Foil systems

In order to determine the scaling coefficients, ct_{1-10} and cp_{1-19}, least-squares linear regression analysis is employed on two-foil configurations at $Re = 4000$, as our first trial. Ultimately, it is noticed that some terms could be eliminated from the formulations as their impact on the results is marginal for the given parameter space. The influence of each term on the scaling estimation is

carefully evaluated. Terms that contribute less than 1% to the estimated value, on average across the dataset, are deemed negligible. This facilitates the establishment of more simplified scaling equations with little compromise on accuracy. Consequently, the terms associated with ct_1, ct_3, ct_4, ct_6, ct_7, ct_8, and ct_9 in the equations for thrust, and cp_1, cp_4, cp_5, cp_{12}, cp_{13}, cp_{14}, cp_{15}, cp_{16}, cp_{17}, and cp_{19} in the equations for power are excluded from the final form of the scaling equations:

$$\overline{C_{T,i}} = \underbrace{ct_2\Lambda_{T2_i} + ct_3\Lambda_{T3_i}}_{\text{induced velocity}} + \underbrace{ct_5\Lambda_{T5_i} + ct_{10}\Lambda_{T10_i}}_{\text{pure-pitching}}, \tag{9.23}$$

$$\overline{C_{P,i}} = \underbrace{cp_6\Lambda_{P6_i} + cp_7\Lambda_{P7_i} + cp_8\Lambda_{P8_i} + cp_{10}\Lambda_{P10_i} + cp_{18}\Lambda_{P18_i}}_{\text{induced velocity}} + \underbrace{cp_9\Lambda_{P9_i} + cp_{11}\Lambda_{P11_i}}_{\text{pure-pitching}}. \tag{9.24}$$

The numerical coefficients are calculated, such that $ct_2 = 0.29$, $ct_3 = -0.84$, $ct_5 = 3.50$, and $ct_{10} = -0.41$ for thrust scaling and $cp_6 = -1.79$, $cp_7 = 146.75$, $cp_8 = -13.01$, $cp_9 = 1.39$, $cp_{10} = 2.70$, $cp_{11} = 8.93$, and $cp_{18} = 4.67$ for power scaling.

Terms in the scaling equations (equation 9.23 and equation 9.24) are classified based on their origin. The "pure-pitching" terms arise from the pitching oscillations of the foils, while the terms for "induced velocity" stem from the interactions between the foils. The pure-pitching terms are plotted alone against the numerical simulation data for the coefficients of thrust and power in figure 9.4a and figure 9.4b, respectively. The figures also comprise the performance of isolated foils, which are essentially for the foils uninfluenced by the effects of induced velocity. They fail to achieve a satisfactory collapse, except for the isolated foils and two-foil systems with significant separation distance. This indicates the insufficiency of the pure-pitching terms in accurately representing complex flows with intense foil-foil interactions. On the other hand, Figs. 9.4c and 9.4d display the fit of the data, where the numerical results demonstrate an excellent linear collapse on the complete scaling equations (equation 9.23 and equation 9.24). It provides a compelling evidence that the derived terms proficiently capture the underlying flow physics. The improved r-squared values, depicting a notable shift from $R^2 = 0.9637$ to $R^2 = 0.9841$ for the thrust scaling and from $R^2 = 0.9672$ to $R^2 = 0.9901$ for the power scaling, unequivocally quantify the critical role played by the induced velocity terms.

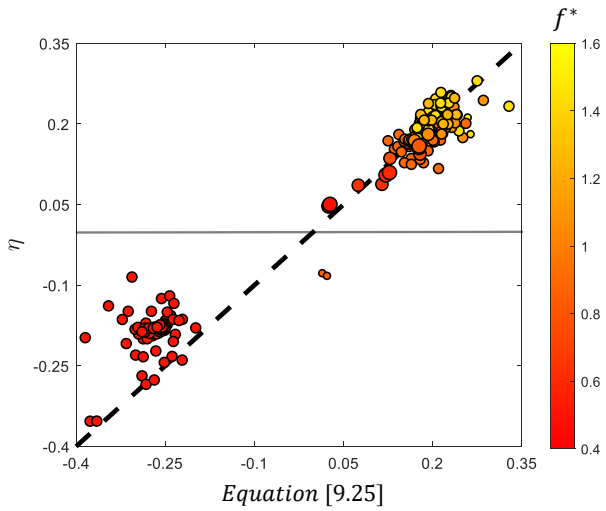

Figure 9.5: Simulation efficiency plotted against scaling efficiency for two-foil configurations at $Re = 4000$. Color and size indicates the radial distance between the foils (y^*) and pitching amplitude (A^*), respectively.

Induced velocity terms in the relation for thrust (equation 9.23), namely Λ_{T2_i} and Λ_{T3_i}, originate from the terms involving $V_{ind_i}^2 U_{eff_i}/U_\infty$ and $c\dot{\theta}_i V_{ind_i}$, respectively. The first term signifies the steady portion of the lift-based forces, whereas the latter results from the combination of the unsteady portion of the lift-based forces and the Coriolis effect from the added mass forces. It is crucial to note that purely pitching foils do not generate any lift-based thrust since their instantaneous angle-of-attack (α_i) is equal to their instantaneous pitching angle (θ_i), causing $\sin(\theta_i - \alpha_i)$ in equation 9.5 to vanish. Therefore, the lift-based thrust generated by schooling foils is attributed to the alterations in α_i due to the induced vertical velocity. The terms Λ_{T5_i} and Λ_{T10_i} represent pure-pitching related features attributed to contributions form added mass and viscous drag, respectively. The added mass term originates from the combination of $c^2\dot{\theta}_i^{\,2}$, highlighting the centrifugal effect, and $c^2\theta_i\ddot{\theta}_i$, representing the influence of the foil acceleration.

The results display certain outliers in figures 9.4c and 9.4d, primarily noticeable in scenarios where the foils are in very close proximity. We categorize these configurations as interfering configurations, such that the leader and follower foils can no longer be considered separate bodies. In such scenarios, the wake of one foil directly influences the wake of another, leading to inaccuracy in the implementation of Kelvin's circulation theorem, which associates circulation around a foil

with the circulation in the wake. Strong interactions between the foils, even in the absence of any interference, may also introduce minor effect on the flow that are not considered in the current formulations. For instance, these interactions could cause the wake of a foil to deflect upwards or downwards based on its kinematics (see figure 4.2 or Dewey et al. (2014)), resulting in deviations in the calculation of the wake geometric properties (ψ_w and r_w). Another impact could be on the circulation of the foils, given that the interaction between the foils exerts a substantial influence on their lift characteristics. In chapter 10, we demonstrated that the formation of leading edge vortices is suppressed on the adjacent surfaces of the foils when placed in a side-by-side arrangement. This phenomenon directly influences the circulation generated by the foils and their wake, resulting in deviation from our initial assumption that the lift follows an ideal sine-wave, *i.e.,* $L_i = L_0 \sin(2\pi ft - \xi_i)$. Likewise, Han et al. (2024) displayed that the induced velocities could result in asymmetric quasi-steady lift variation for pitching foils with ground effect. We conjecture that the inclusion of a lift-correction term for close foil proximity could potentially offer a solution. However, since the deviations are already relatively small, we do not consider changing the form of lift variation.

We calculate the propulsive efficiency of the foils utilizing the scaling equations, given as:

$$\overline{\eta_i} = \frac{\overline{C_{T_i}}}{\overline{C_{P_i}}} = \frac{\text{RHS of equation 9.23}}{\text{RHS of equation 9.24}}. \tag{9.25}$$

However, when plotting efficiency from the scaling relations (equation 9.25) against that from the computational data (equation 2.4), as shown in figure 9.5, we observe that the data has not collapsed as well as those of the coefficients at lower f^*. This outcome motivated us to hypothesize that the traditional definition of efficiency (equation 2.4) may be inadequate for schooling configurations. Therefore, it is necessary to redefine efficiency specifically for these setups. Similar to the previously proposed lift-correction term, the introduction of a moment-correction term could potentially resolve this issue. However, examining and including a moment-correction term falls outside the scope of this study, and we consider it as a potential avenue for our future research.

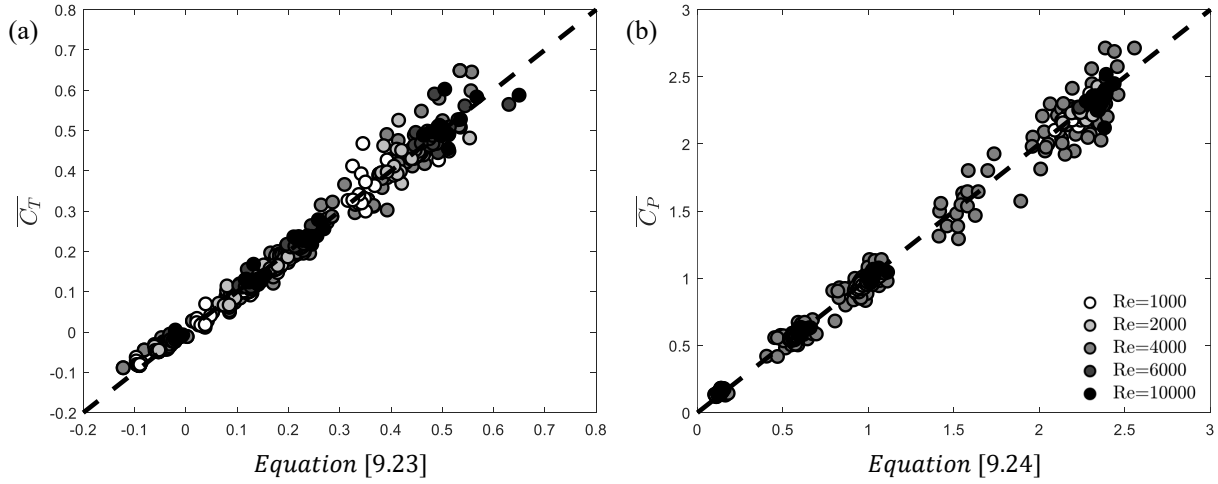

Figure 9.6: (a) Thrust and (b) power scaling results of pitching foils in two-foil configurations at a range of Reynolds numbers.

Yet, equation 9.25 accurately predicts the efficiencies of foils within the thrust-generating regime (positive η), revealing a trend of increased efficiencies at higher f^*, albeit with some scatter. This underscores the significance of the induced velocity effects, particularly considering that the efficiency of purely pitching foils tends to decrease with an increasing f^*, except for very slow foil motions where viscous drag dominates (Floryan et al., 2017). This is attributed to the presence of additional f^* terms included in the induced velocity terms, thereby magnifying the induced effects on efficiency at higher f^*. Nonetheless, discerning a linear relationship between efficiency and f^* is unattainable due to the inherent complexity of the efficiency equation.

9.3.2 Influence of Reynolds number

We demonstrate the predictive capability of scaling relations across various Reynolds numbers. To achieve this, flows around different schooling configurations are simulated at Reynolds numbers of 1000, 2000, 6000, and 10000. Subsequently, a regression analysis is performed to determine the scaling coefficients for each Reynolds number as presented in table 9.4. Figure 9.6 illustrates the collapse of the scaling-based estimation for the thrust and power coefficients in comparison to those from simulations. Additionally, results for $Re = 4000$ in figure 9.4 are incorporated in fig-

Table 9.4: Scaling coefficients for thrust and power equations at different Reynolds numbers.

Re	ct_2	ct_3	ct_5	ct_{10}	cp_6	cp_7	cp_8	cp_9	cp_{10}	cp_{11}	cp_{18}
1000	0.30	-0.62	3.45	-0.69	-1.57	147.76	-12.84	0.54	2.08	9.67	3.89
2000	0.32	-0.68	3.49	-0.51	-1.66	148.02	-12.80	0.62	2.11	9.60	4.11
6000	0.26	-0.86	3.52	-0.34	-1.84	146.07	-12.71	0.85	2.17	9.67	4.73
10000	0.21	-0.88	3.54	-0.28	-1.90	144.73	-12.69	0.79	2.05	9.61	5.02

ure 9.6 for completeness. The data demonstrates an excellent collapse, affirming the adaptability of our newly proposed scaling relations. The influence of Reynolds number on the coefficients of the induced velocity terms appears to be marginal, indicating that the inherent flow physics governing the influence of foil-foil interactions on the propulsive performance of schooling foils is predominantly inviscid. This observation aligns with the conclusion of Kurt et al. (2019), asserting that the equilibrium altitude of a pitching foil near a wall is controlled by added mass and circulatory forces, both of which are inviscid in nature. Conversely, the drag force on the foils, represented by ct_{10}, displays significant dependence on Reynolds number. This outcome is anticipated, considering that the drag force arises from viscous effects and it is expected to be a function of Reynolds number (Floryan et al., 2018; Senturk and Smits, 2019). Moreover, the performance of both single foils (Senturk and Smits, 2019) and foils in parallel configurations (see chapter 8) is not notably affected by Reynolds number beyond $Re = 8000$. Hence, it can be argued that the derived equations maintain their efficacy at higher Reynolds numbers with minimal, if any, adjustments to the coefficients. This implies that our scaling relations coincide with the lower end of the natural swimming Reynolds numbers range of fish (Triantafyllou et al., 1993; Gazzola et al., 2014).

9.3.3 Multi-Foil systems

While the scaling relations presented in this work primarily focus on two-foil configurations, they can be effectively extended to multi-foil systems. This stems from the accurate modelling of foil-foil interactions in accordance with the underlying flow physics. To confirm, we conducted

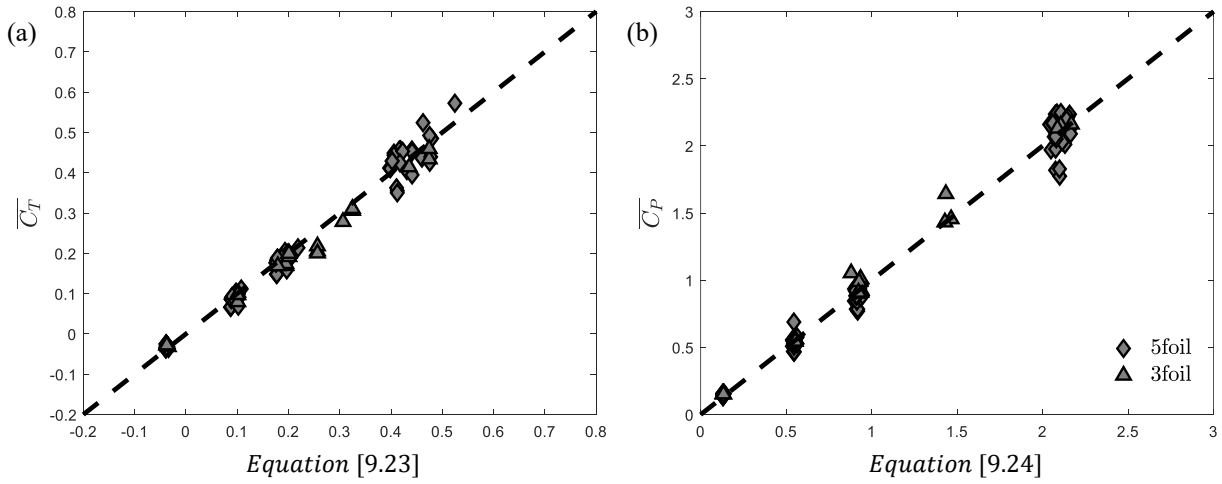

Figure 9.7: (a) Thrust and (b) power scaling results of pitching foils in various three-foil and five-foil schools at $Re = 4000$.

simulations involving three-foil and five-foil configurations at $Re = 4000$. The scaling coefficients that provides the most accurate estimation for the simulation data are $ct_2 = 0.21$, $ct_3 = -0.88$, $ct_5 = 3.54$, $ct_{10} = -0.28$, $cp_6 = -1.90$, $cp_7 = 144.73$, $cp_8 = -12.69$, $cp_9 = 0.79$, $cp_{10} = 2.05$, $cp_{11} = 9.61$, and $cp_{18} = 5.02$. The results in figure 9.7 demonstrates an excellent alignment with the scaling equations for both thrust and power. This further builds confidence on the versatility and robustness of the derived scaling laws to assess the propulsive performance of a variety of multi-foil schooling configurations.

9.4 Summary

This chapter presents a novel approach in developing physics-informed scaling relations that accurately estimate the propulsive performance metrics of pitching foils in various schooling formations. Building on the existing scaling laws established for single oscillating foils, this research extends their applicability to multi-foil systems by incorporating the intricate dynamics of foil-foil interactions. Our analysis considers vortex-induced velocities, imposed by a foil through its circulation on the other foils in the system. The vertical component of the induced velocity is anal-

ogous to the heaving motion, suggesting that pitching foils in multi-foil systems can be treated as simultaneously heaving and pitching bodies. The scaling relations unveil a novel, physics-based methodology for two or more oscillating foils, exhibiting outstanding agreement with numerical simulations. These relations account for the influence of the positioning of foils, phase differences between them, and the amplitudes and frequencies of oscillations. By providing a deeper understanding of the fundamental flow physics of schooling foils, the derived relations are expected to play a crucial role in offering vital insights for the design and optimization of more effective underwater propulsive and energy harvesting systems, thereby fulfilling Objective B. Despite these insights, there remains a need for a comprehensive investigation that categorizes the vortex topologies behind parallel foils and elucidates the fundamental physics governing the wake interactions. Therefore, these critical aspects are addressed in the forthcoming chapter.

Chapter 10

CLASSIFICATION OF VORTEX PATTERNS[†]

Bio-inspired engineering presents a novel strategy for developing highly efficient and advanced engineering systems by emulating the naturally optimized physical forms and functions of biological entities. A quintessential example of this is observed in the ability of flapping insect wings to generate leading-edge vortices and keep them attached on their wing surfaces, even under steep angles of attack. This ability is crucial for generating unsteady aerodynamic forces, granting them exceptional hovering and maneuvering capabilities (Ellington et al., 1996; Sane, 2003). Thus, unraveling the physical mechanisms employed by natural species is essential for engineering advanced propulsion systems.

While prior chapters have illustrated the formation of vortex patterns behind parallel foils, a detailed quantitative analysis of vortex interactions within the wake remains to be addressed. This chapter delves into the merged-separate characteristics of the vortex streets behind pitching foils placed in side-by-side configuration. To this end, a wide range of parameter space, including Strouhal number, phase difference, oscillation amplitude, and separation distance is investigated.

[†]The content of this chapter has been published in whole or part, in *J. Fluid Mech.* with the citation: "Gungor, A., Khalid, M.S.U., & Hemmati, A., (2022) Classification of vortex patterns of oscillating foils in side-by-side configurations *J. Fluid Mech.*, 951, A37."

Outcomes of this chapter aim to strengthen our knowledge of the governing flow physics and control techniques for novel underwater propulsors operating in schooling configurations to attain superior swimming performance. Therefore, this chapter sheds light to three novel points that are currently missing in literature: (i) quantification and classification of vortex patterns behind two parallel pitching foils, (ii) physical mechanisms, governing the wake merging phenomenon, and (iii) influence of the merger on propulsive performance of the system. For this purpose, this chapter is structured as follows. Details of the problem is explained in section 10.1. Section 10.2 includes the results on the wakes of parallel foils and discussions concerning the vortex patterns and wake merging phenomena, which is followed by main conclusions in section 10.3.

10.1 Problem Definition

A wide range of parameter space is utilized to provide a comprehensive classification for wake topology behind parallel oscillating foils. Phase difference between the foils is varied from in-phase ($\phi = 0$) to out-of-phase ($\phi = \pi$) with increments of $\pi/6$, and pitching amplitude is fixed at 8°. However, simulations with $\theta_0 = 5^\circ$, 11°, and 14° also performed for selected cases in order to ensure the validity of the analysis over a range of the pitching amplitude. This analysis reveals that classification of the wake topology remains consistent, while the ranges at which each topology is observed may differ with changing amplitude. This, however, would not concern the core analyses in the current study. The Reynolds number of the flow is fixed at $Re = 4000$. The separation distance between the foils (y^*) is varied from $0.5c$ to $2.5c$ with increments of $0.5c$. St ranges from 0.15 to 0.5 for each value of y^*. The St space covers the formation of BvK, reverse BvK, and reverse BvK regimes in the wake of single oscillating foils (Godoy-Diana et al., 2008) and natural swimming St of various fish species (Triantafyllou et al., 1993). The extent of the parameter space used in the study is summarized in table 10.1.

Table 10.1: Parametric space of the chapter.

y^*	ϕ	θ_0	St	Re
$0.5-2.5c$	0	8°	$0.15-0.5$	4000
$1c$	$0-\pi$	8°	$0.15-0.5$	4000
$1.5c$	0	$5^\circ-14^\circ$	$0.15-0.5$	4000

10.2 Results and Discussion

We begin our analysis with examining vortex dynamics and wake interactions of parallel pitching foils. In chapter 4, we examined transient wake developments of foils, performing in-phase and out-of-phase pitching in side-by-side configurations for $St = 0.15-0.5$ and $y^* = 1c$ at $Re = 4000$. It was demonstrated that wake structures at low St showed quasi-steady characteristics and were in perfect agreement with the findings of Dewey et al. (2014), i.e., merging symmetric wake for in-phase pitching and diverging symmetric wake for out-of-phase pitching foils. However, wake structures and propulsive performance of both in-phase and out-of-phase pitching foils were observed to be highly transient at high St. The wake of in-phase pitching foils initially consisted of two deflected vortex streets parallel to each other. These streets merged after some time and formed a symmetric wake. The merging process coincides with the enhancement in time-averaged thrust and efficiency of the foils. The opposite phenomena was observed in the wake of out-of-phase pitching foils. The foils initially produced diverging symmetric wakes whose symmetry was broken after several oscillation cycles. Here, we expand the parametric space to classify vortex patterns, which elucidate active flow control techniques possibly employed by natural swimmers, to gain a desired hydrodynamic performance. Furthermore, we also present a quantitative explanation for underlying physical mechanisms of the wake merging phenomenon.

10.2.1 Classification of Vortex Patterns

We identify three distinct vortex patterns in the wake of parallel pitching foils (side-by-side configuration) for the given parametric space. Merged−separated characteristics of the wakes were taken

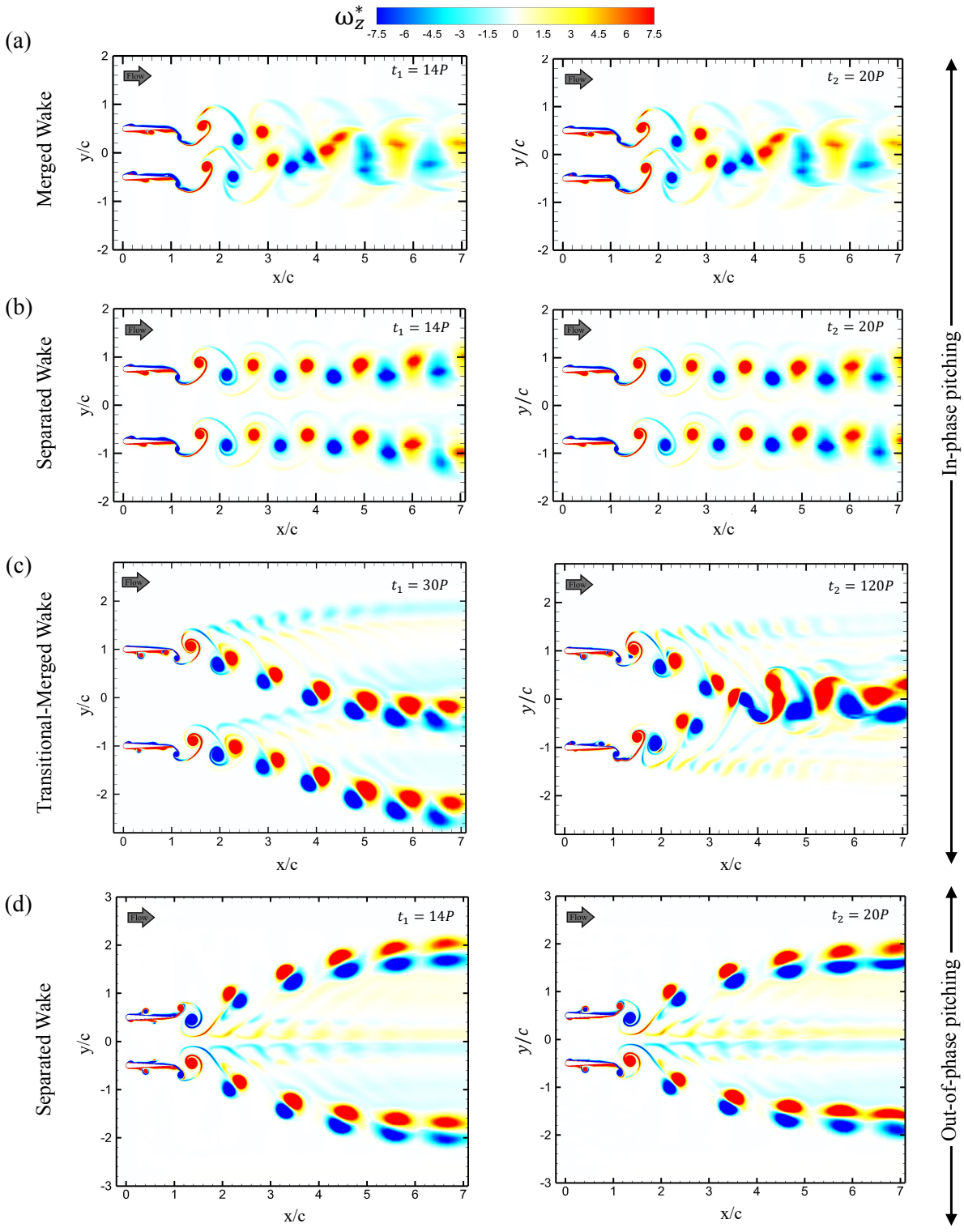

Figure 10.1: Contours of spanwise vorticity ($\omega_z^* = \omega_z\, c/U_\infty$) of parallel foils for (a) $St = 0.25$ and $y^* = 1c$ (merged wake), (b) $St = 0.3$ and $y^* = 1.5$ (separated wake), (c) $St = 0.5$ and $y^* = 2c$ (transitional-merged wake), and (d) $St = 0.4$ and $y^* = 1c$ (separated wake) at different time instants for in-phase and out-of-phase pitching.

into consideration when classifying the wake in figure 10.1. Here, a merged wake corresponds to the vortex topology that involves the vortex streets shed by upper and lower foils merging in mid-wake and forming a single street, which constitutes a new flow configuration. In separated wakes, on the other hand, upper and lower vortex streets do not amalgamate with each other. Separated wakes of in-phase pitching foils consist of two parallel vortex streets whereas “v-shaped" diverging configuration is observed in the separated wakes of out-of-phase pitching foils (see figure 10.1b and 10.1d). In both merged and separated wakes, vortex patterns are formed within several pitching cycles and their merged−separated features remain unchanged during the next oscillation cycles without altering significantly (compare $t_1 = 14P$ and $t_2 = 20P$ of figure 10.1a, 10.1b, and 10.1d, where P is period of the pitching cycle). Note that out-of-phase pitching foils at $St = 0.5$ experience symmetric to asymmetric transition (see figure 4.5b). However, its wake remains separated throughout the process. Conversely, transitional-merged wakes undergo distinct separation and merging stages, primarily transitioning from the former to the latter configuration. As explained earlier, oscillating foils produce deflected *BvK* vortex streets at considerably high St. In the wake of in-phase pitching parallel foils, interaction between vortex streets shed by each foil results in the constitution of the symmetric wake, in which upper and lower wakes amalgamate around the centerline. (see figure 10.1c). The pitching cycle, in which the merging takes place, greatly depends on y^* and St (see table 10.2). For the sake of comparison, the merging process of the wakes occurs around 22nd cycle for $y^* = 1c$ and $St = 0.5$, whereas more than 75 cycles are needed for this phenomenon to occur for $y^* = 2c$ and $St = 0.5$. These vortex patterns were gathered in a $St - y^*$ phase diagram in order to provide a thorough classification of the wakes of in-phase pitching parallel foils in figure 10.2a. In this diagram, separated and merged wakes are observed in upper ($y^* \geq 1.5c$) and lower ($y^* \leq 1c$) regions of the diagram, respectively. On the other hand, transitional-merged wakes fall into the high St region. It is important to note that this type of wakes are formed only at sufficiently high St that facilitate the formation of deflected wakes. The relation between the deflection phenomena, and wake merging is further explained in the next part of this section. Furthermore, another diagram, explaining the wake topology of parallel foils for varying phase

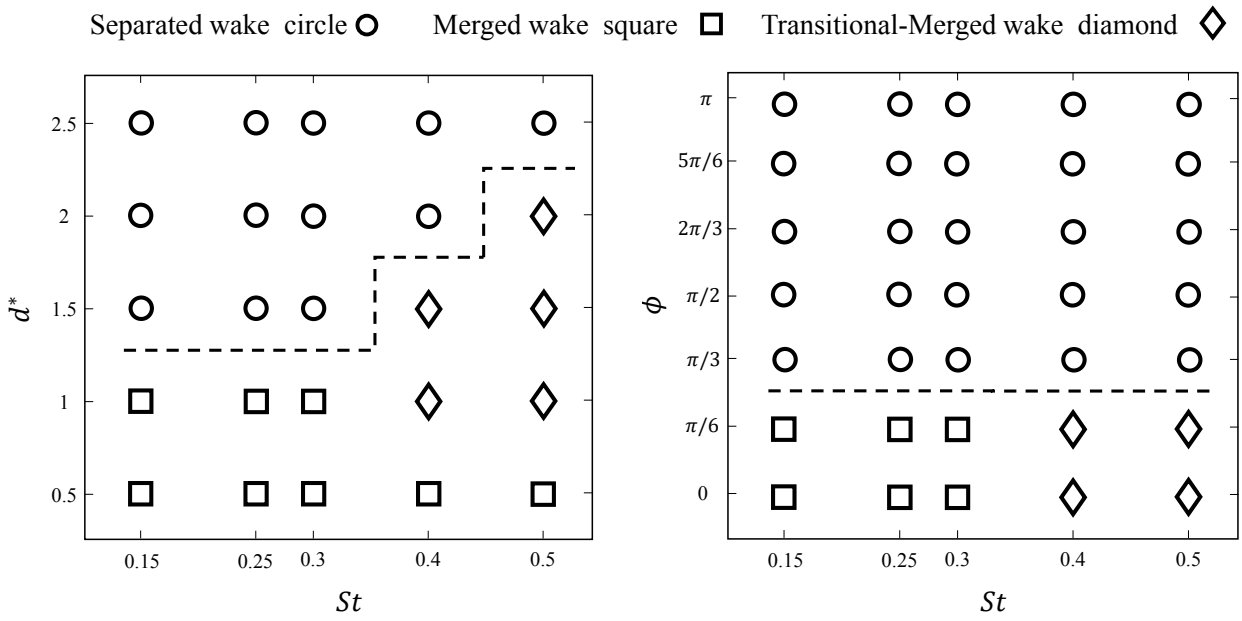

Figure 10.2: Classification of the wake patterns of foils in side-by-side configuration for $Re = 4000$ (a) at a range of separation distance and Strouhal number for in-phase pitching (b) at a range of phase difference and Strouhal number for $y^* = 1c$. Dashed lines correspond to the boundary that distinguished merged and separated wakes.

difference and Strouhal number at fixed separation distance of $1c$, is presented in figure 10.2b. Vortex patterns display strong dependence to phase difference. For $\pi/3 \leq \phi \leq 5\pi/6$, parallel foils constitute separated wakes for each St examined here, which resemble separated wakes of out-of-phase oscillations, i.e., diverging vortex pattern. On the other hand, merged wakes at $\phi = \pi/6$ do not fundamentally differ from those formed by in-phase oscillating foils. Results for intermediate phase difference are not presented here for brevity, because they yields similar conclusions.

Thereafter, we present quantification of important characteristics of the wakes and propose a model that distinguishes emerging vortex patterns. At this point, it is important to recall the dipole model by Godoy-Diana et al. (2009), which presented a quantitative threshold for the wake deflection behind a single oscillating foil. This model also remains valid for the wake of undulating foils (Khalid et al., 2020). The wake of oscillating foils, consisting of a reverse *BvK* vortex street, is dominated by shedding of a counter-clockwise (positive sign) and a clockwise (negative sign) vortex per oscillation cycle. These vortices are located slightly above and below the centerline,

respectively (Koochesfahani, 1989). The structure formed by these two vortices is called a dipole. Circulations of the vortices in a dipole induce velocity normal to the line that connects the vortex centers as described by the two-dimensional Bio-Savart rule (Naguib et al., 2011). When the self-advection velocity of the dipole is strong enough, it diverts the dipole from the centerline, which is followed by the consecutive dipoles. Therefore, the model was based on the offset between advection velocity of the propulsive wake, i.e., U_{phase}, and self-induced translation velocity of the dipole, i.e., U_{dipole}. They can be mathematically defined as follows:

$$U_{phase} = dX_i/dt, \tag{10.1}$$

$$U_{dipole} = \Gamma/2\pi b, \tag{10.2}$$

where X_i is the x-coordinate of a vortex core, Γ denotes the average of magnitudes of circulation of counter-rotating vortices, and b represents the distance between the centers of the vortices (see figure 10.3a). Circulation (Γ) is computed either from a line integral of the velocity field or from a surface integral of voricity over the area bounded by a closed curve. Godoy-Diana et al. (2009) used a rectangular frame, whose size was determined by Gaussian fit, to extract the boundary of each vortex towards calculating Γ. However, this method has a downside of potential numerical errors due to the possibility that rectangular frames may include counter-rotating vortices, particularly in the case of structures traversing in close proximity of one another. Therefore, we use a non-predefined closed curve to accurately capture each vortex proposed earlier by Khalid et al. (2020), which eliminates this error in computing Γ. The boundary of the curve is defined such that it only encompasses the region with magnitude of vorticty (ω) greater than 10% of its value in the flow field. Then, we determine the circulation of each vortex by calculating the line integral of the velocity field around the curve using the following definition:

$$\Gamma = \oint V \cdot dl, \tag{10.3}$$

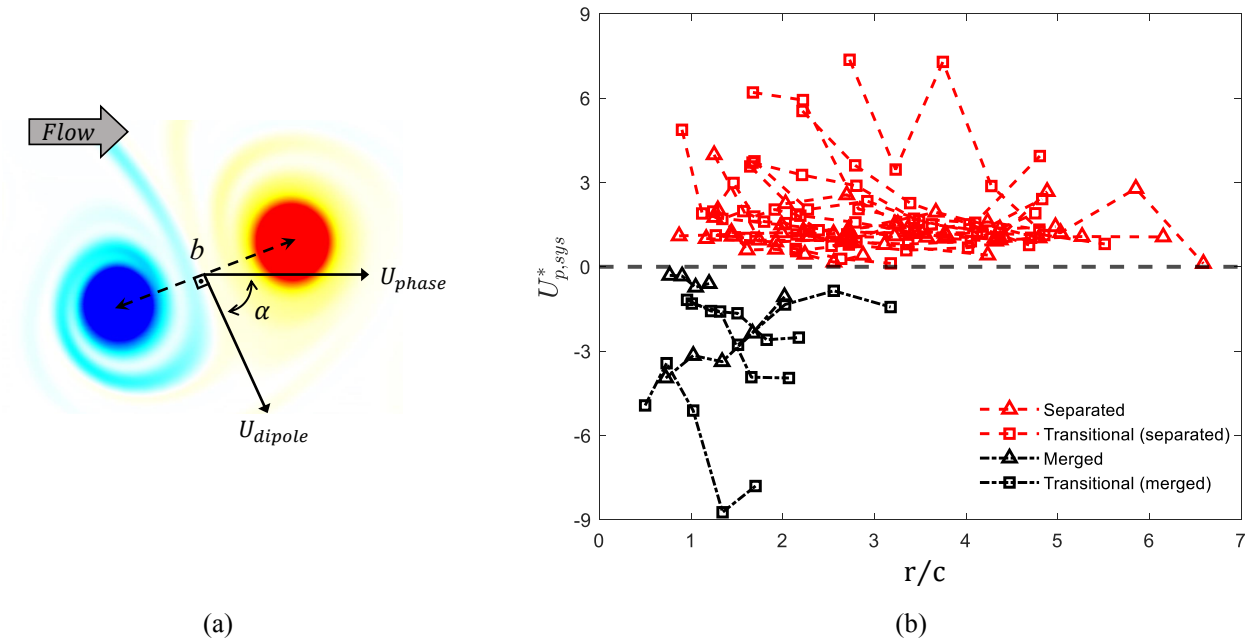

(a) (b)

Figure 10.3: (a) Demonstration of the parameters used in the proposed model. (b) Effective phase velocity of the coupled vortex system with respect to radial displacement of the dipoles.

where V is the velocity, and dl is the infinitesimal length. This method ensures that circulation is computed without any penetration by a neighboring vortex with oppositely-signed vorticity. Hence, regions in which circulations of positive and negative vortices are calculated are entirely separated from each other by non-predefined boundaries around these coherent flow structures.

For the effective phase velocity (U_p^*), Godoy-Diana et al. (2009) defined it in the following manner that yields positive values for deflected wakes:

$$U_p^* = (U_{phase} - U_\infty)cos\alpha^* - U_{dipole}, \tag{10.4}$$

where α^* is the angle between U_{phase} and U_{dipole} as presented in figure 10.3a. Here, we present a model that distinguishes different classes of vortex patterns using U_p^*. Although the model of Godoy-Diana et al. (2009) successfully predicts whether the wake is deflected behind an isolated oscillating foil, but it cannot identify the nature of vortex patterns, i.e., merged or separated, for multiple parallel foils, forming complex wakes in close proximity of one another. In order to con-

struct an effective mathematical model, our current work focuses on differentiating merged and separated wakes and supplying information about the direction of their deflections. To illustrate it further, in-phase pitching transitional-merged wake at $St = 0.5$ and $y^* = 2c$ exhibits deflection during each stage of wake development. During the separated stage at $t_1 = 30P$, both top and bottom wakes are deflected downwards, whereas the wake fully transitions to that of a merged configuration at $t_2 = 90P$. In the latter stage, upwards deflected bottom vortex street and downwards deflected top vortex street is observed (see figure 10.1c). However, the model proposed by Godoy-Diana et al. (2009) cannot distinguish the vortex patterns for these configurations since all the cases consist of deflected wakes. Similarly, separated wake with deflected vortex streets at $St = 0.4$ and $y^* = 2c$ (see figure 10.4a) and separated wake with horizontal vortex streets at lower St and $1.5c \leq y^* \leq 2.5c$ (e.g. figure 10.1b) are treated disparately by the model, although, they are all classified as separated wake. Thus, we introduce the term $\sin\alpha^*$ to the formulation to take the direction of deflection into account, because $\sin\alpha^*$ yields positive values for upwards wakes and negative values for downwards and non-deflected wakes. Moreover, weight factor term, W_i, which yields -1 for diverging separated wakes and 1 for the rest is incorporated into the equation to distinguish the separated wakes of out-of-phase pitching parallel foils. Hence, the *effective phase velocity of the coupled vortex system* or $U^*_{p,sys}$ can now be defined as follows:

$$U^*_{p,sys} = \frac{U^*_{p,upper} \sin\alpha^*{}_{upper}}{U^*_{p,lower} \sin\alpha^*{}_{lower}} W_i \tag{10.5}$$

Here, W_i is the wake weighting function defined as

$$W_i = \begin{cases} 1, & \text{small } \beta \ (|\beta| < \beta^*/\varkappa) \\ sin(\beta)/|sin(\beta)|, & \text{large } \beta \ (|\beta| \geq \beta^*/\varkappa) \end{cases} \tag{10.6}$$

where $\beta = \alpha^*_{lower} - \alpha^*_{upper}$ and $\beta^* = |\alpha^*_{lower}| + |\alpha^*_{upper}|$. Here, $\varkappa$ denotes a positive number, which helps setting up a threshold for different classes of wakes under a broad range of kinematic pa-

rameters. We examine the performance of this weight factor term with $\varkappa = 5$, 7.5, and 10, and all these values serve the purpose very well.

Equation 10.5 yields negative $U^*_{p,sys}$ values for merging wakes, whereas separated wakes produce positive $U^*_{p,sys}$. The model requires U^*_p and $\sin\alpha^*$ for the upper and lower vortex dipoles (see figure 10.4a) that are shed in the same pitching cycle. Although it can be calculated at a certain location, it is preferred to trace these dipoles as they move in the downstream direction. It helps demonstrate that the model is not limited to a specific location but is valid for the whole domain. Figure 10.3b shows variations in $U^*_{p,sys}$ for separated, merged, and transitional-merged wakes with respect to the radial displacement given by $r = \sqrt{(X_1 - X_0)^2 + (Y_1 - Y_0)^2}$, where X_1 and Y_1 define an instantaneous location of a vortex core. Moreover, X_0 and Y_0 provide the location of the vortex core just after its detachment process from the foils is completed. Note that a geometric mean of the respective quantities for the counter-rotating vortices is used as the location of the dipole. Because the counter-rotating vortices are shed alternatively from each foil, it is also important to mention that each dipole is formed by those two counter-rotating vortices that have smaller distance between their centers. It is evident from the plot in figure 10.3b that the proposed model successfully differentiates between separated and merged wakes for the given parametric space.

In this model, separated and merged stage of transitional-merged wakes are treated individually and marked with different colors, since these stages are contradictory to one another in terms of their vortex configuration. It is important to note that merged wake cases are tracked for relatively short radial displacement, i.e., $r/c \leq 3$. This is because their upper and lower vortex streets merge at mid-wake, which inhibits further tracking. However, dipoles of the separated wakes are traceable until circulation of the vortices shrink to negligible values due to the viscous diffusion around $r/c = 5$. To clarify the working mechanism of the model, U^*_p of merged wakes (see figure 10.1a or figure 10.1c at $t_2 = 90$) yields positive values for both bottom and top vortex streets as they are deflected upwards and downwards, respectively. Furthermore, $\sin\alpha^*$ for top and bottom wakes switch signs ($\sin\alpha^* < 0$ for top and $\sin\alpha^* > 0$ for bottom), which results in $U^*_{p,sys} < 0$. On the other hand, horizontal vortex streets in the separated wakes (see figure 10.1b) have $U^*_p < 0$ and

$\sin\alpha^* < 0$, thus leading to $U^*_{p,sys} > 0$. The separated wake, whose vortex streets are deflected (see figure 10.4a), or transitional-merged wake at separated stage (see figure 10.1c at $t_1 = 30P$) yield $U^*_p > 0$ and $\sin\alpha^* < 0$, which translates to $U^*_{p,sys} > 0$. Finally, diverging separated wakes whose vortex streets are deflected in opposite directions yield positive values for U^*_p and opposite signs for $\sin\alpha^*$ ($\sin\alpha^* > 0$ for top and $\sin\alpha^* < 0$ for bottom). However, it gets -1 from the weight factor since $\beta = \alpha^*_{lower} - \alpha^*_{top} < 0$, which translate into $U^*_{p,sys} > 0$.

The classification and mathematical modeling of the vortex patterns presented here is developed for $Re = 4000$. However, it relies on kinematic quantities of coherent structures in the wake, such as the angle between vortex cores, circulation of vortices, and phase velocity of dipoles. Therefore, it is expected to work well for low and medium Re ranges considering all the flow topologies, i.e., von Karman street, reverse von Karman street, and deflected von Karman street, observed for $10 \leq Re \leq 2000$ (Das et al., 2016) already covered in the analysis. It is noteworthy to state that the coherent structures remain the same even though the wake transitions to $3D$ at $Re = 8000$ (Verma and Hemmati, 2021). A similar argument can be made for the range of oscillation amplitude. Patterns of the coherent structures behind oscillating foils for a range of oscillation amplitude (Godoy-Diana et al., 2008; Das et al., 2016) do not fundamentally differ from the ones considered in the current study. This suggests that wakes of oscillating foils at different oscillating amplitudes can be classified and mathematically modeled using the presently proposed procedure. In an effort to test this, we also simulate cases for $\theta_0 = 5^\circ, 11^\circ$, and 14° at a range of St for $y^* = 1.5c$. Their wakes display characteristics of one of the three vortex patterns examined above: separated wake, merged wake, or transitional merged wake. Furthermore, equation 10.5 performs excellently in distinguishing different topologies of the wake. Nevertheless, these results are not shown here for brevity.

10.2.2 Mechanism of Wake Merging

After establishing a mathematical model to quantitatively identify and characterize different wake patterns behind pitching foils in side-by-side (parallel) configuration, we focus our attention to

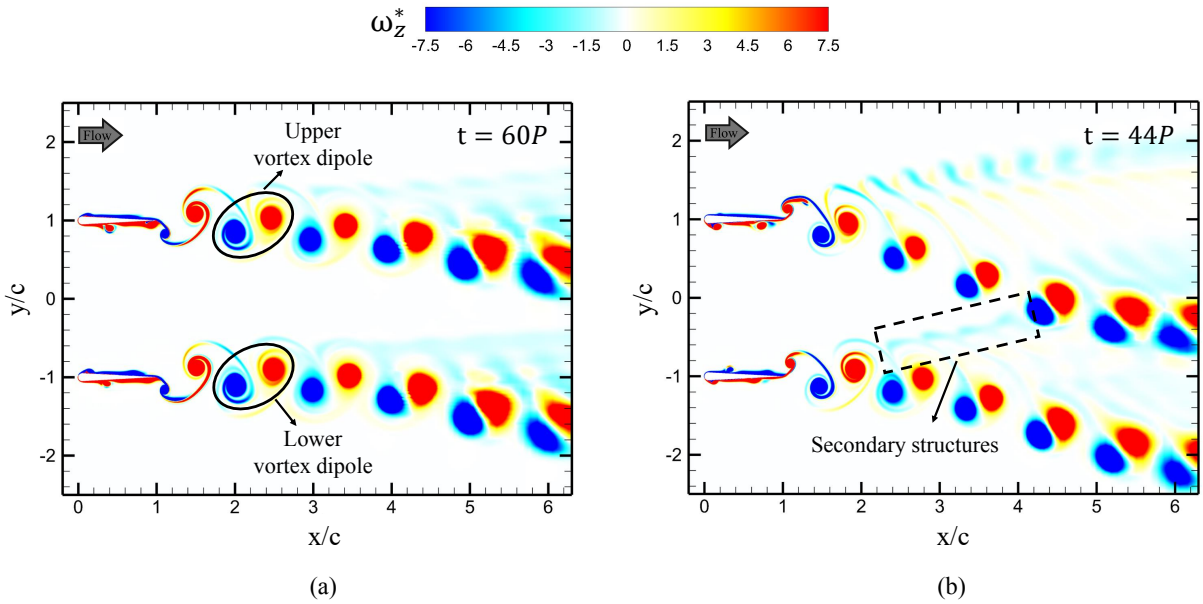

Figure 10.4: Contours of spanwise vorticity ($\omega_z^* = \omega_z\, c/U_\infty$) of in-phase pitching parallel foils at $y^* = 2c$ for (a) $St = 0.4$ (separated wake) and (b) $St = 0.5$ (transitional-merged wake) at different time instants.

identify and explain the mechanism of wake merging. To this effect, we analyze primary transitions in the wake of in-phase pitching foils by associating it with the production and dynamics of secondary vortex structures. When an oscillating single foil produces a deflected wake, secondary structures appear from the primary vortex street to move away from the direction of deflection. Such secondary structures were also observed in the experiments of Godoy-Diana et al. (2008) and Jones et al. (1998) and numerical simulations of Liang et al. (2011). But no further analyses were conducted for this important feature of the wake dynamics. These structures are considerably weaker in their relative strength compared to those in the main street, which is why they have not received adequate attention in literature. We hypothesize that secondary structures play a key role in the merger of upper and lower vortex streets behind parallel oscillating foils. Figure 10.4a shows a separated wake of the foils for the case of $St = 0.4$ and $y^* = 2c$ at $t = 60P$. Even though secondary structures are present in the wake, structures from the lower wake are convected in the downstream direction before reaching the upper wake. At $St = 0.5$ and $y^* = 2c$, in which wakes are merged, however, these secondary structures from the lower foil deflect upward to interact with

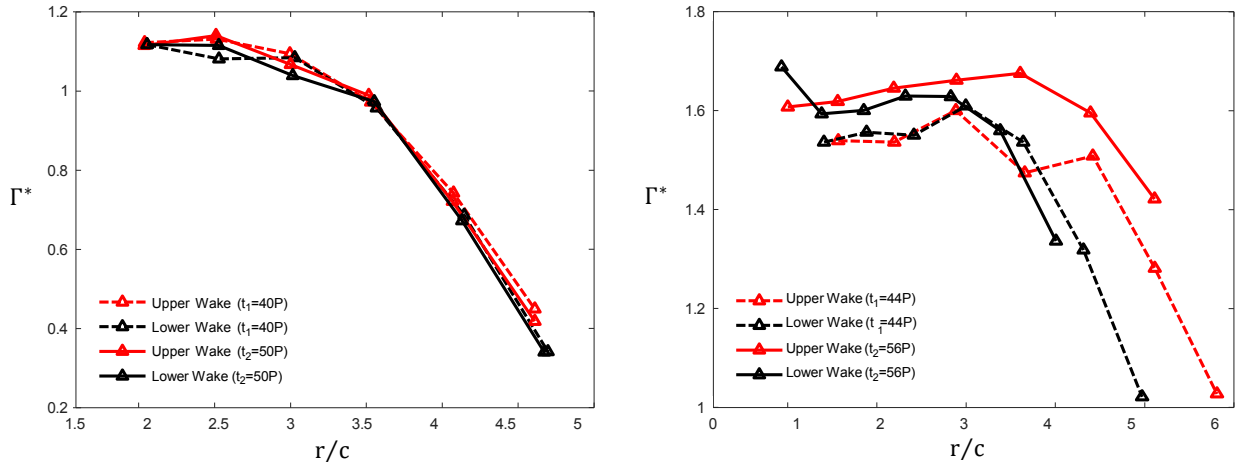

(a) (b)

Figure 10.5: Magnitude of non-dimensional circulation ($\Gamma^* = \Gamma/U_\infty\, c$) of negative vorticity of upper and lower vortex streets at $y^* = 2c$ for (a) $St = 0.4$ (separated wake) and (b) $St = 0.5$ (transitional-merged wake before the merger) at different time instants for in-phase pitching.

primary street of the upper foil, traversing downward (see figure 10.4b). These observations hint that this interaction triggers the wake merging process, because constructive or destructive interference of secondary vortices with the bigger coherent structures change their strengths in terms of circulation (Zhu et al., 2002; Akhtar et al., 2007; Khalid et al., 2021b,a). Furthermore, onset of the complete wake merging appears located very close to the point of interaction between secondary structures and primary street. For instance, secondary structures shed by the lower foil at $St = 0.5$ and $y^* = 2c$ catch the upper main vortex street at $x/c \approx 4$, which coincides with the location for the merging of wakes (see figure 10.1c). Likewise, both the interactions between secondary structures and the upper wake as well as the merging of upper and lower wakes occur at $x/c \approx 3.6$ for $St = 0.5$ and $y^* = 2c$ (see table 10.2). The alignment of spatial merging location and that of vortex interactions strengthens our argument on the role of these smaller structures in initiating and facilitating the wake merging process.

We proceed with providing another quantitative explanation to the impact of secondary structures on the overall wake dynamics. In this manner, locations and circulation of vortex dipoles are traced in the wake to provide evidence for the impact of secondary structures. Figure 10.5 exhibits the change of Γ for negative vortices associated with separated ($St = 0.4$ & $y^* = 2$) and

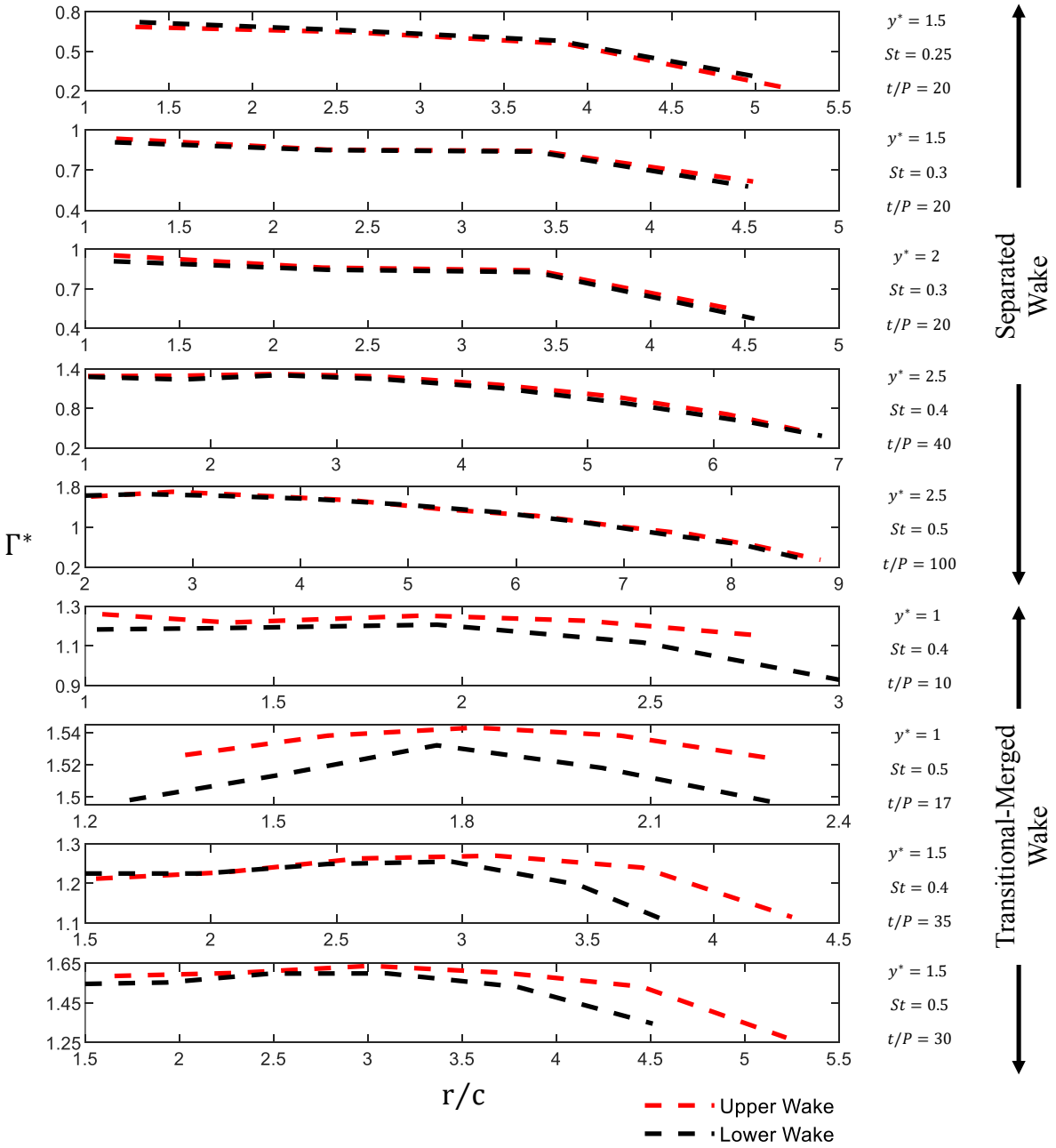

Figure 10.6: Magnitude of non-dimensional circulation ($\Gamma^* = \Gamma/U_\infty\, c$) of negative vorticity of upper and lower vortex streets for transitional-merged wakes before the merger and separated wakes for in-phase pitching.

transitional-merged ($St = 0.5$ & $y^* = 2c$) wakes, as dipoles move downstream. For the transitional-merged wake (figure 10.5b), circulation of the negative vortices of upper and lower wakes overlap in the near wake region. However, proximity in this sense is broken in favor of the upper wake, after which there is constructive interference of secondary structures with negative vorticity at $r/c \approx 3.5$. This observation remains valid at different time instants. Non-dimensional circulation at $t_1 = 44P$ and $t_2 = 55P$ is presented in figure 10.5b. On the contrary, there exists no significant difference in circulation of the upper and lower wakes for the separated wake (figure 10.5a), because the secondary structures have no influence on the upper wake. Similarly, wakes at $t_1 = 40P$ and $t_2 = 50P$ show that this trend is independent of the wake evolution and time. It is apparent that enhancement of the negative vorticity of the upper wake due to the influence of the secondary structures causes alterations in deflection of the vortex street (see equation 10.2 and 10.4). It eventually results in the primary wake transition, i.e., merger of the wakes. We also notice that relatively weaker and smaller secondary structures compared to the primary vortices could be the reason for gradual merging of the vortex streets in transitional-merged wakes. As illustrated in figures 10.5 and 10.6, they have a delicate but significant effect on the upper vortex street, which may result in the crawling merging process. Therefore, the dynamics of secondary structures only account for the merging mechanism and physical process, while the discussion in section 10.2.1 outlines the mathematical model to effectively categorize the wake patterns. Furthermore, circulation of negative vortices of the upper and lower wakes is computed for other separated wakes and transitional-merged wakes to support this explanation for this mechanism. It is evident from figure 10.6 that our illustration stays valid for all transitional-merged wake cases investigated in this study.

10.2.3 Effect of Wake Merging on the Propulsive Performance of the System

We now focus on the relationship between propulsive performance of in-phase pitching parallel foils (side-by-side configuration) and primary transitions in the wake by assessing the cycle-averaged performance metrics. Figure 10.7 shows temporal variations of the coefficients of thrust

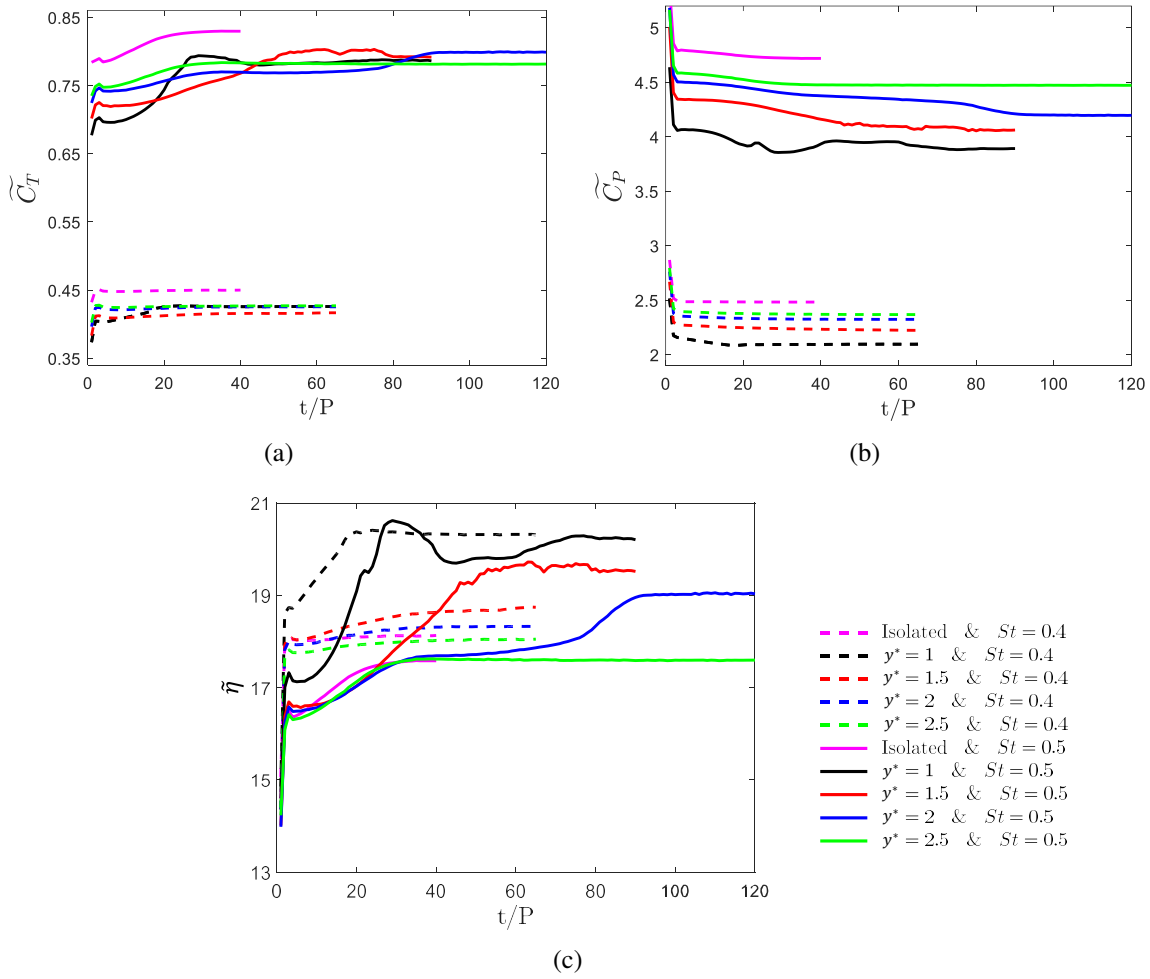

Figure 10.7: The variation of cycle-averaged (a) thrust and (b) power coefficients, as well as (c) efficiency of the system (averaged using Foil 1 and Foil 2), and the isolated foil in time at a range of St and y^* for in-phase pitching.

and power, as well as efficiency at a range of St and y^* for the system (average of Foils 1 and 2) and an isolated foils. The performance parameters of this dynamical system are examined for a large number of oscillation cycles, i.e., until the cases reach quasi-steady conditions for their propulsion. This translates into 40 cycles for isolated cases, 65 cycles for cases with $St = 0.4$, 90 cycles for $y^* = 1c$ & $St = 0.5$ and $y^* = 1.5c$ & $St = 0.5$, and 120 cycles for $y^* = 2c$ & $St = 0.5$ and $y^* = 2.5c$ & $St = 0.5$. Figure 10.7 covers all transitional-merged wakes observed in the current study as well as separated wakes, i.e. $St = 0.4$ and $y^* = 2c$, $St = 0.4$ and $y^* = 2.5c$, $St = 0.5$ and $y^* = 2.5c$, and isolated foils' wakes. In this section, we aim at establishing the impact of

Table 10.2: Streamwise location (x/c) and time instant (t/P) in which the wake merging occurs as well as the percent improvement in the cycle-averaged coefficient of thrust ($\Delta\widetilde{C_T}$) for separated and transitional-merged wake cases at $St = 0.4$ and $St = 0.5$.

	$St = 0.4$			$St = 0.5$		
	$y^* = 1c$	$y^* = 1.5c$	$y^* = 2c$	$y^* = 1c$	$y^* = 1.5c$	$y^* = 2c$
x/c	2.7	4.7	–	2.5	3	3.6
t/P	15	49	–	22	36	78
$\Delta\widetilde{C_T}$	5.15%	1.83%	0.95%	12.60%	10.77%	7.52%

unsteady alterations in wake dynamics on the propulsive performance of the system. Thus, parameters for cases with lower St, i.e., $St \leq 0.3$, are not presented here as they display no significant wake transitions. In chapter 4, it is demonstrated that parallel foils generates highly quasi-steady performance and wake characteristics for lower St at $y^* = 1$. With this background, it is further noticed in the present study that the same attributions persist for other separation distances examined here. Power requirements of the system marginally vary in time, which translates into resembling trends for the cycle-averaged coefficient of thrust and efficiency. The percent improvement in thrust ($\Delta\widetilde{C_T}$) is given in table 10.2 together with the location and time instant of the wake merging. $\Delta\widetilde{C_T}$ is calculated between 5th cycle and the cycle in which the thrust coefficient reaches quasi-steady conditions, e.g., 90th cycle for $y^* = 1c$ & $St = 0.5$, 120th cycle for $y^* = 2c$ & $St = 0.5$. The first 5 cycles are disregarded, considering that the performance metrics of steady cases require 5 cycles to converge as shown in chapter 4. It is evident from figure 10.7a that the generated thrust by transitional-merged wakes improves with time and reaches a steady-state after the primary transition in the wake is established. This indicates that the wake merging process could be a contributing factor for thrust enhancement. Furthermore, it is important to note that the separated wakes presented here ($St = 0.4$ & $y^* = 2c$, $St = 0.4$ & $y^* = 2.5c$, and $St = 0.5$ & $y^* = 2.5c$) experiences trivial alterations in propulsive performance parameters, which further supports our

argument. Thus, we affirm that merging of these wakes improves propulsive thrust of the system by increasing thrust generation through amplification of the circulation associated with amalgamated vortices around the mid-wake. This results in the formation of high momentum jet on the centerline.

There are two consequential inferences from figure 10.7 and table 10.2, which strengthens our argument. First, the time instance of peaks in thrust variation lags the instant of wake merging process. For example, thrust generation for the case of $St = 0.5$ and $y^* = 1c$ has its maximum at $t/P = 29$, whereas its wake merging occurs at $t/P = 22$. Second, thrust enhancement in the system decreases as the streamwise location of the onset of wake merging moves downtream. This is due to the reduction in circulation of the dipoles as they travel downstream the wake (see figures 10.5 and 10.6). When upper and lower vortex streets merge in closer proximity to the foils, amalgamated vortices have greater circulation. This causes an increased momentum jet that is induced by the vortex street. This is consistent with insignificant improvements in thrust for the case of $St = 0.4$ and $y^* = 1.5c$, whose wake merging occurs farther in the wake, i.e., increased distance from the foils.

Propulsive performance metrics of isolated pitching foils are also presented in figure 10.7. This data is tracked for 40 oscillation cycles, negligible alterations are witnessed after 20 oscillation cycles. Note that a single foil with $St = 0.4$ and 0.5 forms deflected wakes with quasi-steady characteristics although it is not demonstrated here for brevity. This range of St agrees well with the threshold St for wake deflection shown in other studies (Jones et al., 1998; Godoy-Diana et al., 2008; Deng et al., 2015, 2016; Das et al., 2016). Pitching foils in side-by-side configurations exhibit superior performance compared to a solitary foil. Although parallel foils with all separation distances produce less thrust compared to a foil in isolation, they require substantially less power. This results in improved efficiency for parallel foils. Similar findings are also presented by Huera-Huarte (2018) and Dewey et al. (2014). It is worth mentioning that efficiency of an isolated foil at $St = 0.4$ does not substantially differ from the case with separated wakes ($y^* = 2c$ and $y^* = 2.5c$). Likewise at $St = 0.5$, an isolated foil attains similar efficiency with a transitionally merged wake

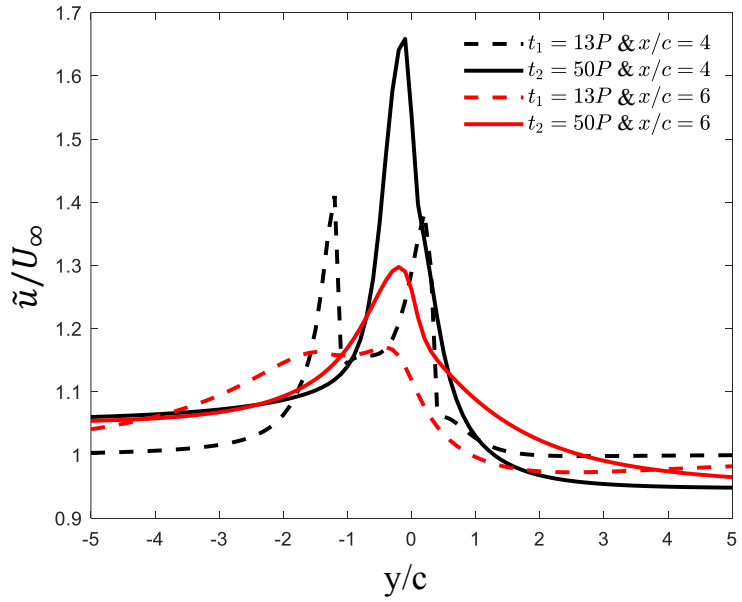

Figure 10.8: Cycle-averaged streamwise velocity ($\widetilde{u}$) profiles of in-phase pitching foils, normalized by U_∞, obtained from the finite-core vortex array model for $St = 0.5$ and $y^* = 1c$ at different time instants ($t_1 = 13P$ and $t_2 = 50P$) and streamwise locations ($x/c = 4$ and $x/c = 6$).

($y^* = 2c$) when it is not merged ($t/P \leq 78$) and a separated wake ($y^* = 2.5c$). On the other hand, efficiency of the two parallel foils, in which the primary wake transition occurs, is greater than an isolated foil for the same St. These observations imply that interactions of wakes favorably impact the performance of these complex dynamical system.

We now proceed with implementing the finite-core vortex array model to our wake data, following Naguib et al. (2011). This model suggests that velocity profiles in the wake can be determined by superimposing finite amount of vortex cores onto a uniform flow. Streamwise and transverse velocity profiles that induced by superposition of N vortices can be determined using:

$$u(x,y) = U_\infty - \sum_{i=1}^{N} \frac{\Gamma_i(r_i)}{2\pi} \frac{(y - y_{ci})}{r_i^2}, \tag{10.7}$$

$$v(x,y) = \sum_{i=1}^{N} \frac{\Gamma_i(r_i)}{2\pi} \frac{(x - x_{ci})}{r_i^2}, \tag{10.8}$$

where r_i is the radial distance from i^{th} vortex center to the point of calculation, and x_{ci} and y_{ci} are the

streamwise and transverse location of the center of the i^th vortex, respectively. The model requires the number of vortices greater than or equal to 10 in order to converge (Naguib et al., 2011). To this end, locations and circulations of vortices within the range of $3 \leq x/c \leq 7$ are measured for $St = 0.5$ and $y^* = 1c$ at $t_1 = 13P$ (separated stage) and at $t_2 = 50P$ (merged stage). The St and y^* of the flow are selected, considering it yields the highest percent improvement in thrust production (see figure 10.7 and table 10.2). Moreover, the range of execution is determined considering that the wake merging occurs following $x/c = 2.5$ and circulation of the dipoles diminishes after $x/c \geq 7$. Mean streamwise velocity profiles calculated using the vortex array model are plotted for $x/c = 4$ and $x/c = 6$ in figure 10.8. High momentum-surfeit regions are observed around the centerline ($y/c = 0$) for the merged wake ($t_1 = 50P$), whereas two distinct peaks associated with the jets created by the upper and lower vortex streets are visible in the separated wake ($t_1 = 13P$). Excessive momentum at the outlet profiles ($x/c = 4$ and $x/c = 6$) created by the single velocity peak is greater than combination of the two peaks. It clearly shows impact of the wake merging on the formation of high-momentum jets, which results in improving thrust production. Furthermore, we compare velocity profiles obtained from the vortex array model with contours of mean horizontal velocity from figure 10.9. The model accurately captures the general trend and locations of the velocity peaks. However, it underestimates the magnitude of peaks in velocity profiles. This limitation may be due to the sampling space given we only consider the region after wake merging in our calculations for the model. This focus on a particular region is driven by our emphasis on the influence of wake merging. Finite-core vortex array model was also developed and utilized by Dewey et al. (2014) to reproduce wake structures and time-averaged velocity fields around parallel foils for in-phase ($\phi = 0$), out-of-phase ($\phi = \pi$), and mid-phase ($\phi = \pi/2$) oscillations. Even though they successfully demonstrated merging of wakes for in-phase pitching foils, they were not able to observe transitional characteristics during evolution of the wake, because Strouhal number of their study was limited to $St = 0.25$.

The formation, growth and interaction of LEVs can be an important mechanism that impact propulsive performance of oscillating foils (Anderson et al., 1998; Pan et al., 2012), while also

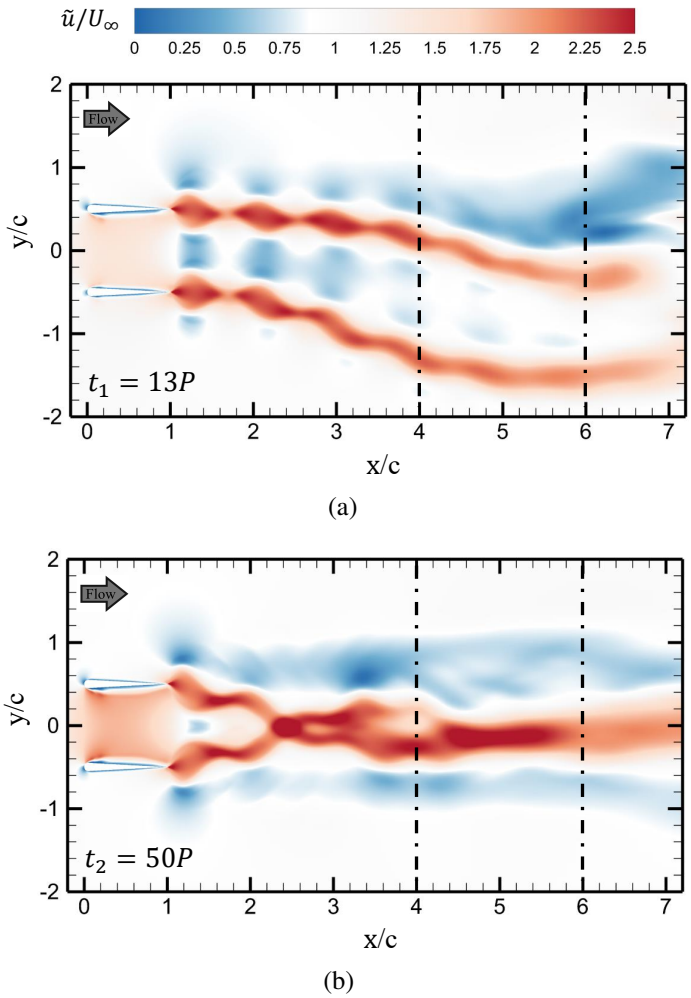

Figure 10.9: Cycle-averaged streamwise velocity ($\widetilde{u}$) contours normalized by U_∞ of in-phase pitching parallel foils for $St = 0.5$ and $y^* = 1c$ at (a) $t_1 = 13P$ and (b) $t_2 = 50P$.

impacting the wake development (Hemmati et al., 2019a). To this effect, we now look at how alterations in the formation and growth of LEVs around the foils influence their propulsive performance during separated-to-merged wake transition. LEVs are formed when the angle of attack is high enough that a separation bubble is formed on the foils. Their presence and evolvement on the surface of a fin or wing is responsible for a large part of thrust and lift generation in aquatic locomotion (Borazjani and Daghooghi, 2013; Bottom Ii et al., 2016; Liu et al., 2017; Xiong and Liu, 2019) and insect flight (Ellington et al., 1996; Birch and Dickinson, 2001; Bomphrey et al., 2005), respectively. Unsteady thrust variations of the foils in the transitional-merged wake ($St = 0.5$ and $y^* = 1c$) throughout the separated and merged time ranges is presented in figure 10.10, which

clearly demonstrates that higher peaks and lower troughs are achieved after the wake merging. Contours of vorticity focusing on surfaces of the foils at time instants that correspond to the highest ($\theta = 8^\circ$) and the lowest ($\theta = 0^\circ$) angles of attack is shown in figure 10.11. This enables comparing this process to the evolution of LEVs around the foils. Note that these instants roughly overlap with the times at which the foils yield their highest and lowest thrust generation, as marked in figure 10.10. Negative (clockwise rotating) and positive (counter clockwise rotating) LEV are formed on the upper and lower surface of the foils at the separated stage of the wake evolution, respectively. On the other hand, constituting positive LEVs on the lower surface of Foil 1 and negative LEVs on the upper surface of Foil 2 is significantly suppressed when the wake is fully merged. Furthermore, it is evident from contour plots in figure 10.11 that stronger LEVs are formed after the wake merging, which hints at a potential factor for thrust enhancement. These observations are valid for the other transitional-merged wake cases with recognizable thrust enhancement as well, although they are not shown here for brevity. Note that profiles of unsteady thrust have two peaks and two troughs per oscillation cycle. The impact of LEVs on thrust generation can be explained through the low pressure region (suction) formed by vortices. LEVs attached close to the anterior part of the foil favorably affect thrust by dropping the pressure in this region, whereas their influence is adverse if located around the posterior part of the foil. For example, Foil 1 at $t_7 = 50.25P$ have enhanced LEV around the front edge comparing to Foil 1 at $t_3 = 13.25P$. However, the distribution of LEVs on rear surfaces of the foils are matching, which translates to thrust enhancements for Foil 1. Likewise, thrust of Foil 2 at $t_5 = 49.75P$ is considerably larger than that of Foil 1. This is due to stronger LEVs formed close to the forehead of Foil 2, while an LEV with large negative vorticity is present on the rear part of the Foil 1.

Merging of vortex streets was accompanied by the restoration of wake symmetry for parallel foils as shown in chapter 4. Both performance and wake characteristics exhibit symmetric behavior with a delay of half pitching period. This lag between the foils is due to the formation process of vortex dipoles. Although TEV_1 and TEV_2 are shed at the same time (e.g., $t_5 = 49.75P$), TEV_2 establishes a dipole with TEV_0 that has been shed half a period prior to these TEVs, whereas

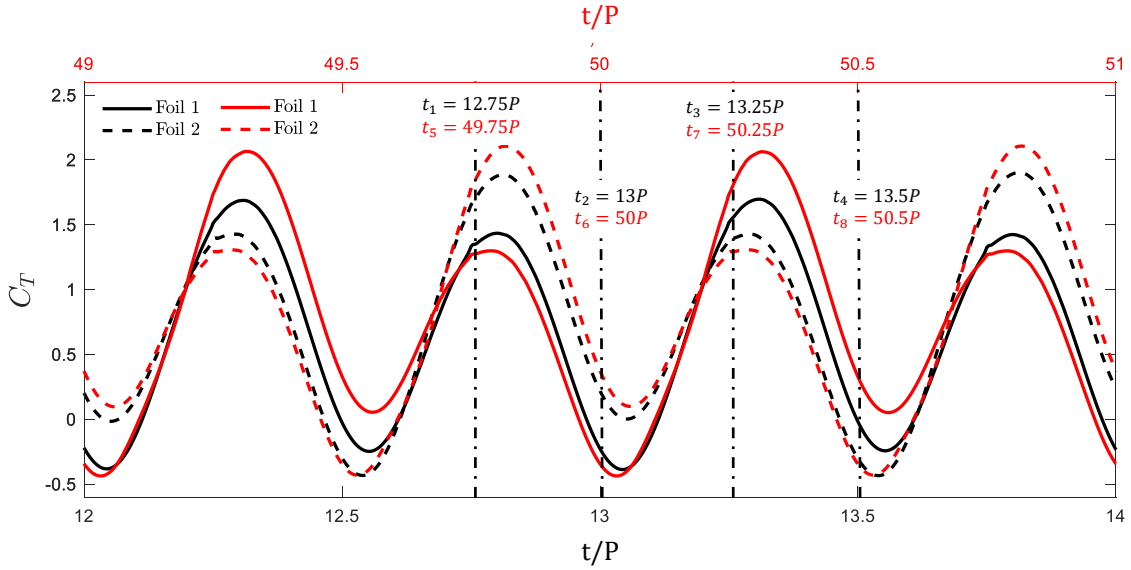

Figure 10.10: Variations in unsteady thrust coefficient of Foil 1 and Foil 2 for $St = 0.5$ and $y^* = 1c$ (transitional-merged wake) for in-phase pitching. Separated stage ($12 \leq t/P \leq 14$) of the wake evolution is illustrated in black and merged stage ($49 \leq t/P \leq 51$) of the wake evolution is illustrated in red.

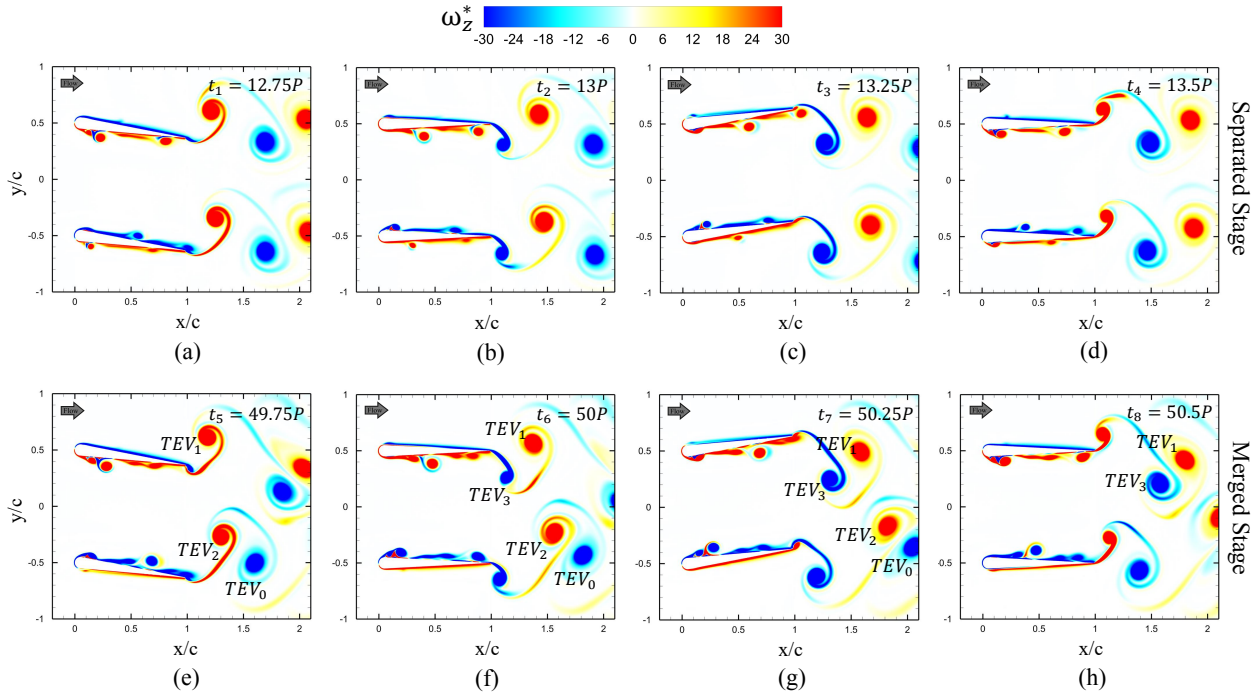

Figure 10.11: Contour of spanwise vorticity ($\omega_z^* = \omega_z c/U_\infty$) around in-phase pitching parallel foils for $St = 0.5$ and $y^* = 1c$ (transitional-merged wake) at various time instants during separated stage: (a) $t_1 = 12.5P$, (b) $t_2 = 13P$, and merged stage: (c) $t_3 = 49.5P$, (d) $t_4 = 50P$.

the coupling of TEV_1 and TEV_3 are delayed by half a cycle. Therefore, distribution of LEVs around Foil 1 and Foil 2 at $t_5 = 49.75$ in figures 10.11e is mirror image symmetric with switched signs of vorticity with that around Foil 2 and Foil 1 at $t_7 = 50.25P$ in figures 10.11g, respectively. Besides, shifting C_T values for Foil 1 by a half period in either direction results in a perfect overlap with those for Foil 2 during the merged stage of the wake evolution, or vice versa (see figure 10.10). Contrarily, there is neither a coherent similarity of the arrangement of LEVs around the foils between different time steps nor a half period lag between performance parameters of Foil 1 and Foil 2 during the separated stage of wake evolution.

10.3 Summary

Numerical simulations on the flow around two pitching foils in side-by-side configuration are examined at a range of Strouhal number, $0.15 < St < 0.5$, phase difference, $0 < \phi < \pi$, pitching amplitude, $5^\circ < \theta_0 < 14^\circ$, and, separation distance, $0.5c < y^* < 2.5c$, at Reynolds number of 4000. First, we classify the vortex patterns in the wake. In the Strohual number$-$separation distance phase map of in-phase pitching foils, separated and merged wakes, which exhibit quasi-steady performance and wake characteristics, are observed at lower Strouhal numbers. Small spacing between the foils yields the constitution of merged wakes, while separated wakes are seen at higher separation distances. On the other hand, transitional-merged wakes, which are often observed at high Strouhal numbers, exhibit wake evolution in time. Two distinct and deflected vortex streets shed by each foil are observed at early stages of the oscillations. Upper and lower vortex streets approach each other in time, which eventually results in merging of the wakes. A novel mathematical model is proposed, which quantitatively establishes the threshold for the two set vortex patterns. This model utilizes the locations and circulations of individual vortices in a dipole. It is further tested using the current parameter space and performs perfectly in determining if the wake is separated or merged.

Then, we proceed with evaluating and explaining the physical mechanism associated with the primary wake transition, observed in in-phase pitching foils. This analysis reveals a novel process in which secondary structures in the wake are responsible in part for the wake merging. The wake merging occurs when secondary structures from the lower vortex street are strong enough to form a constructive interaction with main vortex street of the upper wake. This interaction triggers the merging of wakes by increasing the circulation of negative vortex in the upper vortex street. In turn, this impacts the resultant induced velocity (flow) by the two vortex streets, which now do not match, leading to further deflection of wakes and their subsequent merger. Finally, it is observed that merging of the wakes enhances propulsive performance of the foils by combining circulations of amalgamated vortices. This process induces high-momentum jet around the centerline. Evolution of leading-edge vortices plays a major role in the performance enhancement. Alterations in the distribution of leading-edge structures and the amplification in their strength, which occurrs after the wake merging, is a contributing factor for the improvements in thrust generation.

This chapter, in conjunction with chapters 4-7, tackles the complex dynamics of unsteady wake interactions behind parallel oscillating foils and their impact on propulsive performance metrics, thereby achieving Objective A. The detailed characterization of two-dimensional structures behind parallel oscillating foils, accomplished in these chapters, provides essential motivation and background knowledge for elucidating the intrinsic dynamics of three-dimensional instabilities. Consequently, the focus in the subsequent two chapters shifts to investigating the spanwise instabilities that emerge around parallel pitching foils.

Chapter 11

FOIL PROXIMITY EFFECT INDUCED SHEAR LAYER INSTABILITY[†]

A vortex pair, whether co-rotating or counter-rotating, manifests three-dimensional instabilities both in isolation and within close proximity of another foil, bearing significant relevance to aircraft and submarine wake dynamics (Williamson et al., 2014). This has spurred numerous foundational investigations aimed at characterizing the intricacies of these instabilities within vortex pairs (Leweke and Williamson, 1998; Ortega et al., 2002, 2003; Bristol et al., 2004; Leweke and Williamson, 2011). In their review, Leweke et al. (2016) meticulously examines this subject matter, providing a comprehensive overview that delves into the fundamental attributes of three-dimensional instabilities, particularly focusing on long and short wavelength instability mechanisms. Similarly, significant attention has been directed towards elucidating the three-dimensional aspects of wakes in the context of oscillating foils, as outlined in chapter 2.5. Recent studies (Deng and Caulfield, 2015; Deng et al., 2016; Zurman-Nasution et al., 2020; Chiereghin et al., 2020; Verma and Hemmati, 2021; Son et al., 2022; Verma et al., 2023) offer valuable insights into the complex dynamics of wake instabilities associated with single oscillating foils. Nonetheless, a

[†]The content of this chapter is currently under revision in *J. Fluid Mech.* with the citation: "Gungor, A., Verma, S., Khalid, M.S.U., & Hemmati, A., (2024) Foil Proximity Effect Induced Shear Layer Instability Around Oscillating Foils *J. Fluid Mech.*"

comprehensive exploration of how kinematic parameters affect parallel foils, specifically the gap and phase difference between them, remains an area for further investigation.

The presence of a solid boundary near oscillating foils leads to substantial effects on vortex dynamics around them (Quinn et al., 2014) and their propulsive performance characteristics (Blevins and Lauder, 2013; Mivehchi et al., 2021). Quinn et al. (2014) identified two distinct vortex patterns, emerging in the wake of pitching foils near the ground, based on the separation distance from the wall boundary. The flow around oscillating foils near a solid boundary is akin to that of a pair of parallel foils undergoing out-of-phase oscillations at low frequencies. It can be correlated with the method of images discussed by Dewey et al. (2014). Previously, the key disparities between two-dimensional wake topologies of in-phase and out-of-phase pitching parallel foils is elucidated in chapter 4, followed by a comprehensive classification of their vortex patterns in chapter 10. These studies, however, overlooked three-dimensional characteristics in the flow instabilities. Thus, the objective of this chapter is to examine three-dimensional flow dynamics and the spanwise instabilities that emerge behind parallel foils in the presence of another pitching foil in close proximity. Here, we introduce and explain the nature of a new shear layer instability due to the foil proximity effect. This aspect shapes up the primary novelty of the work presented. This chapter is organized to first present the details of the problem in section 11.1. Subsequently, the main results and discussions are outlined in section 11.2, followed by a summary in section 11.3.

11.1 Problem Definition

The flow around two pitching foils in side-by-side configurations are simulated at a Reynolds number of 8000, in which the flow is anticiptaed to fully transition to turbulence (Verma and Hemmati, 2021). Note that the experimental results of Zurman-Nasution et al. (2020) on the wake transition to 3D at $Re = 5300$ remain valid, even when Re is doubled. The separation distance between these infinite-span teardrop foils is varied from $y^* = 0.5c$ to $y^* = 1.5c$ in increments of

$0.25c$. Both in-phase ($\phi = 0$) and out-of-phase ($\phi = \pi$) motions are considered for the Strouhal numbers of 0.3 and 0.5, which represent low and high St, as detailed in the previous chapters.

11.2 Results and Discussion

The transition to three-dimensionality is not anticipated for the foils oscillating in isolation within the range of kinematic parameters examined in the current study, emphasizing the critical role of the foil proximity effect. Zurman-Nasution et al. (2020) demonstrated that pitching foils produced a two-dimensional wake for $St \approx 0.3 - 0.6$. Deng et al. (2016) also estimated a comparable St for the transition. Both studies also concurred on the observation that the wake of heaving foils exhibited a transition to three-dimensionality at a significantly lower St. Therefore, our present work addresses the primary question of how foil proximity effect influences the vortex dynamics on the surfaces of the parallel foils. In this quest, we also report a novel instability mechanism for the shear layers of developing TEVs. Flow instabilities are first identified and characterized, while quantitative links are presented between the growth of LEVs, roll up of the shear layer, and dislocation of vortex legs on the growing TEVs. This discussion provides a foundation to examine a unique fundamental association between foil proximity effect and vortex instabilities around parallel foils. Lastly, the influence of kinematics of the foils on the newly discovered mechanism is discussed.

11.2.1 Characterization of the Instability

We begin by examining three-dimensional flow features in the vicinity of parallel in-phase pitching foils with a small separation distance between them ($y^* = 0.75c$) and a moderate Strouhal number ($St = 0.3$), under quasi-steady conditions. Iso-surfaces of the Q-criterion, as originally defined by Hunt et al. (1988), are utilized to identify coherent flow structures in the wake. This technique is known for its robustness, and it is commonly employed in wake and flow analyses (Chiereghin et al., 2020; Verma and Hemmati, 2021; Khalid et al., 2021a). Figure 11.1 exhibits temporal pro-

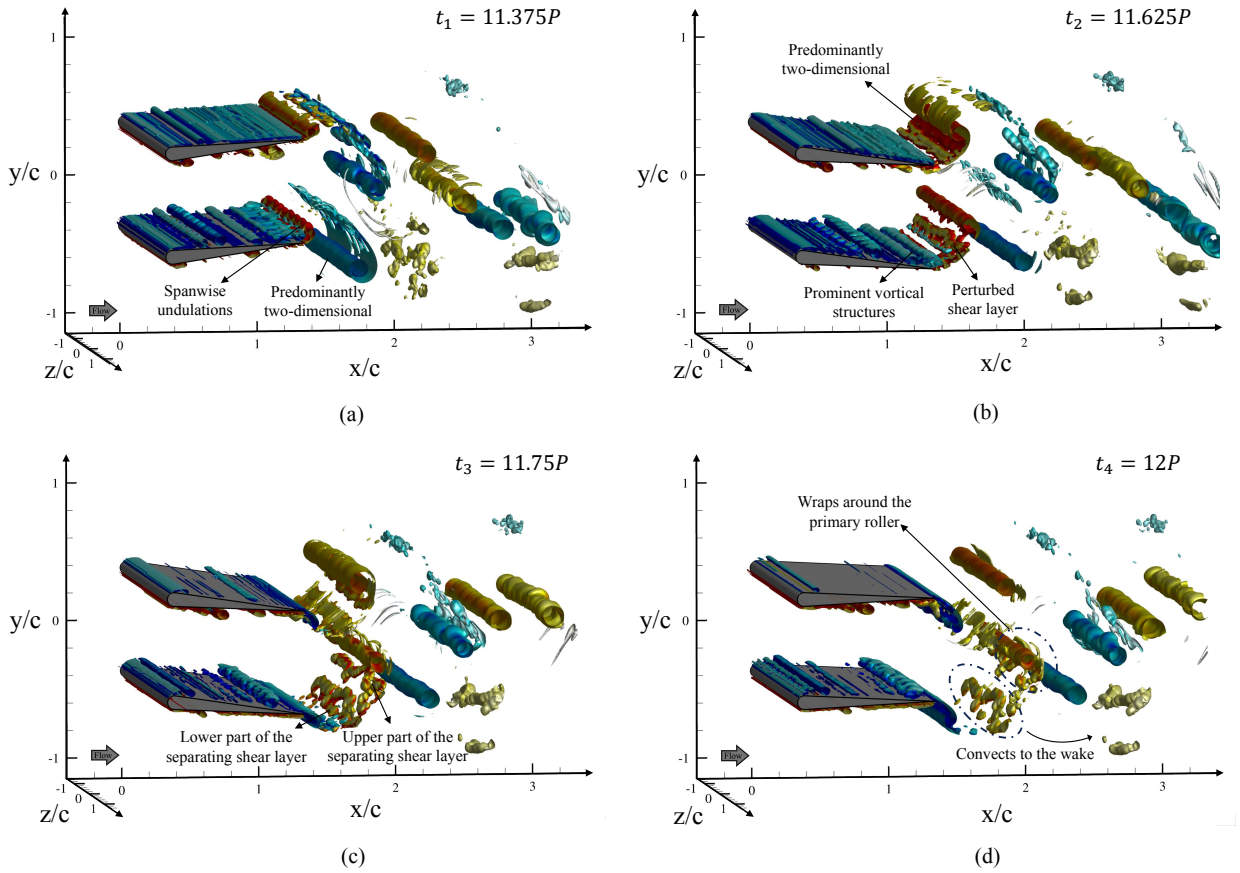

Figure 11.1: Temporal evolution of vortical structures ($Q\,c^2/U_\infty^2 = 10$) around in-phase pitching foils for $St = 0.3$ and $y^* = 0.75c$ at (a) $t_1 = 11.375P$, (b) $t_2 = 11.625P$, (c) $t_3 = 11.75P$, and (d) $t_4 = 12P$. Iso-surfaces are colored using normalized spanwise vorticity ($\omega_z^* = \omega_z\,c/U_\infty = -30$ for blue and $\omega_z^* = 30$ for red)

gression of vortical structures around the foils during the downstroke phase of the pitching cycle, resulting in the formation of positively signed (counter-clockwise rotating) TEVs. Even at the initial stage of their formation in figure 11.1a ($t_1 = 11.375P$), spanwise undulations become apparent with the TEV growing on the bottom foil. This observation aligns with the presence of prominent oppositely signed vortical structures on the upper surface of the bottom foil, near the trailing edge. It is also consistent with chpater 10, where the impact of a side-by-side configuration on the LEV dynamics is illustrated . For the in-phase pitching motion, neighboring surfaces of the parallel foils (the upper surface of the bottom foil and the lower surface of the top foil) exhibit stronger LEVs compared to those of a single foil. LEVs on the outer surfaces (the lower surface of the

bottom foil and the upper surface of the top foil) are observed to be comparatively weaker. This can explain the presence of undulations on the TEV of the bottom foil and their absence on the top foil, which coincides with the stronger vortical structures, more severely straining the TEVs. This is the underlying mechanism for spanwise instabilities (Kerswell, 2002). A quantitative assessment of LEVs, presented later in this section, provides additional support for this argument. As the foils complete their downstroke at $t_3 = 11.75P$ (figure 11.1b), shear layers in the form of legs of TEVs are fully detached from the foils. The perturbed shear layer exhibits highly three-dimensional features, leading to loss of coherence, which disintegrate into two parts (figure 11.1c). The upper part of the shear layer merges with the primary vortex tube, while the lower part is completely detached from the braid region and convected downstream (figure 11.1d). In contrast, the shear layer formed by the leg of the TEV at the top foil maintains its coherence and remains predominantly two-dimensional throughout the shedding process. It coincides with the absence of strong structures formed on the upper surface of the top foil. The exact opposite phenomenon takes place for shedding of the consecutive (clockwise rotating) TEVs during the upstroke, supporting the qualitative link witnessed between the emergence of shear layer instability and LEV dynamics.

To quantify the spanwise instability characteristics, the wavelength of the undulations on the TEV is calculated. Figure 11.2 shows contours of streamwise vorticity plotted on a plane that cuts through the center of the newly developing TEVs. The undulations in the vortex shed from the bottom foil lead to the formation of aligned streamwise vortex pairs along the spanwise direction at $y/c \approx -0.2$. The wavelength of the spanwise instability, denoted by λ_z, is defined as the distance between two consecutive similarly signed vortices, as illustrated in the figure. The average wavelength of the instability is calculated to be $\lambda_z/c = 0.37$, indicating a short wavelength mode. This is consistent with in the Floquet stability analysis of Deng and Caulfield (2015), who observed that the vortices in wake of pitching foils are unstable to short wavelength perturbations at $\lambda_z/c = 0.21$. As expected, no prominent streamwise structures are observed for the TEV shed from the top foil ($y/c \approx 0.6$) considering its mainly two-dimensional structure.

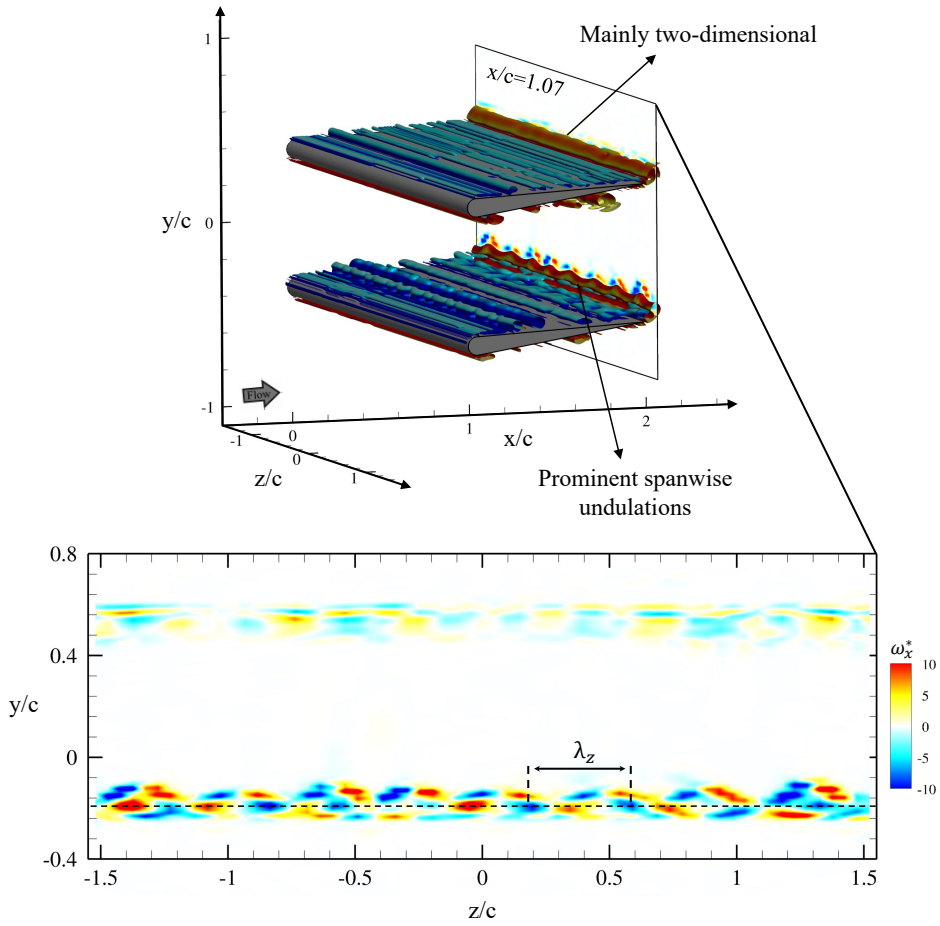

Figure 11.2: Iso-surfaces of Q-criterion ($Q\,c^2/U_\infty^2 = 10$) around in-phase pitching foils, along with contours of streamwise vorticity ($\omega_x^* = \omega_x\,c/U_\infty$) at $x/c = 1.07$ for $St = 0.3$ and $y^* = 0.75c$ at $t = 11.375P$. Iso-surfaces are colored using normalized spanwise vorticity ($\omega_z^* = \omega_z\,c/U_\infty = -30$ for blue and $\omega_z^* = 30$ for red).

The connection between the shear layer instability induced by the foil proximity effect and the formation and growth of LEVs is quantitatively evaluated and linked with qualitative wake visualizations in figure 11.3. A combination of spanwise vorticity contours (ω_z^*) and profiles of span-averaged chord-wise pressure gradients (dp_w/dx) are presented here. Temporal evolution of vortex topology in the vicinity of the foils at the middle plane ($z/c = 0$) for a complete pitching cycle delivers a clear depiction of the alteration mechanism of the LEV in figures 11.3a-11.3d. Variations in span-averaged pressure gradients on the upper surfaces of both foils are tracked over the same pitching cycle to provide a quantitative assessment of this process (figures 11.3e-11.3h). A rapid variation of the pressure gradient on the surface is associated with the presence of a large-

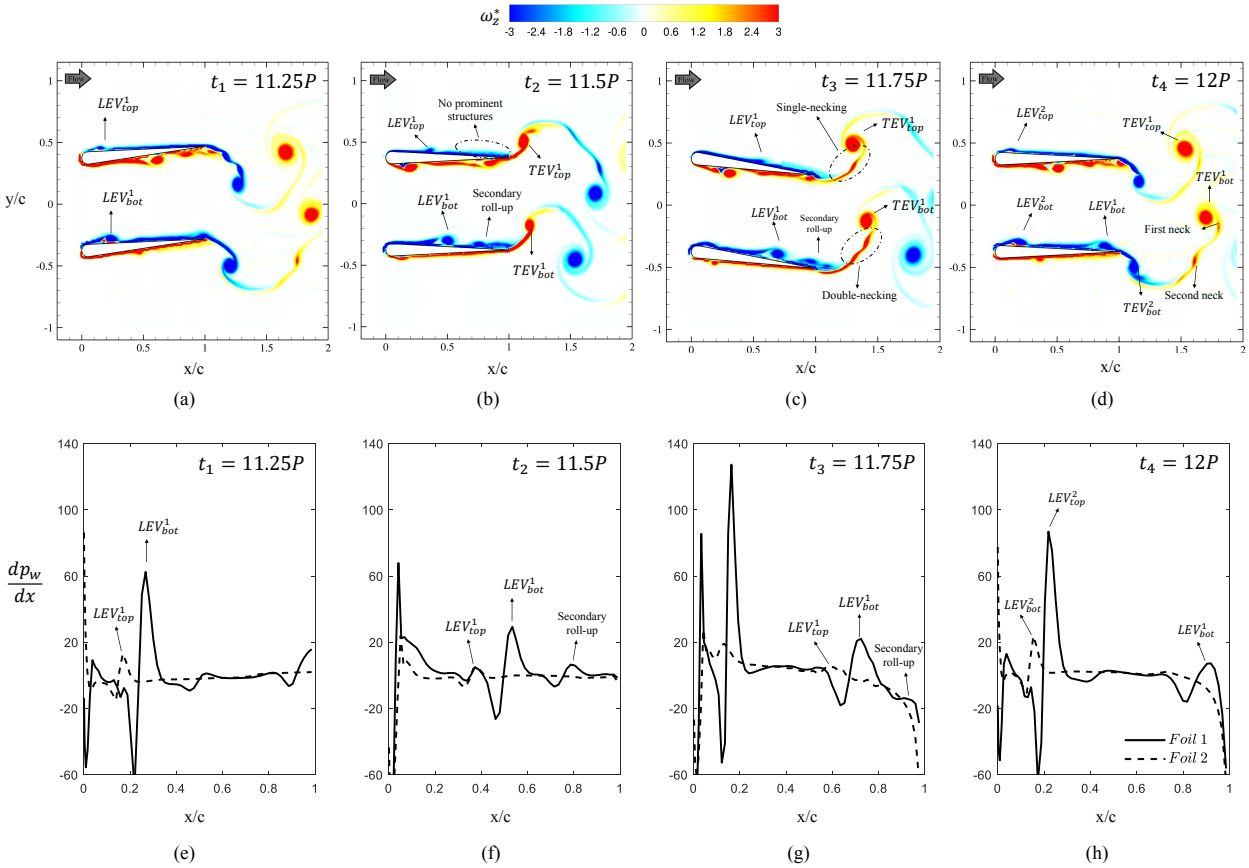

Figure 11.3: Temporal evolution of (a-d) contours of spanwise vorticity ($\omega_z^* = \omega_z\, c/U_\infty$) around in-phase pitching foils, and (e-h) profiles of span-averaged pressure gradient (dp_w/dx) on upper surfaces of the foils for $St = 0.3$ and $y^* = 0.75c$. Time instants are at (a-e) $t_1 = 11.25P$, (b-f) $t_2 = 11.5P$, (c-g) $t_3 = 11.75P$, and (d-h) $t_4 = 12P$.

scale vortex core, as suggested by Obabko and Cassel (2002). This method is also used by Verma et al. (2023) to identify LEV structures forming on the surfaces of oscillating foils in correspondence with transition mechanisms that govern the growth of secondary streamwise structures. At the beginning of the downstroke (figure 11.3a), LEVs start forming on the upper surfaces of the foils. The one formed on the bottom foil (LEV^1_{bot}) is considerably stronger compared to that formed on the top foil (LEV^1_{top}). This is evident from the deviation of the maximum pressure gradients in figure 11.3e, which corresponds to these particular LEVs. By the time both foils reach their middle position parallel to free stream at $t_2 = 11.5P$, a secondary vortex roll-up is visible on the bottom foil near its trailing edge. It coincides with emergence of the newly discovered "double-neck" on

the leg of TEV^1_{bot} prior to its detachment from the foil (figure 11.3c). On the contrary, the top foil exhibits no sign of a secondary roll-up with only a "single-neck" appearing in the shear layer of TEV^1_{top}. Quantitative data also confirms the presence of a secondary roll-up on the bottom foil during the downstroke (figure 11.3f), while it is absent on the top foil. This phenomenon indicates that this new instability is associated with the formation of secondary roll-ups. At the time of complete detachment of TEVs from the foils (figure 11.3d), the single-neck of TEV^1_{top} is drawn into the stronger co-rotating TEV (TEV^1_{top}), resulting in their merger. The first-neck of TEV^1_{bot} undergoes very similar dynamics, eventually merging with TEV^1_{bot}. Contrarily, the second-neck of TEV^1_{bot} is not absorbed into the primary vortex. Instead, it separates from the braid region and convects downstream. An identical process occurs on the lower surfaces of the foils during the upstroke phase of the pitching cycle due to the inherent symmetry of the phenomenon, although it is not marked on the figures for simplicity.

11.2.2 Influence of the Foil Proximity Effect

We now expand on the pivotal role of the foil proximity effect (quantified by spacing between the foils) to further explore dynamics of the shear layer instability. Figure 11.4 displays iso-surfaces of the Q-criterion, along with contours of ω^*_z on the middle plane ($z/c = 0$) at $St = 0.3$. Three distinct cases representing extreme ($y^* = 0.5c$), moderate ($y^* = 1c$), and low ($y^* = 1.5c$) foil proximity effect are selected. The results clearly illustrates the transition from a two-dimensional wake to a three-dimensional wake as the separation distance between foils decreases (right column of figure 11.4). This wake three-dimensionality aligns well with the presence of the secondary roll-up and double-neck structure at the lowermost position of the foils ($t = 11.75P$). The wake behind the pitching foils at $y^* = 1.5c$ (figure 11.4a) is predominantly two-dimensional, where especially the bottom foil experiences neither the double necking nor secondary roll-up. In the case of moderate foil proximity effect ($y^* = 1c$), both double necking and the roll-up of a secondary vortex are qualitatively visible (figure 11.4b). Two-dimensionality of the wake is disturbed with development of the shear layer instability. This process subsequently promotes the detachment of the shear layer

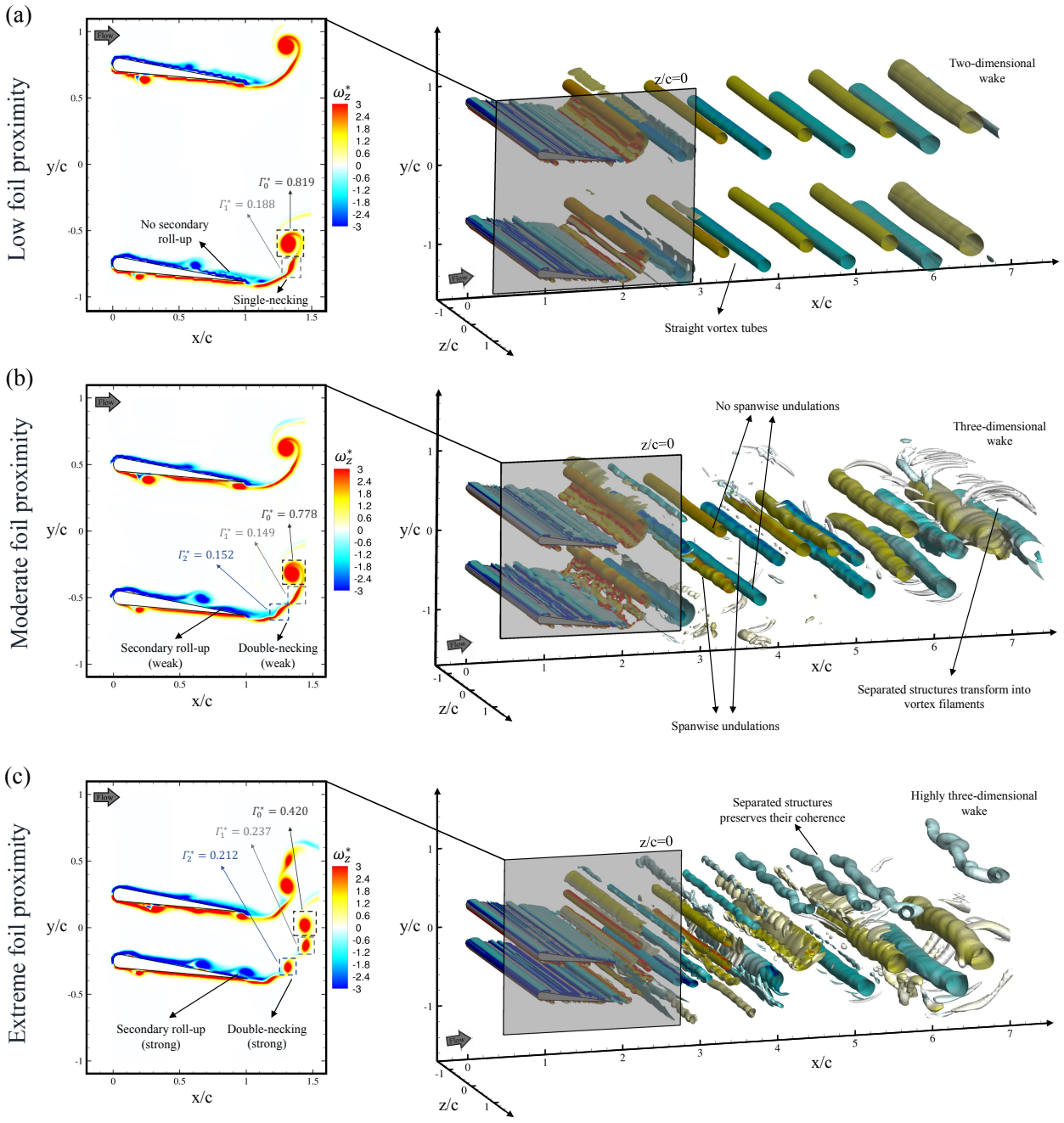

Figure 11.4: Iso-surfaces of Q-criterion ($Q\,c^2/U_\infty^2 = 1.5$) in the wake of in-phase pitching foils at $St = 0.3$, along with contours of spanwise vorticity ($\omega_z^* = \omega_z\,c/U_\infty$) at the mid-plane ($z/c = 0$) at the lowermost position ($t = 11.75P$) for (a) $y^* = 1.5c$, (b) $y^* = 1c$, and (c) $y^* = 0.5c$. Circulation ($\Gamma^* = \Gamma/U_\infty c$) calculations for TEVs and necks are performed within the depicted square regions following Khalid et al. (2020)

.

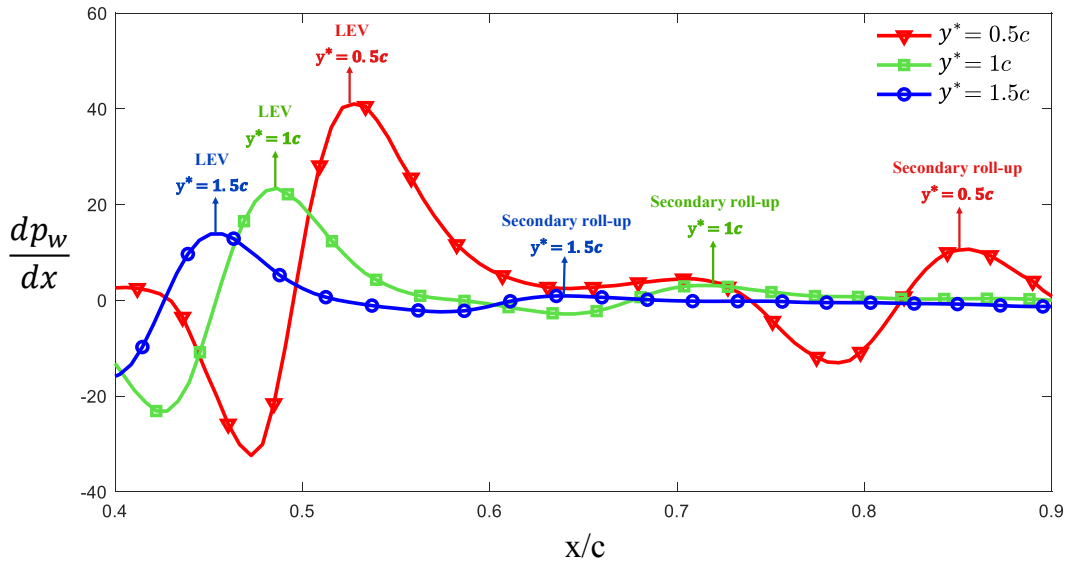

Figure 11.5: Profiles of span-averaged chord-wise pressure gradient (dp_w/dx) along upper surfaces of Foil 2 for $St = 0.3$ at $t = 11.75P$ for various foil proximity effect cases.

from the braid region and its transformation into the streamwise vortex filaments, surrounding the vortex rollers at the mid-wake ($x/c \approx 6$). It also coincides with the growth of spanwise undulations on the counter-clockwise rotating TEVs shed from the bottom foil, and clockwise rotating TEVs shed from the top foil. The necks within the double-neck structure, and the secondary roll-up on the surface, evidently manifest under extreme foil proximity effect at $y^* = 0.5c$ (figure 11.4c). Their sizes become comparable to the shed TEV and the primary LEV, respectively. The detached necks mostly preserve their coherence even at the mid-wake, unlike the case of moderate foil proximity effect (figure 11.4b). This phenomenon is attributed to the change in the strength of primary rollers and the detached necks. A larger imbalance in the strengths of a pair of counter-rotating vortices promotes the transformation of a weaker vortex into vortex filaments (Ryan et al., 2012). This is apparent in the ratio between the circulations of TEVs (Γ_0^*) and second necks (Γ_2^*), yielding $\Gamma_0^*/\Gamma_2^* = 1.98$ and $\Gamma_0^*/\Gamma_2^* = 5.13$ for the extreme and moderate foil proximity effect cases, respectively.

Figure 11.5 quantitatively compares span-averaged pressure gradients on the upper surfaces of the lower foils at different spacings between the two foils. The amplitude of pressure gradient variation, which is linked to the secondary roll-up, is most pronounced under extreme foil proximity

effect conditions ($y^* = 0.5c$) and consistently diminishes with widening foil spacing. At $y^* = 1.5c$, the foil proximity effect features nearly vanish, apparent with the absence of double-necking and wake three-dimensionality (figure 11.4c). A similar trend is observed for LEVs, reaffirming the consistency of wake features associated with foil proximity effect. Furthermore, a remarkable insight derived from this visualization is the chord-wise shift of both LEVs and secondary roll-ups toward the trailing edge with shrinking separation between the foils. This observation further strengthens our argument that the secondary roll-up plays a vital role in perturbing the shear layer, through leg of oppositely signed TEVs.

11.2.3 Effect of Kinematics of the Foils

We proceed with investigating the role of oscillation frequency on physical aspects of the shear layer instability. Increasing *St* can potentially lead to the formation of secondary vortical structures or alter the governing mechanism for their growth (Verma et al., 2023). Nevertheless, primary characteristics of the shear layer instability at lower Strouhal number ($St = 0.3$), as discussed in section 11.2.1, align with those observed at $St = 0.5$. The case of strong foil proximity effect ($y^* = 0.75c$) is selected to elucidate the impact of *St*. The temporal evolution of vortex topology around the foils at $St = 0.5$ and $y^* = 0.75c$ closely resembles that at $St = 0.3$. Therefore, it is not included here for brevity. The key difference is the more pronounced foil proximity effect at the higher *St*, which coincides with the emergence of more prominent structures detaching from the braid region.

Since vortex instabilities result from a resonance between Kelvin modes within the core of vortex filaments and the underlying strain field, their linear growth rate is directly proportional to the strain field (Kerswell, 2002). Hence, we use the strain rate as a tool to elucidate the correspondence between *St* and the shear layer separation instability. Hemmati et al. (2019b) further reported that Q was proportional to the source term in the Poisson equation, which could provide a connection between the vortex core location and the strain rate via $Q = \frac{1}{2\rho}\nabla^2 p = |R|^2 - |S|^2$. Here, $|R|^2$ and $|S|^2$ represent the square of rotation and strain rate tensors, respectively. Menon and Mittal (2021) also

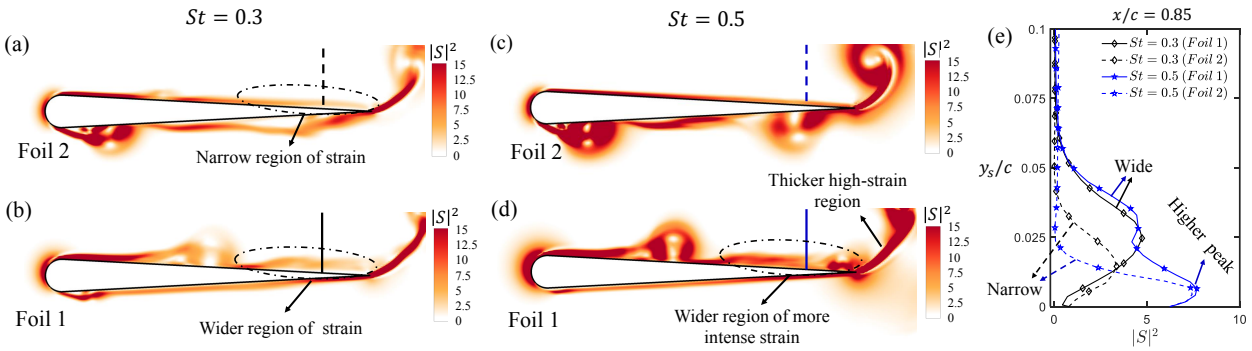

Figure 11.6: Contours of $|S|^2$ around Foil 1 (b-d) and Foil 2 (a-c) at $St = 0.3$ (a-b) and $St = 0.5$ (c-d), along with profiles of $|S|^2$ with respect to vertical distance (y_s) measured from the foil surfaces at $x/c = 0.85$ (marked on the contour plots) for in-phase pitching motion. The data is collected at the mid-plane ($z/c = 0$) during time instants $t = 11.5P$ and $t = 21.5P$ for $St = 0.3$ and 0.5, respectively.

discussed the existing strain-dominated ($Q < 0$) regions, encircling the rotation-dominated core of vortices ($Q > 0$). These considerably impact the vortex dynamics. Figure 11.6 demonstrates the contours of $|S|^2$ around the bottom foil (figures 11.6b-11.6d) and the top foil (figures 11.6a-11.6c) at $St = 0.3$ (figures 11.6a-11.6b) and 0.5 (figures 11.6c-11.6d) for $y^* = 0.75$ in the middle of the downstroke phase. For both cases, the upper surface of the top foil and the lower surface of the bottom foil exhibit only a thin layer of a high-strain region, which coincides with the presence of the weaker LEVs on these surfaces. Contrarily, wider regions of high strain rate are observed on the upper surfaces of the bottom foil near their trailing edge, coinciding with the development of secondary roll-ups. It is also evident from these snapshots that the strain rate is more intense above the upper surface of the bottom foil and along the shear layer of its newly developing TEV leg at the higher Strouhal number. This explains the detachment of more prominent structures. These findings are further supported by the quantitative data illustrated in figure 11.6e, which presents the profiles of $|S|^2$ along a vertical line, starting from the upper surfaces of both foils (y_s) at $x/c = 0.85$ identified in figures 11.6a-11.6d. Notably, profiles of $|S|^2$ are wider for the top foil compared to those for the bottom one for both Strouhal numbers, whereas the peaks of $|S|^2$ at $St = 0.5$ considerably surpass those at $St = 0.3$. It is important to note that these patterns remain consistent across

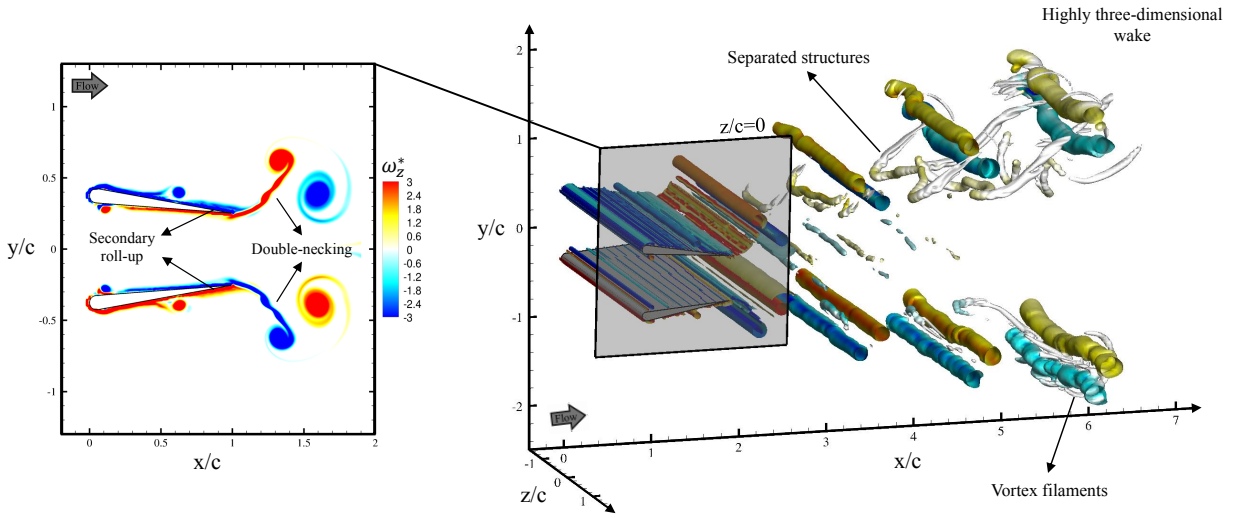

Figure 11.7: Iso-surfaces of Q-criterion ($Q\,c^2/U_\infty^2 = 10$) in the wake of out-of-phase pitching foils, along with contours of spanwise vorticity ($\omega_z^* = \omega_z\,c/U_\infty$) at the mid-plane ($z/c = 0$) for $St = 0.3$ and $y^* = 0.75c$ at $t = 12.25P$.

various streamwise locations along the foil chord, near the trailing edge, which are not displayed here.

The phase difference between the foils represents another crucial kinematic parameter that significantly influence the vortex topology around the foils and the corresponding three-dimensional instabilities. While the manuscript predominantly addresses the foil proximity effect induced shear layer instability in the context of in-phase pitching foils, it is noteworthy to emphasize that this instability also manifests during the out-of-phase motion, as depicted in figure 11.7. This corresponds to the case of $St = 0.3$ and $y^* = 0.75c$. A notable feature of out-of-phase pitching foils is that they simultaneously experience the instability because of the mirror image symmetry of their kinematics. The influence of the foil proximity effect on the LEV dynamics is precisely opposite for in-phase and out-of-phase motions. For the out-of-phase motion, LEVs forming on the outer surfaces of the foils are remarkably stronger than those on the neighbouring surfaces, constituting a crucial nuance from the in-phase motion. However, characteristics of the instability, including the formation of double-necks on the legs of TEVs, and the growth of secondary roll-ups with opposite circulation compared to the double-necks, remains essentially the same for the out-of-

phase motion as we observe for the case of in-phase motion. This consistency provides additional evidence for the association between the newly discovered shear layer instability and the alteration mechanism of the LEVs.

11.3 Summary

Three-dimensional instabilities around pitching foils in side-by-side configurations are numerically evaluated at $Re = 8000$. Foil proximity effect, defined in terms of the influence of a neighbouring foil on vortex dynamics, plays a crucial role in the emergence of three-dimensional structures and a newly discovered shear layer instability. During the downstroke of the in-phase pitching motion, a TEV, shed from the bottom foil, experiences spanwise undulations while its leg (representative of a shear layer) exhibits perturbations. This leads to the formation of secondary spanwise structures that detach from the shear layer and convect downstream. A mirrored phenomenon occurs for the upper foil during the upstroke motion. These phenomena are associated with the development of secondary roll-ups on the upper and lower surfaces of the bottom and top foils near their trailing edges, respectively.

The foil proximity effect has a consistent impact on the newly identified instability, characterized by the emergence of a double-neck structure within the shedding TEVs. Double-necks become more pronounced with intensified foil proximity effect. The secondary roll-up becomes stronger, and it moves closer to the trailing edge. Under low foil proximity effect, the wake predominantly exhibits two-dimensional features, coinciding with the absence of double-necks and secondary roll-up. Increasing the Strouhal number also has a significant influence on the wake three-dimensionality, leading to the detachment of more prominent structures from the shear layer. This impact coincides with the production of a higher strain rate region around the trailing edge and on the shear layer. Despite distinct implications of foil proximity effect on the vortex dynamics around in-phase and out-of-phase pitching foils, the intrinsic attributes of the instability undergo no fundamental alteration.

Chapter 12

ASSOCIATION OF FOIL PROXIMITY EFFECT AND SUPPRESSION OF LEADING EDGE VORTEX INSTABILITY[†]

Understanding the fundamental aspects of vortex dynamics and wake interactions is crucial for unraveling the complex flow phenomena that frequently occur in both natural environments and industrial applications (Leweke et al., 2016). The mechanisms governing the formation and evolution of vortex filaments, along with their interactions with the surrounding environment, are garnering increased attention due to their pivotal role in aircraft wake dynamics (Leweke and Williamson, 1998; Cerretelli and Williamson, 2003; Meunier et al., 2005). Research by Leweke and Williamson (1998) on counter-rotating vortex pairs showed that short-wavelength instabilities developed cooperatively within these structures. It further explored the long-term flow evolution, highlighting interactions between short-wavelength and long-wavelength instabilities. In a separate investiga-

[†]The content of this chapter is currently under preparation and will be submitted to *Phys. Rev. Fluids* with the citation: "Gungor, A., Verma, S., Khalid, M.S.U., & Hemmati, A., (2024) Suppression of LEV Instabilities Under Extreme Foil Proximity Effect. *Phys. Rev. Fluids*"

tion, Cerretelli and Williamson (2003) detailed the physical mechanisms that govern the merging process of two co-rotating vortices, which sequentially experienced phases of diffusion, convection, and merging. This study revealed that induced velocities from the asymmetric vorticity field of the vortex pair drove the centroids of the vortices towards each other, ultimately facilitating their merger.

The study of instabilities in wake structures has recently gained attention due to its relevance in understanding propulsion characteristics in insect flight and aquatic locomotion (Deng et al., 2016). Deng and Caulfield (2015) observed that the transition from symmetric reverse von Kármán wakes to deflected wake modes coincided with the emergence of three-dimensional instability features and increased thrust production. Verma and Hemmati (2021) elucidated the relationship between spanwise instability and the development of streamwise vortical structures, enhancing our understanding of fluid dynamics in biologically inspired propulsion. A more recent study by Verma et al. (2023) explored a broader range of parametric spaces to examine the relationship between foil kinematics and three-dimensional characteristics of its wake. This study identified two distinct mechanisms that govern the growth of secondary structures, and delineated two major pathways characterizing the transition between these mechanisms. Thus, it provides deeper insights into the complex dynamics of wake instability.

Despite considerable efforts to characterize instabilities around a single oscillating foil, the impact of foil proximity on LEV instabilities around parallel oscillating foils remains relatively unexplored. Quinn et al. (2014) demonstrated that the flow around a pitching foil is significantly influenced by the presence of a solid wall, especially when it is positioned very close to the foil. However, the dynamics of the LEVs and the characteristics of three-dimensional instabilities were not addressed. In chapter 11, our focus was on the shear layer instabilities of separating TEVs; now, we shift our attention to LEVs. Using the same parameters as those in chapter 11, this chapter aims to explore the unique LEV instabilities that emerge around foils in side-by-side configurations, influenced by foil proximity effect and wake interactions. Major observations are discussed in section 12.1, and a concise summary of key findings is provided in section 12.2.

12.1 Results and Discussion

We begin by investigating the cases of out-of-phase pitching foils operating under moderate foil proximity effect ($y^* = 1c$) for $St = 0.3$. Since the out-of-phase motion is mirror image symmetric, the bottom (Foil 1) and top (Foil 2) wakes exhibit symmetric features. Therefore, we only focus on the top foil for simplicity. Figure 12.1 illustrates the time evolution of vortical structures around the out-of-phase pitching foils at $St = 0.3$. The left column of figure 12.1 displays iso-surfaces of the Q-criterion on the upper surface of the top foil from a top-down perspective, while the right column of figure 12.1 shows the side view of contours of spanwise vorticity at the mid-plane ($z/c = 0$). An LEV is formed as a result of the upward stroke of the upper foil (see figure 12.1a-b). After its formation, it progresses downstream, while remaining attached to the surface. As a result of this interaction, a spanwise instability starts developing on the vortex at $t = 12.25P$ and becomes very prevalent at $t = 12.5P$. This phenomenon can be best explained with the method of images, which suggests that there is an opposite-sign image vortex forming beneath the surface that satisfies the no-slip boundary condition on the surface. Consequently, the LEV effectively forms a vortex pair with its opposite-sign image. Mutually induced velocities impose on them give rise to the amplification of the sinusoidal undulations on the vortex (Crow, 1970). The emergence of three-dimensional instabilities has been previously shown for vortex-wall interactions (Benton and Bons, 2014) as well as for single oscillating foils with combined heading and pitching motion (Chiereghin et al., 2020; Verma et al., 2023). However, this is the first study to identify them for purely pitching foils due to moderate foil proximity effect. Moreover, the interaction of undulations with the surface lead to disintegration of the vortex before it reaches the trailing edge of the foil, as depicted in figure 12.1g-h. While the LEV on the lower surface of the top foil similarly exhibits spanwise undulations, its evolution is not detailed here for brevity, as it follows a comparable mechanism.

A noteworthy phenomenon occurs at the opposite end of the spectrum: instabilities vanish with severely intensified foil proximity effect. The time evolution of vortex dynamics around the foils in extreme foil proximity effect conditions ($y^* = 0.5c$) is depicted in figure 12.2 for $St = 0.3$.

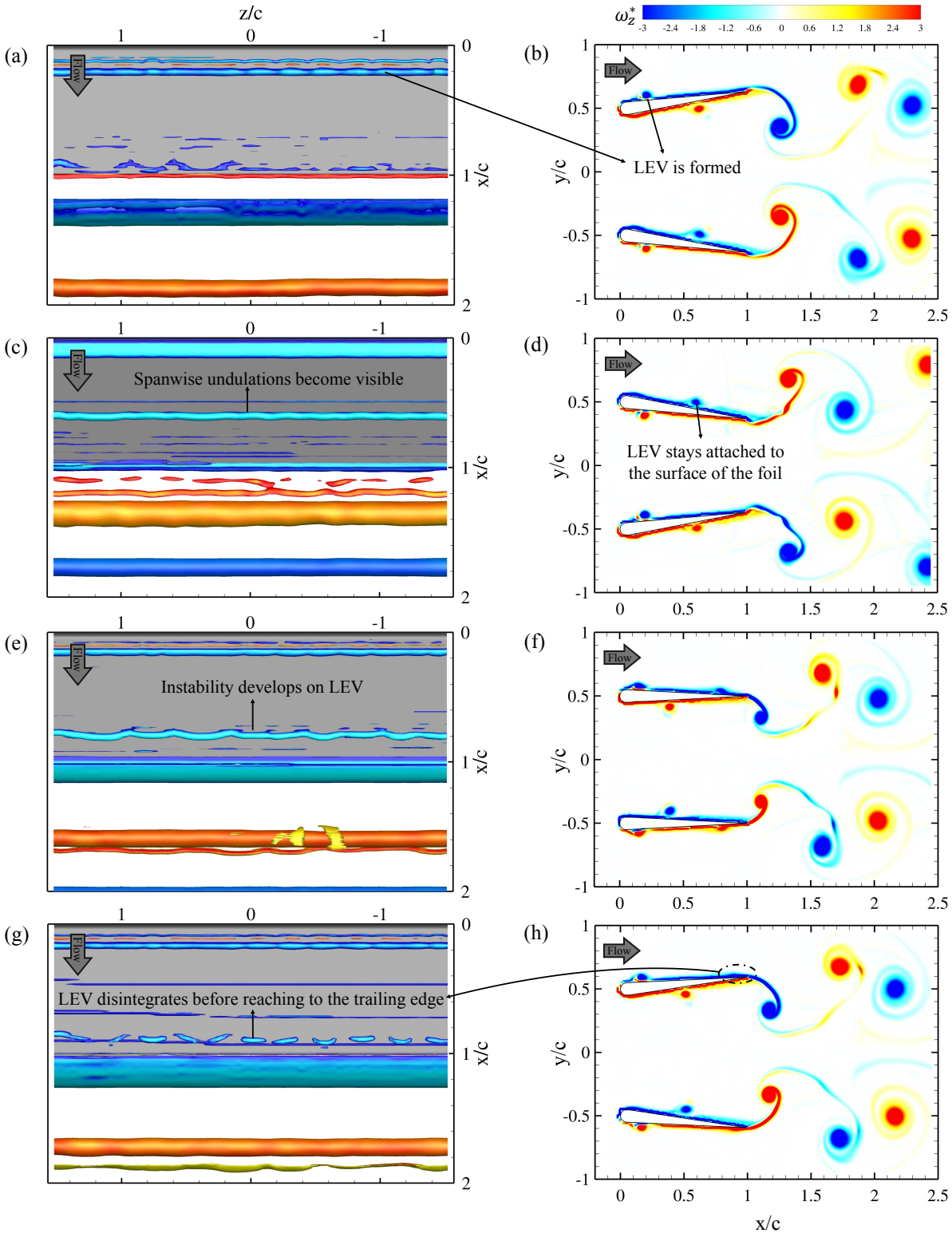

Figure 12.1: Temporal evolution of vortical structures around out-of-phase pitching foils for $St = 0.3$ and $y^* = 1c$ at (a,b) $t = 11.75P$, (c,d) $t = 12.25P$, (e,f) $t = 12.5P$, and (g,h) $t = 12.625P$. Left column displays iso-surface of Q-criterion ($Q\,c^2/U_\infty^2 = 50$) on the upper surface of the top foil viewed from above, while right column shows contours of spanwise vorticity ($\omega_z^* = \omega\,c/U_\infty$) at the mid-plane ($z/c = 0$).

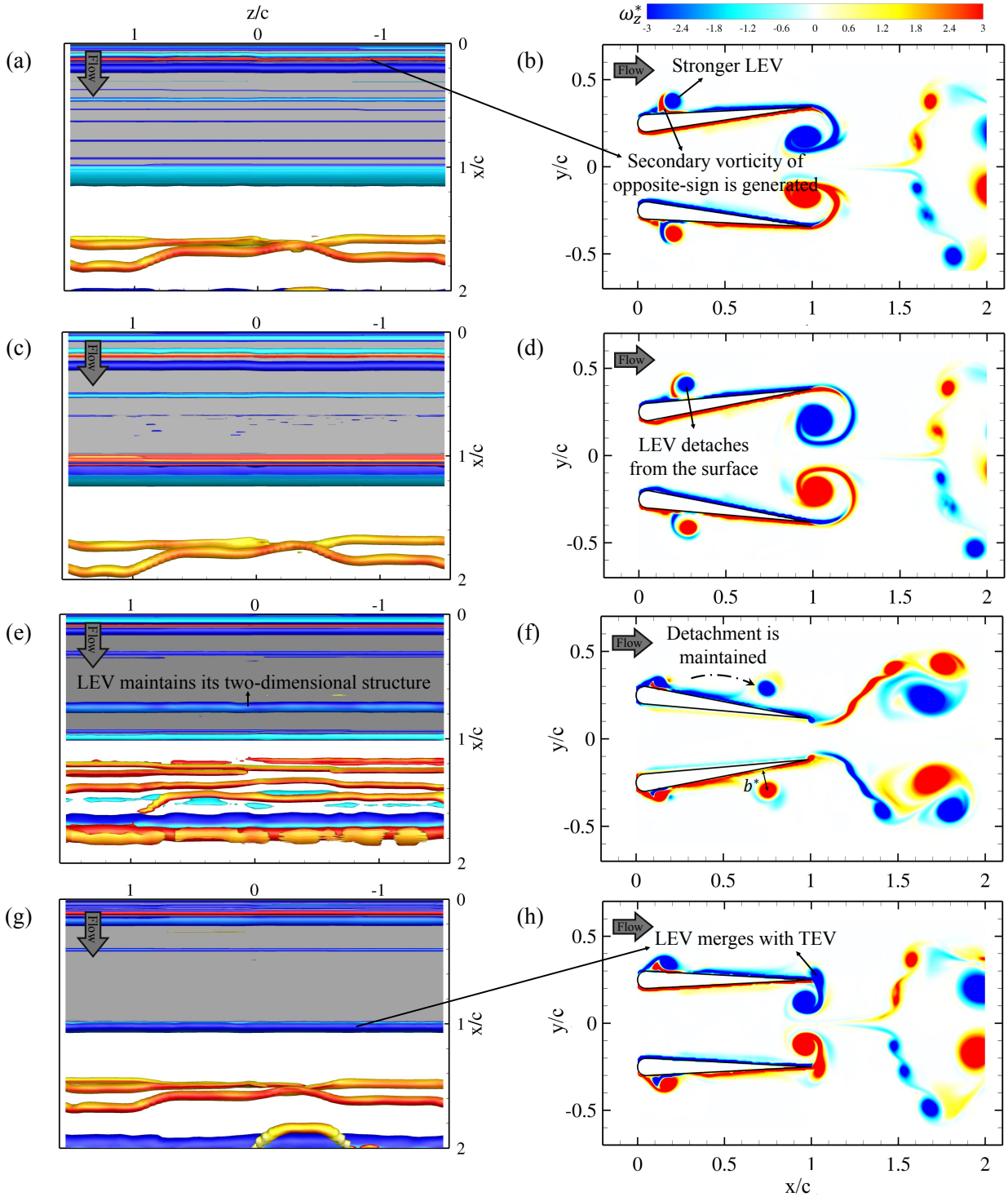

Figure 12.2: Temporal evolution of vortical structures around out-of-phase pitching foils for $St = 0.3$ and $y^* = 0.5c$ at (a,b) $t = 11.625P$, (c,d) $t = 11.75P$, (e,f) $t = 12.25P$, and (g,h) $t = 12.5P$. Left column displays iso-surface of Q-criterion ($Q\,c^2/U_\infty^2 = 50$) on the upper surface of the top foil viewed from above, while right column shows contours of spanwise vorticity ($\omega_z^* = \omega\,c/U_\infty$) at the mid-plane ($z/c = 0$).

Similar to the moderate foil proximity effect case, upstroke motion of the upper foil sheds an LEV. However, this LEV is markedly stronger, as demonstrated by a comparison between figure 12.1b and figure 12.2b. Additionally, a secondary structure with opposite sign vorticity forms beneath the LEV. It is worth noting that the moderate foil proximity effect case also presents secondary structure, but they are significantly weaker and barely visible in figure 12.1b. Interaction between a vortex and a wall leads to the detachment of the boundary layer from the surface, resulting in the formation of a secondary structure opposite to the main vortex (Quinn et al., 2014; Leweke et al., 2016). Vorticity budget analysis by Eslam Panah et al. (2015) shows that the flux of secondary vorticity from the boundary correlates with the leading edge shear layer flux, which can explain the severity of differences between cases. The secondary structure induces an upward velocity, causing the detachment of the LEV from the surface (see figure 12.2). This resembles the interactive behavior of a vortex pair approaching a wall (Harvey and Perry, 1971; Peace and Riley, 1983), where the primary vortex rebounds from the wall due to a formation of the secondary vortex, a process often referred to as "vortex rebounding." Subsequently, the LEV continues downstream, maintaining its distance from the surface until it merges with the newly developing TEV. Unlike the moderate foil proximity effect case, the LEV does not exhibit any significant spanwise undulations and reaches the trailing edge as a two-dimensional vortex tube (see figure 12.2g). The dynamics of LEVs at higher Strouhal numbers exhibit similar characteristics, and thus are not explored in detail here. The main difference is that at $St = 0.5$, the foils generate stronger LEVs, resulting in detachment even at greater separation distances, covering the separation distance range considered in this chapter.

The comparison between extreme and moderate foil proximity effect cases indicates that the detachment of the LEV from the foil surface is crucial in suppressing three-dimensional instabilities. This suppression is likely due to the diminished influence of the image vortex, which is formed due to the LEV's proximity to the foil surface. This plays a central role in the emergence of three-dimensional instability. As the distance between the LEV and the foil increases, the effect of the image vortex weakens, effectively reducing the three-dimensional instabilities. This dynamic

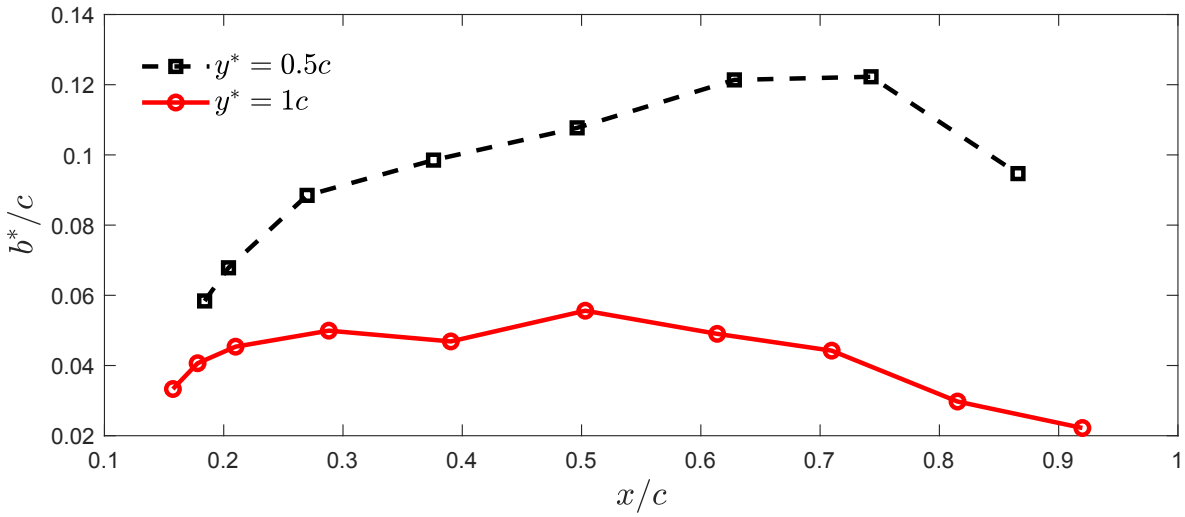

Figure 12.3: Separation distance (b^*) between LEV and foil surface at chordwise locations for the extreme ($y^* = 0.5c$) and moderate ($y^* = 0.5c$) foil proximity effect cases at $St = 0.3$. The definition of b^* is illustrated in figure 12.2f.

is consistent with theoretical models, which suggest that the growth rates of both long-wavelength and elliptic instabilities in a vortex pair are inversely proportional to the square of the separation distance between vortices (b) (Leweke et al., 2016). Figure 12.3 illustrates the separation between the LEV and the foil surface (b^*), measured as the normal distance from the center of the LEV to the foil surface across chordwise positions for both scenarios. This highlights the influence of detachment on the emergence of three-dimensional instabilities. Another notable aspect of the LEV dynamics is the speed at which the detached vortex moves towards the trailing edge compared to its attached counterpart. The detached vortex reaches the trailing edge by $t = 12.5P$ (as shown in figure 12.2h), whereas the attached vortex remains at approximately $x/c \approx 0.8$ at the same time instant (as seen in figure 12.1f). Quinn et al. (2014) observed a similar lagging for a TEV in ground effect. This suggests that the slowing effect is attributed to the influence of the image vortex. The difference in streamwise velocities allows the attached vortex to stay under the influence of its image vortex for an extended period, thus promoting the development of spanwise undulations.

Both the emergence and suppression of three-dimensional instabilities are influenced by the foil proximity effect. As the foil proximity effect diminishes, i.e., as the separation distance between the foils increases, spanwise undulations on LEVs disappear (details not shown here for brevity).

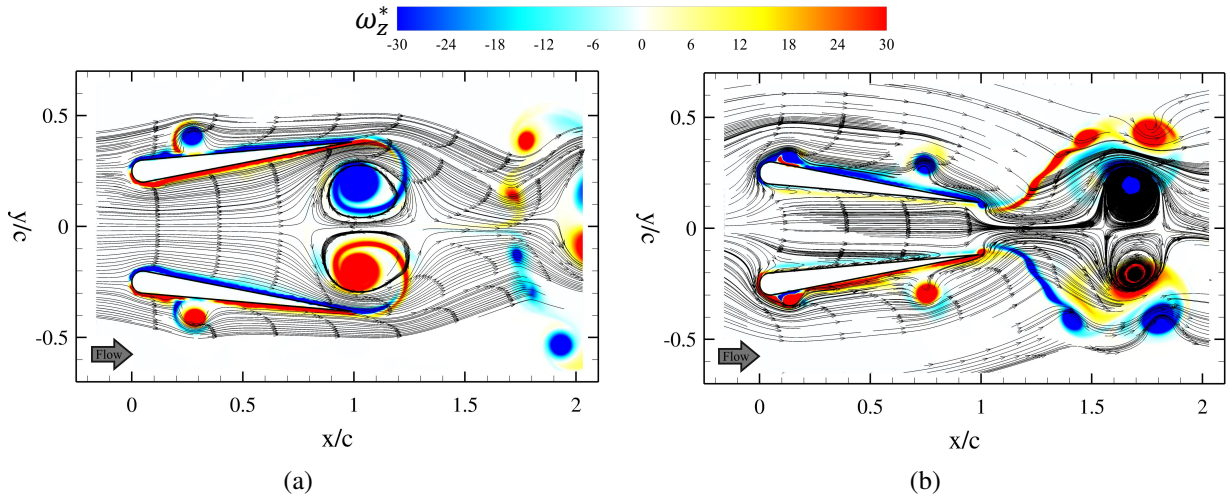

Figure 12.4: Streamlines around the out-of-phase pitching parallel foils for $y^* = 0.5c$ and $St = 0.3$ at (a) $t = 11.75P$, and (b) $t = 12.25P$.

This underscores its role in the emergence of these instabilities. Conversely, the foil proximity effect also plays a critical role in the suppression mechanism by significantly altering LEV dynamics (see chapter 10). For out-of-phase motion, the strength of LEVs formed on the outer surfaces of the foils, i.e., the upper surface of the top foil and the lower surface of the bottom foi, is enhanced. However, the strength of LEVs on the inner surfaces, i.e., lower surface of the top foil and upper surface of the bottom foil, is diminished (see chapter 4). This dynamic is evident in figure 12.2, which shows that the top foil generates a stronger LEV on its upper surface, while shedding of the LEV from the lower surface is inhibited. This aligns with two-dimensional simulations explored in chapter 4. This effect can be attributed to changes in the effective angle of attack due to induced velocity effects from the adjacent foil. Streamlines around the out-of-phase pitching parallel foils are presented in figure 12.4, illustrating that the effective angle of attack of the top foil at the beginning of the downstroke motion (figure 12.4a) is significantly larger compared to the angle at the beginning of the upstroke motion. This discrepancy leads to the formation of a stronger LEV on the upper surface, while inhibiting the formation of an LEV on the lower surface. This observation is consistent with findings of Wong and Rival (2015), who noted that the rate of growth of LEV circulation corresponds to the square of the effective flow velocity. Furthermore, Li et al. (2020b) demonstrated that circulations of both the LEV and the secondary vortex increase with an

increasing maximum effective angle of attack. This aligns perfectly with the current observations. Thus, extreme foil proximity effect is associated with the suppression of LEV instabilities by enhancing the circulation of the secondary vortex beneath the LEV. This increased circulation leads to detachment of the LEV from the foil surface, resulting in the elimination of three-dimensional instabilities.

The suppression of LEV instabilities is also observed in in-phase pitching parallel foils operating under extreme foil proximity effect conditions. However, this phenomenon is not explored in this chapter due to the unique differences between in-phase and out-of-phase motions. These differences significantly impact the dynamics of LEVs, necessitating a dedicated investigation. Consequently, a comprehensive study focused on in-phase pitching motion will be the subject of our future research endeavors.

12.2 Summary

The outcomes of this chapter reveal the presence of a distinct instability mechanism induced by foil proximity effect on the LEVs of two pitching foils arranged side-by-side at $Re = 8000$. Under moderate foil proximity effect, a spanwise instability develops on the LEVs that remain attached to the surface. This instability intensifies due to continuous and prolonged interaction between the LEV and the foil surface. This leads to disintegration of the LEV before it reaches the trailing edge. Contrarily, in the case of extreme foil proximity effect, LEV detaches from the foil, reducing its interaction with the surface and thus preventing any spanwise instabilities. This detachment is facilitated by larger effective angle of attack, which amplifies the growth of secondary vortex beneath the shedding LEV. This effectively pushes the LEV away from the surface. These observations will be further substantiated through quantitative assessments to validate the critical role played by the foil proximity effect in both fostering and suppressing these vortex instabilities. The characterization of three-dimensional instabilities around pitching foils in a side-by-side configuration, as presented in this chapter and in chapter 11, fulfills Objective C—the final objective of this

study. Consequently, the next chapter will conclude this dissertation and provide recommendations for future work.

Chapter 13

CONCLUSIONS

The primary aim of this study was to investigate the vortex dynamics and propulsive performance of pitching foils in various spatial arrangements, representing tailfin of schooling fish. The investigation predominantly focused on the side-by-side configuration of two foils, although staggered and multi-foil arrangements were also examined. The Navier-Stokes equations were solved directly using both two-dimensional and three-dimensional setups. In two-dimensional simulations, mesh morphing method was employed to simulate the pitching motion of the foils, while three-dimensional simulations utilized the Overset Grid Assembly method. The objectives of the study were divided into three key areas: (1) exploring the unsteady vortex dynamics behind parallel pitching foils and their impact on propulsive performance metrics; (2) formulating scaling laws to estimate the steady-state propulsion performance of schooling foils; and (3) examining the three-dimensional instabilities around parallel pitching foils.

The study delved into the unsteady wake characteristics and performance of parallel pitching foils across a range of Strouhal numbers and separation distances, primarily focusing on Reynolds number of 4000. This Reynolds number, selected from a range between 1000 and 12000, was chosen because it is expected to be minimally influenced by viscous effects (Das et al., 2016) and is biologically relevant, representing the swimming of small-scale fish (Gazzola et al., 2014). The results presented here further validated this selection, as the wake patterns and interactions

observed at $Re = 1000$ demonstrated very little difference compared to those at $Re = 4000$. It was discovered that the unsteady wake features are intrinsically linked to both the Strouhal number and separation distance, with significant effects typically manifesting for ($St \geq 0.4$) at intermediate separation distances. In-depth investigations were conducted on in-phase ($\phi = 0$) and out-of-phase ($\phi = \pi$) motions, with a comprehensive analysis of their unique wake interaction mechanisms. At lower Strouhal numbers, the vortex streets generated by in-phase pitching foils converge into a single wake, whereas in the out-of-phase configuration, the wakes diverge from each other. In both scenarios, the wakes behind the foils maintain symmetry. Conversely, at higher Strouhal numbers, in-phase pitching foils undergo a transition from an asymmetric to a symmetric wake pattern. The initially parallel deflected vortex streets, gradually approach to each other over time, merging into a single wake. The final symmetric stage is similar to the pattern observed at lower St. Merging of the wakes coincides with the enhancements in propulsive efficiency by increasing thrust generation without a significant alteration in power requirements. On the contrary, out-of-phase pitching foils exhibit an opposite trend, evolving from a symmetric to an asymmetric pattern, with both states characterized by separated and diverging vortex streets.

The occurrence of symmetric wake patterns aligns with periods of zero total side force production by the foils, transitioning to non-zero values when wake symmetry is disrupted. This transition might reflect the behavior of red nose tetra fish, which are known to swim in parallel configurations and can alter their tail beat synchrony from out-of-phase to in-phase, or vice versa, mid-swimming (Ashraf et al., 2016, 2017). To replicate this natural phenomenon, simulations of four hybrid modes were conducted, where the phase difference is switched abruptly from out-of-phase to in-phase. The total side force production of the system drops to zero after the switch for three of the four modes. Therefore, it was conjectured that phase switching might have been employed by the schooling fish as a strategy to maintain their lateral position. Moreover, after the phase transition, the coefficients of thrust and power align with the metrics observed under pure in-phase pitching conditions, despite the wake structure resembling that of pure out-of-phase pitching foils. This observation implies a complex relationship between the wake dynamics and

the performance metrics of oscillating foils, challenging the notion of a straightforward correlation between the two.

A novel mathematical model was introduced based on fundamental flow variables including velocity, location and circulation of vortices to quantitatively distinguish vortex patterns in the wake. One of the key findings of this study was the elucidation of the physical mechanism of the wake merging process. When an oscillating foil experiences the jet deflection phenomenon, secondary structures separated from the primary street traversed in the other direction by making an angle with its parent vortex street. For in-phase pitching parallel foils, secondary structures from the vortex street of the lower foil interacted with the primary vortex street of the upper foil under certain kinematic conditions. This interaction triggers the wake merging process by influencing circulation of coherent structures in the upper part of the wake.

Two sets of scaling relations were derived to estimate the propulsive performance of pitching foils in schooling configurations. The first approach focuses on side-by-side configurations at a range of Reynolds number ($1000 \leq Re \leq 12000$), Strouhal number ($0.15 \leq St \leq 0.5$), phase difference ($0 \leq \phi \leq \pi$) and separation distance ($0.5c \leq y^* \leq 2c$), introducing two novel scaling terms that empirically incorporate these effects of separation distance and phase difference between the foils. Subsequently, a physics-based approach was employed to further extend these scaling relations to any given staggered configuration. This approach models foil-foil interactions by considering vortex-induced velocities. The developed relationships are anticipated to play a pivotal role in offering essential insights for designing and optimizing bio-inspired underwater propulsors and energy harvesting systems.

The scaling coefficients revealed that only the term representing fluid drag on the propulsors was significantly influenced by Reynolds number, while all other terms showed minimal to no dependence. This supports the earlier conclusion that the fundamentals of wake dynamics remain consistent across different Reynolds numbers. Collectively, these findings suggest that wake interactions between oscillating foils in schooling configurations are primarily governed by inviscid mechanisms, at least within the studied range.

The dynamics of three-dimensional instabilities around infinite span pitching foils placed in side-by-side configurations were explored at a Reynolds number of 8000. A novel instability mechanism, triggered by foil proximity effect on the legs of trailing edge vortices during their roll-up, was identified. This instability presents itself through the formation of secondary vortical structures on the surface of the foil with circulation opposite to that of the trailing edge vortices, leading to a distinctive double-necking phenomenon on the legs of the trailing edge vortices. The first neck is amalgamated into the trailing edge vortex, whereas the second neck detaches from the braid region, moving downstream independently. The foil proximity effect was found to be directly linked to the emergence of intricate three-dimensional wake structures, marked by the distinct presence of coherent structures at reduced distances between the foils. On the other hand, it was also observed that extreme foil proximity effect could suppress the formation of LEV instabilities. This suppression was attributed to the amplification of LEV circulations by the foil proximity effect, which ultimately leads to the detachment of the LEVs from the foil surface. Once detached, the LEVs maintain their two-dimensional structure as their interaction with the surface is significantly reduced. This highlights the role of foil proximity effect in inhibiting the development of three-dimensional structures.

13.1 Future Work

While this study provides a thorough examination of the wake dynamics and performance metrics of schooling foils, several areas warrant further investigation. As noted in chapter 9, although the thrust and power equations align closely with simulation data, the efficiency estimations were less accurate. This discrepancy suggests that the current definition of efficiency may not fully capture the dynamics specific to schooling foils. The complex interactions between bodies and between bodies and vortices in such nonlinear dynamic systems necessitate a more precise definition of efficiency. This issue is particularly pronounced at slower foil motions, where thrust generation can be minimal or even negative, highlighting potential shortcomings in the drag component of the

scaling equations. In this dissertation, the drag term is approximated to scale solely with the frontal area of the foil, overlooking the effects of foil motion. Developing a more comprehensive drag term that accounts for oscillation effects could substantially enrich the existing body of literature.

Although the Reynolds number was shown to have minimal impact on the wake interactions of schooling foils within the studied range, it significantly influences wake patterns behind a single foil for $Re < 1000$ (Das et al., 2016). This suggests that unique wake interaction mechanisms may emerge behind oscillating foils in multi-foil configurations at lower Reynolds numbers. Furthermore, this range is biologically relevant, as the Reynolds number range of $Re = 10 - 1000$ aligns with the natural swimming conditions of larvae (Gazzola et al., 2014). Therefore, a comprehensive analysis within this range could provide valuable insights into a better understanding of larvae swimming in schooling configurations.

Aspect ratio and flexibility are two critical factors influencing the flow dynamics around oscillating foils, with significant effects on the wake and performance characteristics of single oscillating foils. For instance, Marais et al. (2012) demonstrated that foil flexibility could inhibit the formation of deflected wakes. Similarly, Calderon et al. (2014) observed a suppression of deflected wakes in plunging foils with finite aspect ratios. Furthermore, Chiereghin et al. (2020) examined the three-dimensional effects on LEVs of high aspect ratio wings due to tip vortices. Despite these findings, the interplay between these factors and schooling configurations remains largely unexplored. Given their potential impact on wake behavior and propulsion performance, these aspects warrant further investigation.

Bibliography

Akhtar, I., Mittal, R., Lauder, G. V., and Drucker, E. (2007). Hydrodynamics of a biologically inspired tandem flapping foil configuration. *Theoretical and Computational Fluid Dynamics*, 21(3):155–170.

Akoz, E. and Moored, K. W. (2019). Unsteady propulsion by an intermittent swimming gait. *J. Fluid Mech.*, 834:149–172.

Ambolkar, M. and Arumuru, V. (2022). Propulsive performance of a pitching foil in a side-by-side arrangement with auxiliary pitching foil. *J. Fluids Struct.*, 110:103537.

Andersen, A., Bohr, T., Schnipper, T., and Walther, J. H. (2014). Wake structure and thrust generation of a flapping foil in two-dimensional flow. *J. Fluid Mech.*, 812(R4).

Anderson, J., Streitlien, K., Barrett, D., and Triantafyllou, M. (1998). Oscillating foils of high propulsive efficiency. *J. Fluid Mech.*, 360:41–72.

Anderson, J. M. (1996). *Vorticity Control for Efficient Propulsion*. PhD thesis, MASSACHUSETTS INST. OF TECH.

Ashraf, I., Bradshaw, H., Ha, T. T., Halloy, J., Godoy-Diana, R., and Thiria, B. (2017). Simple phalanx pattern leads to energy saving in cohesive fish schooling. *Proc. Natl. Acad. Sci. USA*, 114(36):9599–9604.

Ashraf, I., Godoy-Diana, R., Halloy, J., Collignon, B., and Thiria, B. (2016). Synchronization and collective swimming patterns in fish (hemigrammus bleheri). *J. R. Soc. Interface*, 13:20160734.

Ay, M., Korkmaz, D., Ozmen Koca, G., Bal, C., Akpolat, Z. H., and Bingol, M. C. (2018). Mechatronic design and manufacturing of the intelligent robotic fish for bio-inspired swimming modes. *Electronics*, 7(7):118.

Ayancik, F., Fish, F. E., and Moored, K. W. (2020). Three-dimensional scaling laws of cetacean propulsion characterize the hydrodynamic interplay of flukes' shape and kinematics. *J. R. Soc. Interface*, 17:20190655.

Ayancik, F., Zhong, Q., Quinn, D. B., Brandes, A., Bart-Smith, H., and Moored, K. W. (2019). Scaling laws for the propulsive performance of three-dimensional pitching propulsors. *J. Fluid Mech.*, 871:1117–1138.

Balachandar, S. (2009). A scaling analysis for point–particle approaches to turbulent multiphase flows. *Int. J. Multiph. Flow*, 35(9):801–810.

Bao, Y., Zhou, D., Tao, J. J., Peng, Z., Zhu, H. B., Sun, Z. L., and Tong, H. L. (2017). Dynamic interference of two anti-phase flapping foils in side-by-side arrangement in an incompressible flow. *Phys. Fluids*, 29:033601.

Benton, S. I. and Bons, J. P. (2014). Three-dimensional instabilities in vortex/wall interactions: Linear stability and flow contro. In *52nd Aerospace Sciences Meeting*, page 1267.

Birch, J. M. and Dickinson, M. H. (2001). Spanwise flow and the attachment of the leading-edge vortex on insect wings. *Nature*, 412(6848):729–733.

Blevins, E. and Lauder, G. V. (2013). Swimming near the substrate: a simple robotic model of stingray locomotion. *Bioinspir. Biomim.*, 8(1):016005.

Bomphrey, R. J., Lawson, N. J., Harding, N. J., Taylor, G. K., and Thomas, A. L. R. (2005). The aerodynamics of manduca sexta: digital particle image velocimetry analysis of the leading-edge vortex. *J. Exp. Biol.*, 208(6):1079–1094.

Borazjani, I. and Daghooghi, M. (2013). The fish tail motion forms an attached leading edge vortex. *Proceedings of the Royal Society B: Biological Sciences*, 280(1756):20122071.

Borazjani, I. and Sotiropoulos, F. (2008). Numerical investigation of the hydrodynamics of carangiform swimming in the transitional and inertial flow regimes. *J. Exp. Biol.*, 211(10):1541–1558.

Borazjani, I. and Sotiropoulos, F. (2010). On the role of form and kinematics on the hydrodynamics of self-propelled body/caudal fin swimming. *Journal of Experimental Biology*, 213(1):89–107.

Boschitsch, B. M., Dewey, P. A., and Smits, A. J. (2014). Propulsive performance of unsteady tandem hydrofoils in an in-line configuration. *Phys. Fluids*, 26:051901.

Bottom Ii, R., Borazjani, I., Blevins, E., and Lauder, G. (2016). Hydrodynamics of swimming in stingrays: numerical simulations and the role of the leading-edge vortex. *J. Fluid Mech.*, 788:407–443.

Bratt, J. B. (1950). Flow patterns in the wake of an oscillating aerofoil. Reports and Memoranda 2773, Aeronautical Research Council.

Bristol, R. L., Ortega, J. M., Marcus, P. S., and Savaş, (2004). On cooperative instabilities of parallel vortex pairs. *J. Fluid Mech.*, 517:331–358.

Buren, T. V., Floryan, D., and Smits, A. J. (2019a). *Bio-inspired underwater propulsors*, chapter 11. Cambridge University Press.

Buren, T. V., Floryan, D., and Smits, A. J. (2019b). Scaling and performance of simultaneously heaving and pitching foils. *AIAA J.*, 57(9):3666–3677.

Calderon, D. E., Cleaver, D. J., Gursul, I., and Wang, Z. (2014). On the absence of asymmetric wakes for periodically plunging finite wings. *Phys. Fluids*, 26:071907.

Cerretelli, C. and Williamson, C. H. K. (2003). The physical mechanism for vortex merging. *J. Fluid Mech.*, 475:41–77.

Chandar, D. D. (2019). On overset interpolation strategies and conservation on unstructured grids in openfoam. *Comput. Phys. Commun.*, 239:72–83.

Chiereghin, N., Bull, S., Cleaver, D. J., and Gursul, I. (2020). Three-dimensionality of leading-edge vortices on high aspect ratio plunging wings. *Physical Review Fluids*, 5(6):064701.

Chiereghin, N., Cleaver, D. J., and Gursul, I. (2019). Unsteady lift and moment of a periodically plunging airfoil. *AIAA J.*, 57(1):208–222.

Clark, R. P. and Smits, A. J. (2006). Thrust production and wake structure of a batoid-inspired oscillating fin. *J. Fluid Mech.*, 562:415–429.

Cleaver, D. J., Wang, Z., and Gursul, I. (2012). Bifurcating flows of plunging aerofoils at high strouhal numbers. *J. Fluid Mech.*, 708:349–376.

Coulliette, C. and Plotkin, A. (1996). Aerofoil ground effect revisited. *The Aeronautical Journal*, 100(992):65–74.

Crouch, J. D., Miller, G. D., and Spalart, P. R. (2001). Active-control system for breakup of airplane trailing vortices. *AIAA J.*, 39(12):2374–2381.

Crow, S. C. (1970). Stability theory for a pair of trailing vortices. *AIAA J.*, 8(12):2172–2179.

Daghooghi, M. and Borazjani, I. (2015). The hydrodynamic advantages of synchronized swimming in a rectangular pattern. *Bioinspir. Biomim.*, 10:056018.

Das, A., Shukla, R. K., and Govardhan, R. N. (2016). Existence of a sharp transition in the peak propulsive efficiency of a low-re pitching foil. *J. Fluid Mech.*, 800:307–326.

De Graaff, D. B. and Eaton, J. K. (2000). Reynolds-number scaling of the flat-plate turbulent boundary layer. *J. Fluid Mech.*, 422:319–346.

Deng, J. and Caulfield, C. P. (2015). Three-dimensional transition after wake deflection behind a flapping foil. *Physical Review E*, 91:043017.

Deng, J., Sun, L., and Shao, X. (2015). Dynamical features of the wake behind a pitching foil. *Physical Review E*, 92:063013.

Deng, J., Sun, L., Teng, L., Pan, D., and Shao, X. (2016). The correlation between wake transition and propulsive efficiency of a flapping foil: A numerical study. *Phys. Fluids*, 28(9):094101.

Dewey, P. A., Quinn, D. B., Boschitsch, B. M., and Smits, A. J. (2014). Propulsive performance of unsteady tandem hydrofoils in a side-by-side configuration. *Phys. Fluids*, 26:041903.

Dong, G.-J. and Lu, X.-Y. (2007). Characteristics of flow over traveling wavy foils in a side-by-side arrangement. *Phys. Fluids*, 19(5):057107.

Ellington, C. P., Van Den Berg, C., Willmott, A. P., and Thomas, A. L. R. (1996). Leading-edge vortices in insect flight. *Nature*, 384(6610):626–630.

Eloy, C. (2012). Optimal strouhal number for swimming animals. *J. Fluids Struct.*, 30:205–218.

Eslam Panah, A., Akkala, J. M., and Buchholz, J. H. (2015). Vorticity transport and the leading-edge vortex of a plunging airfoil. *Exp. Fluids*, 56:1–15.

Fish, F. E., Fegely, J. F., and Xanthhopoulos, C. J. (1991). Burst-and-coast swimming in schooling fish (notemigonus crysoleucas) with implications for energy economy. *Comp. Biochem. Physiol*, 100A(3):633–637.

Fish, F. E., Legac, P., Williams, T. M., and Wei, T. (2014). Measurement of hydrodynamic force generation by swimming dolphins using bubble dpiv. *Journal of Experimental Biology*, 217(2):252–260.

Floryan, D., Buren, T. V., Rowley, C., and Smits, A. J. (2017). Scaling the propulsive performance of heaving and pitching foils. *J. Fluid Mech.*, 822:386–397.

Floryan, D., Buren, T. V., and Smits, A. J. (2018). Efficient cruising for swimming and flying animals is dictated by fluid drag. *PNAS*, 115(32):8116–8118.

Floryan, D., Buren, T. V., and Smits, A. J. (2020). Swimmers' wake structures are not reliable indicators of swimming performance. *Bioinspir. Biomim.*, 15:024001.

Floryan, D., Van Buren, T., and Smits, A. J. (2019). Large-amplitude oscillations of foils for efficient propulsion. *Physical Review Fluids*, 4(9):093102.

Garrick, I. E. (1936). Propulsion of a flapping and oscillating airfoil. Rept 567, Langley Memorial Aeronautical Lab.

Gazzola, M., Argentina, M., and Mahadevan, L. (2014). Scaling macroscopic aquatic locomotion. *Nature Physics*, 10(10):758–761.

Godoy-Diana, R., Aider, C. M. J. L., and Wesfreid, J. E. (2009). A model for the symmetry breaking of the reverse bénard-von kármán vortex street produced by a flapping foil. *J. Fluid Mech.*, 622:23–32.

Godoy-Diana, R., Aider, J. L., and Wesfreid, J. E. (2008). Transitions in the wake of a flapping foil. *Physical Review E*, 77:016308.

Gopalkrishnan, R. (1993). *Vortex-Induced Forces on Oscillating Bluff Cylinders*. PhD thesis, Woods Hole Oceanographic Institution.

Gopalkrishnan, R., Triantafyllou, M. S., Triantafyllou, G. S., and Barrett, D. (1994). Active vorticity control in a shear flow using a flapping foil. *J. Fluid Mech.*, 274:1–21.

Griffin, O. M. and Ramberg, S. E. (1959). The vortex-street wakes of vibrating cylinders. *J. Fluid Mech.*, 66(3):553–576.

Han, T., Zhong, Q., Mivehchi, A., Quinn, D. B., and Moored, K. W. (2024). Revealing the mechanism and scaling laws behind equilibrium altitudes of near-ground pitching hydrofoils. *J. Fluid Mech.*, 978:A5.

Harvey, J. K. and Perry, F. J. (1971). Flowfield produced by trailing vortices in the vicinity of the ground. *AIAA J.*, 9(8):1659–1660.

Heathcote, S. and Gursul, I. (2007). Jet switching phenomenon for a periodically plunging airfoil. *Phys. Fluids*, 19:027104.

Hemelrijk, C., Reid, D., Hildenbrandt, H., and Padding, J. (2015). The increased efficiency of fish swimming in a school. *Fish and Fisheries*, 16(3):511–521.

Hemmati, A., Buren, T. V., and Smits, A. J. (2019a). Effects of trailing edge shape on vortex formation by pitching panels of small aspect ratio. *Phys. Rev. Fluids*, 4:033101.

Hemmati, A., Wood, D. H., and Martinuzzi, R. J. (2016). Characteristics of distinct flow regimes in the wake of an infinite span normal thin flat plate. *International Journal of Heat and Fluid Flow*, 62:423–436.

Hemmati, A., Wood, D. H., and Martinuzzi, R. J. (2018). On simulating the flow past a normal thin flat plate. *Journal of Wind Engineering and Industrial Aerodynamics*, 174:170–187.

Hemmati, A., Wood, D. H., and Martinuzzi, R. J. (2019b). Wake dynamics and surface pressure variations on two-dimensional normal flat plates. *AIP Advances*, 9(4).

Herskin, J. and Steffensen, J. F. (1998). Energy savings in sea bass swimming in a school: measurements of tail beat frequency and oxygen consumption at different swimming speeds. *Journal of Fish Biology*, 53(2):366–376.

Huang, M.-K. and Chow, C.-Y. (1982). Trapping of a free vortex by joukowski airfoils. *AIAA J.*, 20(3):292–298.

Huera-Huarte, F. J. (2018). Propulsive performance of a pair of pitching foils in staggered configurations. *J. Fluids Struct.*, 81:1–13.

Hunt, J. C., Wray, A. A., and Moin, P. (1988). Eddies, streams, and convergence zones in turbulent flows. In *Proceedings of the Summer Program 1988*, pages 193—-208. Center for Turbulence Research.

Jones, K. D., Dohring, C. M., and Platzer, M. F. (1998). Experimental and computational investigation of the knoller-betz effect. *AIAA J.*, 36(7):1240–1246.

Kern, S. and Koumoutsakos, P. (2006). Simulations of optimized anguilliform swimming. *J. Exp. Biol.*, 209(24):4841–4857.

Kerswell, R. R. (2002). Elliptical instability. *Annual Review of Fluid Mechanics*, 34(1):83–113.

Khalid, M., Wang, J., Akhtar, I., Dong, H., Liu, M., and Hemmati, A. (2021a). Larger wavelengths suit hydrodynamics of carangiform swimmers. *Physical Review Fluids*, 6(7):073101.

Khalid, M., Wang, J., Akhtar, I., Dong, H., Liu, M., and Hemmati, A. (2021b). Why do anguilliform swimmers perform undulation with wavelengths shorter than their bodylengths? *Phys. Fluids*, 33(3):031911.

Khalid, M. S. U. and Akhtar, I. (2017). Nonlinear reduced-order models for aerodynamic lift of oscillating airfoils. *Journal of Computational and Nonlinear Dynamics*, 12(5):051019.

Khalid, M. S. U., Akhtar, I., and Dong, H. (2016). Hydrodynamics of a tandem fish school with asynchronous undulation of individuals. *J. Fluids Struct.*, 66:19–35.

Khalid, M. S. U., Akhtar, I., and Durrani, N. I. (2015). Analysis of strouhal number based equivalence of pitching and plunging airfoils and wake deflection. *Proceedings of the Institution of Mechanical Engineers, Part G: Journal of Aerospace Engineering*, 229(8):1423–1434.

Khalid, M. S. U., Wang, J., Dong, H., and Liu, M. (2020). Flow transitions and mapping for undulating swimmers. *Phys. Rev. Fluids*, 5:063104.

Koochesfahani, M. M. (1989). Vortical patterns in the wake of an oscillating foil. *AIAA J.*, 27:1200–1205.

Kurt, M., Cochran-Carney, J., Zhong, Q., Mivehchi, A., Quinn, D. B., and Moored, K. W. (2019). Swimming freely near the ground leads to flow-mediated equilibrium altitudes. *J. Fluid Mech.*, 875:R1.

Kurt, M. and Moored, K. (2018a). Unsteady performance of finite-span pitching propulsors in side-by-side arrangements. In *2018 Fluid Dynamics Conference*, page 3732.

Kurt, M. and Moored, K. W. (2018b). Flow interactions of two-and three-dimensional networked bio-inspired control elements in an in-line arrangement. *Bioinspir. Biomim.*, 13(4):045002.

Lagopoulos, N. S., Weymouth, G. D., and Ganapathisubramani, B. (2020). Deflected wake interaction of tandem flapping foils. *J. Fluid Mech.*, 903:A9.

Leweke, T., Le Dizes, S., and Williamson, C. H. (2016). Dynamics and instabilities of vortex pairs. *Annual Review of Fluid Mechanics*, 48:507–54.

Leweke, T. and Williamson, C. H. (1998). Cooperative elliptic instability of a vortex pair. *J. Fluid Mech.*, 360:85–119.

Leweke, T. and Williamson, C. H. (2011). Experiments on long-wavelength instability and reconnection of a vortex pair. *Phys. Fluids*, 23(024101).

Lewin, G. C. and Haj-Hariri, H. (2003). Modelling thrust generation of a two-dimensional heaving airfoil in a viscous flow. *J. Fluid Mech.*, 492:339–362.

Li, G., Kolomenskiy, D., Liu, H., Thiria, B., and Godoy-Diana, R. (2019). On the energetics and stability of a minimal fish school. *PLoS One*, 14(8):e0215265.

Li, L., Nagy, M., Graving, J. M., Bak-Coleman, J., Xie, G., and Couzin, I. D. (2020a). Vortex phase matching as a strategy for schooling in robots and in fish. *Nature communications*, 11(1):1–9.

Li, L., Ravi, S., Xie, G., and Couzin, I. D. (2021). Using a robotic platform to study the influence of relative tailbeat phase on the energetic costs of side-by-side swimming in fish. *Proceedings of the Royal Society A*, 477(2249):20200810.

Li, Z. Y., Feng, L. H., Kissing, J., Tropea, C., and Wang, J. J. (2020b). Experimental investigation on the leading-edge vortex formation and detachment mechanism of a pitching and plunging plate. *J. Fluid Mech.*, 901(A17).

Liang, C., Ou, K., Premasuthan, S., Jameson, A., and Wang, Z. J. (2011). High-order accurate simulations of unsteady flow past plunging and pitching airfoils. *Computers & Fluids*, 40:236–248.

Liao, J. C., Beal, D. N., Lauder, G. V., and Triantafyllou, M. S. (2003). Fish exploiting vortices decrease muscle activity. *Science*, 302(5650):1566–1569.

Liu, G., Ren, Y., Dong, H., Akanyeti, O., Liao, J. C., and Lauder, G. V. (2017). Computational analysis of vortex dynamics and performance enhancement due to body–fin and fin–fin interactions in fish-like locomotion. *J. Fluid Mech.*, 829:65–88.

Liu, L., Zhong, Q., Han, T., Moored, K. W., and Quinn, D. B. (2022). Fine-tuning near-boundary swimming equilibria using asymmetric kinematics. *Bioinspir. Biomim.*, 18(1):016011.

Liu, T., Wang, S., Zhang, X., and He, G. (2015). Unsteady thin-airfoil theory revisited: application of a simple lift formula. *AIAA J.*, 53(6):1492–1502.

Marais, C., Thiria, B., Wesfreid, J. E., and Godoy-Diana, R. (2012). Stabilizing effect of flexibility in the wake of a flapping foil. *J. Fluid Mech.*, 710:659–669.

Marras, S., Killen, S. S., Lindström, J., McKenzie, D. J., Steffensen, J. F., and Domenici, P. (2015). Fish swimming in schools save energy regardless of their spatial position. *Behavioral ecology and sociobiology*, 69(2):219–226.

Marras, S. and Porfiri, M. (2012). Fish and robots swimming together: attraction towards the robot demands biomimetic locomotion. *J. R. Soc. Interface*, 9(73):1856–1868.

Melander, M. V., McWilliams, J. C., and Zabusky, N. J. (1987). Axisymmetrization and vorticity-gradient intensification of an isolated two-dimensional vortex through filamentation. *J. Fluid Mech.*, 178:137–159.

Meng, X., Chen, Z., Zhang, Y., and Chen, G. (2022). Aerodynamic performance and flow mechanism of multi-flapping wings with different spatial arrangements. *Phys. Fluids*, 34(2):021907.

Menon, K. and Mittal, R. (2021). Significance of the strain-dominated region around a vortex on induced aerodynamic loads. *J. Fluid Mech.*, 918:R3.

Meunier, P., Le Dizes, S., and Leweke, T. (2005). Physics of vortex merging. *Comptes Rendus Physique*, 6(4-5):431–450.

Mivehchi, A., Zhong, Q., Kurt, M., Quinn, D. B., and Moored, K. W. (2021). Scaling laws for the propulsive performance of a purely pitching foil in ground effect. *J. Fluid Mech.*, 919:R1.

Moin, P. and Mahesh, K. (1998). Direct numerical simulation: a tool in turbulence research. *Annual Review of Fluid Mechanics*, 30(1):539–578.

Moored, K. W. and Quinn, D. B. (2019). Inviscid scaling laws of a self-propelled pitching airfoil. *AIAA J.*, 57(9):3686–3700.

Naguib, A. M., Vitek, J., and Koochesfahani, M. M. (2011). Finite-core vortex array model of the wake of a periodically pitching airfoil. *AIAA J.*, 49(7):1542–1550.

Najjar, F. M. and Balachandar, S. (1998). Low-frequency unsteadiness in the wake of a normal flat plate. *J. Fluid Mech.*

Newbolt, J. W., Zhang, J., and Ristroph, L. (2019). Flow interactions between uncoordinated flapping swimmers give rise to group cohesion. *Proceedings of the National Academy of Sciences*, 116(7):2419–2424.

Obabko, A. V. and Cassel, K. W. (2002). Navier–stokes solutions of unsteady separation induced by a vortex. *J. Fluid Mech.*, 465:99–130.

Ortega, J. M., Bristol, R. L., and Savas, O. (2002). Wake alleviation properties of triangular-flapped wings. *AIAA J.*, 40(4):709–721.

Ortega, J. M., Bristol, R. L., and Savaş, (2003). Experimental study of the instability of unequal-strength counter-rotating vortex pairs. *J. Fluid Mech.*, 473:35–84.

Pan, Y., Dong, X., Zhu, Q., and Yue, D. K. (2012). Boundary-element method for the prediction of performance of flapping foils with leading-edge separation. *J. Fluid Mech.*, 698:446–467.

Peace, A. J. and Riley, N. (1983). A viscous vortex pair in ground effect. *J. Fluid Mech.*, 129:409–426.

Peng, Z. and Zhu, Q. (2009). Energy harvesting through flow-induced oscillations of a foil. *Phys. Fluids*, 21:123602.

Pourfarzan, A. and Wong, J. G. (2022). Constraining optimum swimming strategies in plesiosaurs: The effect of amplitude ratio on tandem pitching foils. *Phys. Fluids*, 34(5):051908.

Quinn, D. B., Moored, K. W., Dewey, P. A., and Smits, A. J. (2014). Unsteady propulsion near a solid boundary. *J. Fluid Mech.*, 742:152–170.

Rabinovitch, J., Brion, V., and Blanquart, G. (2012). Effect of a splitter plate on the dynamics of a vortex pair. *Phys. Fluids*, 24:074110.

Raj, K. M. and Arumuru, V. (2020). Jet deflection by two side-by-side arranged hydrofoils pitching in a quiescent fluid. *AIP Advances*, 10(10):105128.

Reynolds, O. (1883). Xxix. an experimental investigation of the circumstances which determine whether the motion of water shall be direct or sinuous, and of the law of resistance in parallel channels. *Philosophical Transactions of the Royal society of London*, 174:935–982.

Rossow, V. J. (1978). Lift enhancement by an externally trapped vortex. *J. Aircr.*, 15(9):618–62.

Ryan, K., Butler, C. J., and Sheard, G. J. (2012). Stability characteristics of a counter-rotating unequal-strength batchelor vortex pair. *J. Fluid Mech.*, 696:374–401.

Saffman, P. and Sheffield, J. (1977). Flow over a wing with an attached free vortex. *Studies in Applied Mathematics*, 57(2):107–117.

Sane, S. P. (2003). The aerodynamics of insect flight. *Journal of experimental biology*, 206(23):4191–4208.

Sarkar, S. and Sarkar, S. (2010). Vortex dynamics of a cylinder wake in proximity to a wall. *J. Fluids Struct.*, 26(1):19–40.

Schaefer, J. W. and Eskinazi, S. (1959). An analysis of the vortex street generated in a viscous fluid. *J. Fluid Mech.*, 6(2):241–260.

Schnipper, T., Andersen, A., and Bohr, T. (2009). Vortex wakes of a flapping foil. *J. Fluid Mech.*, 663:411–423.

Scorer, R. S. and Davenport, L. J. (1970). Contrails and aircraft downwash. *J. Fluid Mech.*, 43(3):451–464.

Sedov, L. I. (1965). Two-dimensional problems in hydrodynamics and aerodynamics. *Interscience Publ. (New York)*, Chap. II-6.

Senturk, U. and Smits, A. J. (2018). Numerical simulations of the flow around a square pitching panel. *J. Fluids Struct.*, 76:454–468.

Senturk, U. and Smits, A. J. (2019). Reynolds number scaling of the propulsive performance of a pitching airfoil. *AIAA J.*, 57(7):2663–2669.

Sfakiotakis, M., L., D. M., and D., J. B. C. (1999). Review of fish swimming modes for aquatic locomotion. *IEEE Journal of oceanic engineering*, 24(2):237–252.

Shadwick, R. E. and Syme, D. A. (2008). Thunniform swimming: muscle dynamics and mechanical power production of aerobic fibres in yellowfin tuna (*Thunnus albacares*). *J. Exp. Biol.*, 211(10):1603–1611.

Shao, X.-m. and Pan, D.-y. (2011). Hydrodynamics of a flapping foil in the wake of a d-section cylinder. *Journal of Hydrodynamics, Ser. B*, 23(4):422–430.

Shaw, E. (1962). The schooling of fishes. *Scientific American*, 206(6):128–141.

Shoele, K. and Zhu, Q. (2015). Performance of synchronized fins in biomimetic propulsion. *Bioinspiration & biomimetics*, 10(2):026008.

Simsek, E., Freeman, B., Senturk, U., and Hemmati, A. (2020). Effect of in-line tandem configuration on performance and scaling of pitching hydrofoils. *AIAA J.*, 58(11):4620–4628.

Smits, A. J. (2019). Undulatory and oscillatory swimming. *J. Fluid Mech.*, 874(P1).

Son, O., Gao, A. K., Gursul, I., Cantwell, C. D., Wang, Z., and Sherwin, S. J. (2022). Leading-edge vortex dynamics on plunging airfoils and wings. *J. Fluid Mech.*, 940:A28.

Spalart, P. R. (1998). Airplane trailing vortices. *Annual Review of Fluid Mechanics*, 30(1):107–138.

Strand, E., Jørgensen, C., and Huse, G. (2005). Modelling buoyancy regulation in fishes with swimbladders: bioenergetics and behaviour. *Ecol. Model.*, 185(2-4):309–327.

Svendsen, J. C., Skov, J., Bildsoe, M., and Steffensen, J. F. (2003). Intra-school positional preference and reduced tail beat frequency in trailing positions in schooling roach under experimental conditions. *Journal of fish biology*, 62(4):834–846.

Taylor, G. K., Nudds, R. L., and Thomas, A. L. R. (2003). Flying and swimming animals cruise at a strouhal number tuned for high power efficiency. *Nature*, 425:707–711.

Theodorsen, T. (1935). General theory of aerodynamic instability and the mechanism of flutter. NACA Tech. Rep. 496.

Tisovska, P. (2019). Description of the overset mesh approach in esi version of openfoam. In *Proceedings of CFD with OpenSource Software.*

Triantafyllou, G. S., Triantafyllou, M., and Grosenbaugh, M. A. (1993). Optimal thrust development in oscillating foils with application to fish propulsion. *J. Fluids Struct.*, 7:205–224.

Triantafyllou, M. S. and Triantafyllou, G. (1995). An efficient swimming machine. *Scientific American*, 272:64–70.

Triantafyllou, M. S., Triantafyllou, G., and Gopalkrishnan, R. (1991). Wake mechanics for thrust generation in oscillating foils. *Phys. Fluids*, 3(12):2835–2837.

Triantafyllou, M. S., Triantafyllou, G., and Yue, D. K. P. (2000). Hydrodynamics of fishlike swimming. *Annu. Rev. Fluid Mech*, 32:33–53.

Van Buren, T., Floryan, D., Quinn, D., and Smits, A. J. (2017). Nonsinusoidal gaits for unsteady propulsion. *Physical Review Fluids,*, 2(5):053101.

Van Buren, T., Floryan, D., Wei, N., and Smits, A. J. (2018). Flow speed has little impact on propulsive characteristics of oscillating foils. *Physical Review Fluids*, 3(1):013103.

Verma, S. and Hemmati, A. (2020). Performance of overset mesh in modeling the wake of sharp-edge bodies. *Computation*, 8(3):66.

Verma, S. and Hemmati, A. (2021). Evolution of wake structures behind oscillating hydrofoils with combined heaving and pitching motion. *Journal of Fluid Mech.*, 927:A–23.

Verma, S. and Hemmati, A. (2023). Influence of kinematics on the growth of secondary wake structures behind oscillating foils. *International Journal of Heat and Fluid Flow*, 102:109146.

Verma, S., Khalid, M. S. U., and Hemmati, A. (2023). On the association of kinematics, spanwise instability and growth of secondary vortex structures in the wake of oscillating foils. *Proceedings of the Royal Society A*, 479(2276):20230353.

Viswanathan, K. (2006). Scaling laws and a method for identifying components of jet noise. *AIAA J.*, 44(10):2274–2285.

von Ellenrieder, K. D. and Pothos, S. (2008). Piv measurements of the asymmetric wake of a two dimensional heaving hydrofoil. *Exp. Fluids*, 44:733–745.

Wang, B., Kronenburg, A., Dietzel, D., and Stein, O. T. (2017). Assessment of scaling laws for mixing fields in inter-droplet space. *Proc. Combust. Inst.*, 26(2):2451–2458.

Webb, P. W. (1984). Form and function in fish swimming. *Scientific American*, 251(1):72–83.

Weihs, D. (1973). Hydromechanics of fish schooling. *Nature (London)*, 241:290–291.

Williamson, C. H., Leweke, T., Asselin, D. J., and Harris, D. M. (2014). Phenomena, dynamics and instabilities of vortex pairs. *Fluid Dyn. Res.*, 6(46):061425.

Williamson, C. H. K. (1996). Three-dimensional wake transition. *J. Fluid Mech.*, 328:345–407.

Williamson, C. H. K. and Roshko, A. (1988). Vortex formation in the wake of an oscillating cylinder. *J. Fluid Mech.*, 2:355–381.

Wong, J. G. and Rival, D. E. (2015). Determining the relative stability of leading-edge vortices on nominally two-dimensional flapping profiles. *J. Fluid Mech.*, 766:611–625.

Xiong, Z. and Liu, X. (2019). Numerical investigation on evolutionary characteristics of the leading-edge vortex induced by flapping caudal fin. *Phys. Fluids*, 31(12):125117.

Yu, H., Liu, B., Wang, C., Liu, X., Lu, X. Y., and Huang, H. (2022). Deep-reinforcement-learning-based self-organization of freely undulatory swimmers. *Phys. Rev. E*, 105(4):045105.

Zhang, H., Fey, U., Noack, B. R., Konig, M., and Eckelmann, H. (1994). On the transition of the cylinder wake. *Phys. Fluids*, 7(4):779–794.

Zhang, X., He, G., Wang, S., and Zhang, X. (2018). Locomotion of a bioinspired flyer powered by one pair of pitching foils. *Physical Review Fluids*, 3:013102.

Zhu, Q., Wolfgang, M., Yue, D., and Triantafyllou, M. (2002). Three-dimensional flow structures and vorticity control in fish-like swimming. *J. Fluid Mech.*, 468:1–28.

Zurman-Nasution, A., Ganapathisubramani, B., and Weymouth, G. (2020). Influence of three-dimensionality on propulsive flapping. *J. Fluid Mech.*, 886.

Appendix A

Overlapping Overset Grids

Initially, a numerical setup involving larger overset grids that overlap around the centerline is generated to simulate the flow over infinite span pitching foils. However, preliminary results from this setup exhibited non-physical vortical structures in the flow ahead of the foils, as shown in figure A.1. It is assumed that these structures arise due to the amplification of interpolation errors in the overlapping region, where results are interpolated between the background grid and the two overset grids. Nevertheless, a more comprehensive investigation is needed to determine the exact cause. Consequently, a setup with non-overlapping overset grids, as explained in chapter 3, is generated to avoid this issue.

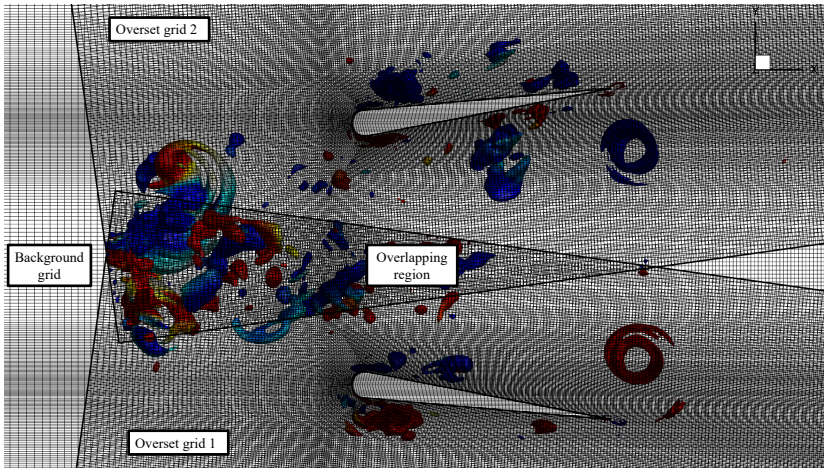

Figure A.1: A numerical setup involving overlapping overset grids depicting iso-surfaces of Q-criterion.